FIRST-PRINCIPLES STUDY OF THE LI ADSORPTION ON VARIOUS CARBON HYBRID SYSTEMS

A Dissertation
Presented to
The Academic Faculty

by

Wonsang Koh

In Partial Fulfillment
of the Requirements for the Degree
Doctor of Philosophy in the
School of Physics

Georgia Institute of Technology
August 2011

FIRST-PRINCIPLES STUDY OF THE LI ADSORPTION ON VARIOUS CARBON HYBRID SYSTEMS

Approved by:

Dr. Seung Soon Jang, Advisor
School of Materials Science and Engineering
Georgia Institute of Technology

Dr. Harold Kim
School of Physics
Georgia Institute of Technology

Dr. Andrew Zangwill
School of Physics
Georgia Institute of Technology

Dr. Meisha Shofner
School of Materials Science and Engineering
Georgia Institute of Technology

Dr. Zhigang Jiang
School of Physics
Georgia Institute of Technology

Date Approved: June 13, 2011

ACKNOWLEDGEMENTS

First of all, I would like to thank Prof. Jang for his unlimited support throughout the pursuit of my Ph.D. degree. It has been my great honor to have him as my advisor. His encouragement and inspiration led me to complete this thesis work. In addition, I also would like to thank Prof. Zangwill, Prof. Shofner, Prof. Jiang and Prof. Kim for serving on my thesis committee. I appreciate their advice and support, which was invaluable to my degree completion.

I also would like to acknowledge the members of the Computational Nanobio Technology (CNBT) group. I specially thanks to Dr. Ji Il Choi for his valuable advice and discussions. I would like to express my gratitude to Seung Geol Lee and Giuseppe Brunello for their technical support and valuable discussions. And I thank all the undergraduate students who have helped my research. I also appreciate all the friends in School of Physics, Dr. Dongjoo Lee, Dr. Bokwon Yoon and Dr. Seungjoo Nah. Especially, I would show my special thanks to my old friend Dr. Seong-O Choi and his family. He always encouraged me to get my Ph.D.degree and was my side whenever I encountered difficulties.

In addition, I would like to say special appreciation to my parents and parents-in-law. For the long time, they always showed their endless love and trust and encouraged me to reach my goal. Especially, I want to show my appreciation and love to my wife, Hyun. Without her endless love, support, patience and trust, I could not finish my study. Finally, I dedicate my thesis to my grand-mother who has showed love for her entire life.

TABLE OF CONTENTS

LIST OF TABLES

Page

LIST OF FIGURES

Page

SUMMARY

Recent carbon allotropes such as carbon nanotubes (CNTs), fullerenes (C_{60}s) and graphene have attracted great interests in both science and engineering due to their unique properties such as excellent electrical and mechanical properties as well as its vast surface area, and have led to many commercial applications. Especially, CNTs have been considered to be one of the promising candidates in the Li ion battery system because of its outstanding properties. However, the experimental results in the pristine CNT system have shown just slight improvement than original graphitic carbon material, which has been attributed to the weak adsorption of Li on CNTs. In this study, we investigated two types of CNT-C_{60} hybrid system consisting of CNTs and C_{60}s to improve Li adsorption capabilities and predict its performance through quantum mechanical (QM) computations. First, we investigated adsorption energy of lithium (Li) on dilute CNT-C_{60} hybrid and CNT-C_{60} nanobud system as well as various electronic properties such as band structure, density of states (DOS), molecular orbital and charge distribution. Then, we expanded our interest to the more realistic condensed structure of CNT-C_{60} hybrid and nanobud system to examine actual electrochemical characteristics. The study of the condensed structure has been expanded to the very unique CNT-C_{60} nano-network system and examined mechanical strength as well as electronic properties. Finally, Li adsorption on other carbon allotropes system such as graphene-C_{60} hybrid and graphene-C_{60} bud system was investigated in order to provide fundamental understanding of electronic interaction between carbon allotrope and effect of Li adsorption.

CHAPTER 1

INTRODUCTION

1.1 Renewable energy

Carbon dioxide (CO_2) is the one of the main gas responsible for the greenhouse effect [1]. As CO_2 emissions from the use of fossil fuels continue to increase, many efforts are being made globally to develop new types of energy. Fossil fuels such as petroleum, natural gas and coal, encompass more than 80% of the current energy consumption, as shown in Figure 1.1, and demands are still increasing. However, within several centuries, these energy sources may be depleted while the CO_2 concentration in the atmosphere will be greatly increased due to combustion. Therefore, many projects are being implemented to decrease the emission of CO_2 gas by introducing renewable energy sources such as solar, wind, biomass and energy storage [2, 3]. Fortunately, the amount of renewable energy is expected to increase gradually to become an increasingly larger fraction of the total energy consumption. Currently, hydropower accounts for one-third of the current renewable sources as presented in Figure 1.1, and half of the total U.S. renewable energy is consumed by industry to produce electricity.

Furthermore, stationary, high-yield, long-lasting, and low-maintenance electrical energy storage solutions are necessary to promote the effective use of low-emission or emission-free energy sources. In 2006, Germany, the leading country in wind energy utilization, wasted 15% of produced energy from wind because of a lack of suitable electrical energy storage [4]. Thus, the significance of energy storage such as fuel cell and lithium-ion batteries with sufficient power, efficiency and cycle life is growing along with increased consumption of renewable energy.

1.2 Li ion battery system

Among the various energy storages, Lithium-ion battery technology has been considered to be the fast growing technology for providing stationary storage solutions to enable the efficient use of renewable energy sources. At present, Li-ion batteries are

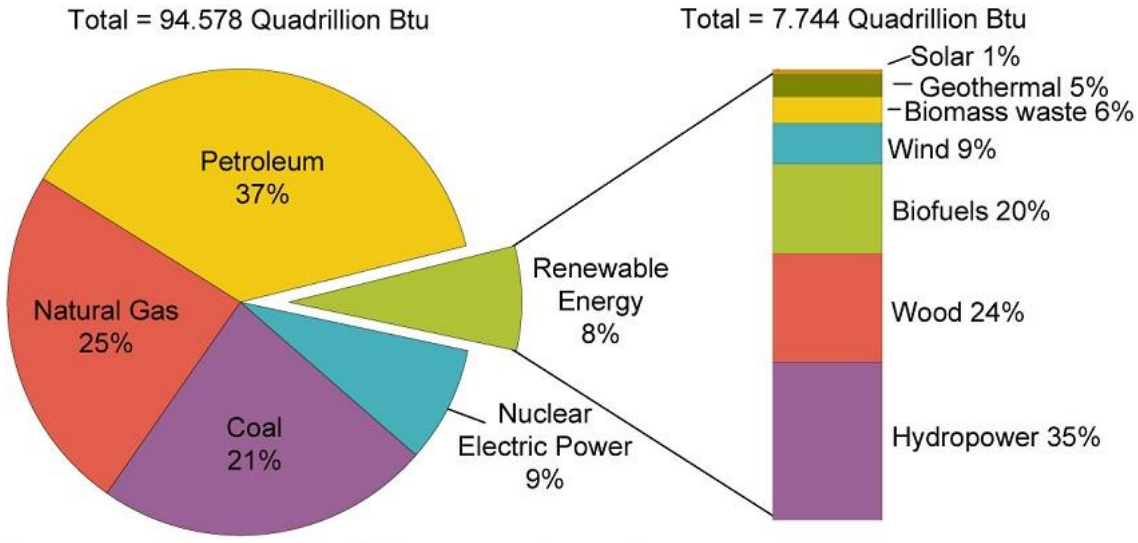

Source: U.S. Energy Information Administration, *Annual Energy Review*, 2009, Table 1.3, Primary energy consumption by energy source, 1949-2009. (August 2010)

Figure 1.1: U.S. Energy consumption by energy source, 2009.

widely used for low-power applications like consumer electronics. In addition, extensive research has lead the technology to a stage where it seems very likely that safe and reliable battery can be used for the high power systems such as hybrid electric and electric vehicles and connected to solar cells and windmills. However, it still faces some problems such as cost, performance, safety and cyclic life to overcome in spite of tremendous progress of technology.

The working unit in a battery is the electrochemical cell, consisting of a cathode and an anode separated and connected by an electrolyte. The electrolyte conducts ions but is an insulator to electrons. The anode contains a high concentration of intercalated lithium (Li) while the cathode is depleted of lithium in a charge state. During the

discharge, intercalated lithium is extracted from the anode and migrates through the electrolyte to the cathode while its associated electron is collected by the external circuit to be used to operate an electric device [5, 6].

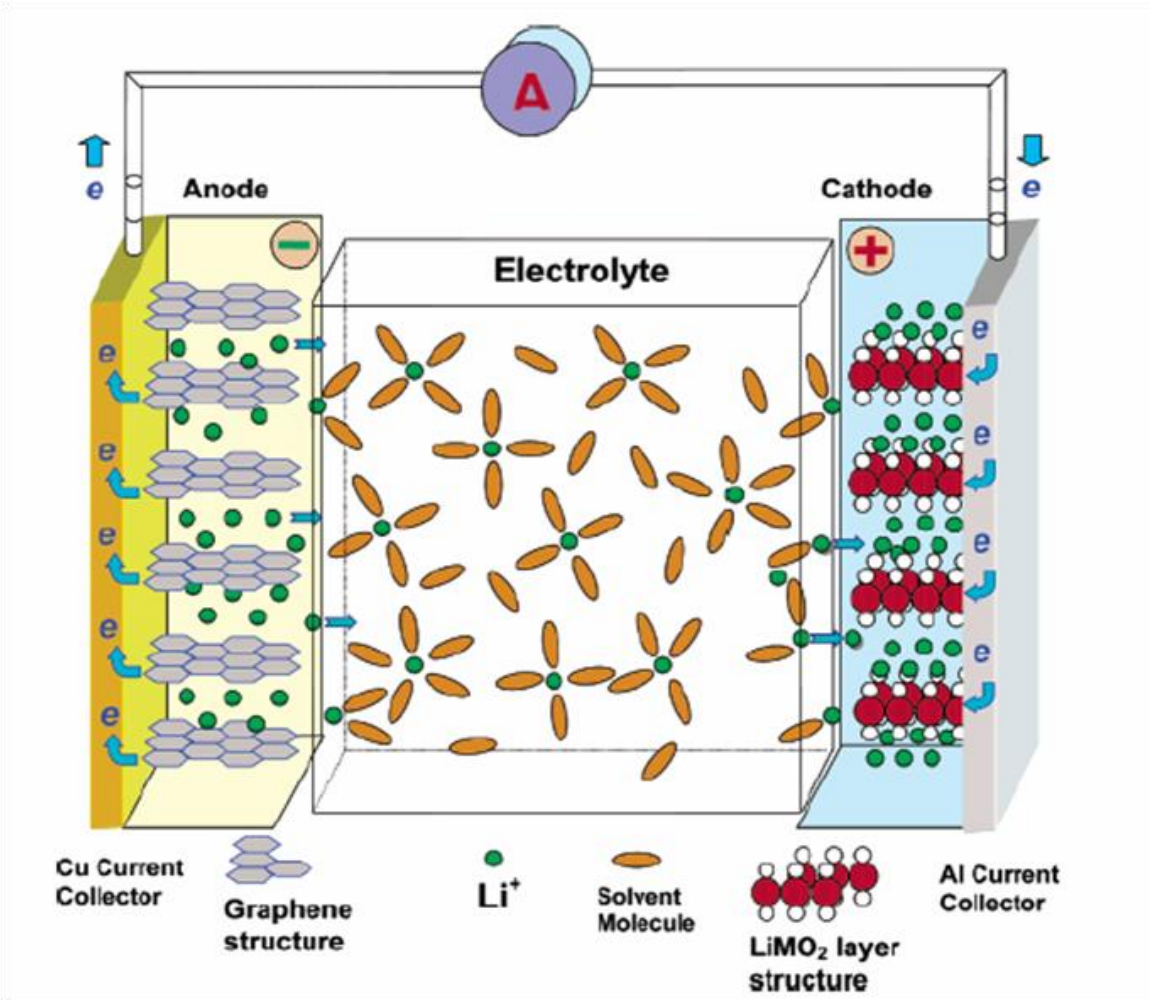

Figure 1.2: A lithium ion electrochemical cell based on lithium-metal oxide as cathode and graphite as anode [7].

In the lithium battery system, lithium-metal oxides such as $LiCoO_2$, $LiMn_2O_4$, vanadium oxides, and $LiFePO_4$ (olivines) are usually used as a cathode [7, 8]. Layered oxides containing cobalt and nickel are the most studied materials and they show a high stability in the high-voltage range but cobalt is toxic and has limited availability in nature, which is a huge drawback for mass production. On the contrary, Manganese

offers a low-cost substitution with a high thermal threshold and excellent rate capabilities but cycling life is limited. Therefore, mixtures of cobalt, nickel, and manganese are often used to derive the best properties and overcome the disadvantages of each material. Vanadium oxides have a large capacity and excellent kinetics, but the material tends to become amorphous due to lithium insertion and extraction and limits the cyclic behavior. Olivines are nontoxic material and have a moderate capacity, but their conductivity is still low.

For the anode materials, graphite, lithium metal, lithium-alloying materials, or silicon are being used [9]. At present, graphite anodes have been widely used in Li ion batteries due to safety and cycle, although lithium metal electrodes are much higher capacity than carbon materials electrodes. To overcome those issues, some efforts with novel graphite varieties and carbon nanotubes have tried to increase the capacity but high cost of the processing is still problematic. Silicon is expected to have a quite high capacity up to 4,199 mAh/g corresponding to a composition of Si_5Li_{22} [10], but poor cycle and safety problem should be resolved in order to be used as an acting material. Therefore, many active researches are still progressing to find a better lithium intercalation material in terms of the power density and cycle.

1.3 Carbon nanotube, fullerene and graphene

Carbon allotrope, such as carbon nanotube (CNT), fullerene (C_{60}) and graphene, have gained a great deal of attention in both science and engineering due to their extraordinary electronic and mechanical properties, leading to many applications in nanotechnology, such as field-effect transistor, composite materials and gas sensors [11-14]. Among them, carbon nanotubes (CNTs, Figure 1.3.a) are a one-dimensional structure, which have garnered much interest after they were discovered in 1991. CNTs have outstanding electrical [15-17], electronic, electrochemical [18], thermal, and mechanical properties [19-24] as well as high surface area and electrochemical stability.

For example, their Young's modulus can exceed 1000GPa, which approaches that of diamonds (1220 GPa), and metallic CNTs can carry an electric current three times more effectively than copper. These near-perfect properties made them ideal electrode materials for various renewable energy applications such as hydrogen storage and super capacitor. In addition, CNTs can be combined with other functional materials to form nano-structured hybrid materials, such as catalysts for applications in fuel cells and inorganic semiconductors for the generation of electro-hole pairs in solar cells. In particular, it is noticed that high performance electrical energy devices such as batteries based on CNTs or their hybrid materials have been developed to promote Li adsorption, which is motivated by increasing demand for better electrochemical materials of higher energy and power density [25].

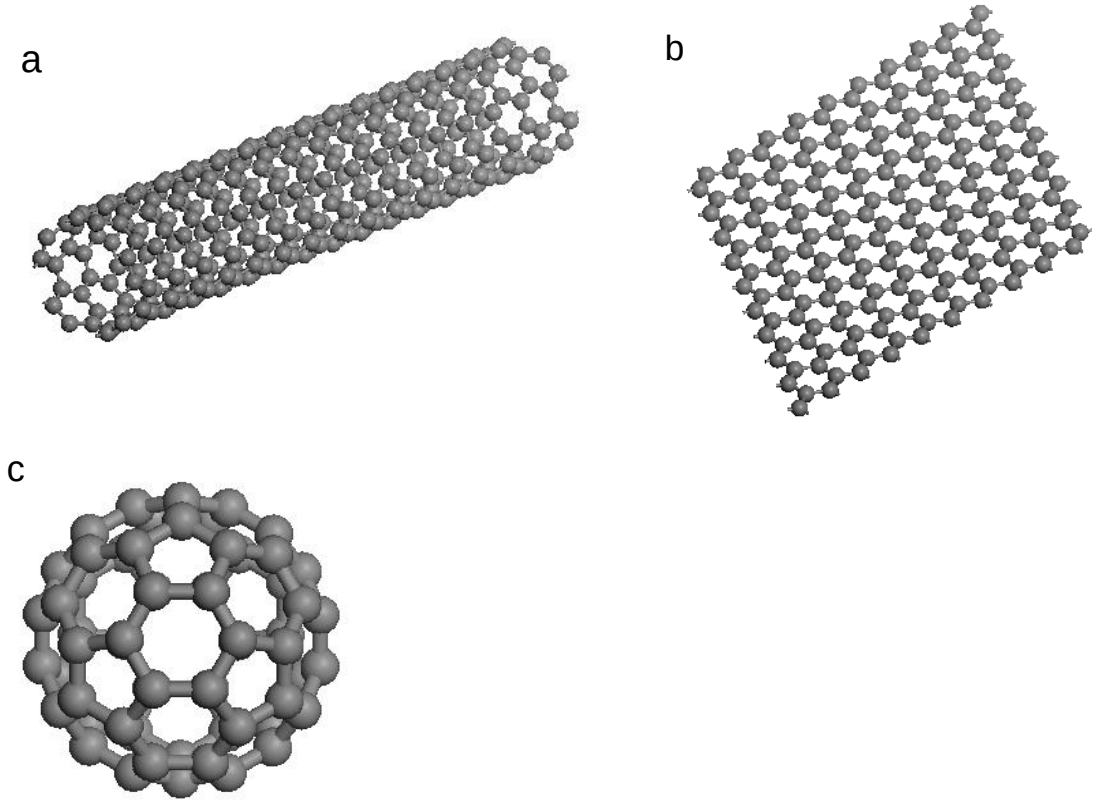

Figure 1.3: Carbon allotropes: (a) single-walled nanotube; (b) graphene; and (c) fullerene (C_{60}).

Graphene (Figure 1.3.b), a single layer of honeycomb lattice carbon atoms, is the most prominent nanoscale materials currently used in both science and technology. The two dimensional (2D) graphene consists of sp^2-hybridized carbon atoms, which allow graphene to possess unique electrical properties resulting from its semi-metallic nature and 2D structure [12, 26-29]. This exceptional property makes it an ideal material for carbon-based nanoelectronics such as a graphene-based field-effect transistor (FET), including transistors to be used in nanoscale electronic circuits, light emitters and detectors and ultrasensitive chemical sensors and biosensors [30].

Fullerene (C_{60}, Figure 1.3.c), which was first discovered in 1985, form unique spherical molecules containing a conjugated π system. Each fullerene represents a closed network of fused hexagons and pentagons. C_{60}s are chemically stable, but sp^2 hybridized carbon atoms induce chemical reactivity [31]. Therefore, the production of various hybrid materials has been attempted to manipulate photo-active or electro-active properties by functionalizing fullerenes with interesting materials such as small organic molecules, polymers and carbon nanotubes. In addition, because C_{60} is a strong electron acceptor and is efficient in charge transfer, its usage in electron harvest material is increasing.

In this study, we investigated various hybrid materials consisting of those carbon materials to utilize the advantages of each material and investigated the possibility for the application of each material in energy technology.

1.4 Computational method

Computational methods use the results of theoretical physics and chemistry, incorporated into efficient computer programs, to calculate the structures and electronic properties of molecules and solids. It has become a useful way to investigate materials

that are too difficult to find or too expensive to measure. It also helps people make predictions before running the actual experiments so that they can be better prepared for taking measurements and understanding physics. In computational study, the Schrödinger equation is the basis for most of the computational methods because the Schrödinger equation describes the atoms and molecules with mathematics. Therefore, we can calculate various properties such as electronic structure, optimized geometry, electron and charge distributions, potential energy surfaces (PES), and energy of reaction by solving the Schrödinger equation. However, in all cases the computation time and computer resources increase rapidly with the size of the system being studied. Thus, computational methods range from highly accurate to very approximate: empirical or semi-empirical employing experimental data and highly accurate methods are typically feasible only for small systems.

1.4.1 Ab initio methods

As mentioned above, computational methods are base on many different quantum mechanical methods that solve the Schrödinger equation associated with the atomic or molecular Hamiltonian. *Ab initi*o methods can be made to converge to the exact solution, when all approximations are sufficiently small in magnitude and when the finite set of basis functions tends toward the limit of a complete set. Hartree-Fock (HF) method is the simplest the type of the *ab initio* calculation, in which the correlated electron–electron repulsion is not specifically taken into account; only its average effect is included in the calculation. Many types of calculations known as post-Hartree-Fock methods begin with a HF and subsequently correct for electron–electron repulsion.

1.4.2 Density functional theory

Density functional theory (DFT) is to describe an interacting system by its density instead many body wave function and widely used in many fields because DFT methods

can be very accurate for little computational cost. It was first realized by Thomas and Fermi and later formalized by Hohenberg and Kohn in 1964. The properties of many electrons system can be determined by functional, which is the spatially dependent electron density. DFT is a successful approach for the description of ground state properties of metals, semiconductors, and insulators and its success expands to complex material such as proteins and carbon nanotubes.

In this study, density functional theory (DFT) is used in order to understand the basic properties of the new hybrid material, which is a fairly recent player in the computational chemistry area.

CHAPTER 2

THEOERY

2.1 Density functional theory

Density Functional Theory (DFT) has become a popular method for calculating the ground state properties of interacting many electron systems such as atoms, molecules or solids in computational physics, quantum chemistry and condensed-matter physics. The main goal of DFT is to solve a many-body interacting system through density and its importance is that it changes the many-body system into a system of non-interacting fermions in an effective field. The theory originates from the conceptual work from Thomas-Fermi model [32, 33] and is further developed by Hohenberg-Kohn [34] and Kohn-sham [35], which claims that properties of a system can be considered to be unique functionals of its ground state density. Combined with the Born-Oppenheimer approximation [36] and Kohn-Sham (KS) ansatz [35], accurate DFT calculations have been possible through the approximation for the so called exchange-correlation (XC) potential, which describes the effects of the Pauli principle and Coulomb potential beyond a pure electrostatic interaction of the electrons. In many cases, the results of DFT calculations for condensed matter systems agreed well with experimental data as well as relatively lower computational costs comparing with the method based on the many-electron wavefunction. Therefore, we will briefly overview the basic concept behind DFT in this chapter.

2.1.1 The Schrödinger equation

The solution of the Schrödinger equation (2.1) gives information about various processes and phenomena occurring in complex systems

$$\left(-\frac{\hbar^2}{2m_e}\sum_{i=1}^{N}\nabla_i^2 + \frac{1}{2}\sum_{i,j=1,j\neq i}^{N}\frac{e^2}{|r_i - r_j|} + \sum_{i=1}^{N} v_{ext}(r_i) \right)\Psi(x_1 \cdots x_N) = E\Psi(x_1 \cdots x_N) \qquad (2.1)$$

, where the first, second and third terms in equation (2.1) represent the kinetic energy, interparticle interaction and interaction with external potential, respectively. In this equation, the electron-electron interaction makes it difficult solve the equation and this effect should be covered in the wavefunction $\Psi(x_1 \ldots x_N)$. Since the exact solution cannot be exactly solved, various theories have been developed from Hartree-Fock (HF) and Thomas-Fermi-Dirac approximation to the modern density functional theory.

2.1.2 The Hohenberg-Kohn theorem

The main objective of density functional theory is to replace the many-body electronic wavefunction with the electronic ground-state density as basic quantity. Whereas the many-body wavefunction is dependent on 3N spatial variables and N spin variables, the density is a function of only three variables and is a simpler quantity to deal with both conceptually and practically. The method is in principle exact and based on two theorems derived and proved by Hohenberg and Kohn in 1964. The Hohenberg and Kohn theorem states that the density of a non-degenerate ground state uniquely determines the external potential (to within a constant) to which the many-electron system is subjected. Consequently, the density determines electronic wavefunction of the system and thus all the electronic properties of the ground state. The proof of the theorem for the $v \longrightarrow \rho$ mapping is based on reductio ad absurdum. Consider two external potentials

$v(r)$ and $v'(r)$ which differ by more than a constant that each yield the same ground-state density and then the two potentials will give rise to different ground-state wavefunctions. Now, we can use the variational principle. From the Schrödinger equation (2.1), we have

$$\left(\hat{T}+\hat{V}_{ee}+\hat{V}\right)\left|\Psi_0\right\rangle = E_0\left|\Psi_0\right\rangle \tag{2.2}$$

$$\left(\hat{T}+\hat{V}_{ee}+\hat{V}'\right)\left|\Psi'_0\right\rangle = E'_0\left|\Psi'_0\right\rangle . \tag{2.3}$$

If Ψ_0 and Ψ_0' were to be the same, then by subtracting (2.3) from (2.2) one would get

$$\left(\hat{V}-\hat{V}'\right)\left|\Psi_0\right\rangle = E_0 - E'_0\left|\Psi_0\right\rangle \tag{2.4}$$

, where $\hat{V}$ and $\hat{V}'$ appear to differ only by a constant if Ψ_0 does not vanish. However, Ψ_0 cannot vanish on a set with nonzero measure by the unique continuation theorem. Thus, we obtain a contradiction with our initial assumption, and hence we can conclude that $\Psi_0 \neq \Psi_0$. We can now prove that two potentials $v(r)$ and $v'(r)$ with corresponding Hamiltonians $\hat{H}$ and $\hat{H}'$ and non-degenerate ground-state wavefunctions Ψ_0 and Ψ'_0 produce two different densities $\rho(r)$ and $\rho'(r)$. Through the variational principle we have that

$$E_0 = \left\langle \Psi_0\left|\hat{H}\right|\Psi_0\right\rangle < \left\langle \Psi'_0\left|\hat{H}\right|\Psi'_0\right\rangle = \left\langle \Psi'_0\left|\hat{H}+\hat{V}-\hat{V}'\right|\Psi'_0\right\rangle . \tag{2.5}$$

So that

$$E_0 < E'_0 + \int \rho'[v(r)-v'(r)]dr . \tag{2.6}$$

Similarly, interchanging primed and unprimed quantities, one finds

$$E'_0 < E_0 + \int \rho[v'(r)-v(r)]dr \tag{2.7}$$

and consequently we conclude that there cannot exist two different external potentials $v(r)$ and $v'(r)$ corresponding to the same density $\rho(r)$. This defines the mapping

$\rho \to v$, and thus the one-to-one mapping $v \leftrightarrow \rho$ is constructed. Therefore, that total energy of a many-electron system in an external static potential can be expressed in terms of the potential energy due to this external potential and of energy functional $F[\rho]$ of the ground-state density,

$$E_0[\rho] = \left\langle \Psi_0[\rho] \middle| \hat{H} \middle| \Psi_0[\rho] \right\rangle = \int \rho(r) v(r) dr + F[\rho] \tag{2.8}$$

with $F[\rho]$ defined in

$$F[\rho] = E_0[\rho] - \int \rho(r) v(r) dr = \langle \Psi_0[v] | \hat{V} + \hat{V}_{ee} | \Psi_0[v] \rangle . \tag{2.9}$$

Note that this functional is defined independently of the external potential $v(r)$, and thus it is a universal functional of the density. This means that if the explicit form is known, it can be used for any system. The second Hohenberg-Kohn theorem states that the exact ground-state density of a system in a particular external potential $v(r)$ minimizes the energy functional

$$E_0[\rho] = \min_{\rho} \{F[\rho] + \int \rho(r) v(r) dr\} \tag{2.10}$$

, where E_0 is the ground-state energy for the system in an external potential $v(r)$. The proof uses the variational principle again. The previous theorem assures that a trial density $\breve{\rho}(r)$, such that $\breve{\rho}(r) \geq 0$ and $\int \breve{\rho}(r) dr = N$, with N number of electrons determines its own potential $\breve{v}(r)$, Hamiltonian $\hat{H}$, and wavefunction $\hat{\Psi}$. This wavefunction can be taken as trial function for the problem of interest having external potential $v(r)$. The variational principle asserts that

$$< \psi_0 | H | \psi_0 > = F[\rho] + \int \breve{\rho}(r) v(r) dr \geq F[\rho] + \int \rho(r) v(r) dr \tag{2.11}$$

, which proves the second Hohenberg-Kohn theorem.

2.1.3 The Kohn-Sham equation

Even if the Hohenberg-Kohn theory implies the reformulation of the many-particle interacting systems in terms of the density, it doesn't guarantee the possibility for the exact solution of such systems. In Hohenberg-Kohn theory, both the kinetic energy and exchange-correlation energy has to be approximated. Kohn and Sham treated the kinetic energy in a much better manner. They replaced the interacting system by an auxiliary non-interacting system whose particle number density is same as the interacting system. For a system of *N* non-interacting electrons, the Hamiltonian reduces to

$$\hat{T} + Vee = 0 + \sum_{j=1}^{N} v(r_j) = \hat{T} + \sum_{j=1}^{N} v(r_j). \tag{2.12}$$

Now, for a non-interacting system,

$$F_{non-ineracting}[\rho] = T_S[\rho] = \min_{\Psi \to \rho} \langle \Psi | \hat{T} | \Psi \rangle = \langle \phi_\rho^{\min} | \hat{T} | \phi_\rho^{\min} \rangle \tag{2.13}$$

Although in practice one can search over any arbitrary N-electron wavefunctions, the minimizing wavefunction $\phi_\rho^{\min}$ for a given density ρ will be a non-interacting wavefunction (a single Slater determinant) for some external potential v_s such that

$$\frac{\delta T_S[\rho]}{\delta \rho(\vec{r})} + v_S(\vec{r}) = \mu_S. \tag{2.14}$$

The newly found KS potential $v_S(\vec{r})$ is also a functional of density $\rho(\vec{r})$. If the effective potential in equation (2.14) will be

$$v_S(\vec{r}) = v(\vec{r}) + \frac{\delta \mu[\rho]}{\delta \rho(\vec{r})} + \frac{\delta E_{XC}[\rho]}{\delta \rho(\vec{r})} \tag{2.15}$$

then by construction μ_S for the auxiliary system and μ for the interacting system are the same. In the above equation, the second and third terns on the right hand side of

represents the Coulomb and exchange-correlation potentials, the latter arising due to Pauli-Coulomb correlations. So the Euler equation for the auxiliary system becomes

$$\frac{\delta T_S[\rho]}{\delta\rho(\vec{r})} + v_S(\vec{r}) = \mu . \tag{2.16}$$

Now we define the exchange-correlation energy, for the interacting system by the equation

$$F[\rho] = T_S[\rho] + U[\rho] + E_{XC}[\rho] \tag{2.17}$$

, where $T_S[\rho]$ is the KS kinetic energy defined by equation (2.13), and it can be written in terms of single particle orbital to be

$$T_S[\rho] = \sum_i \langle \phi_i | -\frac{1}{2}\nabla^2 | \phi_i \rangle \tag{2.18}$$

, $U[\rho]$ is the Coulomb energy and the rest constitutes the exchange-correlation energy $E_{XC}[\rho]$. The procedure is considered to be the better because (i) $T_S[\rho]$ forms typically a very large part of the total kinetic energy, (ii) $T_S[\rho]$ is largely responsible for density oscillations of the shell structure, which are accurately described by the KS method and (iii) $E_{XC}[\rho]$ is better suited for local and semi-local approximations than $E_{XC}[\rho]$. The exchange-correlation energy $E_{XC}[\rho]$ is the sum of independent exchange and correlation terms

$$E_{XC}[\rho] = E_X[\rho] + E_C[\rho] \tag{2.19}$$

, where

$$E_X[\rho] = \langle \phi_\rho^{\min} | V_{ee} | \phi_\rho^{\min} \rangle - U[\rho]. \tag{2.20}$$

When $\phi_\rho^{\min}$ is a single Slater determinant defined by equation (2.13), the equation above is the Fock integral applied to the KS orbitals. Also one can notice that

$$\langle \phi_\rho^{\min} | \hat{T} + \hat{V}_{ee} | \phi_\rho^{\min} \rangle = T_S[\rho] + U[\rho] + E_X[\rho] \tag{2.21}$$

, and in the one electron ($\hat{V}_{ee} = 0$) limit. The correlation energy is

$$E_C[\rho] = \langle \Psi_\rho^{\min} | \hat{T} + \hat{V}_{ee} | \Psi_\rho^{\min} \rangle - \langle \phi_\rho^{\min} | \hat{T} + \hat{V}_{ee} | \phi_\rho^{\min} \rangle = F[\rho] - \{T_S + U[\rho] + E_X[\rho]\} . \tag{2.22}$$

As expected correlation is always negative, since $\Psi_\rho^{\min}$ is the wavefunction which yield density ρ and minimizes the $\langle \hat{T} + \hat{V}_{ee} \rangle$, whereas $\phi_\rho^{\min}$ is that wavefunction which also yields the same density ρ but minimizes $\langle \hat{T} \rangle$ only. Thus, $\langle \Psi_\rho^{\min} | \hat{T} \hat{+} V_{ee} | \Psi_\rho^{\min} \rangle < \langle \phi_\rho^{\min} | \hat{T} + \hat{V}_{ee} | \phi_\rho^{\min} \rangle$. For making DFT practicable, the approximation for the exchange-correlation energy functional is needed. The various local and semi-local approximations like local density approximation (LDA) and generalized gradient approximation (GGA) starts from the pioneering work of Kohn and Sham in 1965. To date there are number of accurate functionals that have been developed and tested for electronic structure calculations of atoms, molecules and solids.

2.1.4 Approximations to the exchange-correlation (XC) functionals

2.1.4.1 Local density approximation (LDA)

The idea is that at each point in a molecule or solid, an electron experiences the same effect from the surrounding electrons as if the electronic density were uniform and

equal to the density where the affected electron is. It is main assumption in this model that we can write E_{XC} in the following, very simple form,

$$E_{XC}^{LDA}[\rho] = \int d^3\vec{r}\rho(\vec{r})\,\varepsilon_{XC}(\rho(\vec{r}))\,. \tag{2.23}$$

Here, $\varepsilon_{XC}(\rho(\vec{r}))$ is the exchange-correlation energy per particle of a uniform electron gas of density $\rho(\vec{r})$. The local energy per particle comes from the exact, known and parameterized exchange-correlation energy of a uniform gas for the exchange correlation energy density at each point in space [35]. It is accurate for uniform and slowly varying densities and is useful in solid-state physics. The exact ground-state energy of the three-dimensional uniform unpolarized Fermi gas, termed Jellium, in the high-density limit is a function of the electronic density [37]:

$$\lim r_S \to 0\,(\frac{E}{N}) = \left[\frac{2.21}{{r_S}^2} - \frac{0.0916}{r_S} + 0.0622\ln r_S - 0.096 + \vartheta(r_S)\right] \tag{2.24}$$

with

$$r_S = \left(\frac{3}{4\pi\rho}\right)^{\frac{1}{s}}. \tag{2.25}$$

The terms in equation (2.24) represent the kinetic contribution, the exchange contribution and the correlation contribution in order. The idea of the LDA is to take the exchange-correlation energy per particle from this uniform gas and to use this in the functional, equation (2.23). The ground-state energy of Jellium is known through analytic forms for the high and low density limits and Monte Carlo calculations for intermediate densities [38]. Accurate parameterizations of the entire energy versus density curve have been constructed and are in use [39]. However, LDA tends to over-emphasize metallic character and overestimate weak bonds like hydrogen bond.

2.1.4.2 Generalized gradient approximation (GGA)

A naive gradient expansion about the local-density approximation is problematic [34, 35], but careful considerations lead to the generalized gradient approximations (GGA) [40-42]. In the GGA, the information about the density $\rho(\vec{r})$ at a particular point $\vec{r}$, but to supplement the density with information about the gradient of the charge density, $\nabla(\rho(\vec{r}))$ in order to account for the non-homogeneity of the true electron density. In other words, we can interpret that the local density approximation as the first term of a Taylor expansion of the uniform density and expect to obtain better approximations of the exchange-correlation functional by extending the series with the next lowest term,

$$E_{XC}^{GGA}[\rho] = \int d^3\vec{r}\rho(\vec{r})\,\varepsilon_{XC}(\rho(\vec{r}),\nabla\rho(\vec{r}))\,. \tag{2.26}$$

GGA's preserve many of the exact features of LDA and provide results which are good for chemistry as well as solid-state physics.

2.2 DFT-D

The van der Waals interactions between atoms and molecules play an important role in many chemical and biological systems. This dispersion interactions balance with electrostatic and exchange-repulsion interactions and they together control, for instances, the structures of proteins, DNA, host-guest complexes, crystal packing and soft materials. However, it is a well-known problem of almost all gradient-corrected density functionals, including various hybrids functional that replace part of the local by nonlocal HF exchange, and then they are unable to describe dispersive interactions. Accurate computations through higher-order *ab initio* based wave functions, such as coupled-

cluster singles and doubles (CCSD(T)) method [43], perform a good level of accuracy with large basis sets. However, these suffer from inacceptable computational costs in terms of computation time and resources even relatively small system. Alternatively, cheaper methods like second-order Møller-Plesset perturbation theory (MP2) [44] which approximately accounts for uncoupled, two-body electron correlations are computationally simpler but it still overestimates the binding energies and underestimates intermolecular distances. Even though PBE can qualitatively account for some dispersive interactions, it seems to be difficult to account for dispersion within the standard DFT. Therefore, a variety of methods for the treatment of dispersion interactions including semi-empirical dispersion corrected functional (B97D) [45, 46] and treatments with specialized functional such as M06 series [47] recently have been developed to address this problem in the DFT field. Among these various attempts, adding an empirical potential of the form $C_6 \cdot R^{-6}$ corrections, where R are interatomic distances and C_6 are the dispersion coefficients, to the standard DFT functionals seems most promising to resolve the problem in a point of robustness and computational efficiency. In this approach, the dispersion corrected total energy is defined as

$$E_{DFT-D} = E_{DFT} + E_{disp} \tag{2.27}$$

, where E_{DFT} is the usual energy as obtained from the chosen DFT and E_{disp} is an empirical dispersion correction given by

$$E_{disp} = -s_6 \sum_{i=1}^{N_{at}-1} \sum_{j=i+1}^{N_{at}} \frac{C_6^{ij}}{R_{ij}^6} f_{dmp}(R_{ij}). \tag{2.28}$$

Here, N_{at} is the number of atoms in the system, C_6^{ij} denotes the dispersion coefficient for atom pair *ij*, s_6 is a global scaling factor that only depends on the DFT used, and R_{ij} is an interatomic distance. In order to avoid near-singularities for small *R*, a damping function f_{dmp} must be used, which is given by

$$f_{dmp}(R_{ij}) = \frac{1}{1+e^{-d(R_{ij}/R_0-1)}} \tag{2.29}$$

, where R_0 is the sum of atomic vdW radii and typically calculated with wave function based methods and scaled by appropriate factor. Equation (2.29) is chosen because it decays at small R fast enough to zero such that the dispersion corrections between atoms well below typical van der Waals distances are negligible and thus, normal bonds are not significantly affected by the correction. The damping factor *d* which determines the steepness of the damping function takes on value between 20 and 23. C_6 in equation (2.27) has been calculated from atomic hybridization states and also determined from LDF calculated IPs and static dipole polarizabilities and C_6^{ij} can be introduced via geometric mean of the form

$$C_6^{ij} = \sqrt{C_6^i C_6^j} \tag{2.30}$$

, which is determined to correctly cover heavier elements as well as light elements.

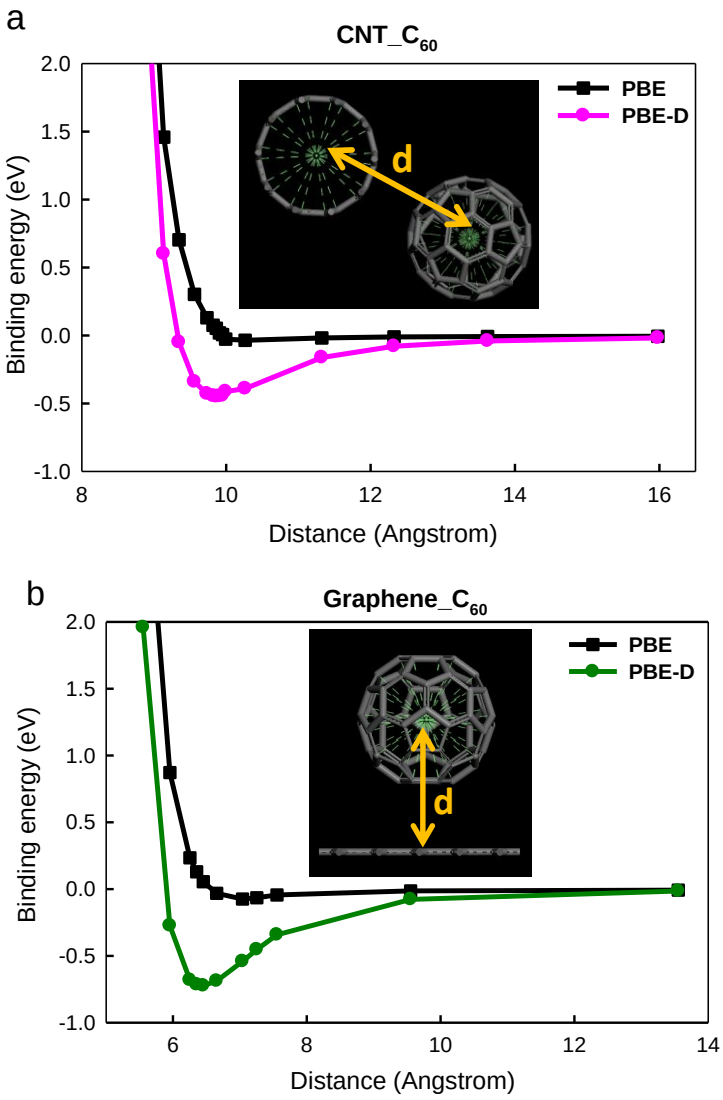

Figure 2.1: DFT-D corrected binding energy of (a) CNT-C_{60} hybrid system; (b) graphene-C_{60} hybrid system.

In this study, this DFT-D correction is incorporated with PBE functional to handle dispersion interaction of the carbon allotrope hybrid system. Figure 2.1 shows binding energy of the CNT-C_{60} and graphene-C_{60} hybrid system after single point energy calculation varying distances between components. While the PBE underestimates the interaction between CNT and C_{60} or between graphene and C_{60} as represented in figure,

DFT-D predicts the dispersion interaction more correctly. For example, the DFT-D calculates 6.45Å between graphene and C_{60}, which agrees well with experimental value of 6.35Å [48].

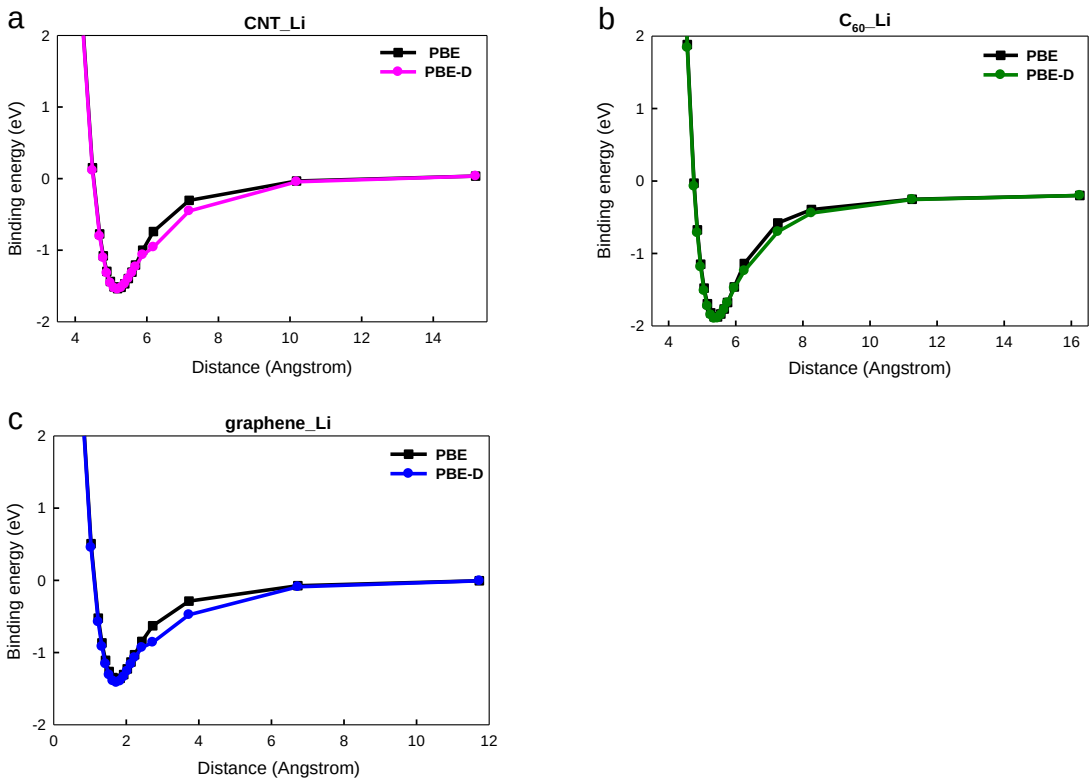

Figure 2.2: DFT-D corrected binding energy between Li and (a) (5,5) CNT; (b) C_{60}; and (c) graphene.

Meanwhile, Figure 2.2 displays the binding energy through the PBE and corrected by DFT-D between Li atom and various carbon allotropes such as CNT, C_{60} and graphene. Unlike the pure carbon systems maintained by the van der Waals interaction, the interaction between Li and carbon system is not affected by the dispersion interaction because Li atom interacts with the carbon through charge transfer from the Li atom to the carbon systems. Therefore, the Li adsorption on the various hybrid systems of our concern can be described without further correction of the dispersion interaction.

CHAPTER 3

FIRST-PRINCIPLES STUDY OF LI ADSOPRTION ON CARBON NANOTUBE-FULLERENE HYBRID SYSTEM

In this chapter, we investigate a new hybridized material system consisting of metallic single-walled carbon nanotube (SWCNT) and semiconducting fullerene (C_{60}) to predict the performance and the change of electronic properties related to the Li adsorption in dilute or condensed phase of the CNT-C_{60} hybrid system.

3.1 Introduction

Currently, graphitic carbon anodes have been widely adapted for the Li ion battery application due to their cycle efficiency and safety, even though metallic Li anode systems have been shown to have better Li capacity than carbon-based anodes [49]. In this context, carbon nanotubes (CNTs) have been studied both theoretically and experimentally [15, 24, 50] in order to increase the Li adsorption capacity for electrode applications because CNTs provide a vast surface area for Li adsorption as well as the above-mentioned outstanding electrical and mechanical properties [51-53]. Early studies were focused on the adsorptions of Li on the outside single-wall carbon nanotubes (SWCNTs) and multi-wall carbon nanotubes (MWCNTS) with various diameters and chiralities [54-61], but later studies have been extended to the diffusion of Li on the interior and exterior of the CNT [62-66]. However, the experimental results of the Li-intercalation on the bare CNT system have shown only slight increases of reversible capacities over that of the graphitic carbon material, which has been ascribed to the weak adsorption of Li on CNTs [53, 67, 68]. Hence, further development has sought to obtain

strong Li adsorption through various modifications such as doping impurities, forming structural defects, and mixing with other carbon-based materials [69-78]. For instance, Shimoda et al. have reported increases in the maximum capacity (~1000 mAh/g) of $Li_{2.7}C_6$ for SWCNTs by intercalating Li into the inside of CNTs through chemical etching of the CNTs [71, 72].

Among those modification methods aiming to improve electrochemical properties, diverse studies of carbon hybrid system between different carbon-base materials have also been actively attempted. In a recent study, Kawasaki et al. prepared the peapod structure by encapsulating fullerenes (C_{60}s) into the inside of SWCNTs and achieved an improvement in reversible capacities compared to the bare SWCNTs [76]. In addition, Kaneko and his coworkers could have successfully produced the SWCNT-C_{60} mixed system through the sonication of SWCNTs and C_{60}s in the toluene solution [73]. Meanwhile, Kauppinen and his coworkers synthesized another form of the CNT-C_{60} hybrid structure, called nanobuds, by covalently bonding C_{60}s to the outer surface of CNT and measured its field-emission properties, which can be utilized as a light-emission device [77, 78]. Moreover, C_{60}-SWCNT complexes were used to enhance the performance of the polymer photovoltaic cells by exploiting the electron accepting property of the C_{60} [79-81]. Hence, it should be very desirable to understand the electronic properties of the CNT-C_{60} hybrid system in order to develop working devices.

In this chapter, therefore, we investigate a new hybridized material system consisting of metallic SWCNT and semiconducting C_{60} to improve the performance related to the Li adsorption without adopting deteriorating processes as well as achieving better electrochemical properties. In addition, investigating the electronic properties of

the CNT-C_{60} hybridized system will be useful because this form of mixed system could be unintentionally produced in the middle of the processes such as peapod and nanobuds. This CNT-C_{60} hybrid system makes use of C_{60} as the electron acceptor from Li, and CNT as the charge transport channel throughout the electrode in the presence of Li atoms. Thus, it is expected that the Li adsorption on the CNT-C_{60} electrode is more favorable than the pure CNT-based electrode due to the higher electron affinity of C_{60} (experiment: 2.65 eV [82]; theory: 2.697eV from GGA PBE), and then, the electrons harvested from Li via C_{60} will be transferred through metallic CNT under electrical potential when battery is discharged.

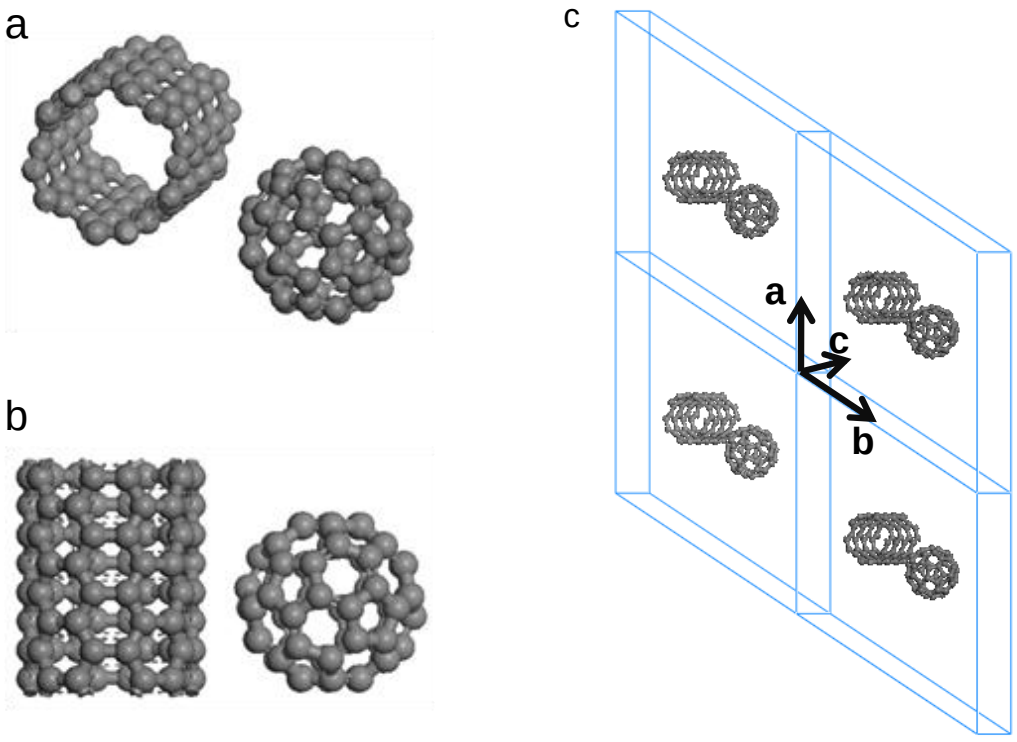

Figure 3.1: The unit cell structure of the (5,5) CNT-C_{60} hybrid system: (a) side view; (b) top view; (c) the structure of the CNT-C_{60} hybrid system in the periodic box. The cell parameters are a = b = 60 Å, c = 9.846 Å, α = β = 90 º and γ = 120 º.

Here, we use the first-principles computational methods, specifically the density functional theory (DFT) through $DMol^3$ from Accelrys [83, 84] in order to investigate the electrochemical characteristics such as adsorption capabilities and charge transfer of such interesting CNT-C_{60} hybrid system. Using density functional theory (DFT), we calculate the Li adsorption energy on the CNT-C_{60} system (Figure 3.1) and the accompanied change in the electronic properties such as band structure, density of states (DOS) and charge distribution as a function of Li adsorption. In addition, we study the mechanism of the Li adsorption in comparison with the Li cluster formation by calculating the Li adsorption energy on the various regions around CNT-C_{60} hybrid system.

3.2 Computational methods

All the DFT calculations in this work were performed using generalized gradient approximation (GGA) Perdew-Burke-Ernzerhof (PBE) functional to treat the electron exchange-correlation energy of interaction electrons with double numerical basis and d-polarization functions basis set [41, 85]. The unit cell dimension was 35 Å × 35 Å × 9.846 Å, which is large enough to ensure that there was no direct interaction between original structure and its self-image in a- and b-axis though the periodic boundary while the dimension in c-axis is determined by the length of the CNT. The k-point samplings for the Brillouin zone were performed using the Monkhorst-Pack special k-point scheme [86] to determine the adsorption energy and other electronic properties such as band structure, density of states and Mulliken charge distribution [87, 88]. Here, we chose metallic tube rather than semiconducting tube because we are interested in the electron conduction capability of metallic CNT for the application towards Li ion battery electrode. (5,5) SWCNT is selected among various metallic tube because it is appropriate

for calculating electronic properties of the various configurations containing many Li atoms in terms of computational time. In order to decide appropriate k-point set, first, we performed the geometry-optimization of the m-(5,5) SWCNT–Li and the CNT–C_{60}–Li system at gamma point (denoted by 1×1) or (1×1×4) k-point (denoted by 1×4). Then, we calculated the Li adsorption energy at various k-point sets. As shown in Figure 3.2, the change of the Li adsorption energy as a function of k-point set was stabilized beyond (1×4) k-point for both cases. Thus we used (1×4) k-point for investigating all the properties of the system. The adsorption of Li was performed at the hexagon sites of SWCNT and the pentagon/hexagon sites of C_{60} because these sites showed most stable adsorption energy from our calculation results.

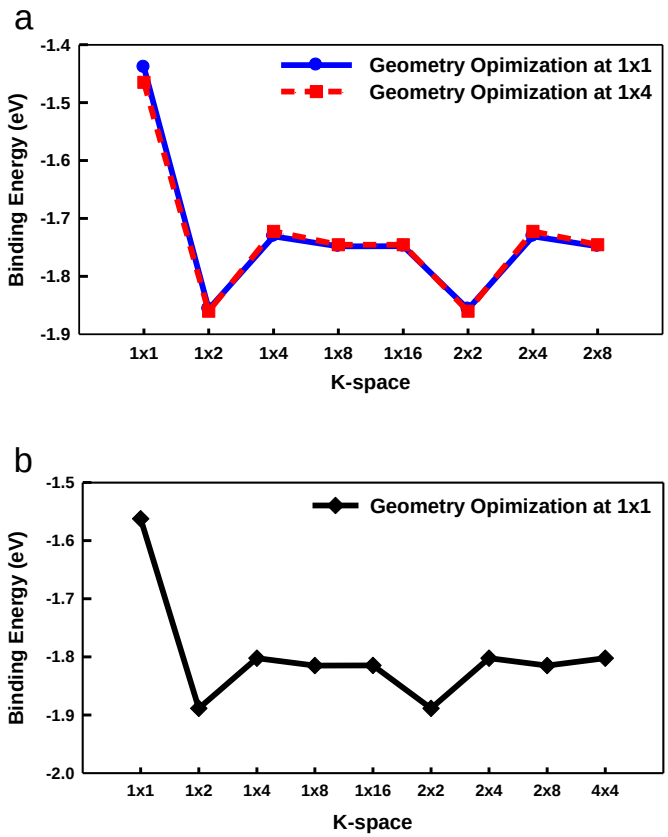

Figure 3.2: Various k-space set samplings to one Li atom on (a) m-(5,5) SWCNT (b) CNT-C_{60} hybrid system.

The adsorption energies and electronic properties of the CNT-C_{60} system were compared with those of the pure metallic (5,5) SWCNT and the C_{60} face-centered cubic (fcc) crystal structure with (111) surface. We define the adsorption energy per Li atom on the CNT-C_{60} hybrid system ($\Delta E_{adsorption}$) as

$$\Delta E_{adsorption} = \frac{E[nLi + hybrid\ \ system] - (E[hybrid\ \ system] + n \times E[Li])}{n} \qquad (3.1)$$

where *n* is the number of the Li atoms, E[*nLi+hybrid System*], E[*hybrid*] and E[*Li*] are the energy of the Li-adsorbed CNT-C_{60} system, the energy of the system without Li and the energy of the single Li in vacuum, respectively.

3.3 Dilute CNT-C_{60} hybrid system

3.3.1 Pure CNT-C_{60} hybrid system

To obtain the configuration of the Li adsorption on the CNT-C_{60} hybrid system, first, we fully optimized the geometry of the CNT-C_{60} hybrid system (Figure 3.1) before placing Li atoms on it. Figures 3.1.a and 3.1.b show the side and the top view of the optimized structure. In the structure, the nearest C-C distance between C_{60} and CNT was 3.267Å while the nearest C-C distance between C_{60} and C_{60} along c axis through the periodic boundary was 3.355Å .

On the other hand, Figures 3.3.a-c display the band structure of the pure (5,5) SWCNT, the pure C_{60} and the CNT-C_{60} hybrid system, respectively. We also investigated several other CNT-C_{60} hybrid systems (metallic (4,4) CNT-C_{60}, (10,10) CNT-C_{60} hybrid system and (10,10) CNT-C_{60} peapod system as shown in the Figures 3.4.a-c) to access the effects of CNT diameters and configuration characteristics. The corresponding band structure of the (4,4) CNT-C_{60}, (10,10) CNT-C_{60} hybrid and peapod system is displayed

in Figures 3.4.d – 3.4.f for comparison with (5,5) CNT-C_{60} system. In these band structures, the Fermi levels are shifted to be located at 0 eV. As shown in Figure 3.3.c, the two energy bands meet at Fermi level (0 eV) keeping the character of the π orbital of the CNT while another two bands appear around ~ 0.56 eV attributed to the t_{1u} state of the neighbor C_{60} chain [89].

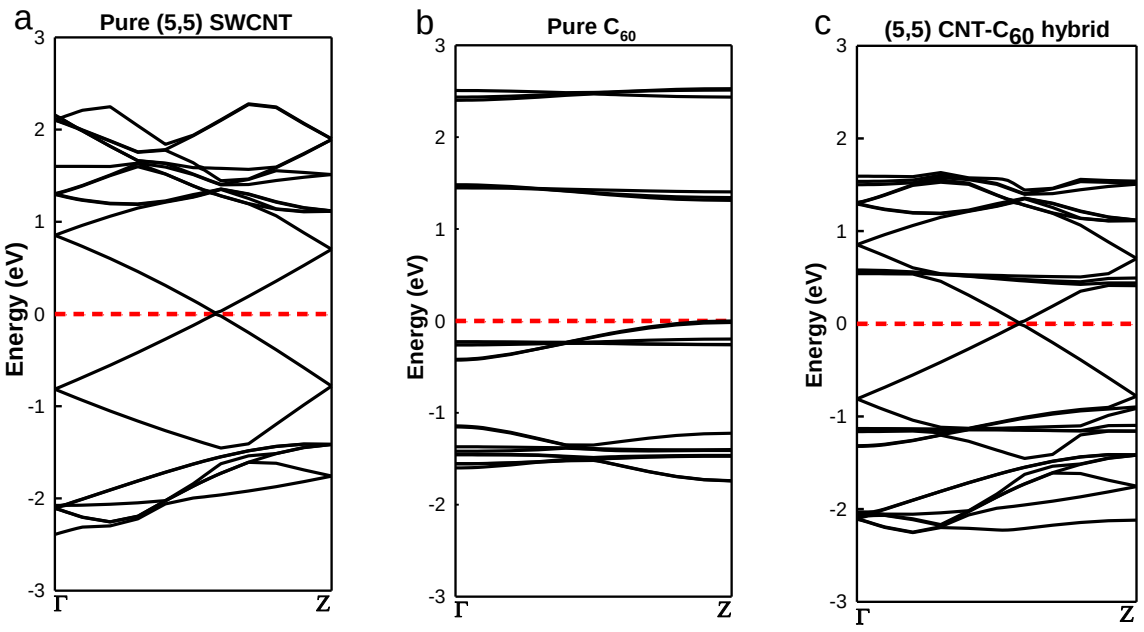

Figure 3.3: (a) The band structure of pure (5,5) SWCNT; (b) the band structure of the pure C_{60}; (c) the band structure of the (5,5) CNT-C_{60} hybrid system.

This band structure of the hybrid system is similar to that of the peapod system in Figure 3.4.f since both systems consist of CNT and C_{60} resulting in some amounts of charge transfer from CNT to C_{60}. However, the extent of hybridization is less in the CNT-C_{60} hybrid system than the peapod because of the weak interaction between each component in the former system, which is mostly known as the dispersion interaction. Due to this weak interaction, the hybridization between CNT and C_{60} is not sensitive to

the curvature (or diameter) of the CNT, which is verified by investigating (4,4) CNT-C_{60} and (10,10) CNT-C_{60} hybrid system shown in Figure.3.4.d and e: all the band structures from (5,5) CNT-C_{60} to (10,10) CNT-C_{60} hybrid system show no significant difference from each other. In our calculations, therefore, the whole hybrid system is metallic due to the metallic (5,5) SWCNT while the electronic structure seems to retain the characteristics of individual components.

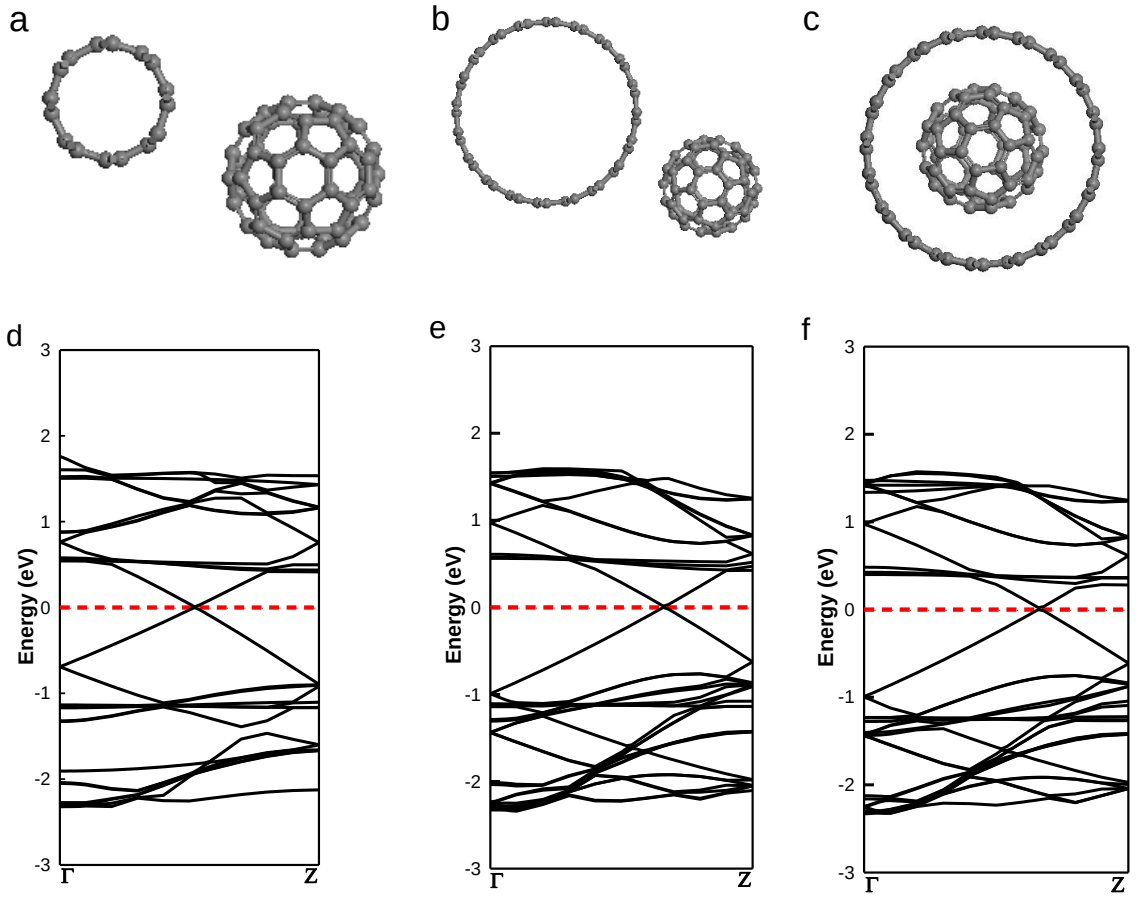

Figure 3.4: The unit cell structure of the (a) (4,4) CNT-C_{60} hybrid system; (b) (10,10) CNT-C_{60} hybrid system; (c) (10,10) CNT-C_{60} peapod system. The band structure of the (d) (4,4) CNT-C_{60} hybrid system; (e) (10,10) CNT-C_{60} hybrid system (f) (10,10) CNT-C_{60} peapod systems.

This is confirmed from the DOS analysis as well in Figure 3.5, showing the DOS of the pure SWCNT, the C_{60} fcc crystal and the CNT-C_{60} hybrid system. It seems that the overall feature of the DOS of the CNT-C_{60} system is a product of the individual components.

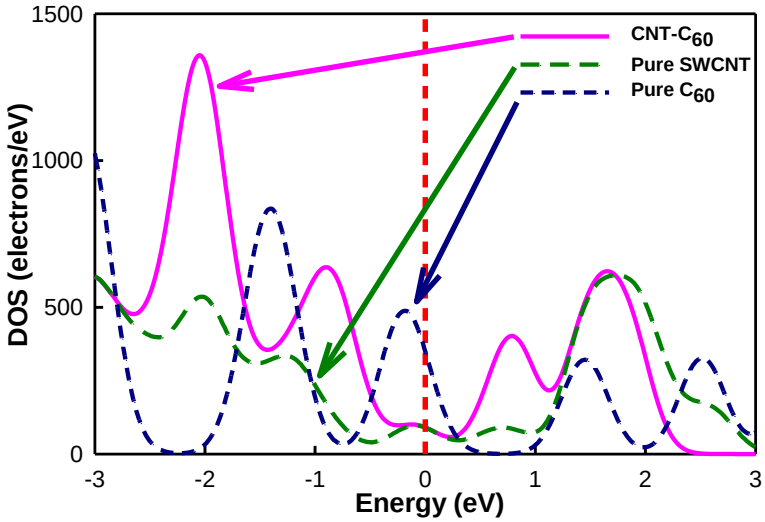

Figure 3.5: The density of states (DOS) of the pristine (5,5) SWCNT, pristine C_{60} fcc crystal and the (5,5) CNT-C_{60} system.

For the conduction band, the peak positions (~0.7 eV and ~1.7 eV) of the CNT-C_{60} are in accordance with those of the pure SWCNT but it seems that they are combined with the downshifted peaks of the C_{60} from their original positions (~1.4 eV and ~2.5 eV). Similarly, the strong peaks of the CNT-C_{60} at ~ -2.1 eV and ~ -0.9 eV combine the peaks of the SWCNT at ~ -2.1 eV and ~ -1.2 eV with those of the C_{60} downshifted from ~ -1.5 eV and ~ -0.2 eV. Again, based on analyzing the band structure and the DOS in which the characteristics of each component is still observed independently except for the shift of some energy levels, it is inferred that the interaction between CNT and C_{60} would be weak.

We also examine the charge distribution of the system using Mulliken population analysis. As summarized in Table 3.1, the charge of the CNT and C_{60} is 0.096e and -0.096e, respectively, which is considered to be due to the relatively strong electron affinity of C_{60}. In addition, the charge transfers on the (4,4) CNT-C_{60} and (10,10) CNT-C_{60} hybrid system show a slight decrease ($|0.089|e$) and increase ($|0.102|e$), respectively compared to the (5,5) CNT-C_{60} hybrid system, which indicates that the charge transfer depends on the diameter of CNT as displayed in Figure 3.6, indicating that the $\pi - \pi$ interaction can be further developed more as the curvature decreases.

Table 3.1: The Li adsorption energy and charge distribution (Mulliken charge) of various CNT-C_{60} hybrid system

System	Charges (e)	
	CNT	C_{60}
(5,5) CNT-C_{60} hybrid	0.096	-0.096
(4,4) CNT-C_{60} hybrid	0.102	-0.102
(10,10) CNT-C_{60} hybrid	0.089	-0.089
(10,10) CNT-C_{60} peapod	0.225	-0.225

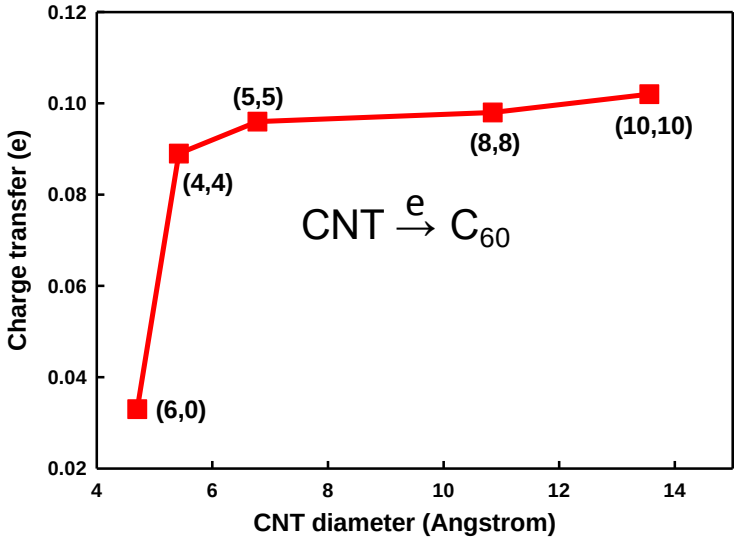

Figure 3.6: Charge transfer (e) as a function of the CNT diameter.

3.3.2 Single Li atom on CNT-C_{60} hybrid system

Next, we simulated the adsorption of Li on various positions on the CNT-C_{60} hybrid system. In this work, we placed the Li atom on the following sites:

(i) the center of the hexagon sites (Center) of CNT since "Center" has lowest Li adsorption energy among the sites on the CNT surface such as top of the carbon atom (Top), above the axial (Axial) or zigzag (Zigzag) carbon-carbon bond (Figure 3.7).

(ii) the pentagon and hexagon site of C_{60} since these sites attain the most stable Li adsorption in the C_{60}.

Figures 3.8.a-b shows that a Li atom is adsorbed on the CNT side (CNT@hybrid) and on the C_{60} side (C_{60}@hybrid), respectively. Through this adsorption, the charge transfer from the adsorbed Li to the CNT-C_{60} hybrid system occurs, and the charge of the adsorbed Li is 0.844e for CNT@hybrid and 0.825e for C_{60}@hybrid.

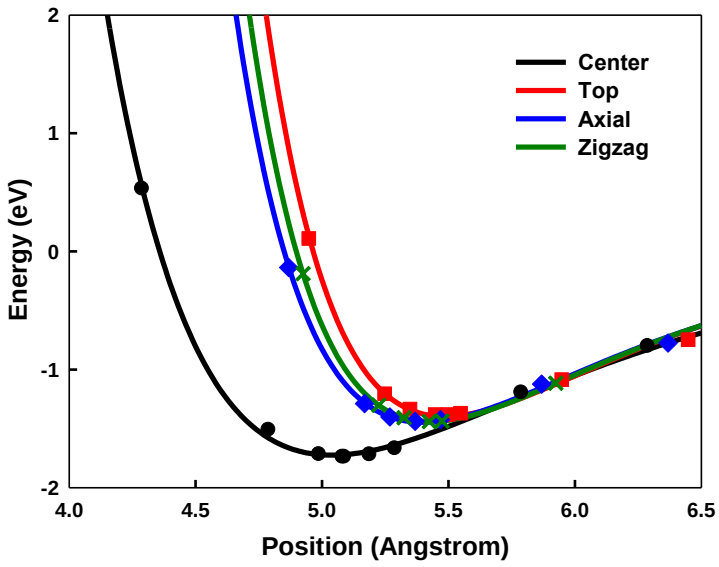

Figure 3.7: Single point energy calculation of the Li atom on the different positions of the hexagonal ring in the (5,5) SWCNT of the function of the distance from the center of the SWCNT: center, top, axial, zigzag.

Table 3.2 shows that the amount of charge transfer in the Li adsorption on the CNT@hybrid (0.844e) is larger than that on the pure CNT (0.835e), which is expected since the hybrid system has more electron affinity due to the presence of C_{60} compared to the pure CNT. However, it should be noted that the Li adsorption on the C_{60}@hybrid with smaller charge transfer (0.825e) than that of the pure CNT, which seems different from our expectation that the charge transfer might be larger for the Li-C_{60}@hybrid than for the Li-CNT@hybrid as well as the Li-CNT.

Table 3.2: Binding energy and charge distribution (Mulliken charge) of a Li atom system

System	Adsorption Energy (eV)	Charges (e)		
		Li	CNT	C_{60}
CNT-C_{60} hybrid	N/A	N/A	0.096	-0.096
1 Li on (5,5) CNT	-1.720(-1.640[35])	0.835	-0.835	N/A
1 Li onCNT@hybrid	-1.802	0.844	-0.640	-0.204
1 Li on C_{60}@hybrid: Pentagonal site	-2.110	0.825	-0.020	-0.805
1 Li on C_{60}@hybrid: Hentagonal site	-2.108	0.847	-0.012	-0.835
1 Li on (111) Surface of C60 fcc	-2.256(-1.820[33])	0.848	N/A	-0.848

We think that this can be understood by considering the charge distribution of the CNT-C_{60} hybrid system. That is, before adsorbing Li atom, some amounts of charges are already transferred from CNT to C_{60} in the CNT-C_{60} system and thereby the CNT is positively charged whereas the C_{60} is negatively charged. Thus the additional charge transfer from the adsorbed Li could take place more for the CNT@hybrid rather than the C_{60}@hybrid.

The Li adsorption energies are calculated as -1.802 eV and -2.110 eV for the CNT@hybrid and the C_{60}@hybrid, respectively, which are larger than that of the pure SWCNT (5,5) (-1.720 eV). This result shows that the Li adsorption capability of the hybrid system is superior to the pure CNT system.

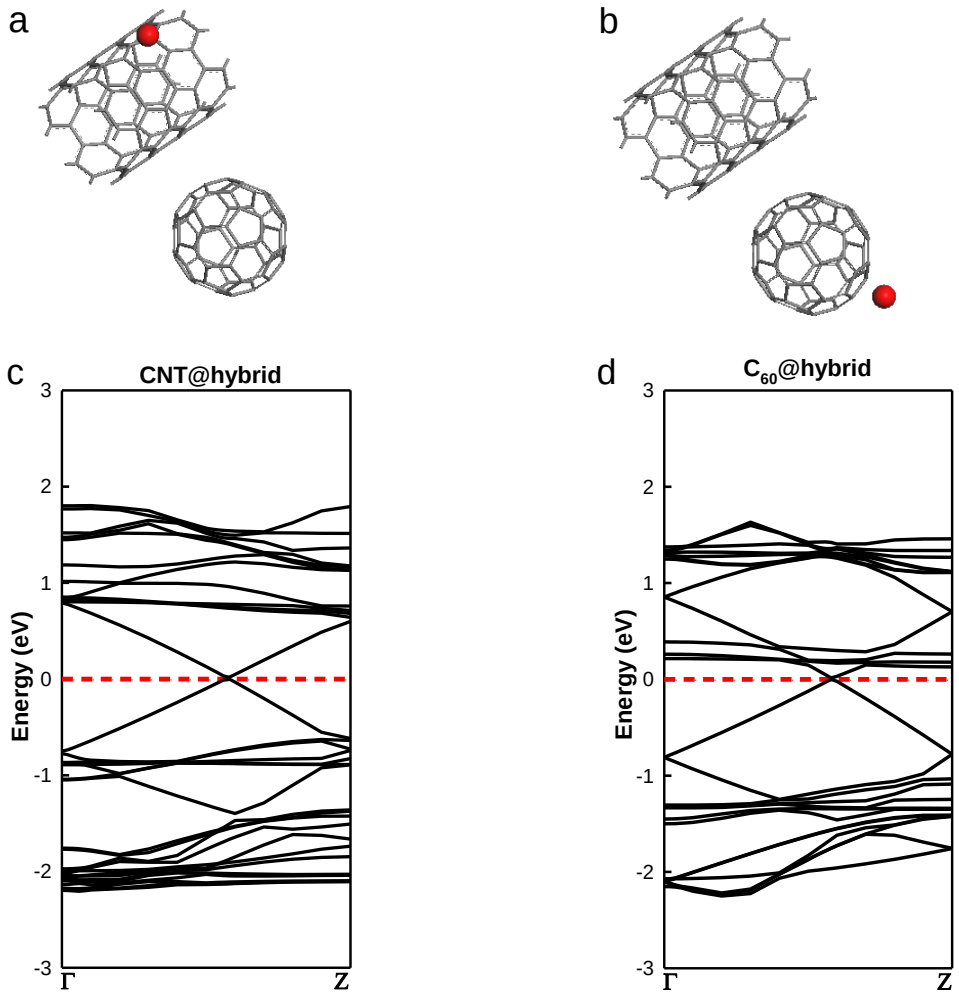

Figure 3.8: One-Li adsorption: (a) CNT@hybrid; (b) C_{60}@hybrid. The band structure of one-Li adsorbed hybrid system: (c) CNT@hybrid; (d) C_{60}@hybrid.

We believe that it is driven by the C_{60} as the (111) surface of C_{60} Face-Centered Crystal (fcc) system shows the largest adsorption energy (-2.256 eV) among the systems we investigated. Therefore, it seems obvious that the Li adsorption and the charge transfer

are driven by the C_{60} in the CNT-C_{60} system. The corresponding band structures of the one-Li-adsorbed hybrid systems are shown at Figures 3.8.c and 3.8.d. When Li atom is adsorbed at CNT@hybrid, the band structures are not changed much as reported already in the previous study [55]. On the contrary, for the Li adsorption on C_{60}@hybrid, it is clearly observed that two bands originated from C_{60} are significantly shifted down.

Based on the above result, we define four distinct regions around the hybrid system as shown in the Figures 3.9.a-c: (i) CNT side (region1, red), (ii) between CNT and C_{60} (region2, yellow), (iii) between C_{60}s (region3, blue) and (iv) C_{60} side (region4, orange) in order to describe the Li adsorption mechanism on the CNT-C_{60} hybrid system more systematically [90]. While the Li atoms can interact with either only CNT in the region1 or only C_{60} in region3 and the region4, they can interact with both CNT and C_{60} simultaneously in region2. After defining four regions, we simulated the adsorption of one Li atom on various positions at each region around the CNT-C_{60} hybrid system.

A Li atom is adsorbed on the CNT (from Pos1_CNT@hybrid to Pos10_CNT@hybrid as shown in Figures 3.10.a and b) and on the C_{60} (from Pos1_C_{60}@hybrid to Pos8_C_{60}@hybrid as shown in Figures 3.10.c and d). By performing geometry optimization for each adsorption position, we obtained the stable structures (Figures 3.11.a-d) and their corresponding adsorption energies (Table 3.3). For the CNT@hybrid sites, it seems that the adsorption energy of the Li in region2 becomes relatively lower in comparison to other regions. We think this is because Li atoms is exposed to C_{60} as well as CNT and has interactions with both components. For the C_{60}@hybrid sites, it is found that the Li adsorption energy has lowest value (-2.649 eV) in the middle of the C_{60}s (region3).

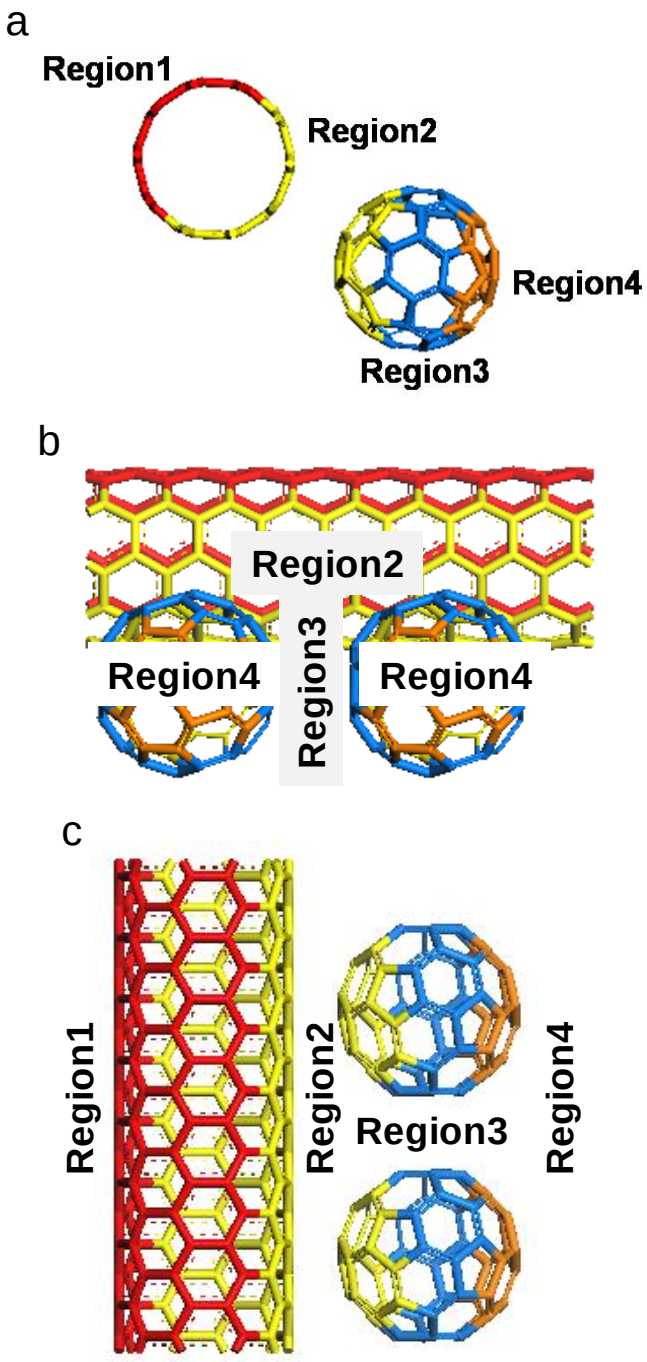

Figure 3.9: The basic structure of the (5,5) CNT-C_{60} hybrid system with different regions: (a) front view; (b) top view; (c) side view; Region1-red, Region2-yellow, Region3-blue, and Region4-orange.

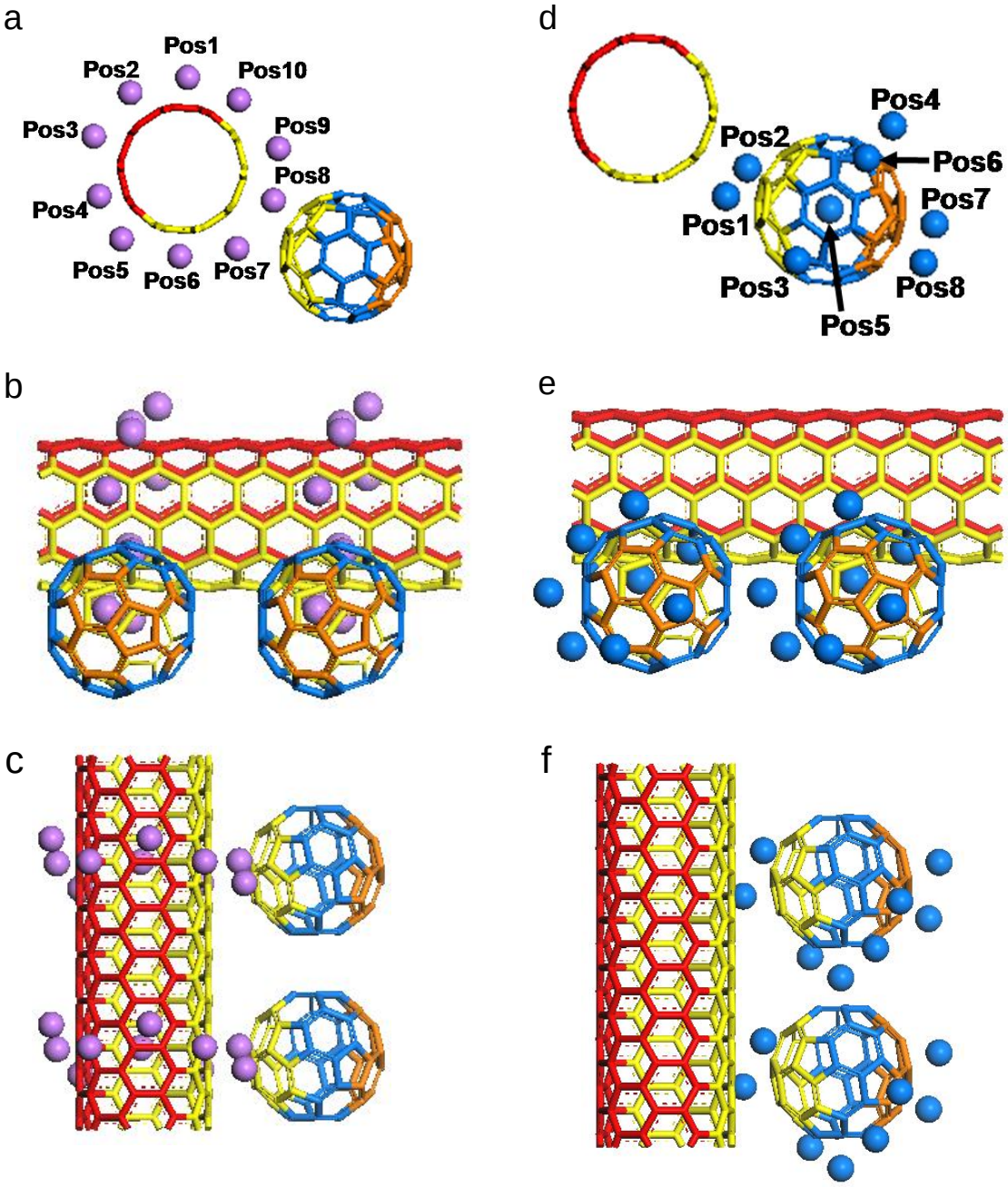

Figure 3.10: Initial structures of one-Li adsorption on various positions around CNT@hybird: (a) front view (b) side view; and C_{60}@hybrid: (c) front view (d) side view.

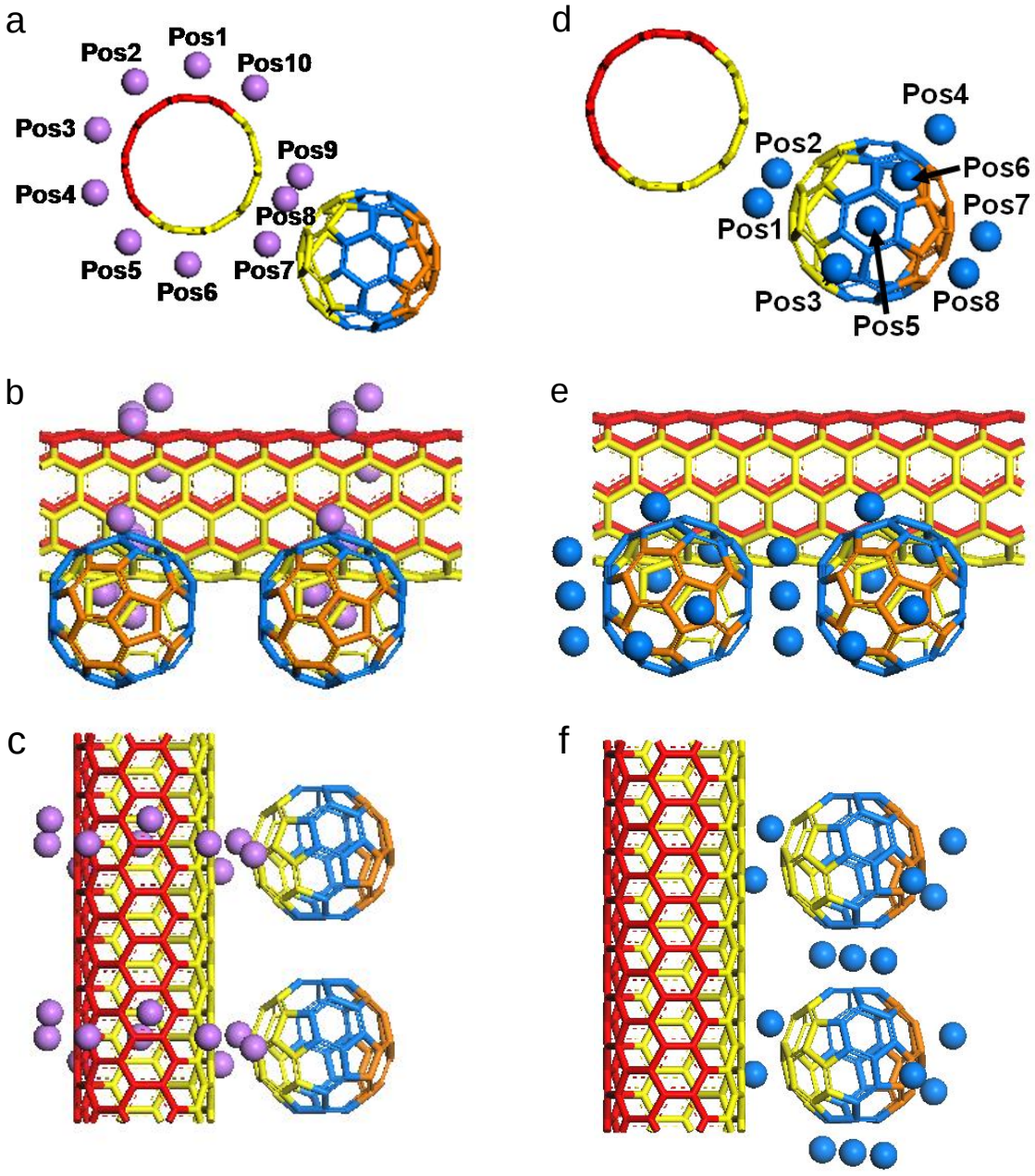

Figure 3.11: One-Li adsorption on various positions around CNT@hybird: (a) front view, (b) side view; around C_{60}@hybrid: (c) front view, (d) side view.

Such strong Li adsorption in the region3 is also attributed to the interaction with C_{60}, so we can conclude that the Li adsorption becomes stronger as the Li atom is placed closer to the C_{60}.

On the other hand, region1 has relatively weak Li adsorption (-1.797 eV) because the Li atom is located in the blind site from the C_{60} even though the adsorption energy in region1 is still lower than that on the bare SWCNT system (-1.720 eV). Considering that the Li adsorption energy in region4 also has a relatively lower value (-2.110 eV), we believe that Li atoms will favorably occupy the C_{60} sites first, especially the mid-space between C_{60}s or between C_{60} and CNT and then the remaining side of C_{60} and CNT sites in order. Through this adsorption, the charge transfer from the adsorbed Li to the CNT-C_{60} hybrid system takes place, and its amount ranges from 0.825*e* to 0.975*e* depending on the positions.

We also performed an energy decomposition analysis to distinguish the contributions of electrostatic (ES) and non-electrostatic (NES) interactions to the adsorption energy. The electrostatic energy (Es) was calculated from a point charge model. The non-electrostatic energy (E_{NES}) was obtained from the difference between the Li adsorption energy and the electrostatic energy (Es) ($E_{NES} = \Delta E_{adsorption} - E_{ES}$). It is clearly shown in Table 3.4 that the electrostatic interaction is dominant in the Li adsorption on the CNT-C_{60} system. The positive values of E_{NES} indicate that the Li-C distances are too short for dispersive interaction, which is actually in the range of repulsive interaction. This negative electrostatic energy with such short Li-C distances confirms that the nature of Li adsorption on the CNT-C_{60} system is a chemi-sorption through charge transfer.

Table 3.3: The adsorption energy and charge distribution (Mulliken charge) of one-Li atom system

System	Adsorption Energy (eV)	Charges (e)		
		Li	CNT	C_{60}
Pos1_CNT@hybrid (region1)	-1.802	0.844	-0.640	-0.204
Pos2_CNT@hybrid (region1)	-1.797	0.844	-0.644	-0.200
Pos3_CNT@hybrid (region1)	-1.801	0.844	-0.649	-0.195
Pos4_CNT@hybrid (region1)	-1.799	0.844	-0.648	-0.196
Pos5_CNT@hybrid (region1)	-1.809	0.844	-0.634	-0.210
Pos6_CNT@hybrid (region2)	-1.859	0.852	-0.600	-0.252
Pos7_CNT@hybrid (region2)	-2.558	0.902	-0.287	-0.615
Pos8_CNT@hybrid (region2)	-2.571	0.950	-0.414	-0.536
Pos9_CNT@hybrid (region2)	-2.471	0.853	-0.333	-0.520
Pos10_CNT@hybrid (region2)	-1.829	0.847	-0.620	-0.227
Pos1_C_{60}@hybrid (region2_pentagon)	-2.569	0.904	-0.274	-0.630
Pos2_C_{60}@hybrid (region2_hexagon)	-2.576	0.975	-0.294	-0.681
Pos3_C_{60}@hybrid (region3_pentagon1)	-2.624	0.860	0.024	-0.884
Pos4_C_{60}@hybrid (region3_pentagon2)	-2.111	0.828	-0.032	-0.796
Pos5_C_{60}@hybrid (region3_hexagon1)	-2.514	1.484	0.045	-1.529
Pos6_C_{60}@hybrid (region3_hexagon2)	-2.649	0.863	0.026	-0.889
Pos7_C_{60}@hybrid (region4_pentagon)	-2.110	0.825	-0.020	-0.805
Pos8_C_{60}@hybrid (region4_hexagon)	-2.108	0.847	-0.016	-0.831

Table 3.4: Energy decomposition analysis for one-Li systems

System	Adsorption energy (eV)	Es* (eV)	E_{NES}** (eV)
Pos3_CNT@hybrid (region1)	-1.801	-2.514	0.713
Pos8_CNT@hybrid (region2)	-2.571	-4.042	1.471
Pos2_C_{60}@hybrid (region2_hexagon)	-2.576	-4.134	1.558
Pos6_C_{60}@hybrid (region3_hexagon2)	-2.649	-3.090	0.441
Pos7_C_{60}@hybrid (region4_pentagon)	-2.108	-2.588	0.480

*Es: Electrostatic energy, **E_{NES}: Non-electrostatic energy

3.3.3 Adsorption of two Li atoms on CNT-C_{60} hybrid system

We added another Li atom at various sites in each region near the first Li atom to investigate the Li adsorption mechanism. Because the energy density of Li battery is proportional to the number of Li atoms on the electrode, it is very important to investigate how efficiently Li atoms utilize the vast amount of surface provide by the CNT-C_{60} hybrid system. At a glance, a maximum Li capacity could be obtained by depositing Li atoms at all carbon rings of the CNT-C_{60} system. In this point, however, a question could be raised asking the possibility of Li cluster formation. So far, it has been reported that Li atoms remain as an isolated individual atom adsorbed on C_{60} rather than form a cluster on C_{60}, which was rationalized by the binding energy: the Li-C binding energy is larger than the Li-Li binding energy [91]. Although this previous report checked only the pentagon sites as the binding site, the picture generated from this study [91] was that Li atoms would wrap a C_{60} first before forming their cluster. Therefore, we need a systematic study to understand adsorption direction on the hybrid system from various adsorption sites. For this purpose, we provided the second Li atom in relation to the first Li atom in each region of the hybrid system, although it is not easy to explicitly define all the possible

configurations for accommodating two Li atoms. Thus, we selected the positions for the second Li atom (blue) based on the adsorption energy of the first atom (purple). Here we assumed that the second Li atom is adsorbed on the nearest neighboring (N.N.) site or the next nearest neighboring (N.N.N.) site in either the radial or axial direction along the axis of the CNT surface for the CNT@hybrid (Figure 3.12.a). We also assumed that the second Li atom is adsorbed on the pentagonal or hexagonal ring in C_{60}@hybrid following either direction along the axis of the CNT making the N.N. or the N.N.N. configuration (Figure 3.12.b).

The Li adsorption energies of the two Li atoms using equation (3.1) are listed in Table 3.5 and some representative arrangements in each region are displayed in Figure 3.13. Figures 13.3.a and 13.3.b show the optimized structures in region1 representing the N.N.N. and the N.N. site in radial direction from the first Li atom positioned at Pos1_CNT@hybrid, respectively, and the adsorption energy at the N.N.N. site (Figure 3.13.a, -1.670 eV) is the lowest among the other configurations in region1. Although these values are higher than that of the one-Li adsorption energy, they are still lower than the Li-Li binding energy (experiment: -1.030 eV [92]; Dmol^3: -1.008 eV [93]), which means the second Li atom prefers adsorption on the hybrid system rather than the binding with the given Li atom. Please note that the adsorption energy in region1 is the highest because those Li atoms are not able to interact with $C_{60.}$ On the other hand, the Li adsorption on the C_{60}@hybrid in region4 seems to be more sensitive to the adsorption site (Figures 3.13.g and 3.13.h): the adsorption energy of the second Li atom is calculated as -2.312 eV for the pentagonal site (Figure 3.13.g, the N.N.N. site of the pentagonal site) and -1.839 eV for the hexagonal site (Figure 3.13.h, the N.N. site of the pentagonal site)

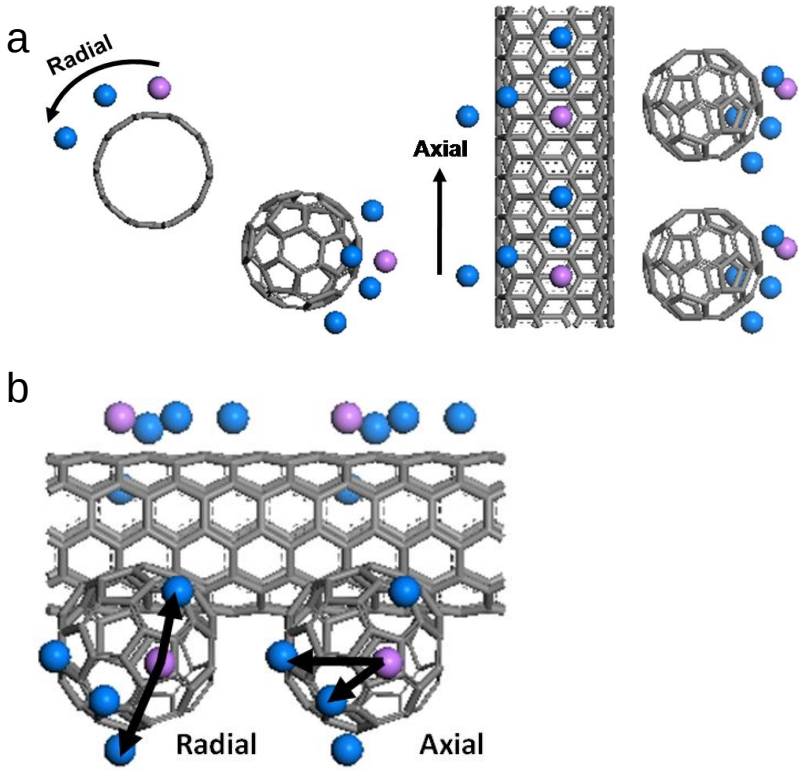

Figure 3.12: The radial and axial direction of the second Li atom adsorption on the two-Li atom system around (a) CNT@hybird; (b) C_{60}@hybrid (1st Li atom: purple, 2nd Li atom: blue).

to the axial direction starting from the Pos7_C_{60}@hybrid, which seems that the Li adsorption will take place using the N.N.N. sites of the pentagon site for C_{60}.

The Li adsorption energies in the region2 (Figures 3.13.c and 3.13.d) show the low values from -2.188 eV (at the N.N.N. site in the radial direction from the first Li atom at Pos8_CNT@hybrid) to -2.632 eV (at the N.N.N. site in the axial direction from Pos1_C_{60}@hybrid). In region2, the interaction with both CNT and C_{60} enhances the Li adsorption on the hybrid system, while it seems Li adsorption does not depend on the adsorption sites within this region, compared to region1 and 4.

Table 3.5: The adsorption energy of two- Li aomts adsorption systems

System	Adsorption Energy (eV)
2 Li on region1: Radial (N.N.N.[a] site)	-1.670
2 Li on region1: Radial (N.N.[b] site)	-1.523
2 Li on region1: Axial (N.N.N. site)	-1.529
2 Li on region1: Axial (N.N. site)	-1.381
2 Li on region2 (CNT): Radial (N.N.N. site)	-2.188
2 Li on region2 (CNT): Radial (N.N. site)	-2.405
2 Li on region2 (CNT): Axial (N.N.N. site)	-2.456
2 Li on region2 (CNT): Axial (N.N. site)	-2.475
2 Li on region2 (C_{60}): Radial (N.N.N. site)	-2.297
2 Li on region2 (C_{60}): Radial (N.N. site)	-2.195
2 Li on region2 (C_{60}): Axial (N.N.N. site)	-2.632
2 Li on region2 (C_{60}): Axial (N.N. site)	-2.475
2 Li on region3: Radial (N.N.N. site)	-2.601
2 Li on region3: Radial (N.N. site)	-2.623
2 Li on region4: Radial (N.N.N. site)	-2.014
2 Li on region4: Radial (N.N. site)	-1.864
2 Li on region4: Axial (N.N.N. site)	-2.312
2 Li on region4: Axial (N.N. site)	-1.839

a. N.N.N.: Next Nearest Neighbor, b. N.N.: Nearest Neighbor

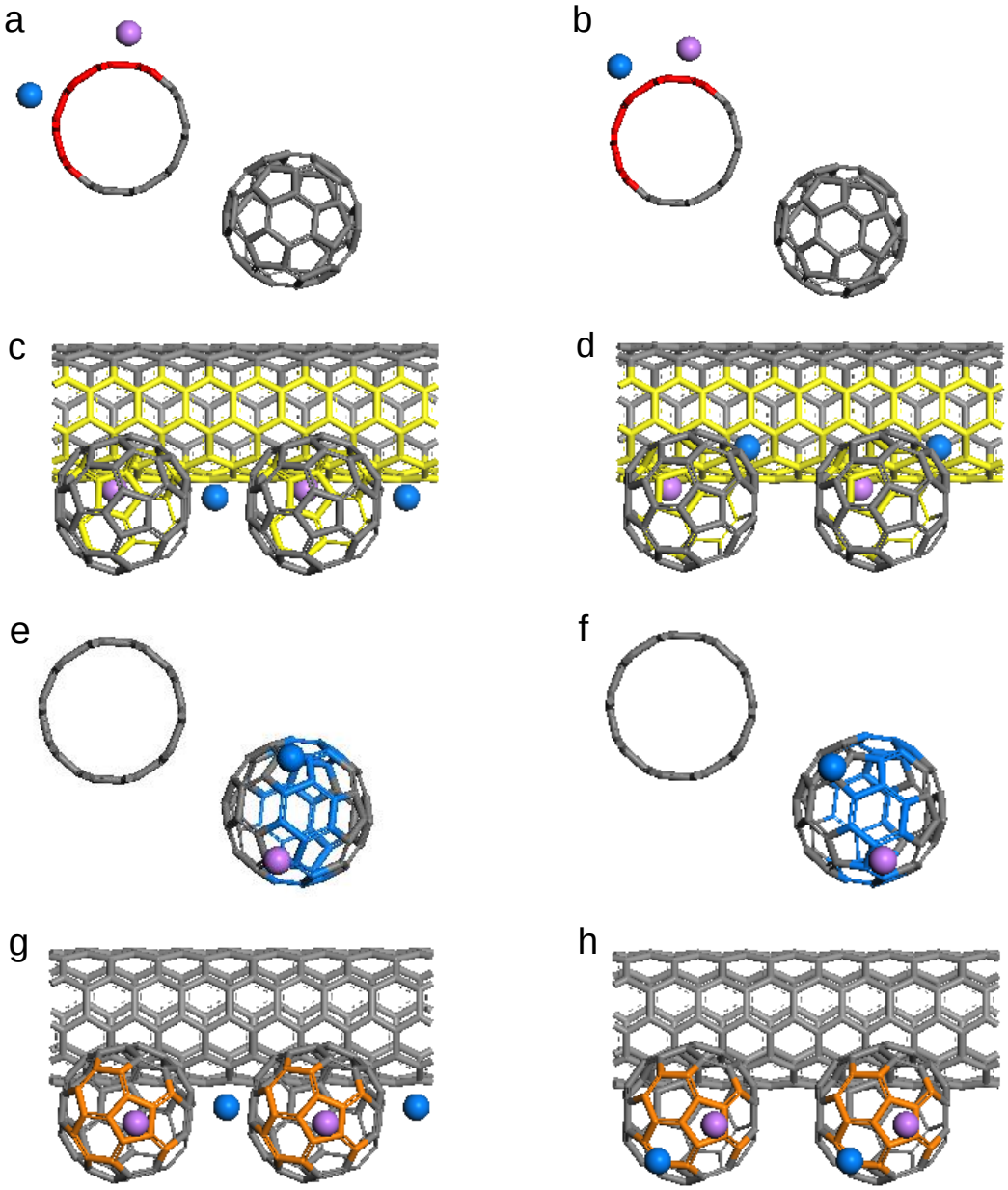

Figure 3.13: Two-Li adsorption on various regions. For region1: (a) next nearest neighboring (N.N.N.) site; (b) nearest neighboring (N.N.) site to radial direction at CNT@hybrid. For region2: (c) next nearest neighboring (N.N.N.) site; (d) nearest neighboring (N.N.).

The Li adsorption energy in region3 is also low: -2.601 eV at the N.N.N. site and -2.63 eV at the N.N. site in the radial direction from the first atom at the Pos3_C_{60}@hybrid (Figures 3.13.e and 3.13.f). For both cases, the adsorption energy is low because the Li atoms are located between C_{60}s which have strong electron affinity. From the calculation results, we could expect that Li adsorption starting from around C_{60} will proceed in the direction that maximizes the exposure to C_{60} of high electron affinity.

We also checked the corresponding changes in the band structures of some two Li atoms systems as shown in Figures 3.14, showing some significant band shifts compared to the one-Li adsorption: specifically, the two-Li adsorption on CNT@hybrid (Figures 3.14.c and 3.14.d) shifts down the energy bands originated from CNT while the two-Li adsorption on C_{60}@hybrid (Figures 3.14.g and 3.14.h) shifts down the bands from the C_{60}. This is actually because the Fermi level is increased due to the extra electrons injected to the CNT-C_{60} system from Li atoms.

3.3.4 Multiple Li atoms adsorbed on CNT-C_{60} hybrid system

Now, we may ask the following question: if the Li adsorption energy is decreased with increasing number of Li atom, what would be the Li adsorption energy when the entire surface of the system is covered by Li atoms? Assuming that the Li adsorption will proceed on the N.N.N. sites, the number of absorbed Li atoms is 20 for CNT@hybrid, 12 for C_{60}@hybrid, and therefore, totally 32 Li atoms wrap up the hybrid system. The initial structure is presented in the Figure 3.15. After the geometry optimization, the positions of the Li atoms are adjusted as shown in Figures 3.16.a–f. From the optimized structures displayed, it is observed that Li atoms that initially attached on the CNT@hybrid sites (Figures 3.16.a and 3.16.e) are attracted toward C_{60}, while the Li atoms around C_{60}, as

shown in the Figures 3.16.c and 3.16.e, keep their original positions because the C_{60} sites have lower Li adsorption energy than CNT sites.

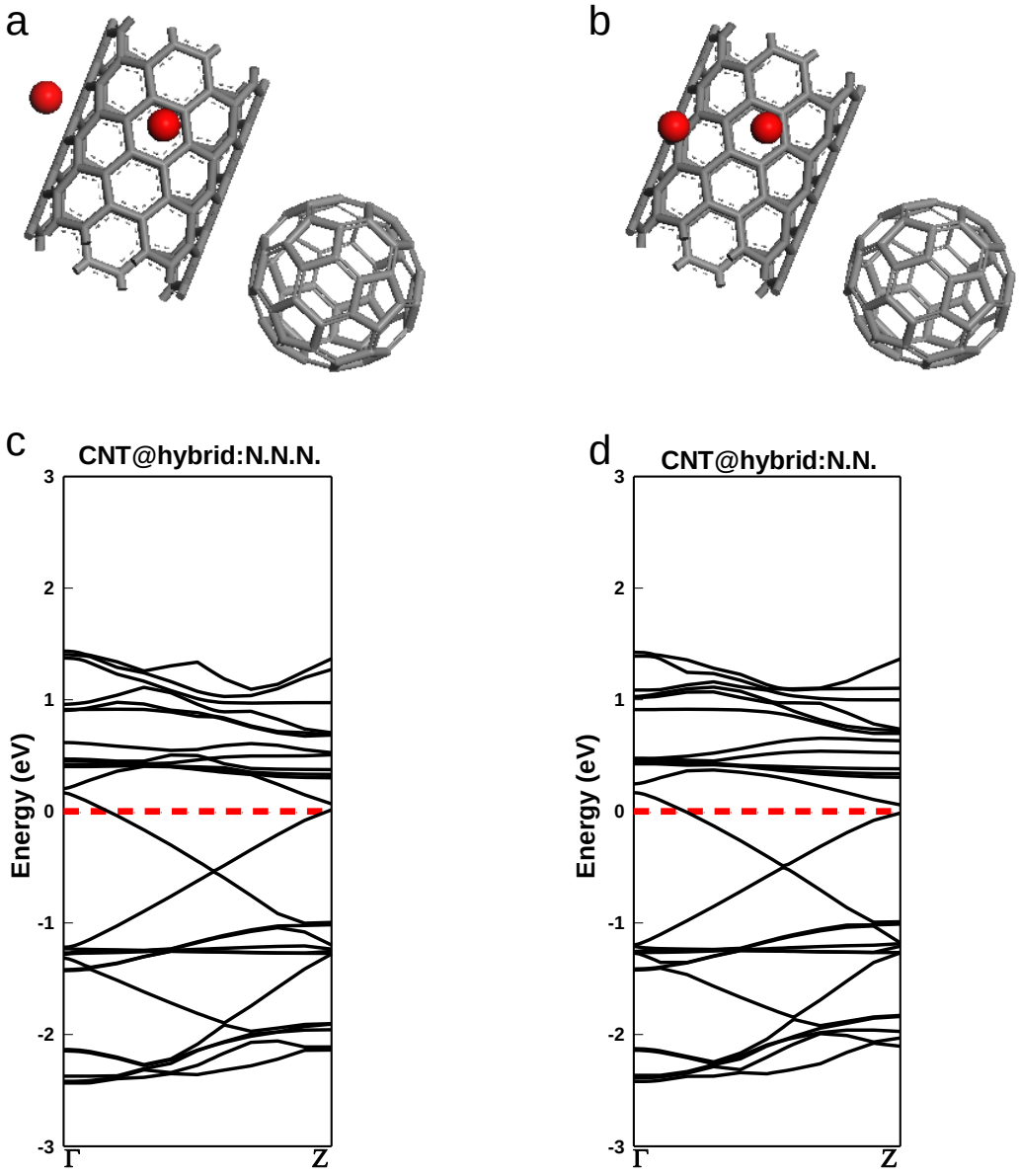

Continued

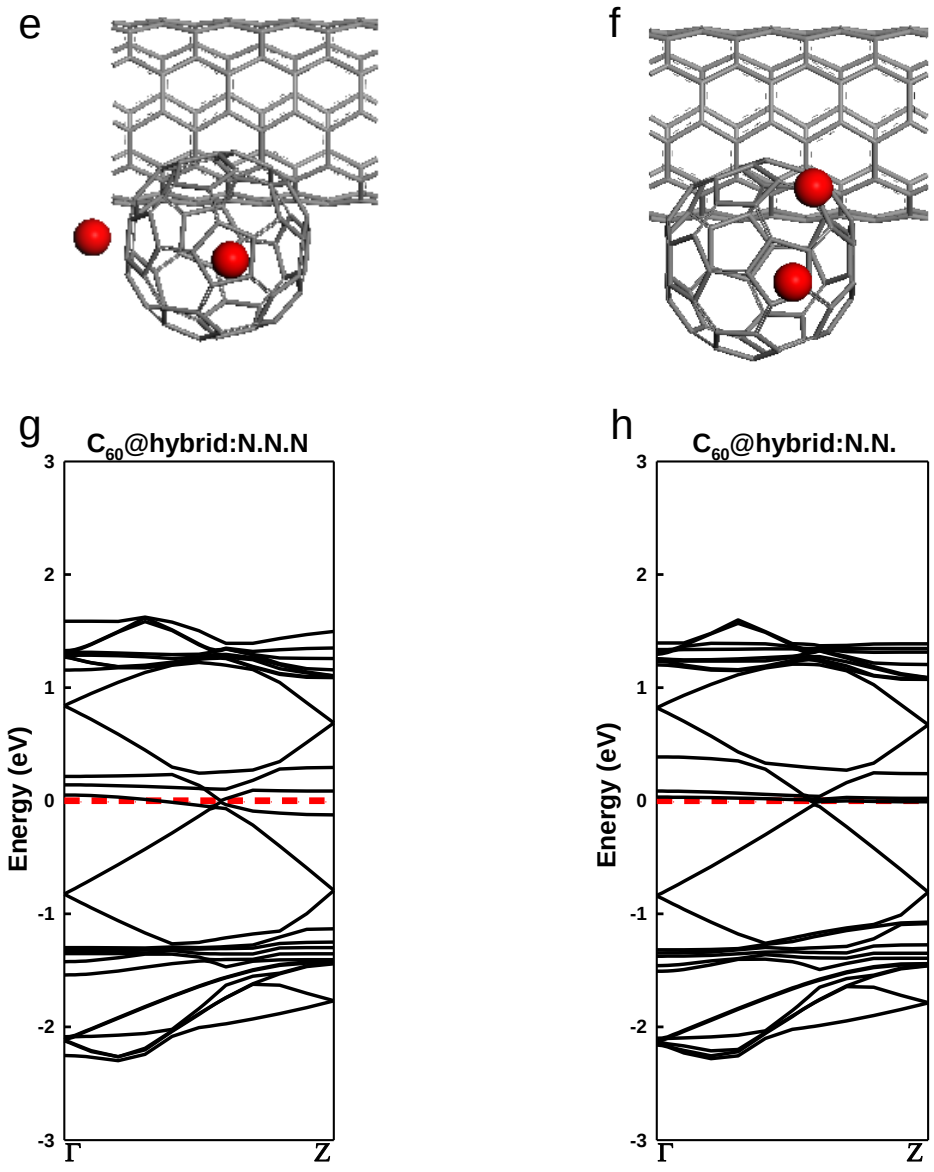

Figure 3.14: Two-Li adsorption on CNT@hybrid: (a) next nearest neighboring site; (b) nearest neighboring site: The corresponding band structures: (c) next nearest neighboring site and (d) nearest neighboring site of CNT@hybrid. Two-Li adsorption on C_{60}@hybrid: (e) next nearest neighboring site: (f) nearest neighboring site. The corresponding band structures: (g) next nearest neighboring site and (h) nearest neighboring site of C_{60}@hybrid.

Such positional adjustment agrees well with the results observed for the two-Li system, showing the lowest Li adsorption energy around C_{60}, which drives Li atoms from the CNT sites toward C_{60}. The adsorption energies for the multiple Li adsorption are -1.745 eV for CNT@hybrid, -2.147 eV for C_{60}@hybrid and -1.809 eV for the entire hybrid system (Table 3.6), indicating that the Li adsorption will take place on the C_{60} side (especially starting from the sites between CNT and C_{60}) until all the available sites on the C_{60} are completely consumed, and the Li adsorption will subsequently proceed to the sites on the CNT side. Although the Li adsorption energy decreases with increasing numbers of Li atoms, all these adsorption energies are lower than the Li-Li binding energy, indicating that the Li cluster formation is not likely to occur until all the available sites on the CNT-C_{60} hybrid system are covered.

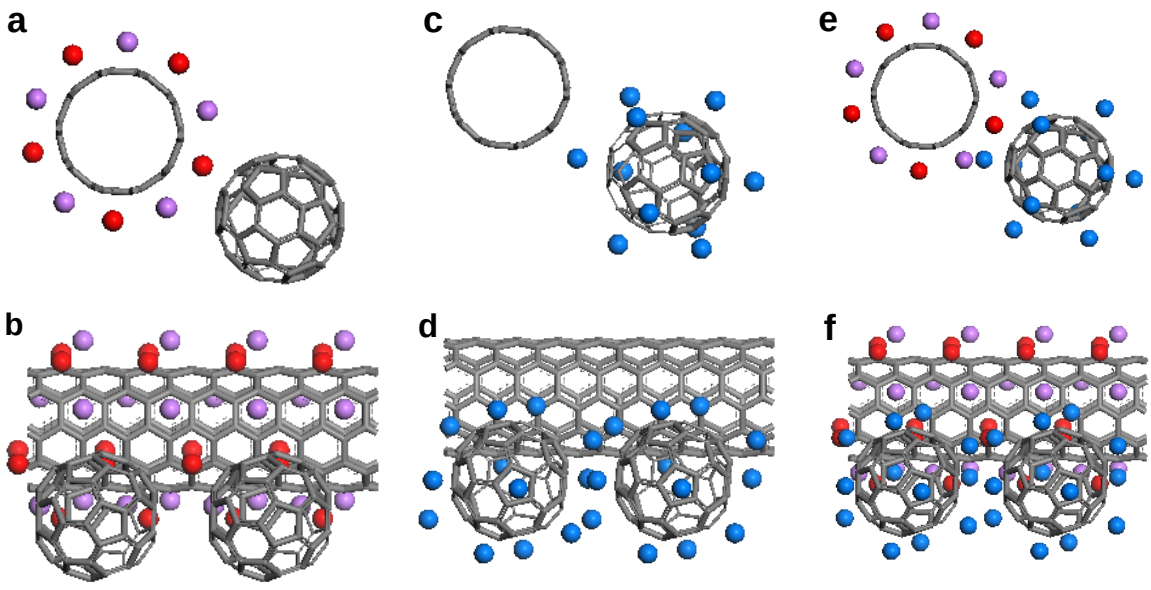

Figure 3.15: Initial structure: Initial structure: Front and side view of multiple-Li adsorption on the CNT-C_{60} hybrid system: (a), (b) 20 Li atoms on the CNT@hybrid; (c), (d) 12 Li atoms on the C_{60}@hybrid; (e), (f) 32 Li atoms on the CNT-C_{60} system.

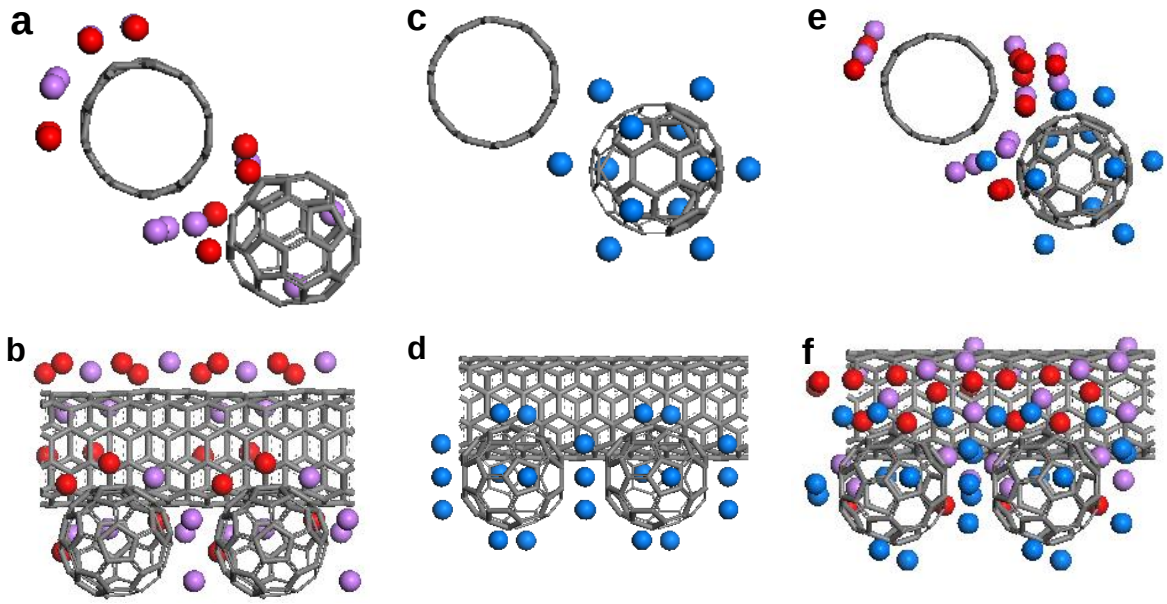

Figure 3.16: Front and side view of multiple-Li adsorption on the (5,5) CNT-C_{60} hybrid system: (a), (b) 20 Li atoms on the CNT@hybrid; (c), (d) 12 Li atoms on the C_{60}@hybrid; (e), (f) 32 Li atoms on the CNT-C_{60} system.

Table 3.6: The adsorption energy of many Li adsorption systems

System	Adsorption Energy (eV)
20 Li atoms on CNT@hybrid	-1.745
12 Li atoms on C_{60}@hybrid	-2.147
32 Li atoms on CNT-C_{60} hybrid	-1.809
Li-Li (experiment)	-1.030 [51]
Li-Li (theory:Dmol^3)	-1.008

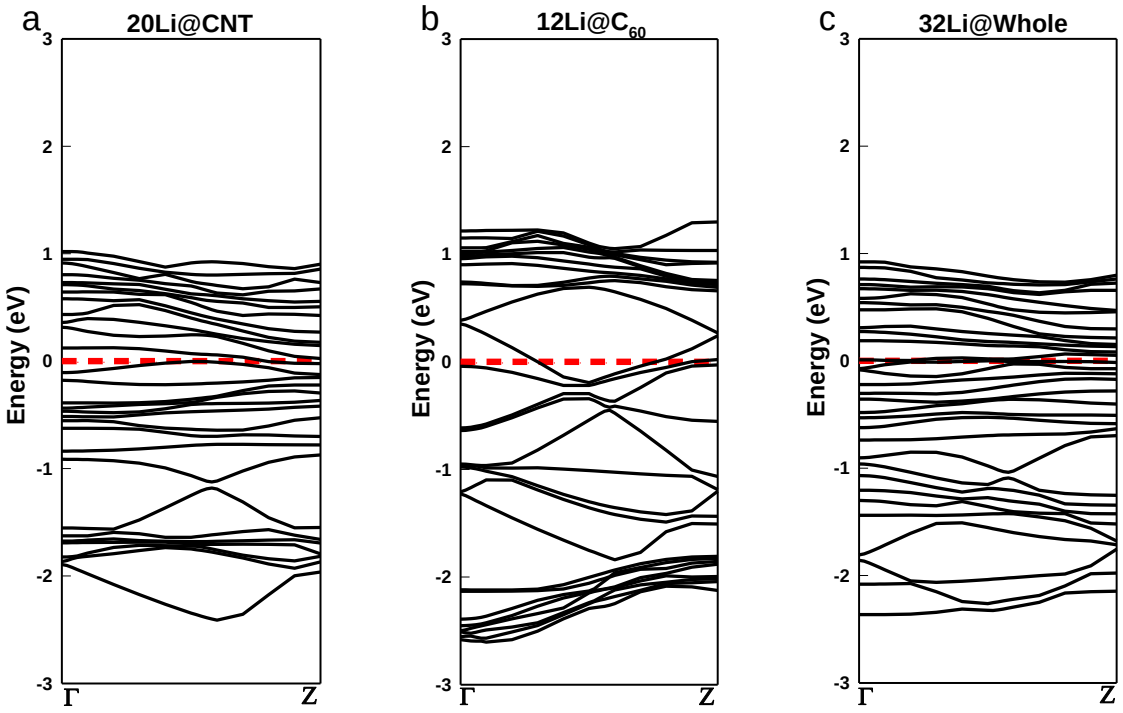

Figure 3.17: The corresponding band structures: (d) 20 Li atoms on the CNT@hybrid; (e) 12 Li atoms on the C_{60}@hybrid; (f) 32 Li atoms on the CNT-C_{60} system.

Figures 3.17.a-c shows the band structure of the multiple-Li adsorbed CNT-C_{60} systems. The most noticeable point from these band structures is that the number of available energy bands around the Fermi level is now significantly increased in the CNT-C_{60} system, which implies that the Li adsorption enhances the metallic character of the system such as conductivity. This finding is again confirmed from the DOS in Figures 3.18.a and 18.b: compared to the bare CNT-C_{60} hybrid system, the Li adsorbed systems have more DOS around the Fermi level, meaning the enhanced metallic character of the CNT-C_{60} system. Such enhancement of the metallic character could increase the electron transport property (note that the C_{60} is a semiconductor originally).

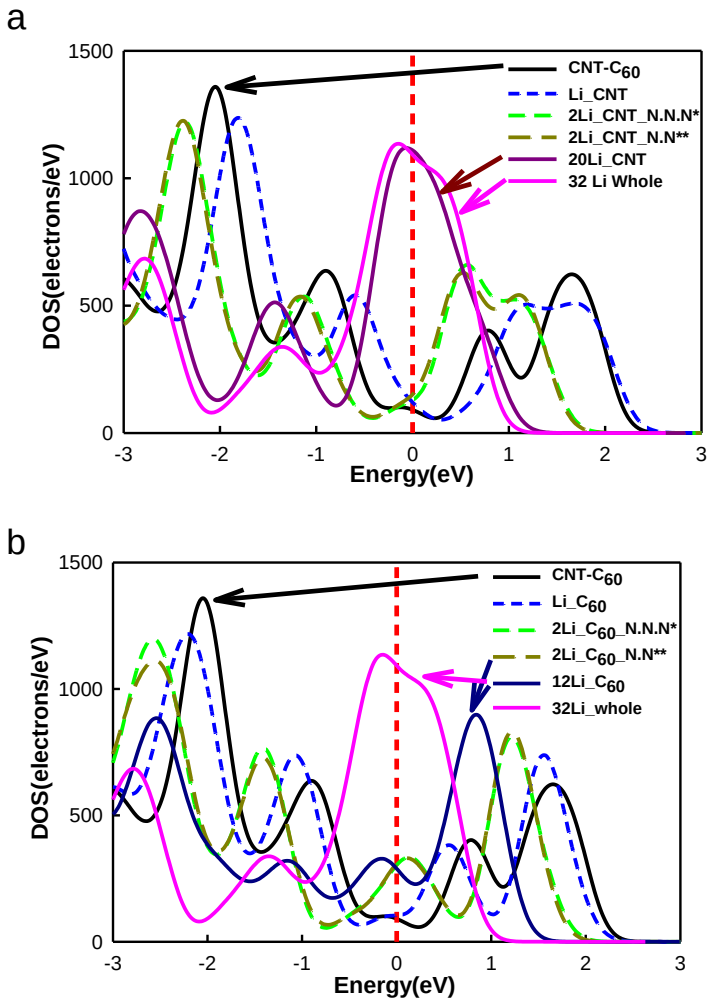

Figure 3.18: Density of states for various numbers of Li atoms adsorbed on (a) CNT@CNT-C_{60} system and on (b) C_{60}@CNT-C_{60}. N.N.N. and N.N. denote the next nearest neighbor site and the nearest neighbor site, respectively.

3.3.5 Electronic properties of the CNT-C_{60} hybrid system

Finally, we investigated electronic properties as a function of the number of Li atoms on the CNT-C_{60} hybrid system in order to analyze the effect of Li adsorption. Figures 3.19.a-g show the highest occupied molecular orbital (HOMO) and the lowest unoccupied molecular orbital (LUMO) of some of the systems: one Li atom (Figures 3.19.b-d) and many Li atoms around the hybrid system (Figures 3.19.e-g). In the pristine

hybrid system shown in the Figure 3.19.a, the HOMO is primarily formed on the CNT side, while LUMO is in the C_{60} side. For the molecular orbital of the one Li atom systems such as CNT@hybrid (Figure 3.19.b), CNT:C_{60} middle (Figure 3.19.c) and C_{60}@hybrid (Figure 3.19.d), the LUMO is mostly formed at the components that are close to a Li atom depending on the Li position. It should be noted, however, that the overall feature of molecular orbital is dominated by the CNT-C_{60} system. Thus, the energy levels of HOMO and LUMO for one Li systems (Figures 3.19.b, 3.19.c and 3.19.d) are somehow similar to those of the pure CNT-C_{60} hybrid system without Li (Figure 3.19.a).

On the other hand, when many Li atoms are absorbed (Figures 3.19.e, 3.19.f and 3.19.g), the molecular orbital are mostly governed by the Li atoms, so the energy levels and distribution of the HOMO and LUMO for the multiple Li adsorption systems undergo significant changes compared to those for the pure CNT-C_{60} hybrid system. Additionally, the HOMO-LUMO difference is seriously reduced; the averaged difference is 1.331 eV and 0.195 eV for the one Li atom system and the multiple Li atom system, respectively. This result indicates that as the number of adsorbed Li atoms increases, the CNT-C_{60} hybrid system is more metalized, and its electronic structure becomes more polarizable due to the decreasing electronic hardness. Thus, we expect that the electrons can easily flow through the hybrid system.

The DOS of the CNT-C_{60} hybrid system was also calculated to investigate the effect of Li adsorption on the electronic structure of the hybrid system in comparison with bare CNT system or bare C_{60} system. The DOS of bare (5,5) SWCNT and (5,5) hybrid system in which Li atoms are adsorbed preferably on CNT side is displayed in the Figure 3.20.a, showing similar electron distribution over the Fermi level representing

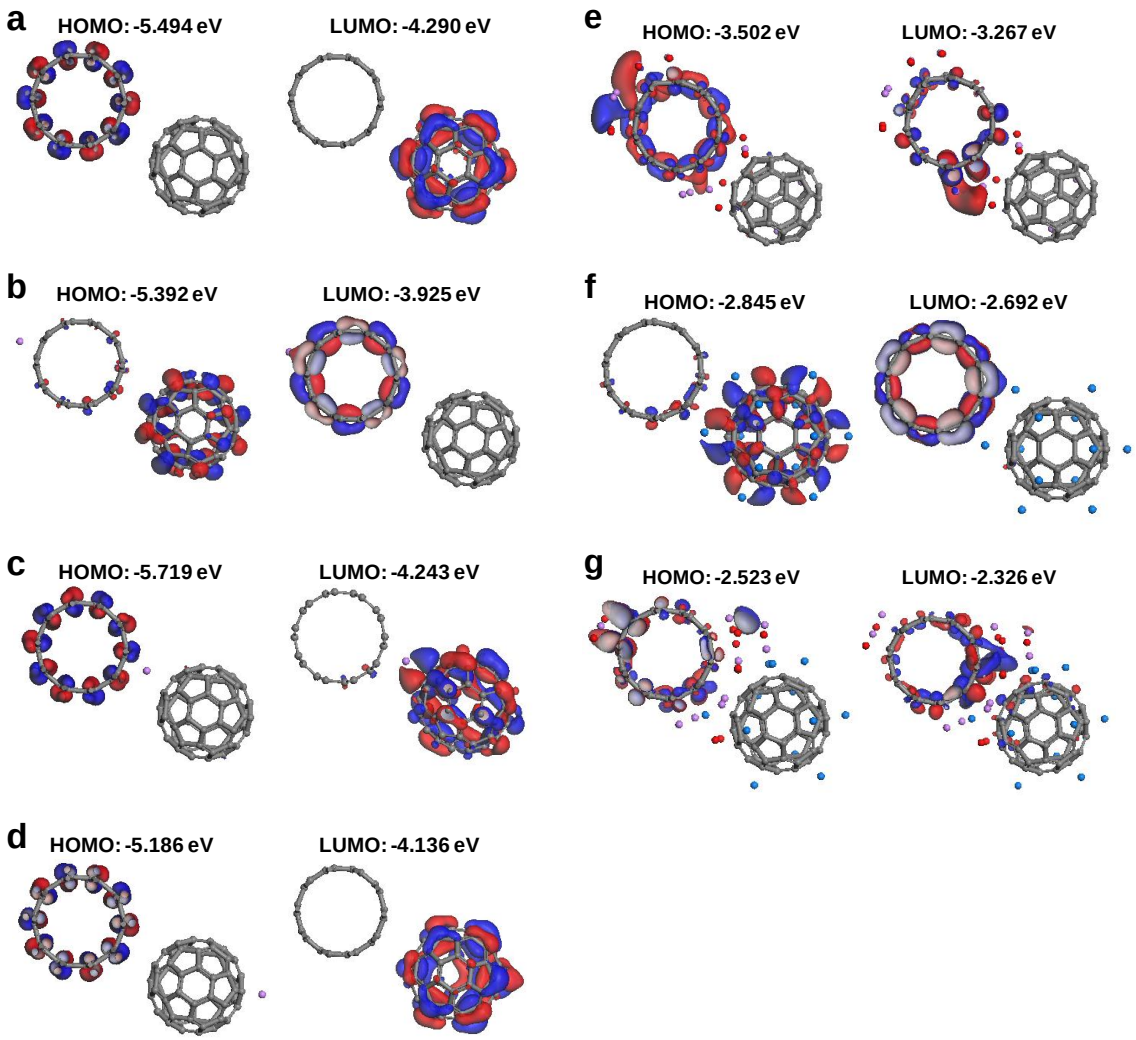

Figure 3.19: HOMO and LUMO of the CNT-C_{60} hybrid systems at different numbers of Li atoms: (a) No Li on the system; one Li atom (b) on the CNT side; (c) between CNT and C_{60}; (d) on the C_{60} side; (e) 20 Li atoms around CNT; (f) 12 Li atoms around C_{60}; (g) 32 Li atoms around CNT and C_{60}. (The isovalue of HOMO and LUMO surface is 0.02).

metallic behavior. Specifically, it is noted that the adsorbed Li atoms provide more electrons to the hybrid system around the Fermi level, which indicates that the hybrid system could be more conductive than bare SWCNT system. Similarly, Figure 3.20.b compares the DOS of bare C_{60} and hybrid system in which Li atoms are adsorbed

preferably on the C_{60} side, showing that the Li adsorption on the C_{60} side generate more available electrons around Fermi level, in which we expect a better conductivity of the system as discussed in Figure 3.20.a.

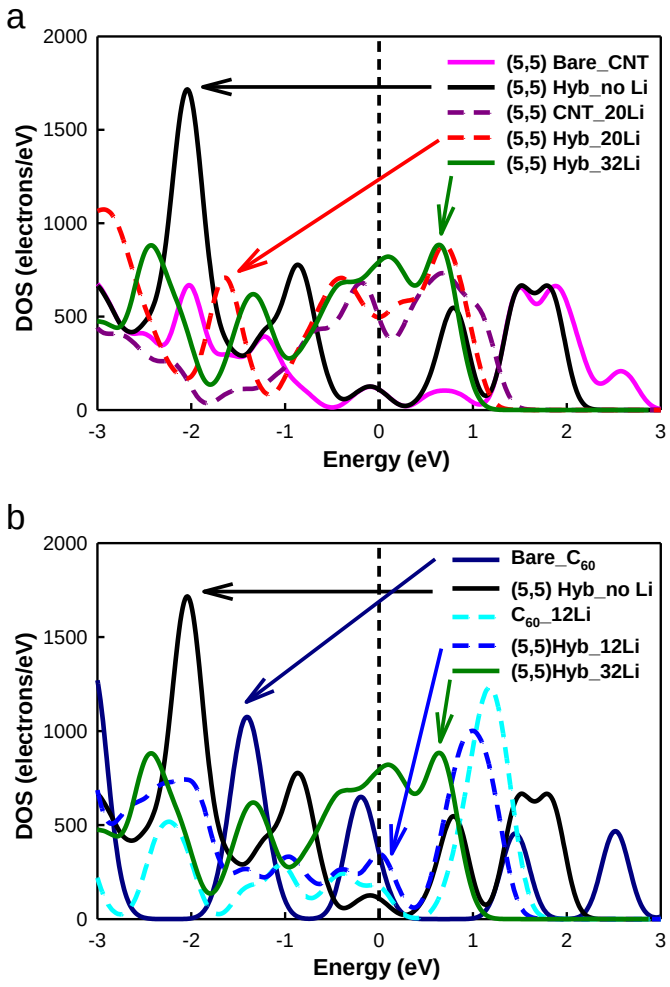

Figure 3.20: Density of states of many Li atoms system on (a) (5,5) CNT and (5,5) CNT-C_{60} hybrid and (b) C_{60} and (5,5) CNT-C_{60} hybrid.

3.3.6 Conclusion

We investigated the Li adsorption on the CNT-C_{60} hybrid system using DFT with GGA PBE. Although it is found that this hybrid system retains the characteristics of its

components such as CNT and C_{60} in the electronic structure, it is clearly observed that the charges are transferred from CNT to C_{60} making the CNT positively charged (+0.096e) and the C_{60} negatively charged (-0.096e). This positively charged CNT could achieve lower Li adsorption energy (-2.571 eV) than the bare CNT system (-1.720 eV), which indicates that the CNT-C_{60} hybrid system has better Li adsorption capability compared to the bare CNT.

Analyzing the Li adsorption as a function of various regions in the CNT-C_{60} hybrid system, we found that the Li adsorption will occur preferably on the C_{60} side, more specifically on the mid-space between C_{60}s (region3) or between CNT and C_{60} (region2), and then subsequently proceed toward the CNT side instead of forming Li cluster since the Li-C adsorptive interaction (e.g., -2.138 eV in overall average for the two Li system) is more stable than the Li-Li binding interaction (-1.030 eV). In other words, it is thermodynamically probable that Li atoms do not form Li cluster unless all the available sites on the hybrid system are occupied by Li atom since these adsorption energies are always larger than the Li-Li binding energy.

Although there is no significant change in the band structure after one Li atom is adsorbed on the hybrid system, additional Li adsorptions shift down the energy bands due to the electron injection from Li to the system. In addition, the change of the electronic properties such as molecular orbital and DOS in the hybrid system were also investigated as a function of the number of Li atoms. From this calculation, it is found that HOMO-LUMO gap is decreased and electron distribution around Fermi level increased concurrently, which means the system becomes more metalized as the number of Li atoms in the hybrid system increases. Therefore, it is to be expected that the CNT-C_{60}

hybrid system has enhanced conductivity and superior Li adsorption capability compared to the bare CNT system.

3.4 Condensed CNT-C_{60} hybrid system

3.4.1 Pure condensed CNT-C_{60} hybrid system

We also investigated the condensed phase of the hybrid system including interactions between each component, which is expected to affect the adsorption energy of the Li atom. To determine the appropriate structure, four new systems (Figures 3.21.b-e) were prepared by adjusting the position of the C_{60} and varying the cell size, before single point energy calculations were performed. Calculated energies are displayed in Figure 3.21.f, which shows the structure in Figure 3.21.c (New2) with the lowest energy among the possible structures of 18.35Å . We suggest the low energy can be explained by the symmetric structure of New2, which allows equivalent interactions of each component to stabilize. The New2 structure was further optimized to adjust geometry without changing the cell size. Figure 3.22.a shows an expanded view of the optimized unit structure (a=b=18.35Å and c=9.846Å) of the condensed phase. The corresponding band structure and DOS are represented in Figures 3.22.b and c, respectively. From the band structure and DOS, we found that the hybrid system was also metallic while retaining the characteristics of each component; therefore, there was no difference in the electronic properties between the dilute and condensed phase systems. This finding can be explained from the weak dispersion interaction between the CNT and C_{60} so that the electronic properties of the system are not affected by the density. However, the amount of charge transfer from the CNT to C_{60} increased from $|0.096|e$ to $|0.141|e$ because C_{60}s are surrounded by other CNTs in the condensed phase.

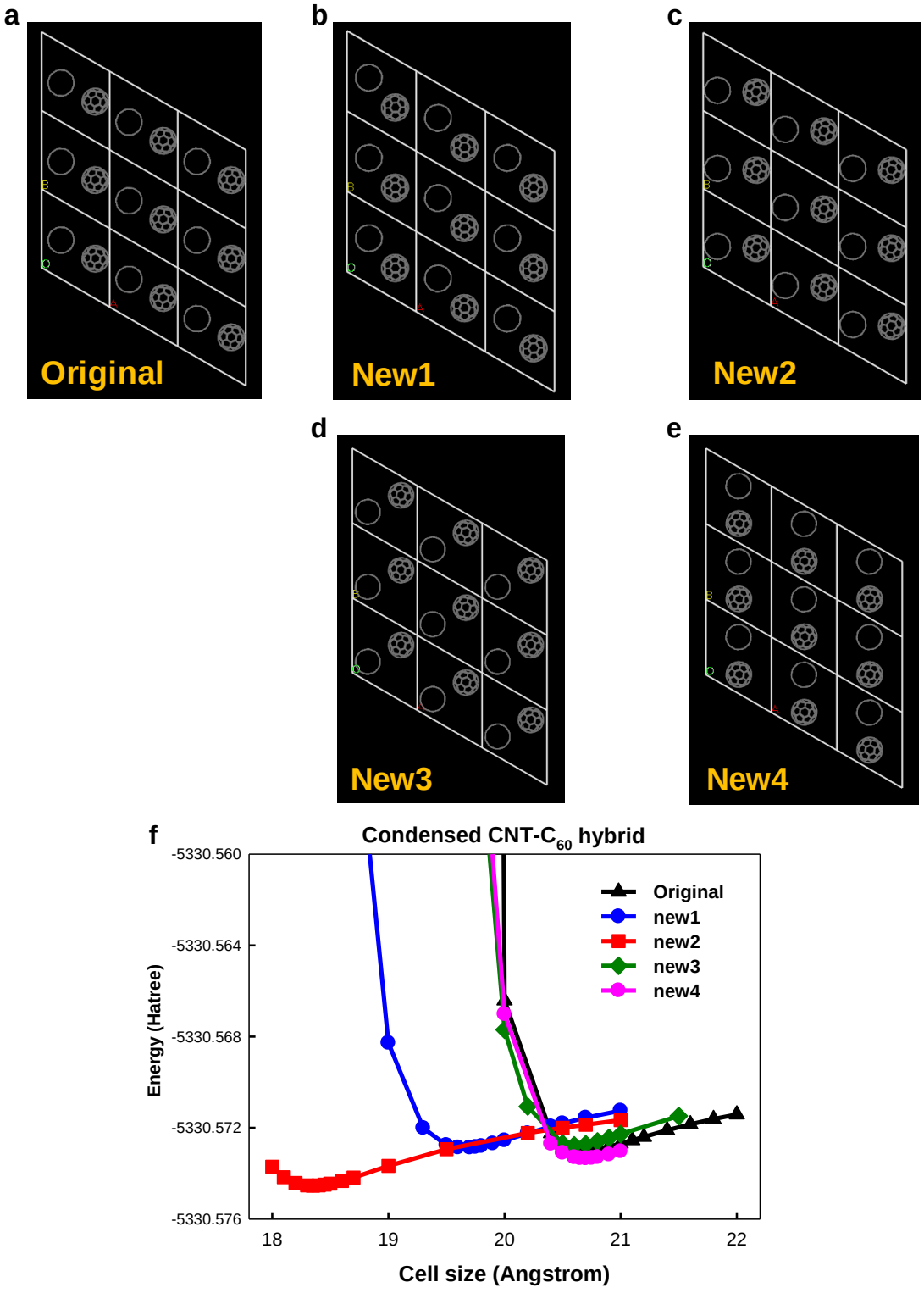

Figure 3.21: Initial structures of the condensed CNT-C_{60} hybrid systems (a) Original; (b) New1; (c) New2; (d) New3; (e) New4; (f) Energy curve of each system in varying cell.

3.4.2. One Li atom on a condensed CNT-C_{60} hybrid system

We investigated the adsorption of one Li on various positions of the condensed system similar to the dilute system. However, we did not assign different regions in this case because it was expected that this symmetric structure made an equal contribution to the Li adsorption regardless of the region. The position of the added Li atom was also chosen on either the center of the hexagon sites of the CNT or on the pentagon and hexagon sites of the C_{60}. A Li atom is located on the CNT from Pos1_CNT@hybrid to Pos10_CNT@hybrid, as shown in Figure 3.23.a, and on the C_{60} from Pos1_C_{60}@hybrid to Pos10_C_{60}@hybrid, as shown in Figure 3.23.d. We acquired the optimized structures (Figures 3.23.b-c and e-f) by performing geometry optimization for each adsorption position and their adsorption energies are listed in Table 3.7. The Li adsorption energy of most spots revealed a narrow distribution range from -2.481eV to -2.642eV compared with the dilute phase of the hybrid system due to interactions with both components. Increased charge transfer (0.141*e*) from the CNT to C_{60} also affects the enhancement of the adsorption energy for the CNT@hybrid sites. Therefore, the increased Li adsorption in the condensed phase can be attributed to the more positively charged CNT surface and to the decreased space with C_{60}, as in region2 in the dilute phase. Furthermore, Pos4_CNT@hybrid and Pos7_CNT@hybrid have high adsorption energy because they are positioned away from C_{60}, which affects Li adsorption as shown in Figure 3.23.c. However, the adsorption energy and the amount of charge transfer at these sites are still better than those of the dilute system because of the closely packed structure. The Li adsorption energy (-2.542eV ~ -2.628eV) and charge transfer for most C_{60}@hybrid sites are quite similar to the values observed in CNT@hybrid systems because of the symmetric and packed structures.

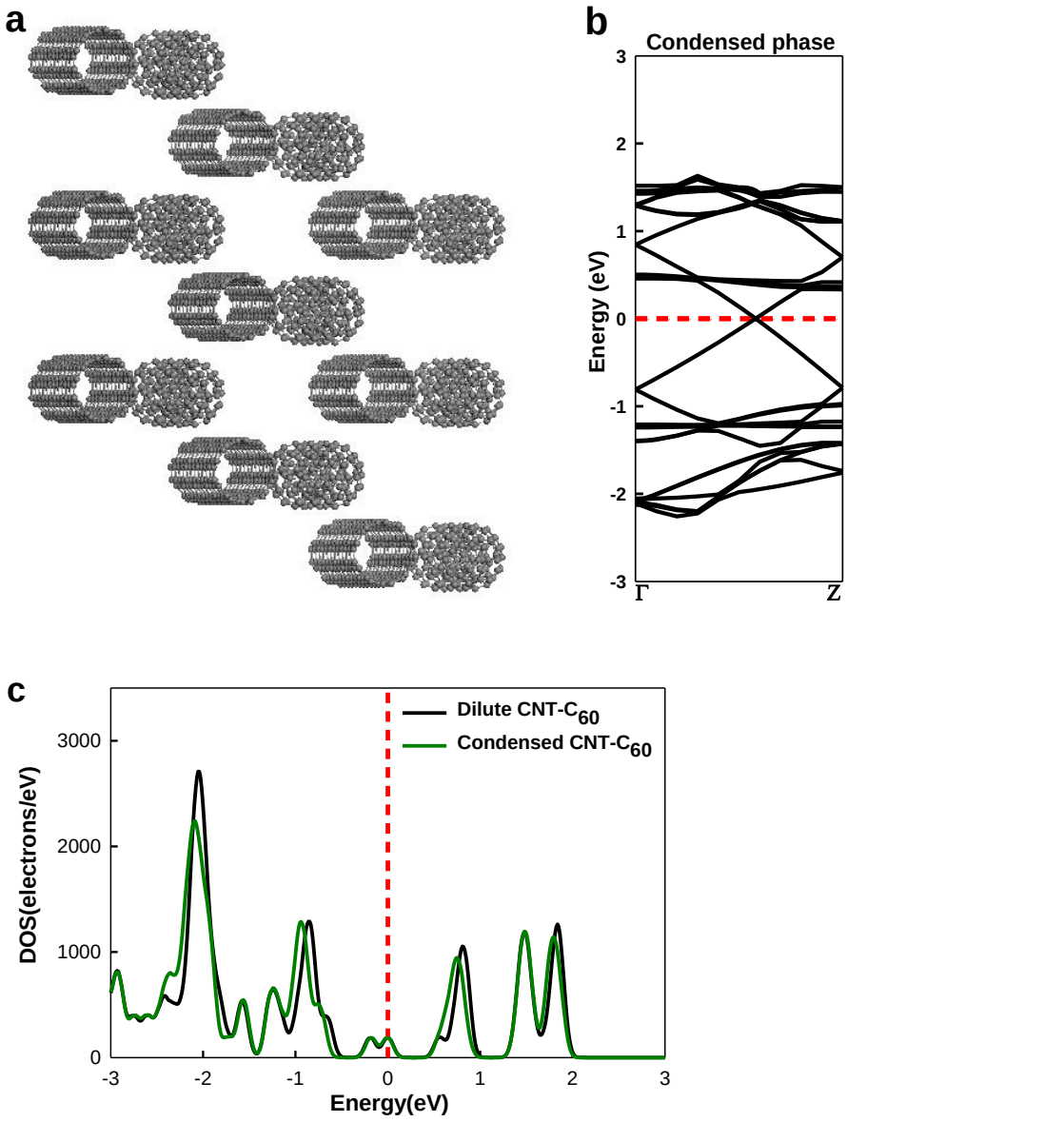

Figure 3.22: Condensed CNT-C_{60} hybrid system: (a) expanded view (3x3x3) of the optimized unit structure; (b) band structure; (c) density of states (DOS) of condensed and dilute phase in the hybrid system (Unit cell: a=b=18.35Å , c=9.846Å).

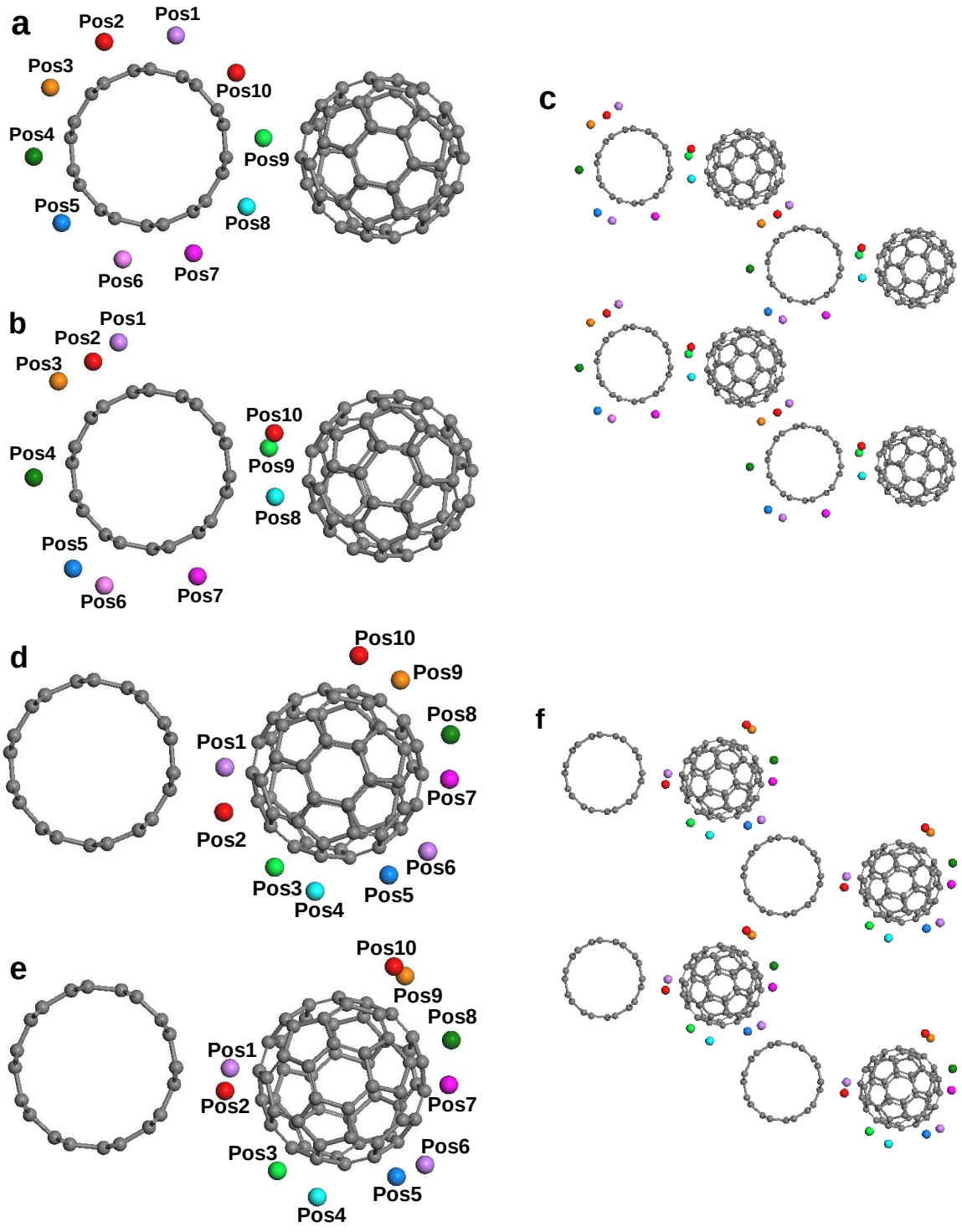

Figure 3.23: One-Li adsorption on various positions around CNT@hybrid on condensed hybrid system: (a) initial structure (b) final structure (c) expanded view of final structure; (d) initial structure (e) final structure (f) expanded view of final structure of one-Li adsorption on various positions around C_{60}@hybrid on condensed hybrid system.

Table 3.7: The adsorption energy and charge distribution (Mulliken charge) of one-Li atom system on the condensed (5,5) CNT-C_{60} hybrid system

System	Adsorption Energy (eV)	Charges (e)		
		Li	CNT	C_{60}
Condensed (5,5) CNT-C_{60} hybrid	N/A	N/A	0.141	-0.141
Pos1_CNT@hybrid	-2.580	0.905	-0.230	-0.675
Pos2_CNT@hybrid	-2.642	1.054	-0.329	-0.725
Pos3_CNT@hybrid	-2.506	0.891	-0.266	-0.625
Pos4_CNT@hybrid	-1.917	0.862	-0.503	-0.359
Pos5_CNT@hybrid	-2.536	0.920	-0.313	-0.607
Pos6_CNT@hybrid	-2.572	0.944	-0.349	-0.595
Pos7_CNT@hybrid	-1.919	0.862	-0.503	-0.359
Pos8_CNT@hybrid	-2.614	0.944	-0.241	-0.703
Pos9_CNT@hybrid	-2.584	0.928	-0.342	-0.586
Pos10_CNT@hybrid	-2.481	0.876	-0.258	-0.618
Pos1_C_{60}@hybrid	-2.542	0.962	-0.227	-0.735
Pos2_C_{60}@hybrid	-2.628	0.956	-0.239	-0.717
Pos3_C_{60}@hybrid	-2.090	0.859	-0.058	-0.801
Pos4_C_{60}@hybrid	-2.151	0.849	-0.087	-0.762
Pos5_C_{60}@hybrid	-2.591	0.989	-0.257	-0.732
Pos6_C_{60}@hybrid	-2.590	0.977	-0.278	-0.699
Pos7_C_{60}@hybrid	-2.096	0.861	-0.059	-0.802
Pos8_C_{60}@hybrid	-2.137	0.845	-0.077	-0.768
Pos9_C_{60}@hybrid	-2.580	0.982	-0.243	-0.739
Pos10_C_{60}@hybrid	-2.625	0.976	-0.244	-0.732

Additionally, four positions (Pos3,4,7,8_C_{60}@hybrid), which were faced away from the CNT, as shown in Figure 3.23.f, have higher adsorption energies and lower charge transfers compared to the other positions. The band structures of several one-Li-adsorbed systems are shown in Figure 3.24. Regardless of whether the Li atom was adsorbed on the CNT@hybrid (Figures 3.24.a-b) or C_{60}@hybrid sites (Figures 3.23.c-d), the band structures were very similar except for the position of the two bands generated from C_{60} in the band structure. Those two bands moved down to the Fermi level because Li was placed near C_{60} sites, similar to the dilute phase, which allowed these bands to shift down to the Fermi level in the sites at C_{60}@hybrid as displayed in Figures 3.24.c-d.

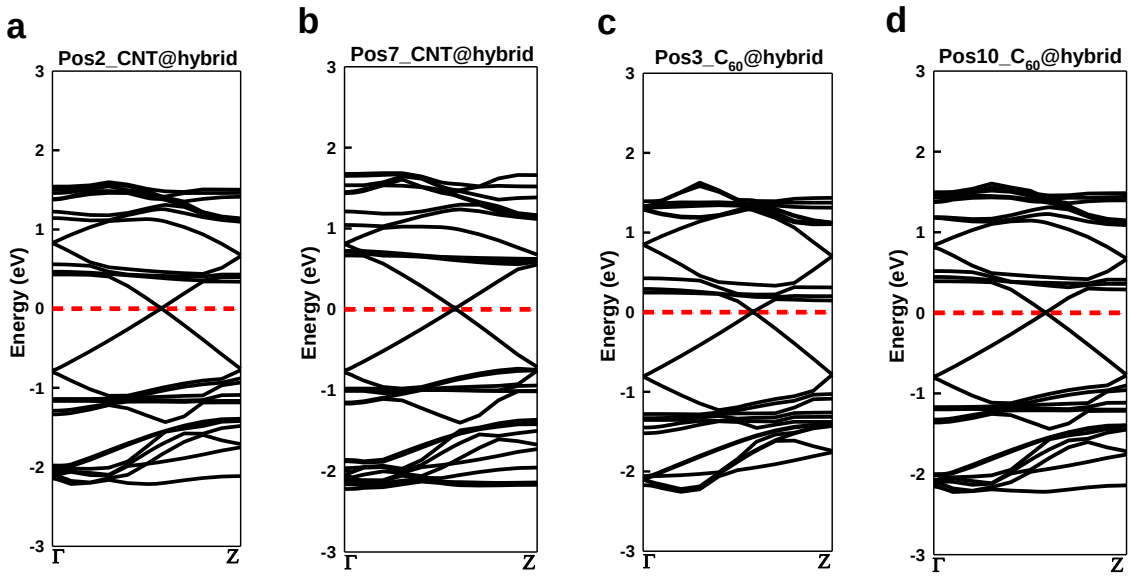

Figure 3.24: The band structure of one-Li system in condensed phase: (a) Pos2_CNT@hybrid; (b) Pos7_CNT@hybrid; (c) Pos3_C_{60}@hybrid; (d) Pos10_C_{60}@hybrid.

3.4.3 Multiple Li atoms on a condensed CNT-C_{60} hybrid system

We added another Li atom (blue) near the first Li atom (purple) of low adsorption energy on CNT@hybrid or C_{60}@hybrid to study the Li adsorption mechanism. Some of

the two-Li atom adsorbed systems are displayed in Figure 3.25, and adsorption sites were discriminated in the same manner as defined in the dilute phase (Section 3.3.3). Hence, the second atom is adsorbed on the next nearest neighboring site (N.N.N.) or the nearest neighboring site (N.N.) in either the radial or axial direction along the axis of the CNT surface starting from first Li atom positioned at CNT@hybrid or C_{60}@hybrid.

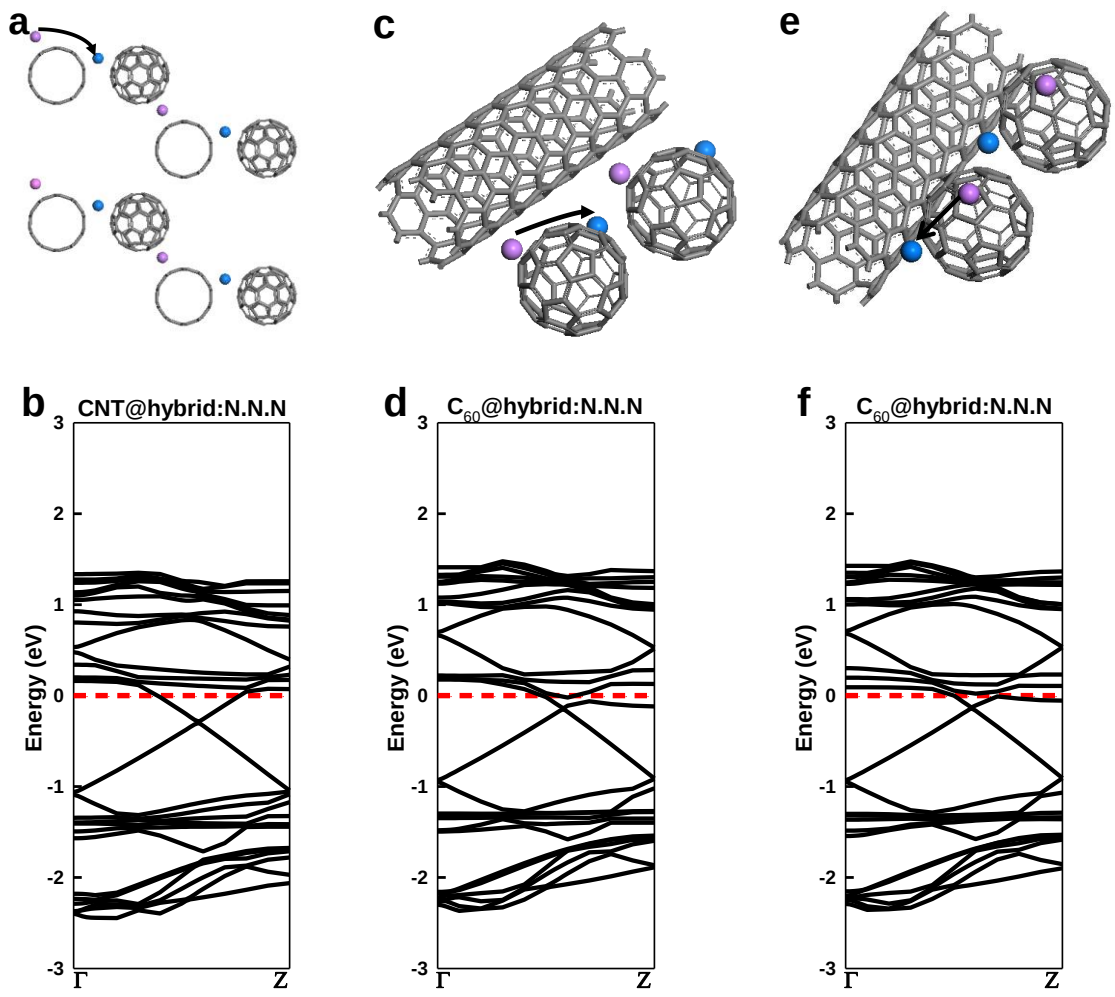

Figure 3.25: Two-Li adsorption on various regions: (a) next nearest neighboring (N.N.N.) site to radial direction starting at Pos2_CNT@hybrid; (b) the corresponding band structure; (c) next nearest neighboring (N.N.N.) site to axial direction starting at Pos2_C_{60}@hybrid; (d) the corresponding band structure; (e) next nearest neighboring (N.N.N.) site to axial direction starting at Pos10_C_{60}@hybrid (f) the corresponding band structure.

Table 3.8: The adsorption energy of two- Li atoms adsorption systems on condensed (5,5) CNT-C_{60} hybrid system

Starting position	Direction	Adsorption Energy (eV)
2Li starting from Pos2_CNT@hybrid	Radial (N.N.N.[a] site)	-2.524
	Radial (N.N.[b] site)	-2.454
	Axial (N.N.N. site)	-2.460
	Axial (N.N. site)	-2.444
2Li starting from Pos2_C_{60}@hybrid	Radial (N.N.N. site)	-2.351
	Radial (N.N. site)	-2.474
	Axial (N.N.N. site)	-2.622
	Axial (N.N. site)	-2.469
2Li starting from Pos10_C_{60}@hybrid	Radial (N.N.N. site)	-2.431
	Radial (N.N. site)	-2.397
	Axial (N.N.N. site)	-2.636
	Axial (N.N. site)	-2.606
31 Li atoms on condensed CNT-C_{60} hybrid	N.N.N. site	-1.862

a. N.N.N.: Next Nearest Neighbor, b. N.N.: Nearest Neighbor

As shown in Table 3.8, the Li adsorption energies of the two Li systems are quite similar (-2.351eV ~ -2.636eV) and lower than the values obtained in the dilute system. Although the N.N.N. sites have slightly lower energy than the N.N. sites in most cases, it appears that Li adsorption is mainly driven by the compact structure of the condensed phase. Therefore, for example, the N.N. site energy of the Pos2_C_{60}@hybrid is lower (-

2.474eV) than the N.N.N. site (-2.351eV) because the location of the second Li atom in the N.N.N. configuration becomes distant from the CNT. Meanwhile, the second Li atoms in the other configurations are still located between CNT and C_{60} or C_{60} and C_{60}, which can maximize Li adsorption. Therefore, Li adsorption will preferentially occur from the space between CNT and C_{60} or between C_{60} and C_{60} because C_{60}s provide better adsorption sites due to their high electron affinity. We also observed significant band shifts after additional Li adsorption as displayed in Figures 3.25.b,d and f, and the slight differences in each band structure mainly relied on the position of the Li atoms. In all of the cases, the Fermi level increased through electron injection from Li atoms in condensed structure so that bands that originated from the CNT and C_{60} shifted down to or below the Fermi level.

Finally, the entire surface of the hybrid system is covered with multiple (31) Li atoms assuming N.N.N. sites are preferred because it is important to predict the Li adsorption energy with respect to Li cluster formation. Figures 3.26.a-d shows the initial and optimized structure of the multi-Li system, band structure and the density of states. The Li adsorption energy calculated from equation (3.1) was -1.863eV, which is much lower than the Li-Li binding energy (-1.030eV). Therefore, we can expect that Li atoms will remain on the surface of the hybrid system rather than forming clusters with improved Li adsorption. Simultaneously, we can confirm the enhancement of the metallic behavior of the system through the band structure and DOS, which show significant increases in the number of bands (Figure 3.26.c) or electron density (Figure 3.26.d) across the Fermi level than appeared in the dilute phase of the CNT-C_{60} hybrid system.

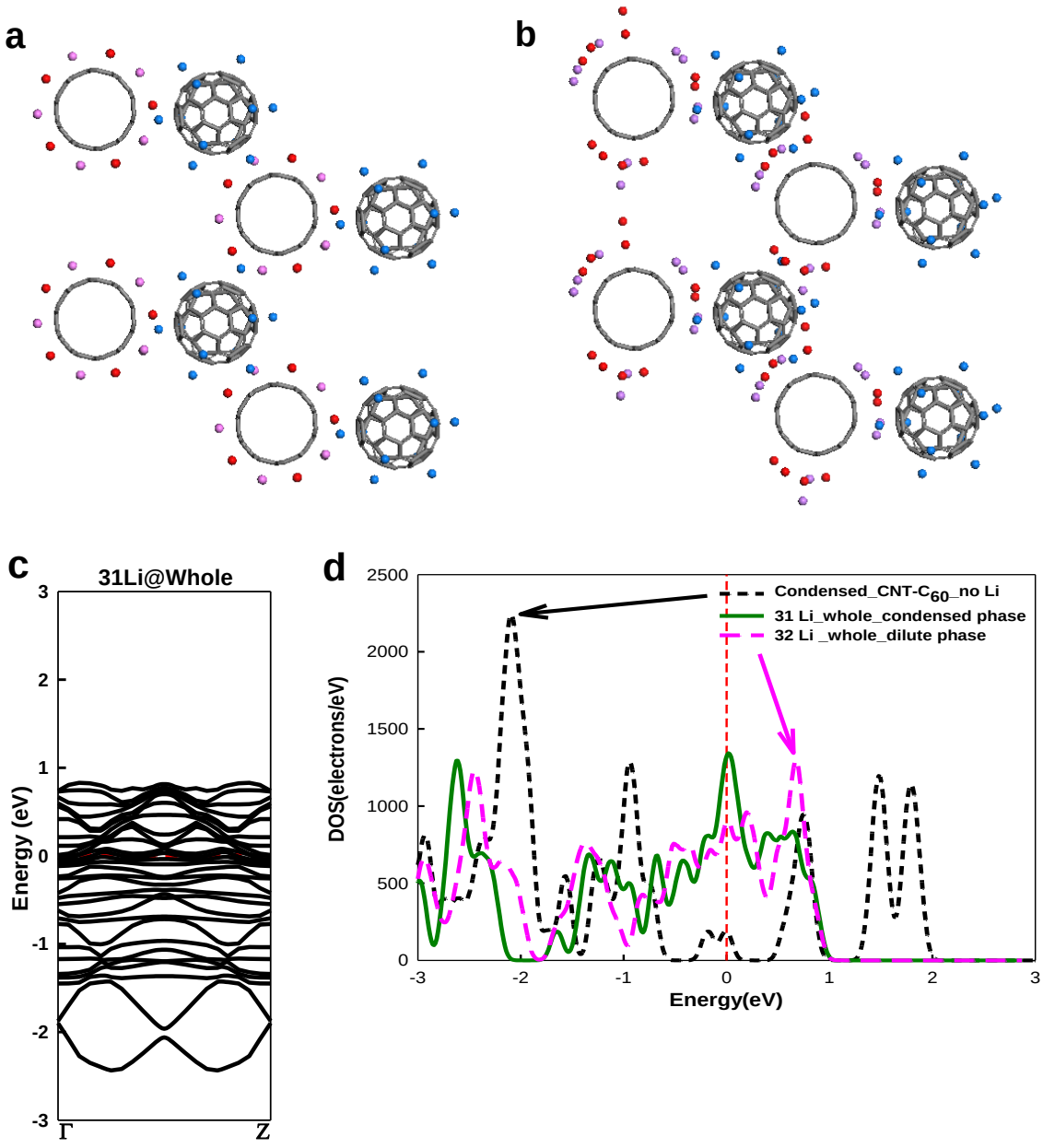

Figure 3.26: Multiple (31)-Li atoms adsorption on whole hybrid system: (a) initial structure; (b) optimized structure; (c) the corresponding band structure; (d) density of states with pure condensed phase and 32 Li atoms on the dilute phase hybrid system.

3.4.4 Conclusion

In this section, we examined Li adsorption on the CNT-C_{60} hybrid system in the condensed phase using the density functional theory. We also demonstrated that Li

adsorption energy was increased comparison to pure CNT due to charge transfer (from CNT to C_{60}) and C_{60} of higher electron affinity. This Li adsorption capability is further enhanced when the condensed phase of the hybrid system is formed. Although it retains the characteristics of its components in the condensed phase, the compact and symmetric structure enables more charges to transfer from CNT to C_{60} (0.141*e*) and increased interactions with both the CNT and C_{60}, similar to region2 of the dilute phase. Consequently, the Li adsorption capabilities are increased and adsorption energy becomes uniform at most of the positions throughout the compact structure. Therefore, Li atoms will be adsorbed on the space between CNT and C_{60} or between C_{60} and C_{60} and fill the empty space which is away from the C_{60} supporting stronger adsorption site. Moreover, increased Li adsorption enhances the metallic character of the system, which is confirmed from the band structure and the DOS. In conclusion, the CNT-C_{60} hybrid system seems to be promising as a new type of electrochemical electrode material because of its increased Li adsorption capabilities.

CHAPTER 4

FIRST-PRINCIPLES STUDY OF LI ADSOPRTION ON CARBON NANOTUBE-FULLERENE NANOBUD SYSTEM

In this chapter, we investigated another hybridized material system consisting of metallic single-walled carbon nanotubes (SWCNTs) and semiconducting fullerene (C_{60}), which is called "nanobud". We first examined the properties of the various nanobuds produced on the different CNTs, which can be zigzag, armchair, metallic or semiconducting CNTs. We also predicted the performance and changes in the electronic properties related to Li adsorption on (5,5) CNT-C_{60} in the dilute or condensed phases.

4.1 Introduction

In the previous chapter, we studied a new type of CNT-C_{60} hybrid system mainly maintained by dispersion interactions. Even though this hybrid system is bound by weak van der Waals interactions, it showed improved Li adsorption properties compared to a pristine CNT system in terms of its Li adsorption capabilities. Additionally, the Kauppinen group synthesized another form of a CNT-C_{60} hybrid structure by covalently binding C_{60}s to the outer surface of CNT and measuring the field-emission properties, which can be utilized as light-emission devices as shown Figure 4.1 [77, 94]. Although experimentally prepared nanobuds [95-97] are created in a variety of sizes and shapes, the detailed structure and the exact atomic positions in these materials is not yet clear. However, nanobuds can be divided in two different types, depending on how the fullerene is attached to the sidewall of the CNT. First, a complete fullerene is covalently bonded to a CNT by way of sp^3 hybridization of carbon atoms such as [2+2]

cycloaddition and [6+6] cycloaddition (Type I) [98]. Second, all carbon atoms are sp^2 hybridized, and fullerene can be considered to be a part of the CNT (Type II) [78, 99-103]. Here, we focus on the Type I nanobuds, which are prepared by the cycloaddition reaction, because both types are reported in the previous experiments.

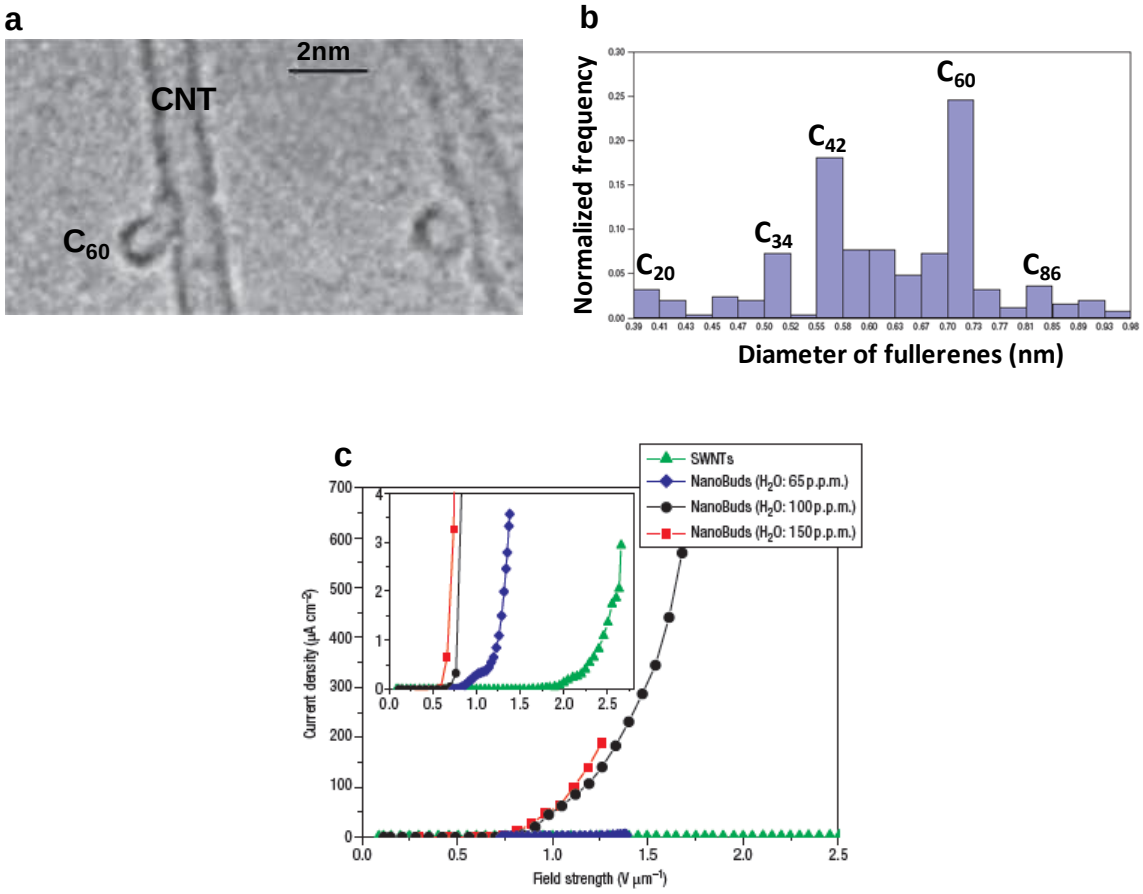

Figure 4.1: A hybrid carbon material; CNT-C_{60} nanobud: (a) high-resolution TEM image; (b) frequency-size distribution of fullerenes measured from high-resolution TEM images; and (c) field-emission properties of nanobuds.

Moreover, Type II might not be suitable to study the electron conduction capabilities with which we are concerned because it was reported that Type II nanobuds on zigzag CNTs

became semiconducting, regardless of whether the zigzag CNTs were metallic or semiconducting [78].

In this work, we first chose the proper nanobud (Type I) through the calculation of pure nanobud systems. We then added Li atoms to that system and investigated the Li adsorption strength and the electronic properties. We also studied the Li adsorption properties of the selected nanobud in the condensed phase. Please note that in this paper, we refer to all of the structures in which C_{60} is covalently attached to any CNT as nanobuds.

4.2 Computational details

In this work, generalized gradient approximation (GGA) Perdew-Burke-Ernzerhof (PBE) functional was also introduced to calculate the electron exchange-correlation energy [41, 85]. All the DFT calculations were performed using a double numerical basis set with d-polarization functions (DND) through $DMol^3$ from Accelrys [83, 84], which is the same condition used for calculating CNT-C_{60} hybrid system.

We tested various metallic as well as semiconducting SWCNT because there were several different calculation results [78, 98, 99] depending on the SWCNT and bond formation type. The unit cell dimension was set to 50 Å × 50 Å × 12.297 Å to avoid direct interaction between original structure and its self-images in a- and b-axis through the periodic boundary, while the c-axis dimension was determined by the length of the CNT. Monkhorst-Pack k-point scheme [86] was used for k-point sampling to determine the adsorption energy and other electronic properties such as band structure, density of states and Mulliken charge distribution [87, 88]. We chose (1x1×4) k-point for investigating all the system properties as well [93]. The adsorption energy per Li atom on

the CNT-C_{60} nanobud system is calculated using equation (3.1) and the negative value of the adsorption energy indicates a favorable Li adsorption whereas the adsorption is not favorable if the value is positive as we defined previously.

4.3 Dilute CNT-C_{60} nanobud system

4.3.1 Pure CNT-C_{60} nanobud systems

Before we investigated the Li adsorption capabilities at the CNT-C_{60} nanobud systems, we examined nanobud systems built on diverse carbon nanotubes from metallic to semiconducting and from zigzag to axial CNTs. Even though little is known about the detailed structure of nanobuds, they usually can be divided into two different types, depending on how the fullerene is attached to the sidewall of the carbon nanotube. Type I refers to a fullerene that is covalently bonded to a CNT by way of sp^3 hybridization of carbon atoms via the cycloaddition reaction. Type II refers to a C_{60} in which all of the carbon atoms are sp^2 hybridized, and C_{60} can be considered to be a part of the CNT. Meng et al. conducted detailed research on Type II nanobud systems and found that nanobuds produced on both metallic and semiconducting zigzag CNTs became semiconducting, while nanobud produced on armchair CNTs retained their metallic properties [78]. Therefore, we chose armchair (5,5), (8,8) and zigzag (9,0), (12,0) CNTs for the metallic CNTs, and zigzag (8,0), (10,0), (14,0) CNTs for the semiconducting CNTs. Two C-C covalent bonds between CNT and C_{60} were connected via a cycloaddition reaction ([2+2] cycloaddition) to stabilize the system for preparing Type I nanobuds. We chose [2+2] cycloaddition because Wu et al. reported using their DFT calculation that a single covalent C-C bond is unstable, whereas six covalent C-C bonds between a hexagonal face of C_{60} and a hexagonal ring of CNT by way of a cycloaddition

reaction ([6+6] cycloaddition) require a binding energy approximately 3-4 times higher than [2+2] cycloaddition [98].

There are two possible C-C bonds in the C_{60};a bond between two hexagonal faces (h) and a bond between a hexagonal face and pentagon face as denoted in Figure.4.2.a.

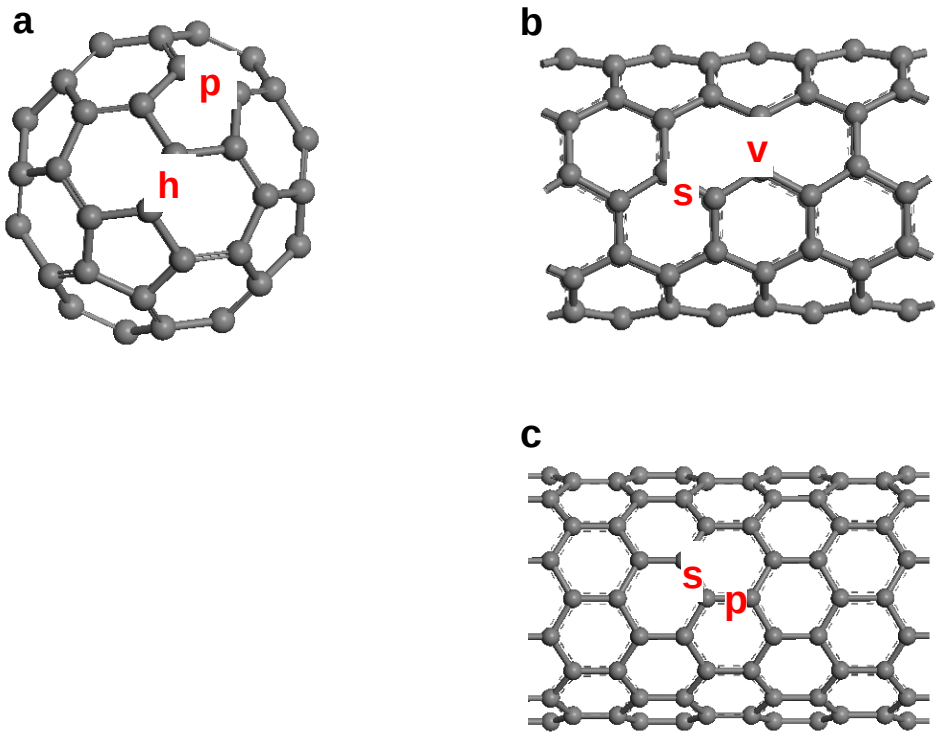

Figure 4.2: The following notation is used for the bond connections between C_{60} and the CNT to form nanobud systems through the [2+2] cycloaddition reactions; (a) h: the bond between hexagon and hexagon in C_{60} and, p: the bond between hexagon and pentagon in C_{60}; (b) v: the bond vertical to the tube axis in the armchair CNT; and (c) p: the bond parallel to the carbon nanotube axis in the zigzag CNT and s: the bond slope of the carbon nanotube axis for both types of CNTs (Arrow displays the carbon nanotube axis).

Alternatively, we can define the C-C bonds in the armchair CNTs, such as the vertical bond (v) and the slope bond (s), relative to the carbon nanotube axis.(Figure 4.2.b) In the same manner, C-C bonds at the zigzag CNTs can be defined as parallel bonds (p) and

slope bonds (s) to the tube axis. (Figure 4.2.c) Thus, nanobuds produced by [2+2] cycloaddition reaction are denoted as (5,5) CNT-C_{60}: hs, depending on the bond position in CNT and C_{60}. We excluded the system originating from the bond between the hexagon and the pentagon (p) in fullerene because it required a binding energy 40% higher than that required for starting with a bond between two hexagons (h).

After the connecting carbon nanotube to fullerene, the nanobud systems were fully optimized with GGA PBE. Optimized structures are displayed in Figures 4.3.a-d and i-l in which metallic carbon nanotubes were used to form nanobuds, while Figures 4.4.a-d and i-j show optimized structures in which semiconducting carbon nanotubes were employed. The corresponding binding energy ($E_{binding} = E_{nanobud} - E_{CNT} - E_{C60}$) and the bond lengths between C-C bonds are listed in Table 4.1. From this table, we found that binding energy had positive values, which showed that [2+2] cycloaddition reaction was endothermic. At the same time, carbon atoms involved in the covalent bonding protruded from the CNT surface because their bonding was switching from sp^2 to sp^3 hybridization as explained in a previous study [98]. In particular, the calculated results on the (5,5) and (10,0) nanobud systems agreed well with those reported by Wu et al. when the difference in lengths of the CNTs was considered. Through this comprehensive selection, we also found that the binding energy was lower when the bond was formed between the hexagonal face site (h) of the C_{60} and the parallel site (p) of the zigzag CNTs, whereas the slope site (s) of the axial CNTs offers lower binding energy. This tendency was previously explained through phi (π) bonding, so that two π bonds of the C-C bonds participating in the reaction are broken while two sigma (σ) bonds are created. In zigzag CNTs, parallel (p) bonds are less distorted, while vertical (v) bonds are less distorted in

the armchair CNTs because π bonds in carbon nanotubes are deformed due to the tubular bending of different extents [98]. Similarly, bond lengths change with the binding energy, which implies that the bonds become closer as the binding energy decreases.

Table 4.1: Binding energy and bond length of the each CNT-C_{60} nanobud systems

CNT type (Radius, Å)	Nanobud system	Binding energy (eV)	Bond length (Å)
Armchair Metallic (6.78)	(5,5) CNT-C_{60}: hs	1.326	1.613
	(5,5) CNT-C_{60}: hv	1.464	1.619
Zigzag Metallic (7.05)	(9,0) CNT-C_{60}: hs	1.545	1.632
	(9,0) CNT-C_{60}: hp	0.984	1.608
Zigzag Metallic (9.39)	(12,0) CNT-C_{60}: hs	1.906	1.635
	(12,0) CNT-C_{60}: hp	1.440	1.617
Armchair Metallic (10.85)	(8,8) CNT-C_{60}: hs	1.913	1.620
	(8,8) CNT-C_{60}: hv	2.062	1.627
Zigzag Semiconducting (6.26)	(8,0) CNT-C_{60}: hs	1.368	1.626
	(8,0) CNT-C_{60}: hp	0.785	1.602
Zigzag Semiconducting (7.83)	(10,0) CNT-C_{60}: hs	1.758	1.628
	(10,0) CNT-C_{60}: hp	1.305	1.611
Zigzag Semiconducting (10.96)	(14,0) CNT-C_{60}: hs	2.049	1.633
	(14,0) CNT-C_{60}: hp	1.633	1.619

We also examined the band structures of these optimized systems and displayed in Figures 4.3.e-f and m-p as well as Figures 4.4.e-f and k-l. Band gaps of all of the different nanobud systems are summarized in Table 4.2. There was a clear change in the band structure due to the covalent bond between CNT and C_{60}, even though the

characteristics of each component were similar to those in the hybrid system. Furthermore, it was found that nanobuds produced on the armchair carbon nanotube ((5,5) & (8,8)), which were originally metallic, created small band gaps (0.19eV and 0.17eV) when C_{60} was connected to the slope C-C bond in CNT, unlike the Type II nanobud.

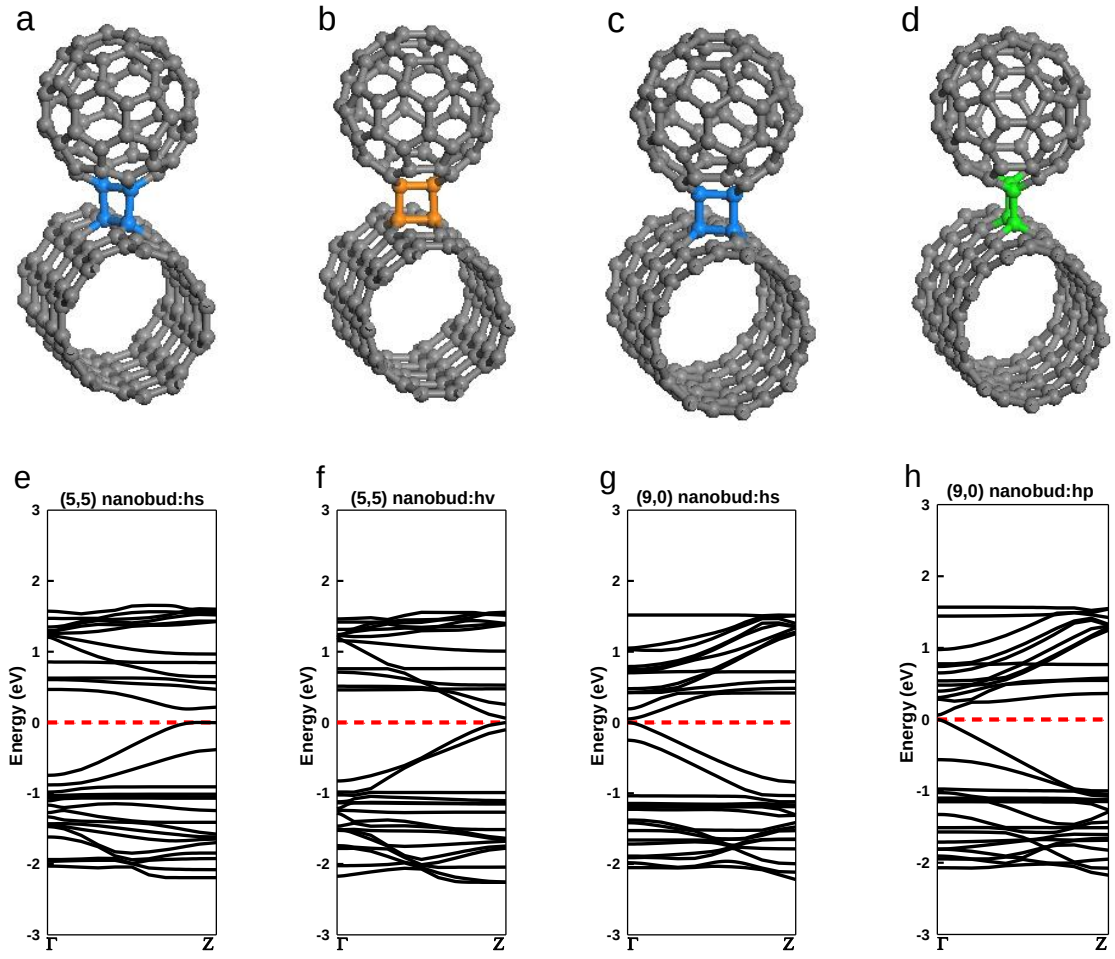

Figure 4.3: Metallic CNT series: Optimized structures of the various nanobud systems formed by [2+2] cycloaddition: (a) m-(5,5) CNT-C_{60}:hs nanobud; (b) m-(5,5) CNT-C_{60}:hv nanobud; (the cell parameters are a = b = 50 Å, c = 12.30 Å) (c) m-(9,0) CNT-C_{60}:hs nanobud; (d) m-(9,0) CNT-C_{60}:hp nanobud. The corresponding band structures for each nanobud system are as follow: (the cell parameters are a = b = 50 Å, c = 12.78 Å) (e) m-(5,5) CNT-C_{60}:hs nanobud; (f) m-(5,5) CNT-C_{60}:hv nanobud; (g) m-(9,0) CNT-C_{60}:hs nanobud; and (h) m-(9,0) CNT-C_{60}:hp nanobud.

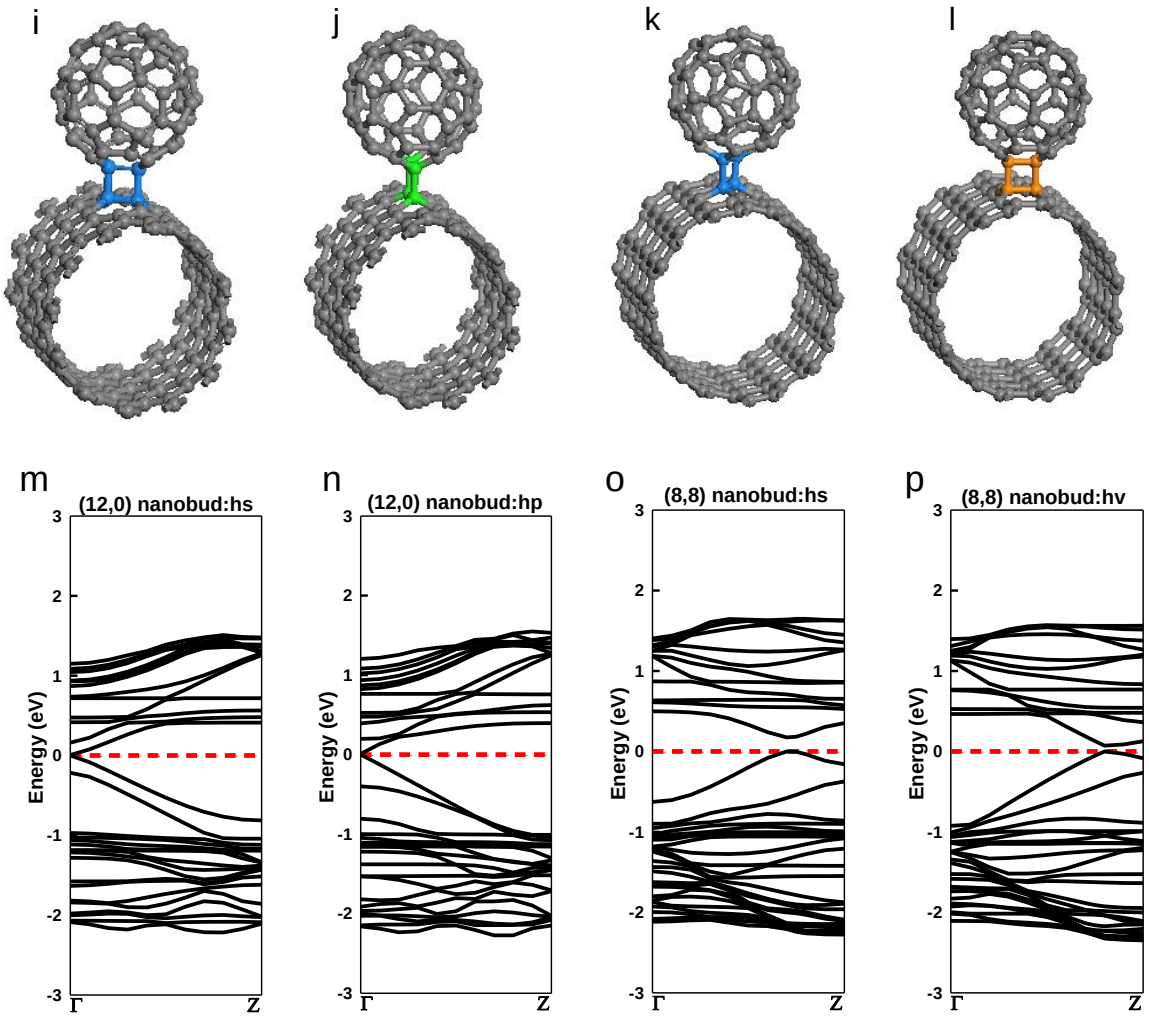

Figure 4.3 (continued): Metallic CNT series: Optimized structure of the various nanobud systems formed by [2+2] cycloaddition: (i) m-(12,0) CNT-C_{60}:hs nanobud; (j) m-(12,0) CNT-C_{60}:hv nanobud; (the cell parameters are a = b = 50 Å, c = 12.78 Å) (k) m-(8,8) CNT-C_{60}:hs nanobud; (l) m-(8,8) CNT-C_{60}:hv nanobud. (the cell parameters are a = b = 50 Å, c = 12.30 Å) The corresponding band structures for each nanobud system are as follows: (m) m-(12,0) CNT-C_{60}:hs nanobud; (n) m-(12,0) CNT-C_{60}:hv nanobud; (o) m-(8,8) CNT-C_{60}:hs nanobud; and (p) m-(8,8) CNT-C_{60}:hv nanobud.

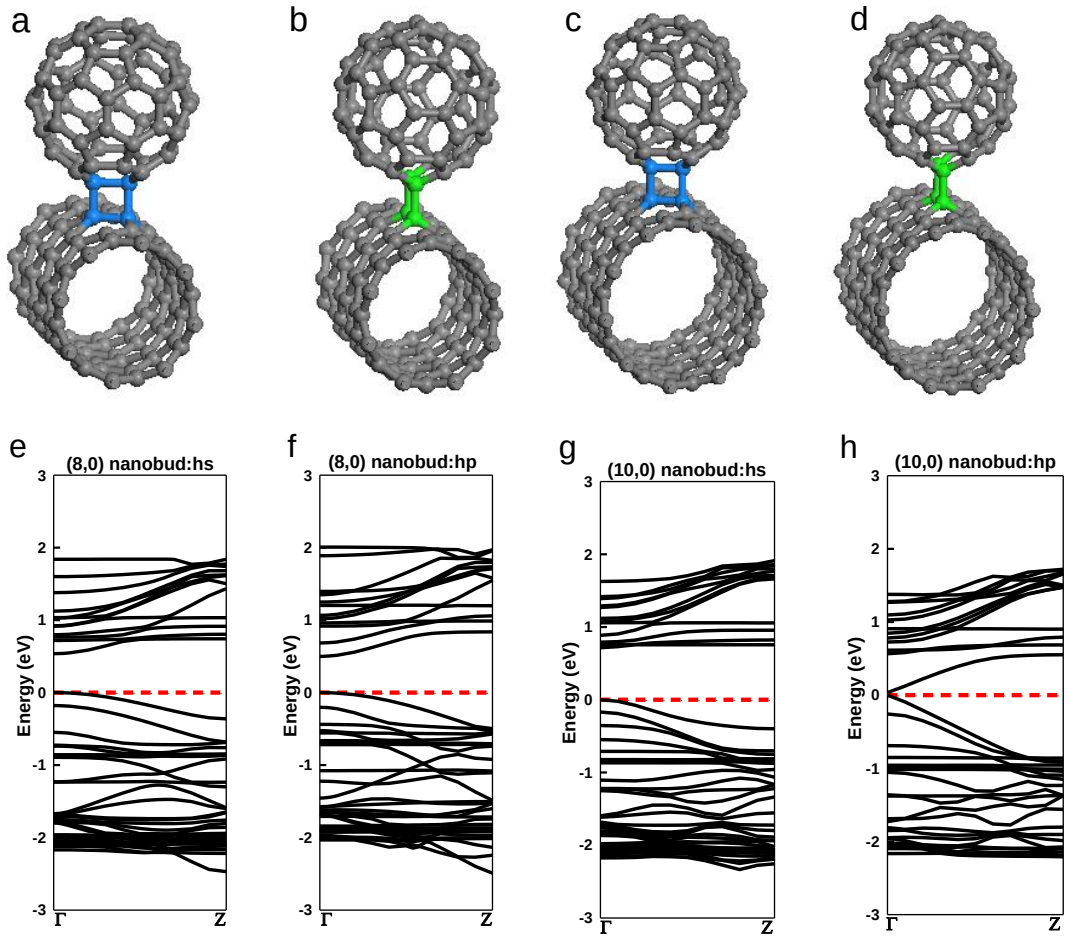

Figure 4.4:: Semiconducting CNT series: Optimized structures of the various nanobud systems formed by [2+2] cycloaddition: (a) s-(8,0) CNT-C_{60}:hs nanobud; (b) s-(8,0) CNT-C_{60}:hp nanobud; (c) s-(10,0) CNT-C_{60}:hs nanobud; (d) s-(10,0) CNT-C_{60}:hp nanobud. The corresponding band structures of each nanobud system are as follows: (e) s-(8,0) CNT-C_{60}:hs nanobud; (f) s-(8,0) CNT-C_{60}:hp nanobud; (g) s-(10,0) CNT-C_{60}:hs nanobud; and (h) s-(10,0) CNT-C_{60}:hp nanobud.

continued

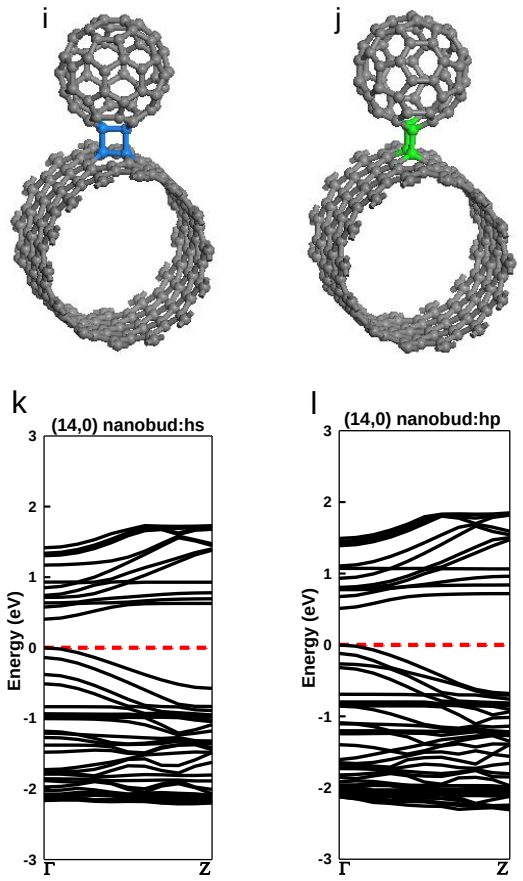

Figure 4.4 (continued): Semiconducting CNT series: Optimized structure of the various nanobud systems formed by [2+2] cycloaddition: (i) s-(14,0) CNT-C_{60}:hs nanobud; (j) s-(14,0) CNT-C_{60}:hp nanobud. The corresponding band structures of each nanobud system are as follows: (k) s-(14,0) CNT-C_{60}:hs nanobud; (l) s-(14,0) CNT-C_{60}:hp nanobud (The cell parameters are a = b = 50 Å, c = 12.78 Å).

Alternatively, nanobuds on the metallic zigzag carbon nanotube ((9,0) and (12,0)) did not form a band gap and retained its original metallic property. In the case of nanobuds on the zigzag semiconducting carbon nanotube ((8,0) & (10,0) & (14,0)), the band gap was decreased from the original band gap of the CNT in all of the cases. Therefore, it appears that different nanobuds can be used to tune the band gap by changing the type of CNT and that Type I nanobuds work differently than Type II nanobuds due to different hybridization.

Table 4.2: Band gap and charge distribution of the each CNT-C_{60} nanobud systems

Nanobud system	Band gap (eV)	Pure CNT Band gap (eV)	Charges (e)	
			CNT	C_{60}
(5,5) CNT-C_{60}: hs	0.19	0.01	0.092	-0.092
(5,5) CNT-C_{60}: hv	0.06		0.064	-0.064
(9,0) CNT-C_{60}: hs	0.05	0.08	0.070	-0.070
(9,0) CNT-C_{60}: hp	0.06		0.080	-0.080
(12,0) CNT-C_{60}: hs	0.01	0.01	0.075	-0.075
(12,0) CNT-C_{60}: hp	0.01		0.092	-0.092
(8,8) CNT-C_{60}: hs	0.17	0.01	0.091	-0.091
(8,8) CNT-C_{60}: hv	0.07		0.076	-0.076
(8,0) CNT-C_{60}: hs	0.54	0.62	0.041	-0.041
(8,0) CNT-C_{60}: hs	0.5		0.056	-0.056
(10,0) CNT-C_{60}: hs	0.71	0.82	0.055	-0.055
(10,0) CNT-C_{60}: hs	0.03		0.067	-0.067
(14,0) CNT-C_{60}: hs	0.4	0.69	0.076	-0.076
(14,0) CNT-C_{60}: hs	0.51		0.087	-0.087

We also found that all of the nanobuds showed the same charge transfer direction from CNT to C_{60} as listed in Table 4.2 through Mulliken charge analysis. It appears that there is no direct relationship between the diameter of the CNT and the degree of charge transfer; however, the amount of charge transfer depends on the binding energy. In other words, charge transfer increases when the nanobud can be formed with less energy (the formation nanobud is easier).

4.3.2 Single Li atom on a (5,5) CNT-C_{60} nanobud system

We chose the (5,5) CNT-C_{60}: hs nanobud system to predict Li adsorption capabilities on the covalently bonded hybrid system. This (5,5) bud system was selected because of its low binding energy with a higher charge transfer compared to the (5,5) CNT-C_{60} hybrid system discussed in the previous chapter. We followed the same method as the hybrid system to position the Li atom so that the "center" on the CNT and the pentagon and hexagon site on the C_{60} was selected as the Li adsorption sites. In addition, we assigned four different regions to both nanobud systems using the same method as the hybrid system: (i) the CNT side (region 1, red); (ii) between the CNT and C_{60} (region 2, yellow); (iii) between C_{60}s (region 3, blue); and (iv) the C_{60} side (region 4, orange) for the systematic study. Figure 4.5.a shows the initial structure of the one-Li adsorbed system on each region, and the optimized structure of the (5,5)bud:hs system is displayed in Figure 4.5.b. In this study, however, we reduced the number of the Li adsorption sites in region 1 because the binding energy in this region is expected to be similar due to the lack of interaction with C_{60}. The Li adsorption energy, charge distribution and band gap are listed in Table 4.3. While most of the Li atoms remain in their original positions, the Li atoms such as Pos1,2,3_C_{60}@55bud, which are initially located close to the [2+2] cycloaddition bonds, are repelled outwards. This effect may be a result of the *sp3* bonds in the junction because this strong bond does not allow the Li atom to form a bond with the carbon atom near the junction and forces the Li atom to move out of the C-C bonds. The adsorption energies are generally higher than the (5,5) CNT-C_{60} hybrid system, but it still follows the same regional dependence as the hybrid system. As a result, region 2 (between CNT and C_{60}, (5,5)bud:hs: -2.319 eV) and region 3 (between C_{60}s, (5,5)bud:hs: -2.141 eV) have the lowest values followed by region 4 (C_{60} side, (5,5)bud:hs: -1.860 eV)

and region 1 (CNT side, (5,5)bud:hs: -1.675 eV). In other words, Li adsorption is strongly affected by C_{60} in the nanobud, and the adsorption energy decreases as the Li atoms are arranged more closely to the C_{60}.

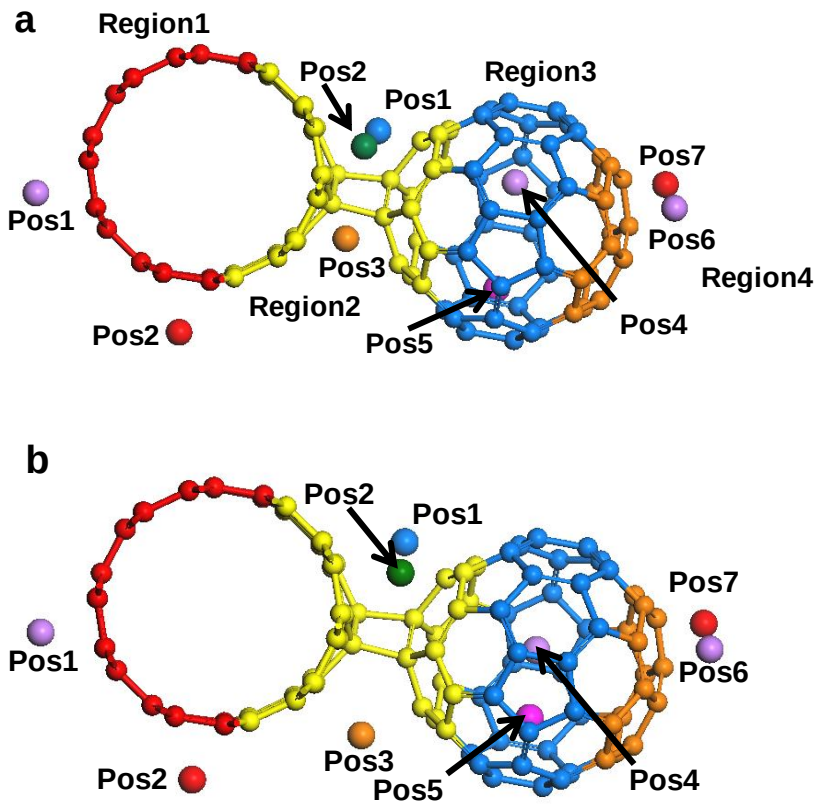

Figure 4.5: One-Li adsorption on various positions in each region around the (5,5) CNT-C_{60} nanobud: (a) initial structure and (b) optimized structure (region1: red; region2: yellow; region3: blue; region4: orange).

Therefore, Li adsorption in the nanobud system is expected to start from the sites close to the mid-space between the CNT and the C_{60} (region 2, but away from the covalent bonds) or between C_{60}s (region 3) and proceed to cover the remaining sites of C_{60} (region 4) and CNT (region 1). The amount of charge transfer after one-Li adsorption ranges from 0.792*e* to 0.859*e* for the (5,5) bud:hs depending on the adsorption sites and is much lower

than the amount of charge transfer in the hybrid system (0.825*e* - 0.975*e*). We suggest that the decreased charge transfer can also be explained by the C-C bonds on the junction. After the bond formation, not only the space between the CNT and C_{60} decreases, but the covalent bonds also already share some amounts of the charge. Therefore, the Li atom cannot be positioned exactly in the middle between the CNT and C_{60} even though the adsorption and charge transfer were large in the hybrid system. In addition, this covalent bond already retains some amounts of the charge, which prevents it from allowing charge transfer among materials. As shown in Table 4.4, the charges on the carbon atoms in the junction did not change much even though the Li atom was positioned close to junction.

Table 4.3: The adsorption energy, charge distribution (Mulliken charge) and band gap of one-Li atom on (5,5) CNT-C_{60} bud system (55bud)

System	Adsorption Energy (eV)	Charges (e)			Band gap (eV)
		Li	CNT	C_{60}	
(5,5) CNT-C_{60} Nanobud	N/A	N/A	0.049	-0.049	0.19
Pos1_CNT@55bud (region1)	-1.612	0.810	-0.650	-0.160	0.18
Pos2_CNT@55bud (region1)	-1.675	0.813	-0.628	-0.185	0.2
Pos1_C_{60}@55bud (region2_penta)	-2.178	0.834	-0.364	-0.470	0.21
Pos2_C_{60}@55bud (region2_hexa)	-2.319	0.837	-0.415	-0.422	0.21
Pos3_C_{60}@55bud (region2)	-2.182	0.809	-0.375	-0.434	0.20
Pos4_C_{60}@55bud (region3_penta)	-2.141	0.859	-0.017	-0.842	0.19
Pos5_C_{60}@55bud (region3_hexa)	-1.992	0.853	-0.030	-0.823	0.16
Pos6_C_{60}@55bud (region4_hexa)	-1.818	0.810	-0.020	-0.790	0.19
Pos7_C_{60}@55bud (region4_penta)	-1.860	0.792	-0.018	-0.774	0.19

For example, the charge of the carbon atoms in the CNT and C_{60} after Li adsorption remained at around -0.160*e* and -0.113*e*, respectively. Consequently, charge transfer from Li to the nanobud system does not occur efficiently unlike the hybrid system, in which the charge distributes evenly throughout the system. Therefore, the covalent bonds affect the charge transfer and Li adsorption capabilities to some extent in the nanobud system. However, the band structure does not seem to be affected by Li adsorption in the nanobud system. Figure 4.6 shows the band structures of the one-Li adsorption systems on the different regions. The 0.16-0.21 eV band gap in the (5,5) CNT-C_{60} still exists even after Li adsorption.

Table 4.4: The Mulliken charge of the carbon atoms in the CNT-C_{60} junction without or with the Li atom on the (5,5)bud:hs nanobud system

System	CNT		C_{60}	
	C1	C2	C1	C2
(5,5) CNT-C_{60} Nanobud	-0.160	-0.159	-0.111	-0.113
Pos1_C_{60}@55bud (region2)	-0.160	-0.170	-0.135	-0.113
Pos2_C_{60}@55bud (region2)	-0.160	-0.148	-0.113	-0.114
Pos3_C_{60}@55bud (region2)	-0.157	-0.156	-0.112	-0.094

4.3.3 Multiple Li atoms adsorption on the (5,5) CNT-C_{60}

The second Li atom (blue) is added at various sites starting from the first Li atom (pink) which had the lowest adsorption energy in each region to study the adsorption mechanism. The investigation of the Li adsorption mechanism is important as mentioned

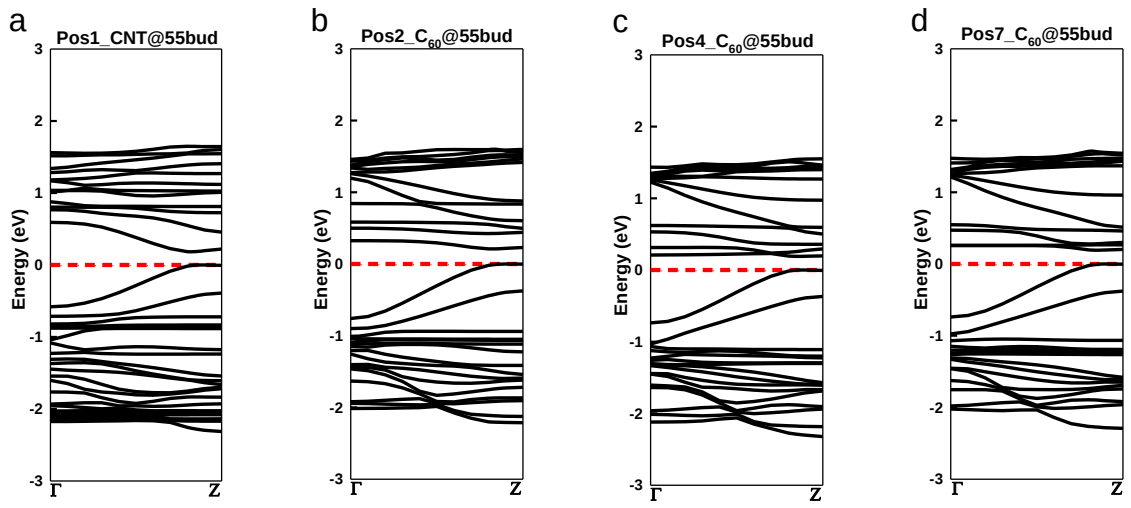

Figure 4.6: The band structure of one-Li adsorption on various positions around (5,5)CNT-C_{60} nanobud: (a) region1; (b) region2; (c) region3; and (d) region4.

earlier in that the utilization efficiency of the vast area of the nanobud surface could affect energy density in an actual Li battery system. We followed the same definition used in the hybrid system so that the second Li atom is provided on the nearest neighboring (N.N.) site or the next nearest neighboring (N.N.N.) site in either the radial or axial direction along the axis of the CNT surface. We also assumed that the second Li atom could be adsorbed on the pentagonal or hexagonal ring in the C_{60}@hybrid to make the N.N. or the N.N.N. configuration. Some representative arrangements in each region are displayed in Figure 4.7 for (5,5) CNT-C_{60}. Li adsorption energies are listed in Table 4.5. Figures 4.7.a and b show the optimized structures in region1 representing the N.N.N. and the N.N. sites in radial direction from the first Li atom positioned at Pos1_CNT@hybrid, respectively. The adsorption energy at the N.N.N. site (Figure 4.7.a; -1.474 eV) is the lowest in region1, but the adsorption energy in region1 is the highest because those Li atoms are not able to interact with C_{60}.

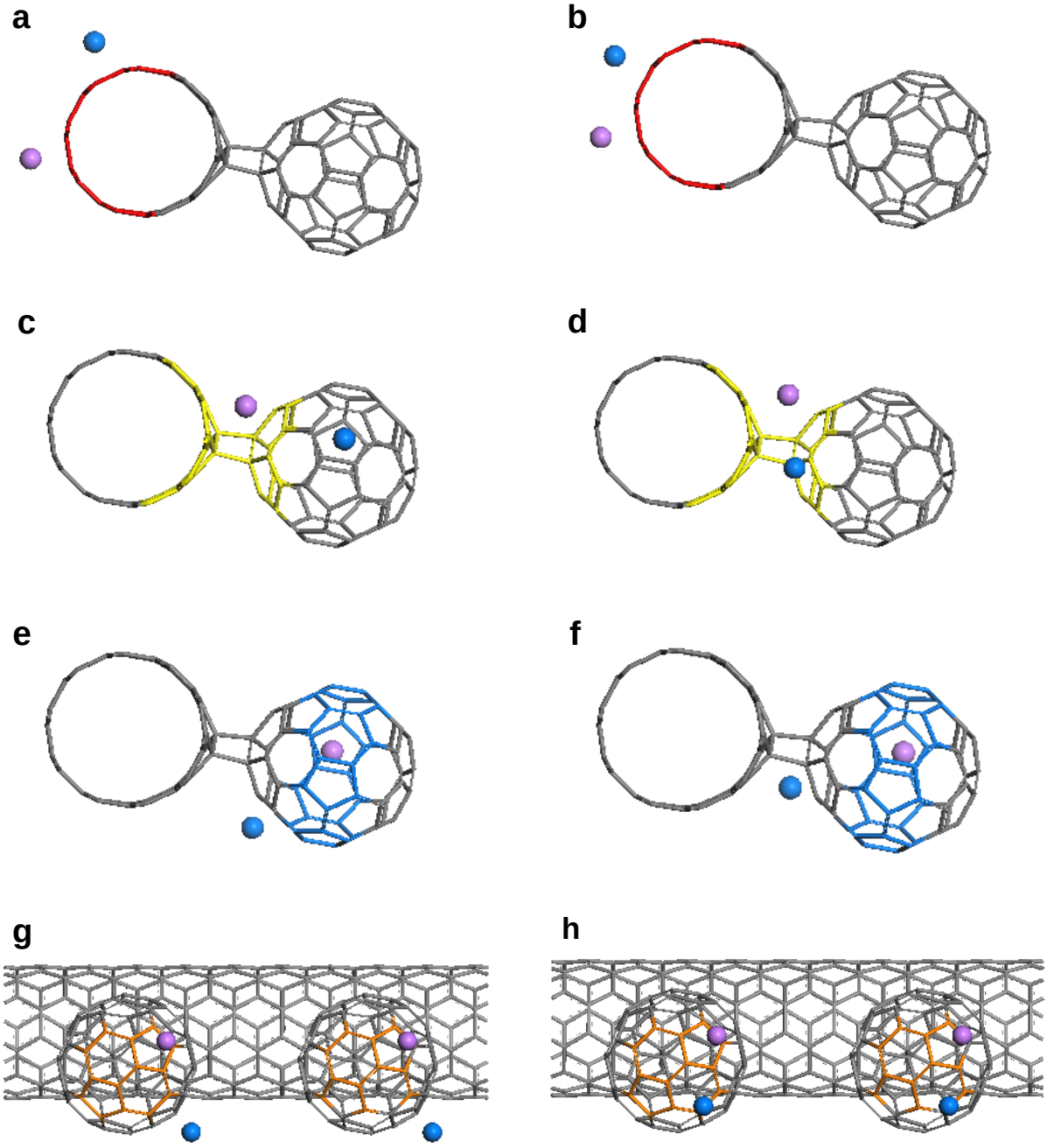

Figure 4.7: Two-Li adsorption on various regions. For region 1: (a) next nearest neighboring (N.N.N.) site and (b) nearest neighboring (N.N.) site in the radial direction at the CNT@55bud. For region 2: (c) next nearest neighboring (N.N.N.) site and (d) nearest neighboring (N.N.) site in the radial direction at CNT:C_{60} middle. For region 3: (e) next nearest neighboring (N.N.N.) site and (f) nearest neighboring (N.N.) site in the radial direction at the C_{60}@55bud. For region 4: (g) next nearest neighboring (N.N.N.) site and (h) nearest neighboring (N.N.) site in the radial direction at the C_{60}@55bud.

Table 4.5: The adsorption energy of two-Li adsorption systems on the (5,5)bud

System	Adsorption Energy (eV)
2 Li on region1: Radial (N.N.N.[a] site)	-1.474
2 Li on region1: Radial (N.N.[b] site)	-1.323
2 Li on region1: Axial (N.N.N. site)	-1.374
2 Li on region1: Axial (N.N. site)	-1.215
2 Li on region2: Radial (N.N.N. site)	-2.105
2 Li on region2: Radial (N.N. site)	-2.175
2 Li on region2: Axial (N.N.N. site)	-2.235
2 Li on region2: Axial (N.N. site)	-2.046
2 Li on region3: Radial (N.N.N. site)	-2.039
2 Li on region3: Radial (N.N. site)	-2.194
2 Li on region4: Radial (N.N.N. site)	-1.827
2 Li on region4: Radial (N.N. site)	-1.638
2 Li on region4: Axial (N.N.N. site)	-1.786
2 Li on region4: Axial (N.N. site)	-1.617
Many (31) Li atoms (N.N.N. site)	-1.412

a. N.N.N.: Next Nearest Neighbor, b. N.N.: Nearest Neighbor

Li adsorption in region 4 (Figures 4.7.g and h) also prefers N.N.N sites: the adsorption energy of the second Li atom is calculated as -1.827 eV for the N.N.N. site (Figure 4.7.g) and -1.638 eV for the N.N. site (Figure 4.7.h) in the radial direction starting from the Pos6_C_{60}@hybrid. This finding suggests that Li adsorption would occur using the N.N.N.

sites of the pentagon site in C_{60}. In region 2, the Li adsorption energy is increased due to the interaction with both the CNT and C_{60} (Figures 4.7.c and d) ranging from -2.046 eV at the N.N. site to -2.235 eV at the N.N.N. site in the axial direction from the Pos2_C_{60}@hybrid. It also appears that Li adsorption does not depend on the adsorption sites within this region as it does in the hybrid system. However, the adsorption energies are much higher than those of the hybrid system. This higher adsorption energy is also related to the bonds in the junction as mentioned in the previous section. Thus, the second Li atom cannot be positioned close to middle of the components due to the strong covalent bonds; therefore, its position away from the middle might lead to a little increase in adsorption energy. Because of the finite size of C_{60}, the Li adsorption direction in region 3 is only possible at the N.N.N site (-2.039 eV) and N.N. site (-2.194 eV) in the radial direction from the first atom at the Pos4_C_{60}@hybrid (Figures 4.7.e and 4.7.f). In region 3, the low adsorption energy may be primarily attributed to the strong electron affinity of C_{60}. However, adsorption is also influenced by the covalent bonds. Therefore, the adsorption energy cannot reach the same level as it does in the hybrid system, and Li adsorption is expected to occur starting from around C_{60} and progress in the direction that maximizes exposure to high electron affinity $C_{60.}$ However, the covalent bonds work as a barrier to enhanced adsorption capabilities.

Band structures of the lowest adsorption energies in each region are examined in Figure 4.8. Additional Li adsorption resulted in some significant band shifts compared to the one-Li adsorption in the hybrid cases. The energy bands shifted down in all of the two-Li adsorption systems; this occurred because the Fermi level was increased due to the electrons injected from the Li atoms to the nanobud system. Therefore, the system

became metallic by overcoming the small band gap of the nanobud system as the number of the Li atoms increased. In detail, the band shift is affected by the position of the Li atoms, which causes the energy bands from the components closest to the Li to shift downward.

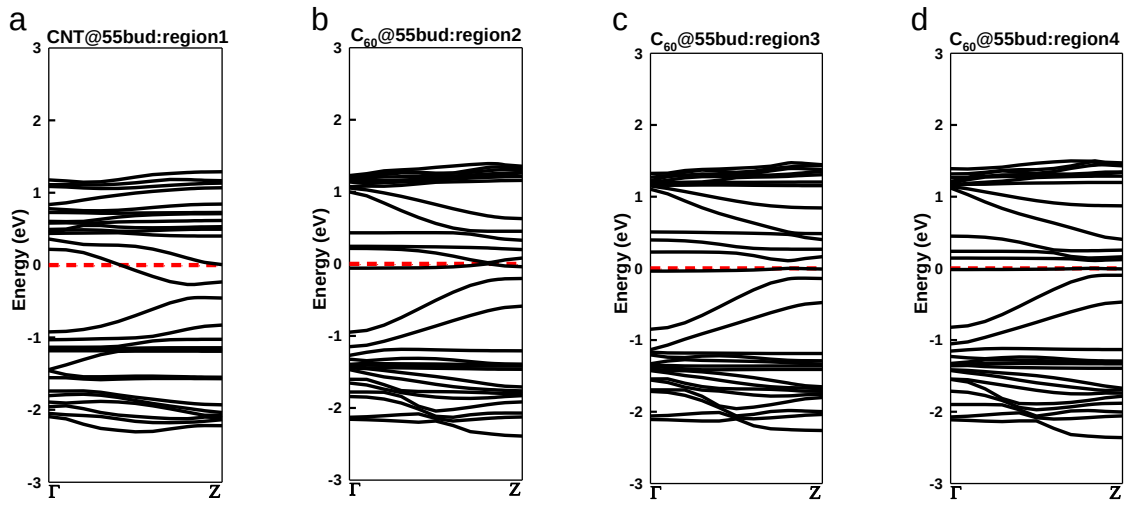

Figure 4.8: The band structure of two-Li adsorption on various positions around a (5,5) CNT-C_{60} nanobud: (a) region1; (b) region2; (c) region3; (d) region4.

Consequently, these adsorption energies are still lower than the Li-Li binding energy (experimental: -1.030 eV [92]) even though these values are higher than the values in the one-Li adsorption energy and hybrid system. Hence, the adsorption of the second Li atom on the nanobud system is still preferred as opposed to the formation of a Li-Li bond.

We finished the whole surface of the nanobud system with 31 Li atoms still assuming the preferred N.N.N. sites of adsorption on the CNT and C_{60} surfaces. The initial structure is presented in Figure 4.9.a. The positions of the Li atoms are adjusted after optimization of the geometry as shown in Figure 4.9.b. From the optimized structure, we found that some Li atoms that were initially attached to the CNT were attracted to the

C_{60}, while the Li atoms on the blind sites of the C_{60} were still rearranged around the CNT. In addition, the Li atoms initially positioned in close proximity to the bond connecting the CNT and C_{60} were pushed away from the bond because Li cannot bind with the carbon atoms associated with a covalent bond. Thus, structures that are different from the hybrid system are formed. Many Li atoms on the CNT attracted to C_{60} and arranged the middle between CNT and C_{60} to maximize the exposure to C_{60} in the hybrid system. However, fewer Li atoms on the CNT side are able to move to the C_{60} because of the limited space between the CNT and C_{60} in the nanobud. Therefore, the hybrid structure could accept more Li atoms on the C_{60} providing strong adsorption sites and resulting in an adsorption energy difference between the nanobud (-1.412 eV) and hybrid systems (-1.809 eV). However, the binding energy would still be larger than the Li-Li binding energy of -1.030 eV, which demonstrates that Li cluster formation is unlikely until all of the available sites on the nanobud system are occupied. Figures 4.9.c and d shows the band structure and density states of many Li systems on the nanobud system. From the band structure, we observed that the energy bands around the Fermi level significantly increased and that the original band structure including the small band gap disappeared and appeared to be similar to the band structure of the many Li atoms on the hybrid system. This observation indicates that Li adsorption enhances the metallic characteristics of the system such as conductivity and can be identified through DOS. DOS in multi-Li adsorbed systems demonstrates more electron states around the Fermi level compared to the pure nanobud system. This also indicates that the enhanced metallic character of the CNT-C_{60} nanobud system is expected and that such enhancement of the metallic character could contribute to the electron transport properties.

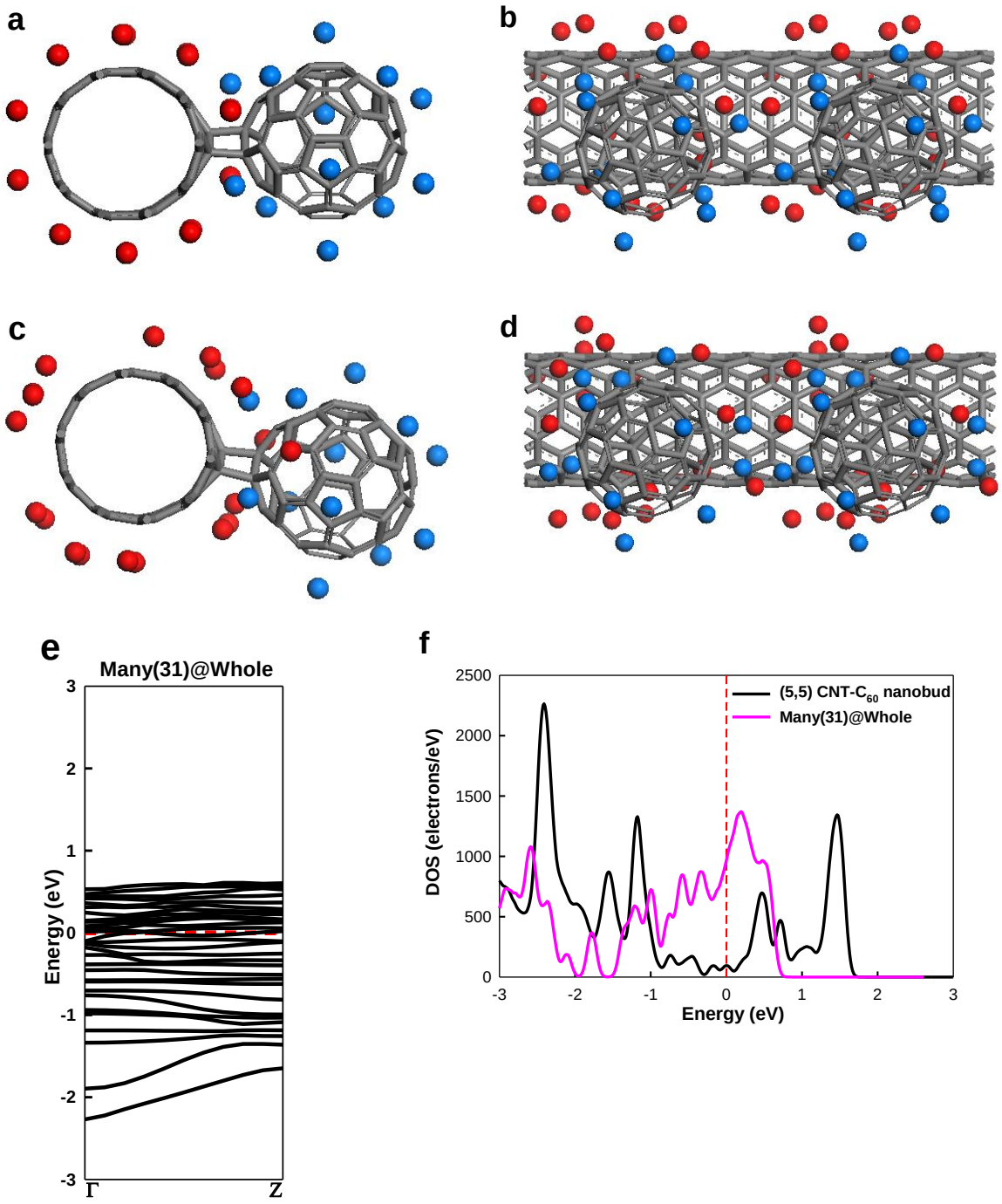

Figure 4.9: Multiple Li atom adsorption on a whole (5,5)CNT-C_{60} nanobud system. Initial structure: (a) front view; (b) side view; optimized structure; (c) front view; (d) side view; (e) the corresponding band structure; and (f) density of states (DOS).

4.3.4 Conclusion

In this chapter, we investigated another type of hybridized material system consisting of the carbon nanotube and fullerene called nanobud. A fullerene is covalently bonded to a CNT through sp^3 hybridization of carbon atoms via the [2+2] cycloaddition reaction (Type I). The original property of the CNT is changed after the nanobud is formed; thus, some metallic systems have a small band gap, while the band gap of the semiconducting system is decreased. Therefore, it appears that the nanobud could be used to tune the band gap for electronic devices by manipulating the chirality of the CNT, the density of the C_{60} or the bond type. We also studied the Li adsorption capabilities and electronic properties in a (5,5) CNT-C_{60} nanobud system. The adsorption energy of the one or two-Li systems was much higher than that of the hybrid system due to the covalent bond in the junction, but it still followed the same adsorption mechanism as the hybrid system. Therefore, Li will start to be adsorbed on the C_{60} side, especially on the CNT:C_{60} middle (region 2) or between C_{60}s (region 3) and subsequently fill the CNT side (region 1). In addition, we can confirm that Li cluster formation (-1.030 eV) will not occur by comparing the bond energy to the adsorption energy (-1.412 eV) of the multi-Li system. We also found that a small band gap could be overcome after two Li atoms are adsorbed on the system and that the band structure is completely changed, which reflects enhanced metallic behavior after multi-Li adsorption. Hence, the CNT-C_{60} nanobud system is also expected to demonstrate an enhanced Li adsorption capability and mechanical strength compared to the pure CNT system and can be potentially used in electrodes in electrochemical devices.

4.4 Condensed phase of a (5,5) CNT-C_{60} nanobud system

4.4.1 Pure condensed CNT-C_{60} hybrid system

In this section, we considered the condensed phase of the (5,5) CNT-C_{60} nanobud system allowing each component to interact with neighboring components, which would affect the Li adsorption capabilities. Four new systems (Figures 4.10.b-e) were prepared to determine the ideal structure by varying the position of the C_{60} and the cell size. Then, single point energies of the structures were calculated. Figure 4.10.f describes the energies with varying cell sizes for each structure. The New2 structure (Figure 4.10.c) had the lowest energy among the tested structures at a and b=17.60 Å and at c=12.30 Å. The symmetric structure of New2 also imposes uniform interactions between neighboring elements as in the hybrid structure and eventually forms a stable structure. Further optimization of the New2 structure was performed to determine the optimal geometry for a given cell size. Figure 4.11.a shows a 3x3x3 expanded view of the optimized unit structure (a and b=17.60 Å and c=12.30 Å), and the corresponding band structure and DOS are represented in Figures 4.11.b and c, respectively. The band structure and DOS in the condensed phase does not change, which allows the nanobud to have a narrow band gap (0.19 eV). Narrow band gap is still present because the covalent bonds still work strongly in the condensed phase and do not cause any electronic property changes in spite of the increased density of the metallic carbon nanotube. However, charge transfer from the CNT to C_{60} still increased from $|0.092|e$ to $|0.147|e$ because of the increased surface area of C_{60} facing the CNT, while the charges on the bonds (CNT- C1: -0.157*e* and C2: -0.157*e*; C_{60}-C1: -0.110*e*; and C2: -0.112*e*) remained unaffected.

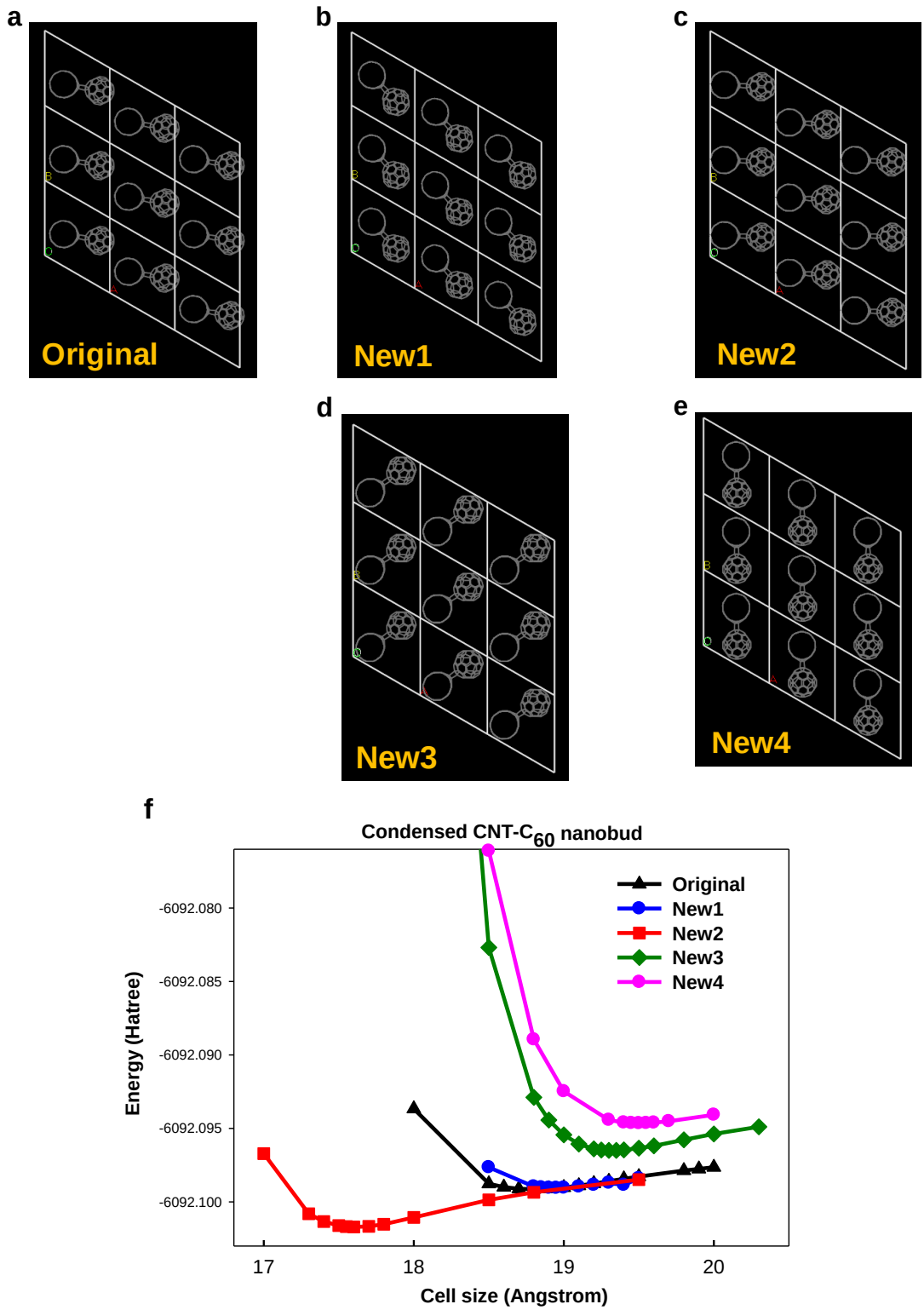

Figure 4.10: Initial structures of the condensed CNT-C_{60} hybrid systems (a) original; (b) New1; (c) New2; (d) New3; (e) New4; and (f) energy of each system in varying cell size.

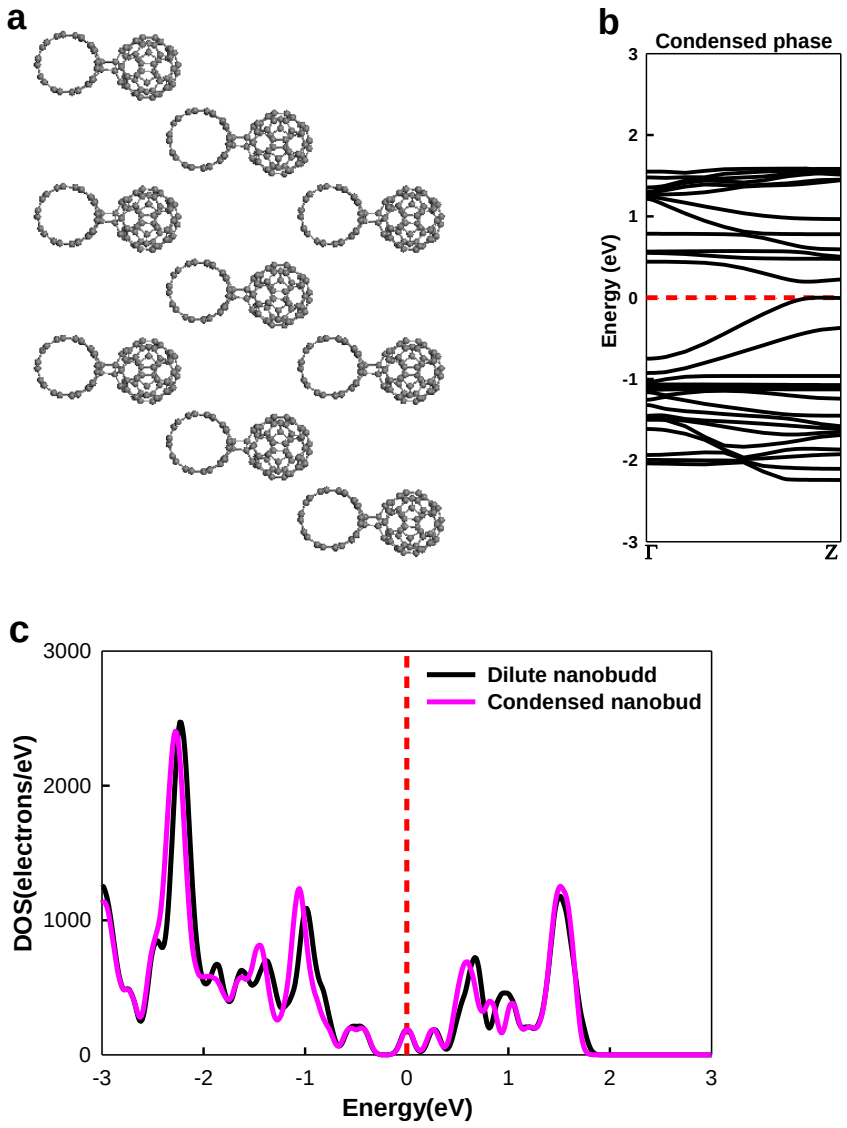

Figure 4.11: Condensed CNT-C_{60} nanobud system: (a) expanded view (3x3x3) of the optimized unit structure; (b) band structure; and (c) density of states (DOS) of the condensed and dilute phases in the nanobud system. (Unit cell: a=b=17.60 Å , c=12.30 Å).

4.4.2 Single Li atom on a condensed (5,5) CNT-C_{60} nanobud system

A Li atom is located on various positions on the condensed system, as in the dilute system. The position of the added Li atom is again chosen on either the center of the hexagon sites of the CNT or on the pentagon and hexagon sites of the C_{60}. A Li atom

is located on the CNT from Pos1_CNT@nanobud to Pos9_CNT@nanobud and on the C_{60} from Pos1_C_{60}@nanobud to Pos8_C_{60}@nanobud as shown in Figures 4.12.a and d, respectively. Optimized structures with their expanded view are represented in Figures 4.12.b-c, e-f, and the adsorption energy, charge distribution and band gaps are listed in Table 4.6. The Li adsorption energies (-2.374 eV ~ -2.565 eV) in the CNT@nanobud are increased to a much greater degree than in the dilute system and reach a comparable range (-2.481 eV ~ -2.642 eV) to the hybrid system in the condensed phase. The lowered adsorption energies may also be attributed to the symmetric geometry of the system, which permits simultaneous interactions with both components so that the Li atom may be located on any sites between C_{60} and the CNT (Figures 4.12.c and e) leading to an increase in the Li adsorption energy. It is noteworthy that the adsorption energy is slightly higher between C_{60} and the neighboring CNT-forming CNT-C_{60} hybrid structure than in the covalently bonded area. The charge transfer from Li to the nanobud is increased in the condensed phase of the nanobud system throughout its packed structure. The charge transfer increases from 0.864*e* to 1.020*e* except in the region that is covalently bonded to form the nanobud. Therefore, we can confirm that the covalent bond in this region still dominates regardless of the nanobud density, which prevents a change in the degree of the charge transfer (0.809*e* and 0.836*e*) compared to the values in the dilute phase.

The corresponding band structures of some representative one-Li-adsorbed systems are represented in Figure 4.13. As shown in Figure 4.13.a-d, band structures appear to be similar to those of the dilute nanobud system, and band gaps still exist due to the strong covalent bond wherever one Li atom is adsorbed around the nanobud system.

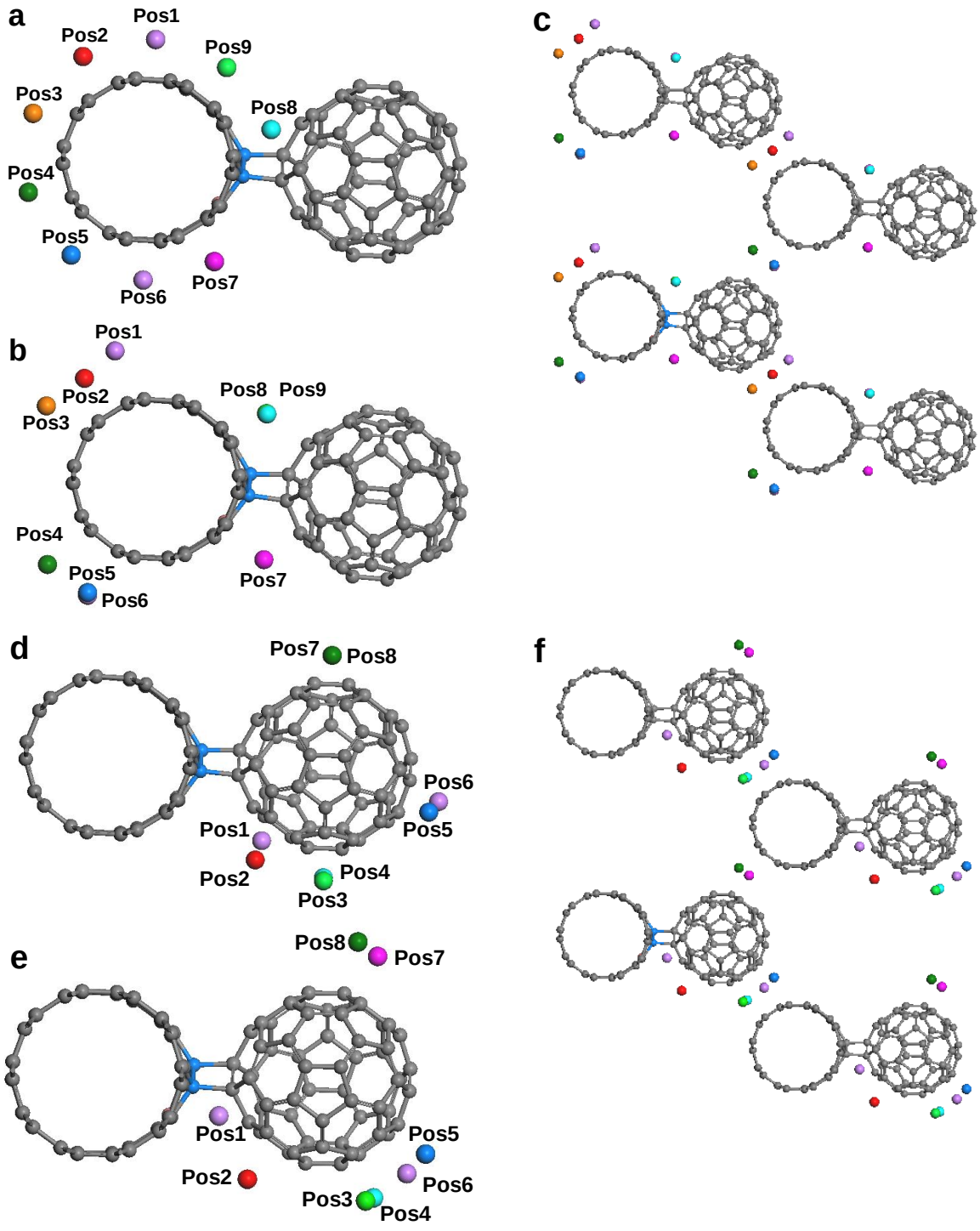

Figure 4.12: One-Li adsorption on various positions around the CNT@hybrid on the condensed nanobud system: (a) initial structure; (b) optimized structure; (c) expanded view of optimized structure; (d) initial structure; (e) optimized structure and (f) expanded view of optimized structure of one-Li adsorption on various positions around the C_{60}@hybrid on a condensed nanobud system.

Table 4.6: The adsorption energy and charge distribution (Mulliken charge) of one-Li atom on the condensed (5,5) CNT-C_{60} nanobud system

System	Adsorption Energy (eV)	Charges (e)			Band gap (eV)
		Li	CNT	C_{60}	
Condensed (5,5) CNT_C_{60} nanobud	N/A	N/A	0.147	0.147	0.196
Pos1_CNT@ nanobud	-2.439	0.869	-0.274	-0.595	0.197
Pos2_CNT@ nanobud	-2.489	1.020	-0.364	-0.656	0.198
Pos3_CNT@ nanobud	-2.466	0.872	-0.313	-0.559	0.198
Pos4_CNT@ nanobud	-2.467	0.874	-0.318	-0.556	0.197
Pos5_CNT@ nanobud	-2.565	0.994	-0.371	-0.623	0.200
Pos6_CNT@ nanobud	-2.559	1.009	-0.339	-0.670	0.200
Pos7_CNT@ nanobud	-2.390	0.812	-0.327	-0.485	0.211
Pos8_CNT@ nanobud	-2.386	0.809	-0.322	-0.487	0.209
Pos9_CNT@ nanobud	-2.374	0.809	-0.321	-0.488	0.21
Pos1_C_{60}@ nanobud	-2.506	0.839	-0.358	-0.481	0.214
Pos2_C_{60}@ nanobud	-2.105	0.826	-0.121	-0.705	0.201
Pos3_C_{60}@ nanobud	-2.496	0.888	-0.319	-0.569	0.200
Pos4_C_{60}@ nanobud	-2.514	0.908	-0.352	-0.556	0.195
Pos5_C_{60}@ nanobud	-2.431	0.876	-0.274	-0.602	0.199
Pos6_C_{60}@ nanobud	-2.551	0.971	-0.351	-0.620	0.204
Pos7_C_{60}@ nanobud	-2.489	0.927	-0.331	-0.596	0.199
Pos8_C_{60}@ nanobud	-2.432	0.864	-0.314	-0.550	0.197

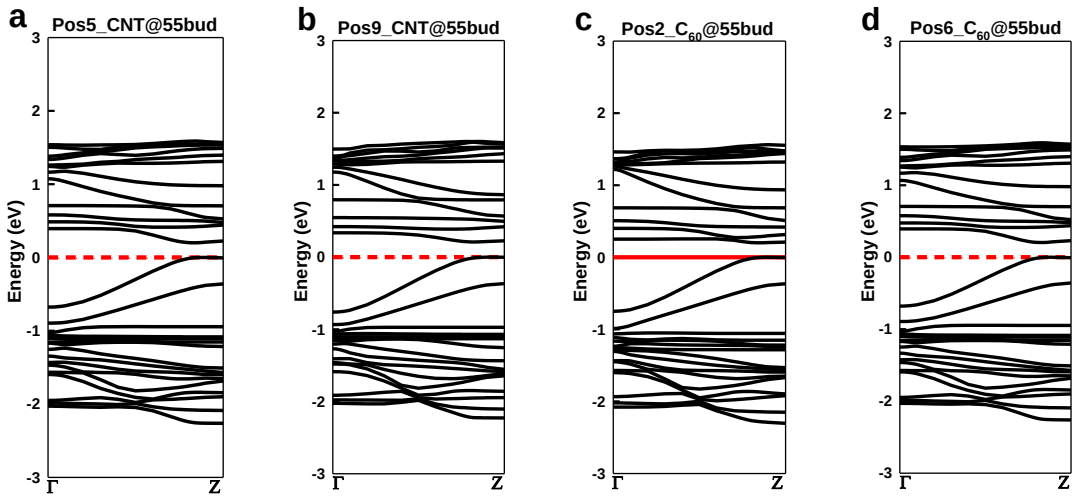

Figure 4.13: The band structure of a one-Li system in the condensed phase: (a) Pos5_CNT@55bud; (b) Pos9_CNT@55bud; (c) Pos2_C_{60}@55bud; and (d) Pos6_C_{60}@55bud.

4.4.3 Multiple Li atoms on a condensed CNT-C_{60} hybrid system

We added another Li atom (blue) near the first Li atom (pink) at the low adsorption energy site at the CNT@nanobud or C_{60}@nanobud to investigate the mechanism for Li adsorption. Some of the two-Li adsorbed systems with corresponding band structures are displayed in Figure 4.14, and Li adsorption sites were defined as described in Section 4.3.3. Therefore, the second atom is adsorbed to the next nearest neighboring site (N.N.N.) or the nearest neighboring site (N.N.) in either the radial or axial direction along the axis of the CNT surface starting from the site which had the lowest Li adsorption energy at the CNT@nanobud or C_{60}@nanobud. Table 4.7 provides the Li adsorption energies of these two-Li systems. The adsorption energies (-2.248 eV ~ -2.503 eV) are much lower than calculated in the dilute system, but they are slightly higher than those in the hybrid system in the condensed phase.

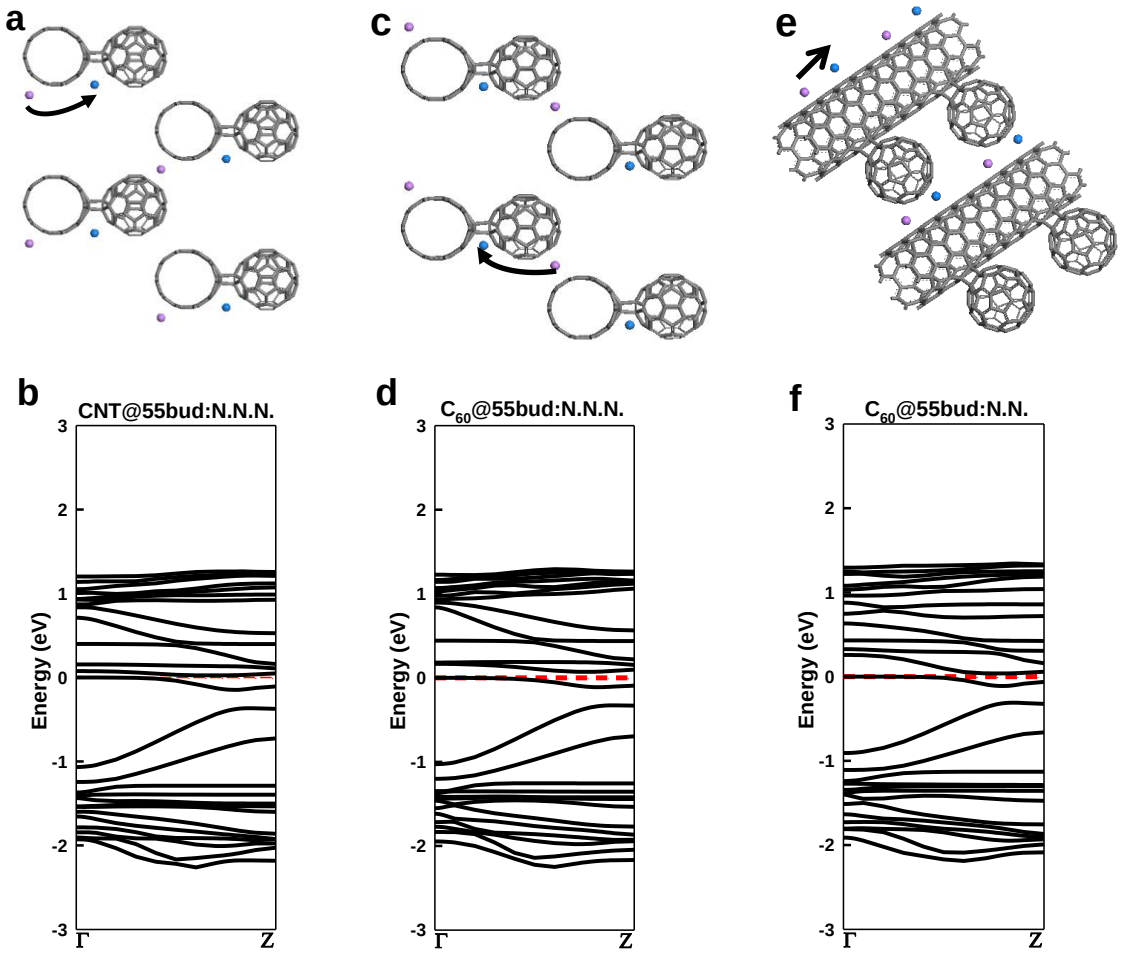

Figure 4.14: Two-Li adsorption on various regions; (a) next nearest neighboring (N.N.N.) site in the radial direction starting at the Pos5_CNT@55bud; (b) the corresponding band structure; (c) next nearest neighboring (N.N.N.) site in the radial direction starting at the Pos6_C_{60}@55bud; (d) the corresponding band structure; (e) nearest neighboring (N.N.) site in the axial direction starting at the Pos6_C_{60}@55bud; and (f) the corresponding band structure.

We found that N.N.N. sites have a slightly lower value than the N.N. sites in general throughout the table; however, Li adsorption in the condensed phase is mainly driven by the compact structure, as in the hybrid system. The adsorption is lowered by positioning another Li atom closely to the high electron affinity C_{60}, but N.N.N sites still seemed to be preferred. Hence, the hybrid area (between C_{60} and the neighboring CNT) is selected

Table 4.7: The adsorption energy of many-Li atoms adsorption systems on condensed (5,5) CNT-C_{60} nanobud system

Starting position	Direction	Adsorption Energy (eV)
2Li starting from Pos5_CNT@nanobud	Radial (N.N.N.[a] site)	-2.411
	Radial (N.N.[b] site)	-2.457
	Axial (N.N.N. site)	-2.380
	Axial (N.N. site)	-2.360
2Li starting from Pos6_C_{60}@nanobud	Radial (N.N.N. hexagon site)	-2.296
	Radial (N.N.N. pentagon site)	-2.503
	Radial (N.N. hexagon site)	-2.248
	Radial (N.N. pentagon site)	-2.311
	Axial (N.N.N. hexagon site)	-2.326
	Axial (N.N.N. pentagon site)	-2.418
	Axial (N.N. hexagon site)	-2.363
	Axial (N.N. pentagon site)	-2.459
31 Li atoms on condensed CNT-C_{60} nanobud		-1.778

a. N.N.N.: Next Nearest Neighbor, b. N.N.: Nearest Neighbor

as a starting position for the first Li adsorption, and adsorption proceeds between C_{60}s or to the closest sites over the covalent bonds even though the covalent bonds still prevent further enhancement of the Li adsorption capabilities. The possibility of the Li cluster forming in the nanobud system does not appear to be high considering that the adsorption energy shown in Table 4.7 is higher than the Li-Li binding energy. The band structure in Figures 4.14.b, d, and f shows that, like in the dilute system, the energy band shifts as a

result of the increase in the Fermi level after the addition of the Li atom on the system. Consequently, injected electrons from Li atoms to the nanobud system change the system to exhibit metallic characteristics. Because the Li atoms face the CNT and C_{60} simultaneously in the condensed phase, the shape of all three of the band structures appear to be similar to each other from the uniform interaction with each component.

Finally, we surrounded the entire nanobud surface in condensed phase with multiple (31) Li atoms on the preferred N.N.N. sites to predict the Li adsorption energy and electronic properties compared to Li cluster formation. Figure 4.15 represents the initial and optimized structure of the multi-Li adsorbed system with band structures and density of states (DOS) of the system. The structure in the condensed phase is actually a combination of the hybrid and nanobud structure, in which one side of the CNT is bonded to C_{60} and the other side faces the next C_{60}. Therefore, enhancement of Li adsorption is expected from this mixed structure compared to the dilute phase, and the optimized structure shown in Figure 4.15.b confirms this. The Li atoms initially placed on the CNT were attracted to C_{60}s around the CNT, but Li atoms around the bond adjusted their position. In addition, Li atoms in the nanobud system were uniformly distributed around the CNT in the nanobud system, while all of the Li atoms were located between the CNT and C_{60} in the hybrid system. Therefore, the enhancement of the adsorption was more apparent in the nanobud system than in the hybrid system (-1.809 eV: dilute system and -1.862 eV: condensed system). The Li adsorption energy of the many Li system in the condensed phase was -1.778 eV, which was much lower than that in the dilute phase (-1.412 eV) and reflected the advantage of the mixed (hybrid and nanobud) structure. Additionally, the Li adsorption energy of the nanobud system (-1.778 eV) was higher

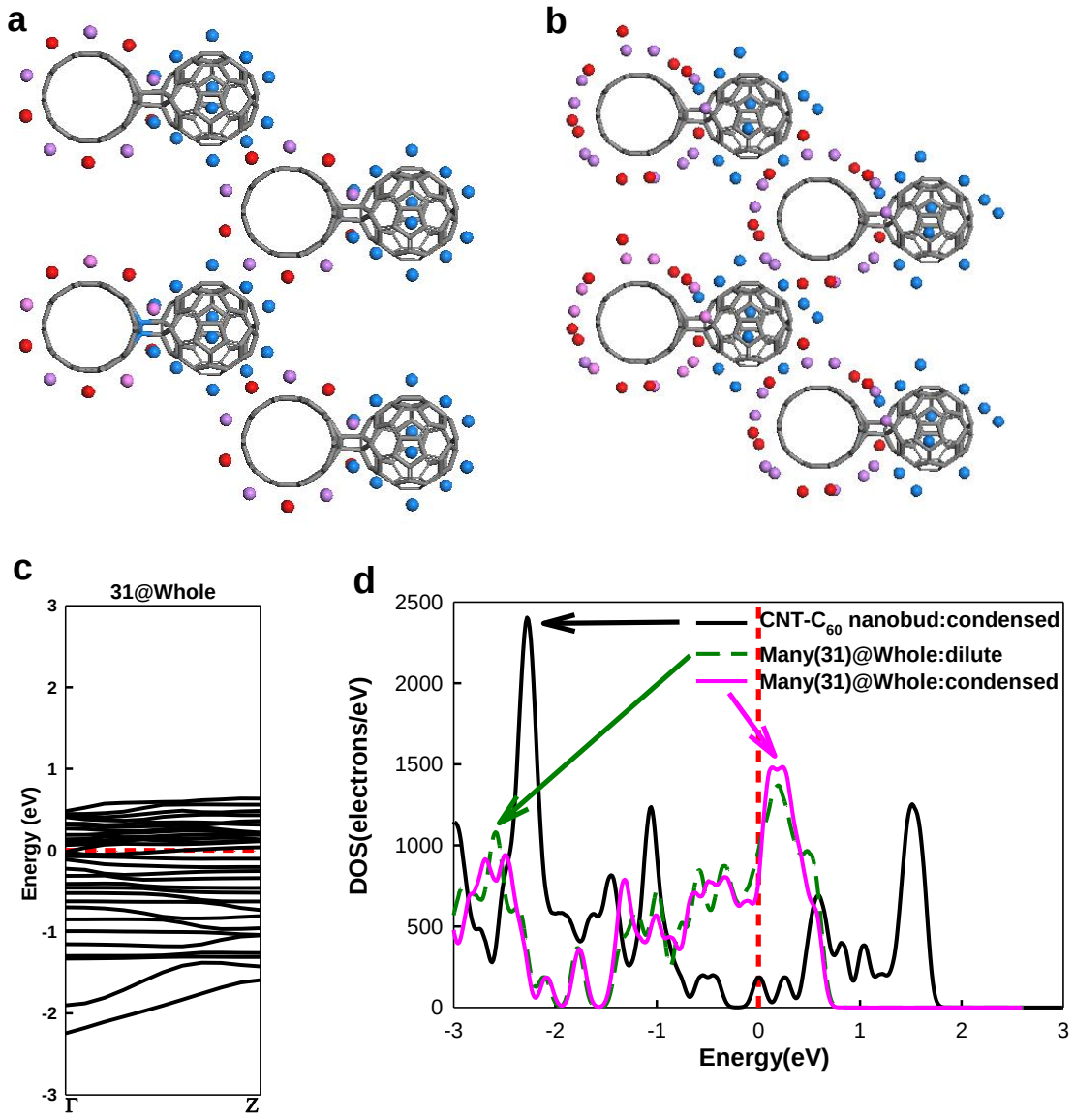

Figure 4.15: Multi(31)-Li atoms adsorbed on the whole hybrid system: (a) initial structure; (b) optimized structure; (c) the corresponding band structure; and (d) density of states (DOS) with pure condensed phase and 31 Li atoms on the dilute phase of the nanobud system.

than that of the hybrid system (-1.862 eV) because of the limited site by the bond between the CNT and C_{60}. The corresponding band structure and DOS shown in Figure 4.9.c appear to be similar to those obtained from multi-Li atom systems in the dilute phase. Therefore, energy bands around the Fermi level significantly increased along with

an increased number of electron states, although a slightly larger number of electron states existed over the conduction band as displayed in Figure 4.15.d. Band structure also reflects the enhanced metallic character of the system after the adsorption in any CNT-C_{60} hybridized (hybrid or nanobud) system.

4.4.4 Conclusion

In this section, we studied Li adsorption on the CNT-C_{60} nanobud system in the condensed phase using GGA PBE. The nanobud system shows more charge transfer (0.147*e*) from the CNT to C_{60} than in the dilute phase (0.092*e*), while the band structure and the DOS remain unchanged. However, the Li adsorption capability was further enhanced in the condensed phase system along with uniform distribution of the adsorption energy except in sites that were distant from C_{60}. Hence, Li adsorption will occur on the C_{60} side, especially between the CNT and C_{60} or between C_{60}s, and progress to the CNT side following the N.N.N. scheme. Moreover, additional Li adsorption enhances the metallic character of the system, which is confirmed from the band structure and density of states as well as the Li adsorption energy that is lower than in the dilute phase. Therefore, it seems that the CNT-C_{60} nanobud system in the condensed phase may be promising as a possible electrode in a Li battery system via its enhanced Li adsorption and mechanical strength.

CHAPTER 5

FIRST-PRINCIPLES STUDY OF LI ADSOPRTION ON CARBON NANOTUBE-FULLERENE NANO-NETWORK SYSTEM

In this chapter, we designed a theoretical 3D "nano-network" structure of the carbon nanotube (CNT) - fullerene (C_{60}) system, which extends the structure of the nanobud system by binding all of the CNT-C_{60}. First, we examined properties of the pristine nano-network system such as electronic and mechanical properties. And then, we investigated the performance and the change in electronic properties related to Li adsorption on the nano-network system.

5.1 Introduction

With increasing concern for clean and renewable energy sources, many studies have been performed to develop energy storage such as hydrogen storage [104-107] or Li ion battery systems [51-53] by using carbon nanotubes (CNTs) as electrodes. Although CNTs show superior electrical and mechanical properties, pristine CNTs do not meet the standards of these applications because of the weak Li adsorption in a Li battery system or the lack of well-defined samples in the measurement of hydrogen uptake. Thus, various hybrid [73, 75-77, 93] or network materials [108-114] have been exploited to overcome those disadvantages and meet appropriate standards for application. Recently, Barnes et al. prepared single-walled carbon nanotubes (SWCNTs) network films (Figure 5.1.a) using an ultrasonic spray method to be used as transparent and conductive electrodes for organic solar cells [111]. Additionally, Weck et al. designed novel carbon nano-frameworks (Figure 5.1.b) consisting of (5,0) and (3,3) CNTs constrained by phenyl

spacers and investigated the electronic structures and stabilities using the density functional theory [114].

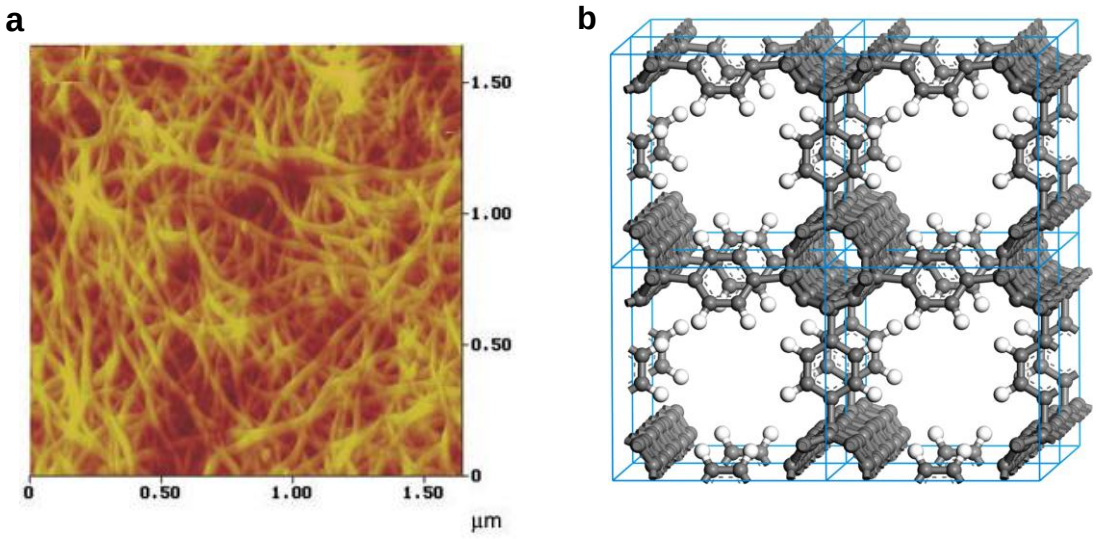

Figure 5.1: A carbon nanotube network material: (a) AFM image of a 150-nm-thick transparent single-walled carbon nanotube (t-SWCNT) network film and (b) an optimized nano-framework structure consisting of (5,0) SWCNTs constrained by phenyl spacers.

In this chapter, we report the development of a novel type of network system consisting of CNTs and C_{60} covalently bound to each other. This system is actually an expanded structure of a CNT-C_{60} nanobud. Furthermore, this nano-network system can utilize the advantages of each component by combining the high mechanical strength of CNTs and the strong electron affinity of C_{60} to enhance Li or hydrogen adsorption capabilities while maintaining high mechanical strength.

In this study, we used the first-principles computational method to study the electronic and mechanical properties of the pristine CNT-C_{60} network system and the Li adsorption mechanism on the nano-network system. The Li adsorption mechanism can be examined in detail by calculating the Li adsorption energy as performed in the previous

two chapters. We also investigated changes in electronic properties such as band structure, density of states and charge distribution as a function of the number of Li atoms.

5.2 Computational details

In this study, generalized gradient approximation (GGA) Perdew-Burke-Ernzerhof (PBE) functional was also introduced to calculate the electron exchange-correlation energy. All the DFT calculations were performed using a double numerical basis set with d-polarization functions (DND) through DMol^3 from Accelrys.

The unit cell dimension was set to 15.9 Å × 15.0 Å × 12.297 Å after geometric optimization of the nano-network system. Monkhorst-Pack k-point scheme [86] was used for k-point sampling to determine the adsorption energy and other electronic properties such as band structure, density of states and Mulliken charge distribution [87, 88]. Thus, gamma (1x1×1) k-point was used for geometry optimization and (1x1x4) k-point was used for looking into all the system properties. The adsorption energy per Li atom on the CNT-C_{60} network system is also calculated the same way in the chapter 3 (equation 3.1). The negative value of the adsorption energy indicates a favorable Li adsorption whereas the adsorption is not favorable if the value is positive as we defined previously.

5.3 Results and discussion

5.3.1 Pure CNT-C_{60} nano-network system

To prepare the CNT-C_{60} network structure, we used a (5,5) CNT-C_{60} nanobud system in the condensed phase as an initial structure. First, the unit cell of the nanobud system (Figure 5.2.a) was adjusted to produce a symmetric structure, and each CNT and C_{60} was connected to form a 3-dimensional (3D) nano-network structure. In this process,

we attempted various bond connections between the CNT and C_{60} starting from the preferred hs (h denotes the C_{60} bond between two hexagonal faces and s denotes a slope bond to the tube axis in the armchair CNT: Figure 4.2) connection to obtain the reasonable structure. However, we used a classical molecular mechanics tool (Forcite from Accelrys) for checking various structures in advance before full geometry optimization by Dmol^3. The results of the optimization showed that all three of the bond connections were not energetically preferred hs connections after geometry optimization. Instead, the only reasonable structure was calculated when new two bond connections were formed in a pv bond (p denotes a C_{60} bond between a hexagonal face and pentagonal face and v denotes a vertical bond to the tube axis in the armchair CNT). The optimized structure through molecular mechanics was further optimized by DFT to obtain a stable structure. Figure 5.2.b shows the expanded view of the optimized structure and it is clear that the unit structure was slightly smaller compared to the nanobud in the condensed phase. The corresponding binding energy ($E_{binding} = E_{network} - E_{CNT} - E_{C60}$) was 6.268 eV, which indicated that this conceptual structure needed more energy than the nanobud (1.326 eV) system realized via a [2+2] cycloaddition reaction. Bond lengths are summarized in the Table 5.1. We can clearly see the change of the electronic property of the nano-network system through the band structure and the density of states.

Table 5.1: Mulliken charge distribution and bond length in the nano-network system

	Charges (e)		Bond length (Å)					
	CNT	C_{60}	1		2		3	
CNT-C_{60} network system	0.187	-0.187	1.592	1.591	1.596	1.627	1.622	1.595

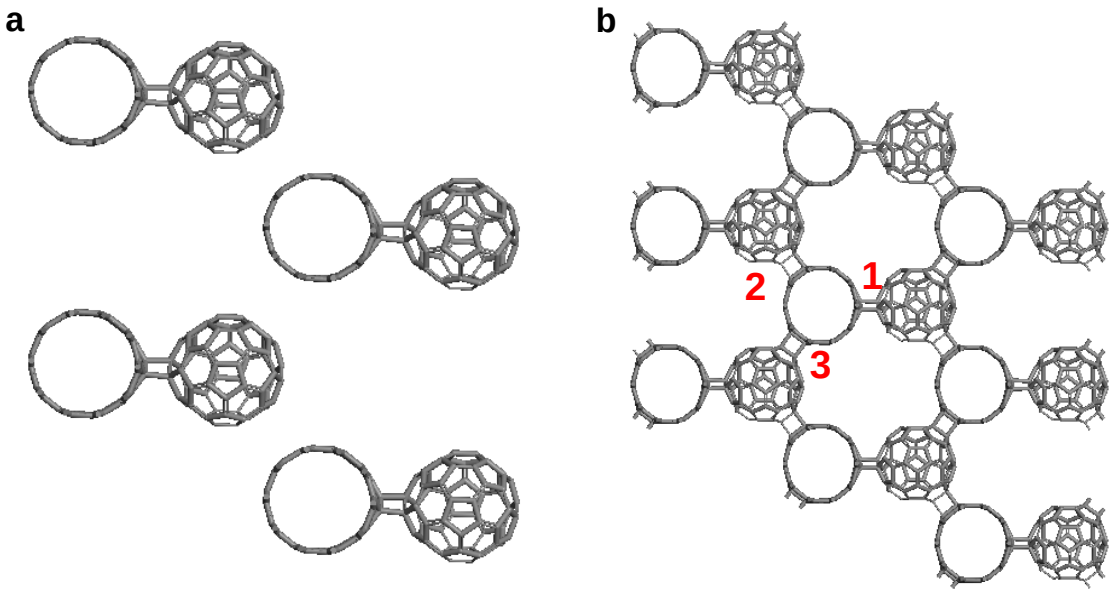

Figure 5.2: (a) The initial nanobud structure in the condensed phase (unit cell parameters: a=b= 17.6 Å, c = 12.3 Å, α=β=90° and γ=120°) and (b) the 3x3 expanded optimized (5,5) CNT-C_{60} network structure (unit cell parameters: a =15.9 Å, b = 15 Å, c = 12.3 Å, α=102.5°, β=85° and γ=118°).

The band structure of the nano-network system and density of states (DOS) are represented in Figure 5.3 along with the hybrid and nanobud systems in the condensed phase. From the figure, it is shown that the band gap evolves as the number of bonds between the CNT and C_{60} increases. Thus, the nano-network system has a 0.34 eV gap, while the nanobud has a 0.19 eV or no band gap in the hybrid system. However, the band structure appeared to differ from other CNT-C_{60} systems. As shown in Figure 5.3.a, the band from C_{60} moves down to the Fermi level in the nano-network structure, whereas the same band exists around 0.56 eV in other hybridized system. Therefore, it appears that the nano-network system is semiconducting with a small band gap (~ 0.34 eV) because CNT work like dopants in the semiconducting C_{60}. Therefore, electrons from the CNT will fill the band of the C_{60}, which results in an increased DOS level around the Fermi

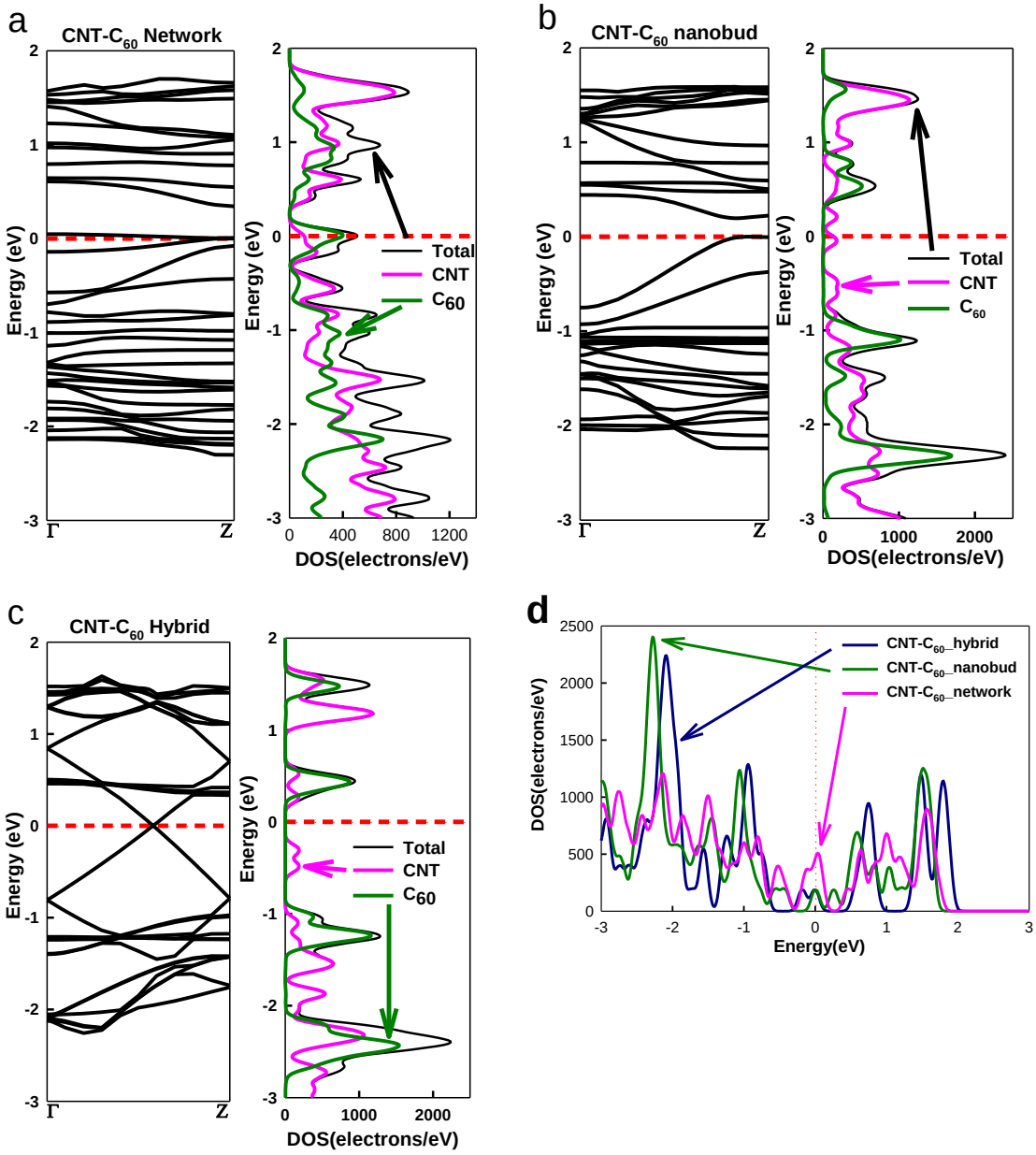

Figure 5.3: The band structure with DOS of the (a) CNT-C_{60} network system; (b) (5,5) CNT-C_{60} nanobud system in condensed phase and (c) (5,5) CNT-C_{60} hybrid system in condensed phase. The projected DOS of CNT and C_{60} are represented with pink and green lines, respectively. The total DOS is plotted with a black line.

level compared to the nanobud or hybrid system as shown in Figure 5.3.d. The network system still shows a charge transfer from CNT to C_{60} in the nano-network system

amounting to $|0.187|e$, which is higher than the hybrid ($|0.141|e$) or nanobud system ($|0.147|e$) in the condensed phase. This increased charge transfer can be attributed to the smaller unit size of the nano-network system (a=15.9 Å, b= 15 Å) than the hybrid (a=b=18.35 Å) or nanobud systems (a=b=17.6 Å). This implies that CNT and C_{60} are closely located so that the charge transfer between each component can occur easily.

We also investigated mechanical properties such as Young's modulus, bulk modulus and shear modulus of the network system as well as the CNT-C_{60} hybrid and nanobud systems in condensed phase. Table 5.2 describes the mechanical strength of pure CNT, the CNT-C_{60} hybrid, the CNT-C_{60} nanobud and the CNT-C_{60} network systems in the condensed phase. Elastic moduli were calculated using a constant strain minimization method [115]. In general, the stress in a solid is defined as the change in the internal energy per unit volume with respect to the strain. In this method, small strains are applied to a periodic structure at an energy minimum, and the application of strain is accomplished by uniformly expanding the dimensions of the simulation cell in the direction of the deformation and re-scaling the new coordinates of the atoms to fit within the new dimensions. The structure is minimized again while fixing the lattice parameters and the resultant stress in the minimized structure is measured. This is repeated for a series of strains and the variation of the measured stress as a function of applied strain is used to derive the stiffness matrix using the following equation:

$$C_{ij} = \frac{1}{V}\frac{\partial^2 U}{\partial \varepsilon_i \partial \varepsilon_j} = \frac{\partial \sigma_i}{\partial \varepsilon_j} = \frac{\sigma_+ - \sigma_-}{2\varepsilon_j} \tag{5.1}$$

, where V, U, ε and σ are the volume, internal energy, strain and stress on the system, respectively. Here, a small strain (ε=±0.003%) is applied to the hybridized system in the

direction of the x, y and z-axes, and a subsequent energy minimization is performed. The obtained mechanical strength of the hybridized system is lower than that of the pure CNT in the bundle because the CNT faces a smaller C_{60} instead of other CNTs. However, mechanical strength increases again as the CNT and C_{60} form covalent bonds, which allows the network system to increase its mechanical strength in all directions as shown in Table 5.2. The strength in the radial direction (~ 70 GPa) along the axis of the carbon nanotube is especially enhanced compared to the pure CNT bundle (~ 4 GPa),

Table 5.2: Young's, bulk and shear modulus of the CNT-C_{60} systems (Unit: GPa)

	Yxx	Yyy	Yzz	Bulk	Shear
(5,5) CNT	3.658	3.650	760.760	75.495	27.280
CNT-C_{60} hybrid	0.531	0.491	225.505	12.337	7.101
CNT-C_{60} nanobud	0.944	1.088	240.380	13.226	7.998
Nano-network	67.964	71.649	309.632	48.680	28.343

which is known to be rather soft in the radial direction [116] compared to the axial direction. Therefore, the nano-network structure consisting of CNT-C_{60} will have enhanced mechanical properties compared to the previous hybridized system.

5.3.2 Single Li atom on a CNT-C_{60} network system

We added Li atoms on various positions in the CNT-C_{60} network system to investigate its Li adsorption capabilities. In this work, we placed the Li atom on the center of the hexagon sites (Center) in CNT and the pentagon or hexagon sites in C_{60} as was done in previous experiments. Figure 5.4 shows the initial and final structure of the one-Li adsorption system on the CNT side and C_{60} side. It appeared to be difficult to

distinguish sites in this network system because of its nearly symmetric and condensed structure. Therefore, we chose sites between bonds and placed the Li atom closer to the CNT or C_{60} side making a CNT@network or C_{60}@network. The adsorption energy is also low, ranging from -2.224 eV to -2.727 eV as a hybrid or nanobud system in condensed phases due to the simultaneous interaction between CNT and C_{60}. However, some energy differences remain depending on the position because the nano-network system is not perfectly symmetric (having different bond lengths), and Li adsorption is strongly affected by the covalent C-C bond, as in the nanobud system. In addition, it appears that the adsorption energy was slightly lower when the Li atom was located close to the CNT (Pos1,2,3_CNT@network or Pos5,6_C_{60}@network). This finding could be explained by the positively charged CNT surface (0.187*e*) relative to C_{60}. Thus, the additional charge transfer from the adsorbed Li to the network system somewhat enhanced the Li adsorption energy. Conclusively, the Li adsorption in the nano-network system is mainly driven by the high electron affinity C_{60}, but the slightly asymmetric structure and increased charge transfer can generate adsorption energy differences.

We also investigated the band structure of several one-Li adsorbed systems in Figure 5.5. The overall band structure appeared to be similar to the pristine nano-network system even though the band from the CNT moved slightly toward the Fermi level, thus decreasing the bang gap slightly (0.26 eV) after one-Li atom adsorption as shown in Figure 5.5. Thus, it appears that one-Li adsorption does not affect the system property as much as the other hybridized systems.

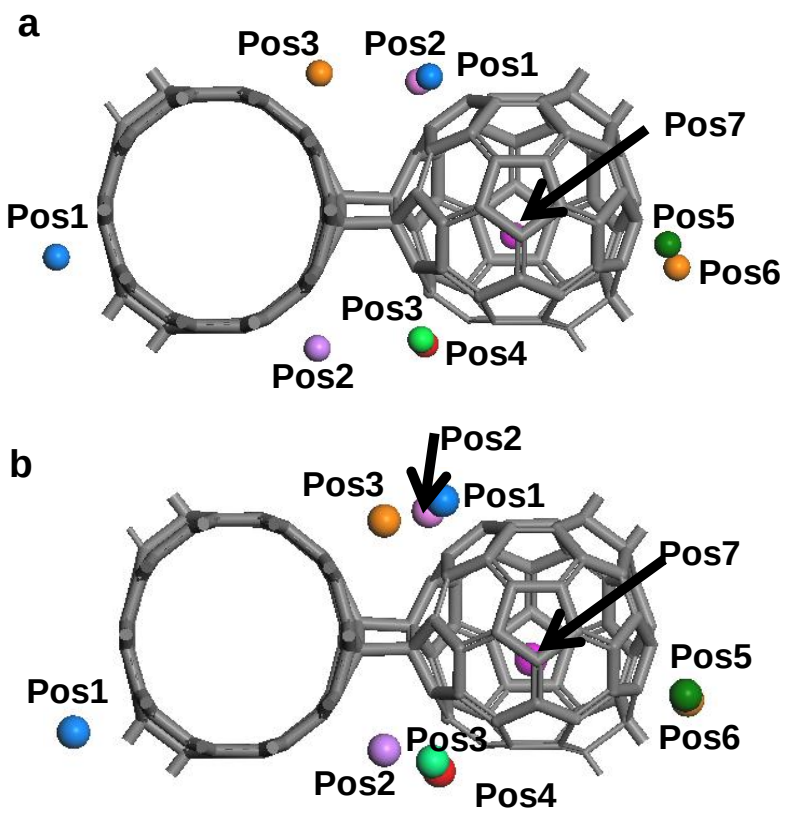

Figure 5.4: One-Li adsorption on various positions in each region around the (5,5) CNT-C_{60} network: (a) initial structure and (b) optimized structure.

5.3.3 Multiple Li atoms on a CNT-C_{60} network system

Subsequent to this first Li atom (purple) adsorption, we added another Li (blue) at different sites near the initial Li atom to investigate the Li adsorption mechanism in the network system. For practical purposes, it is important to predict how efficiently Li atoms utilize the surface area of the CNT-C_{60} network system against Li cluster formation, which can be explained by the binding energy. For this reason, we added the second Li atom starting from the sites having the lowest energy on each side. However, we chose only two sites as a starting position in this network system, one at the CNT@network and the other at the C_{60}@network, because these sites are expected to have very similar

adsorption energies when a second Li atom is added regardless of which Li atom is first selected due to the nearly symmetric and packed structure in the nano-network system. Figure 5.6.a shows the schematic view of the two-Li atom adsorption system starting from the Pos1_CNT@network to C_{60} or the CNT following the next nearest neighboring (N.N.N.) scheme. Alternatively, there may be various possibilities in determining the position of the second Li atom.

Table 5.3: The adsorption energy and charge distribution (Mulliken charge) of one-Li atom on the (5,5) CNT-C_{60} network system

System	Adsorption Energy (eV)	Charges (e)		
		Li	CNT	C_{60}
(5,5) CNT_C_{60} network	N/A	N/A	0.187	0.187
Pos1_CNT@ network	-2.727	0.821	-0.130	-0.691
Pos2_CNT@ network	-2.551	0.800	-0.204	-0.596
Pos3_CNT@ network	-2.544	0.799	-0.201	-0.598
Pos1_C_{60}@ network (pentagon)	-2.224	0.817	-0.064	-0.753
Pos2_C_{60}@ network (hexagon)	-2.374	0.815	-0.057	-0.758
Pos3_C_{60}@ network (pentagon)	-2.227	0.817	-0.065	-0.752
Pos4_C_{60}@ network (hexagon)	-2.367	0.815	-0.053	-0.762
Pos5_C_{60}@ network (pentagon)	-2.668	0.809	-0.158	-0.651
Pos6_C_{60}@ network (hexagon)	-2.553	0.819	-0.239	-0.580
Pos7_C_{60}@ network (pentagon)	-2.506	0.854	0.031	-0.885

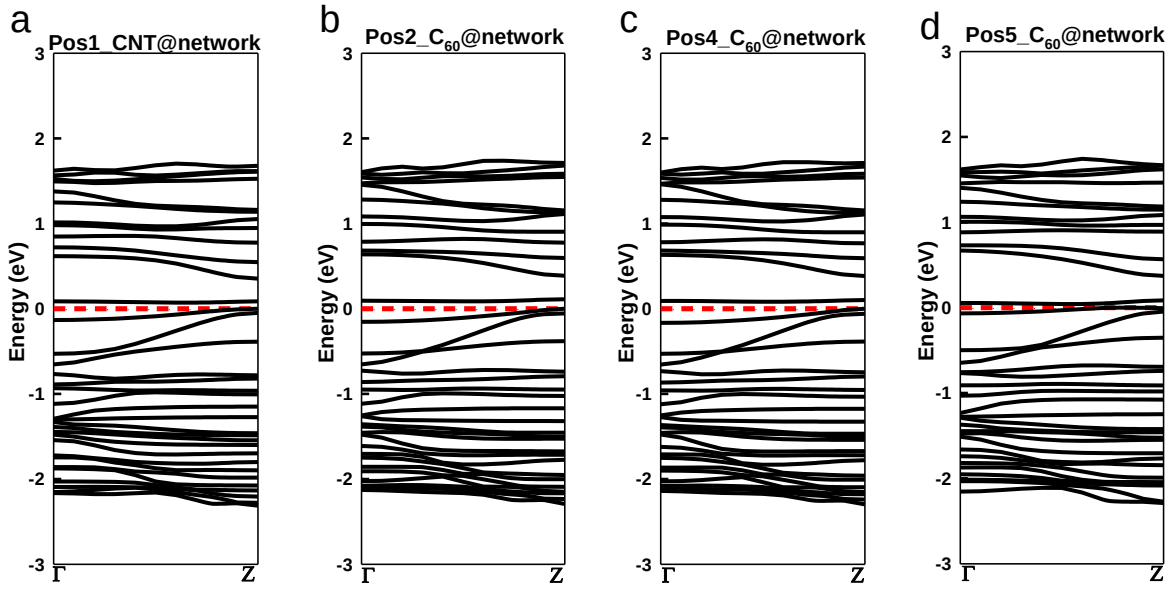

Figure 5.5: The band structure of a one-Li system in a CNT-C_{60} network system: (a) Pos1_CNT@network; (b) Pos2_C_{60}@network; (c) Pos4_C_{60}@network; and (d) Pos5_C_{60}@network.

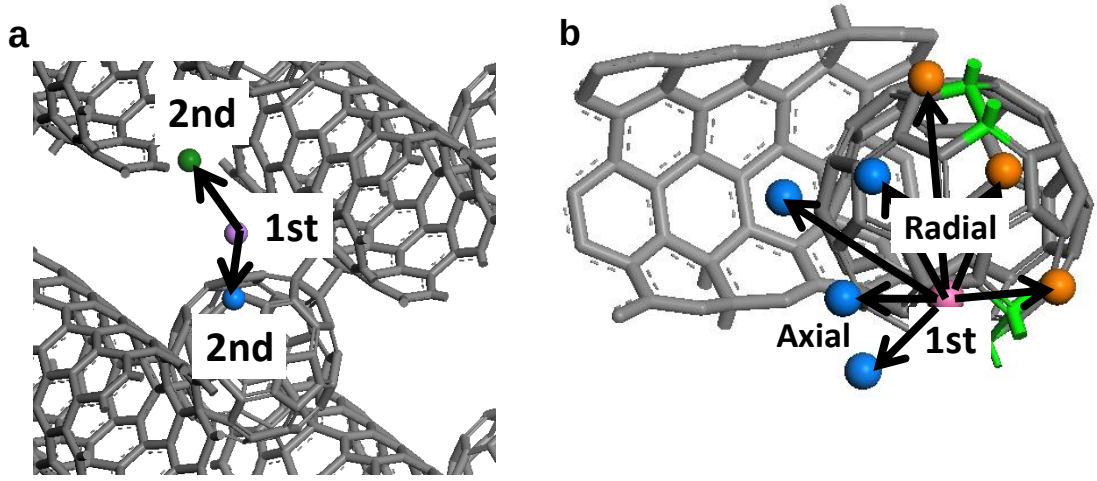

Figure 5.6: Two-Li adsorption directions; (a) next nearest neighboring (N.N.N.) site to either CNT or C_{60} starting at Pos1_CNT@network and (b) the radial and axial direction/ next nearest neighbor (N.N.N.) and nearest neighbor (N.N.) of the second Li atom adsorption location starting from the Pos5_C_{60}@network (1^{st} Li atom: purple and 2^{nd} Li atom: blue, green or orange).

Therefore, we divided the second Li either toward the covalent bond side or toward the unbounded bond side along with our usual definition (radial/axial and N.N.N./N.N. scheme) shown in Figure 5.6.b. Some representative arrangements in two-Li adsorbed systems are displayed in Figure 5.7, and the Li adsorption energies of the two Li atoms are listed in Table 5.4. From the table, we observed that the adsorption energy of the two-Li system was quite similar between -2.410 eV and -2.681 eV in the two sites on the C_{60}. Additionally, it appears that Li adsorption attempts to occur in the middle between the CNT and C_{60} (Figures 5.7.a-b: -2.681 eV) but away from the covalent bond because the C-C bond was already strongly coupled. (Figure 5.7: -2.669 eV) The only exception (-0.921 eV) is the N.N.N. scheme toward the covalent bond, which might be strongly trapped in the middle of the bond or a Dmol^3 error.

We also confirmed that the Li adsorption will start from C_{60} sites when we compared adsorption energy in Table 5.4, in which the energy toward another C_{60} (-2.410 eV) site was lower than energy toward a CNT (-2.258 eV) site. Therefore, enhanced Li adsorption is expected to occur in the nano-network system as a hybrid or nanobud system in the condensed phase rather than forming Li clusters and will proceed similarly (C_{60} sites first followed by CNT) to previous hybrid systems. However, it seems Li adsorption will depend on the Li location rather than the N.N.N. scheme because covalent bonding strongly affects the adsorption and the condensed structure of the network system.

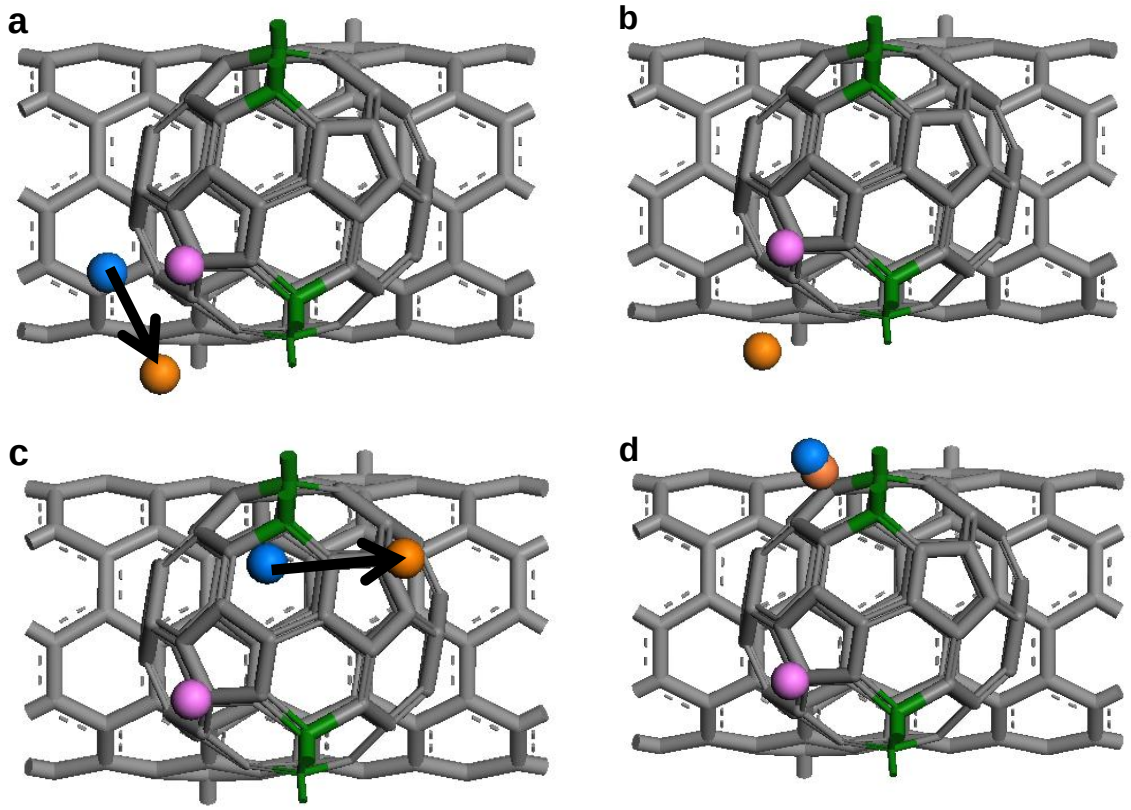

Figure 5.7: Optimized structures of two-Li adsorption toward the nonbonded side including (a) nearest neighboring (N.N.) site in the axial direction starting at the Pos5_C_{60}@network and (b) next nearest neighboring (N.N.N.) in the radial direction starting at the Pos5_C_{60}. Optimized structures toward bonded side including (c) nearest neighboring (N.N.) site in the radial direction starting at the Pos5_C_{60}@network and (d) next nearest neighboring (N.N.N.) in the radial direction starting at the Pos5_C_{60}@network (1^{st} Li atom: purple and 2^{nd} Li atom: blue (initial) and orange (final)).

Table 5.4: The adsorption energy of many Li adsorption systems on the (5,5) CNT-C_{60} network

Starting position	Direction	Adsorption energy (eV)
2Li starting from Pos1_CNT@network	To CNT (N.N.N. site)	-2.258
	To C_{60} (N.N.N. site)	-2.410
2Li starting from Pos5_C_{60}@network	Nobond_Radial (N.N.N. pentagon site)	-2.681
	Nobond_Radial (N.N. hexagon site)	-2.561
	Nobond_Axial (N.N.N. pentagon site)	-2.573
	Nobond_Axial (N.N. hexagon site)	-2.681
	Bond_Radial /Axial (N.N.N. pentagon site)	-0.921
	Bond_Radial (N.N. hexagon site)	-2.669
	Bond_Axial (N.N. hexagon site)	-2.567
32 Li atoms on CNT-C_{60} network system		-1.655

Even though the CNT-C_{60} hybrid or nanobud systems showed a band shift after two-Li adsorption, the nano-network system did not exhibit the same behavior, retaining its band gap (0.24 eV) with additional Li atoms. (Figure 5.8) This result can be confirmed from the DOS in Figure 5.9 because the DOS on neither the CNT nor the C_{60} side changes until many Li atoms are adsorbed on the network system. Therefore, the electronic properties of the strongly bonded network system are still not affected by the small number of Li atoms adsorbed to the structure, and additional electrons fill up the band in the CNT.

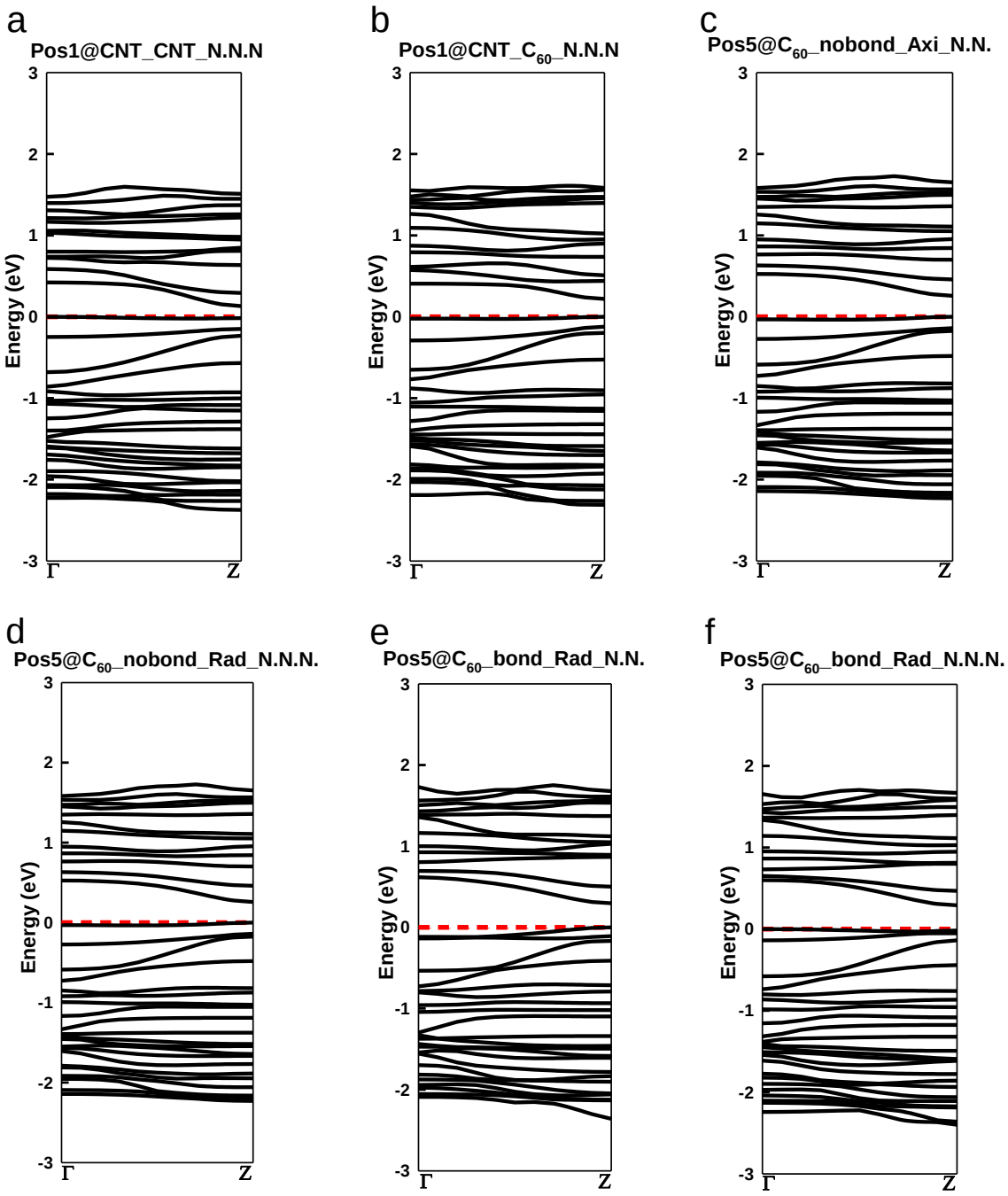

Figure 5.8: The band structures of a two-Li adsorption network system: next nearest neighboring (N.N.N.) site to (a) CNT and (b) C_{60} starting at Pos1_CNT@network. Toward the nonbonded side: (c) nearest neighboring (N.N.) site in the axial direction and (d) next nearest neighboring (N.N.N.) in the radial direction. Toward the bonded side: (e) nearest neighboring (N.N.) site and (f) next nearest neighboring (N.N.N.) in the radial direction starting at the Pos5_C_{60}@network.

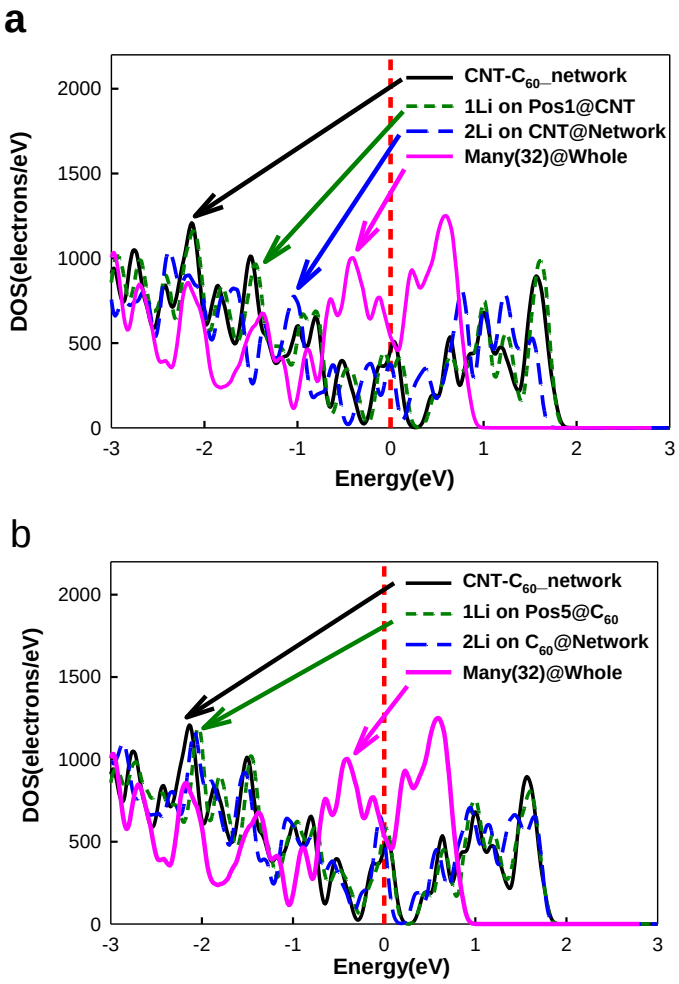

Figure 5.9: Density of states (DOS) with varying numbers of Li atoms on a (a) CNT@network and (b) C_{60}@network.

Finally, we covered the entire surface of the nano-network system with multiple (32) Li atoms following the N.N.N. scheme as usual. Figures 5.10.a and b show the initial and optimized structures of the multi-Li system. The optimized structure shows similar Li distribution as the CNT-C_{60} hybrid or nanobud system in the condensed phase, in which Li atoms are mainly positioned between the CNT and C_{60} after optimization. It indicates that Li adsorption can also be enhanced in the nano-network structure and the adsorption energy was calculated to be -1.655 eV. However, the adsorption energy is higher than in

the hybrid (-1.862 eV) or nanobud (-1.778 eV) system because the three bonds between CNT and C_{60} limit the adsorption sites between the CNT and C_{60}. Furthermore, it is still lower than the Li-Li binding energy (-1.030 eV). Thus, it is likely that Li will fill the network system on the available sites on the surface of the network system before Li-Li clusters form.

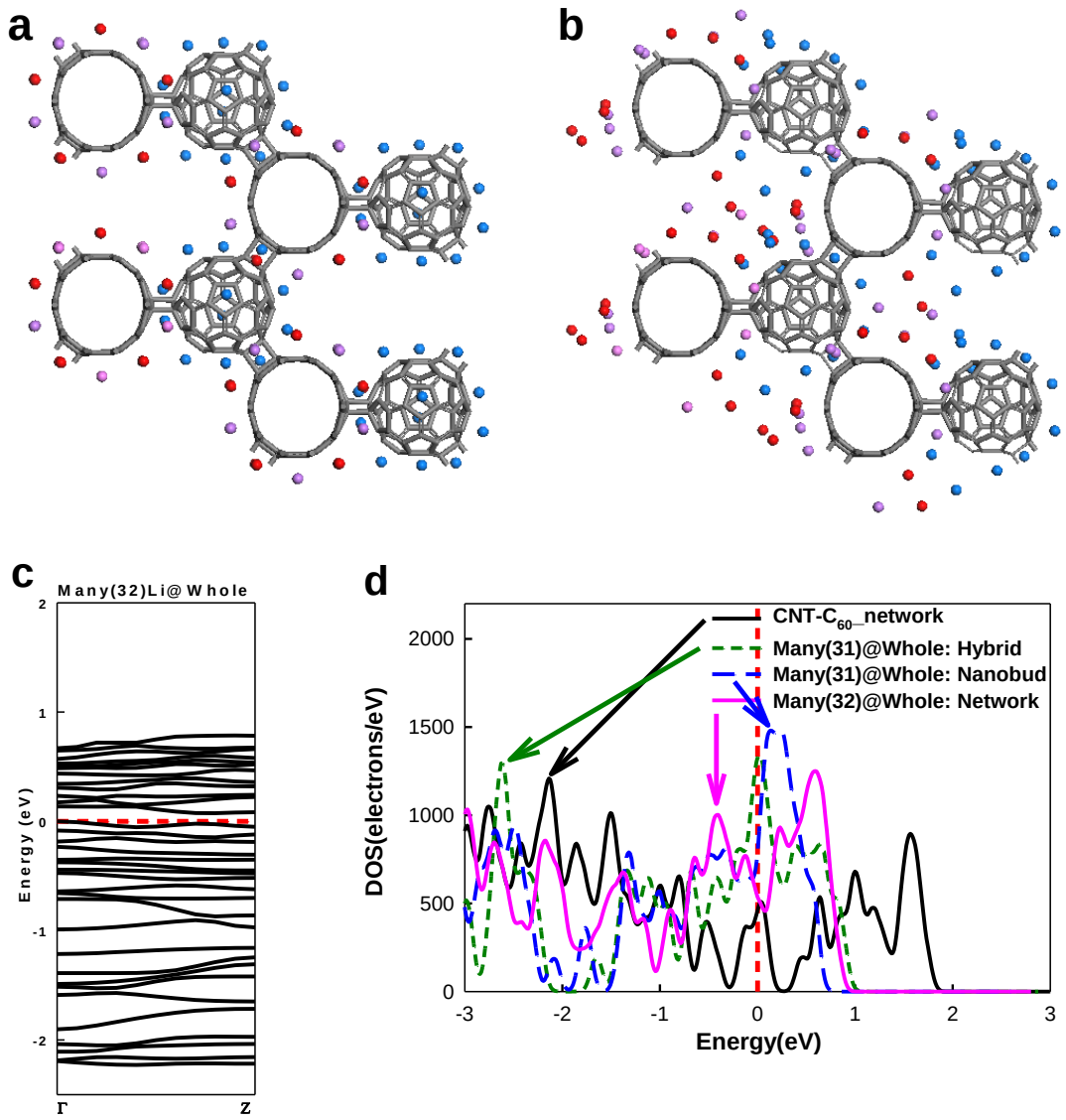

Figure 5.10: Multi-(32)Li atom adsorption on a whole network system: (a) initial structure; (b) optimized structure; (c) the corresponding band structure and (d) density of states (DOS) with pure and 32 Li atoms on a network system.

The corresponding band structure and DOS are displayed in Figures 5.10.c and d. The band appears to be entangled as other hybridized system that has many Li atoms due to the increased number of Li atoms, but it still shows a discrete band structure with a 0.07 eV band gap. The difference between the systems can also be observed in the DOS in Figure 5.10.d. The network system had fewer electrons across the Fermi level compared to other systems, although the states were continuously distributed over the Fermi level. Hence, many Li atoms need to be adsorbed to overcome the initial band gap to obtain metallic behaviors and utilize the material as an electrode.

5.4. Conclusion

In this chapter, we studied a 3D nano-network structure consisting of CNT and C_{60} using the DFT, which is simply the extended structure of the nanobud system formed by connecting CNT to C_{60}. We found that the mechanical strength of the network system was greatly increased, especially in the radial direction of the CNT axis, which is commonly known as being weak relative to the axial direction. The calculated Young's modulus in the radial direction was 70 GPa, which is larger than the Young's modulus for pure CNT (~ 4 GPa) in the same direction and demonstrated a large Young's modulus of 310 GPa in the axial direction. We found that the nano-network system was semiconducting with a band gap of 0.34 eV and increased its density of states (DOS) around the Fermi level as a result of the filling of the C_{60} band. The charge transfer from CNT to C_{60} was $|0.187|e$, which is slightly higher than the hybrid or nanobud systems in the condensed phase due to a smaller unit size of the network system. Furthermore, Li adsorption was also enhanced in the network system due to the condensed structure

enabling simultaneous interactions between CNT and C_{60}, and the adsorption energy in the two-Li atoms system was still low. In addition, Li adsorption will occur preferentially on the high electron affinity C_{60} side, but it will depend on the adsorption site and will not follow the N.N.N scheme. The adsorption energy of many Li-adsorbed systems is -1.655 eV, which is lower than the Li-Li binding energy. Therefore, network systems will provide appropriate structures for the Li adsorption. The band structure and DOS changes only slightly until many Li atoms are present in the system because the electronic properties of the nano-network system are influenced by C_{60}. DOS reflects this property because the initial states (before Li adsorption) near the Fermi level were higher than the hybrid or nanobud systems in the condensed phase. This is likely a result of the electrons in the CNT filling the semiconducting C_{60} bands after network formation (like doping) so that the additional Li atoms slightly affect the electronic property of the system. Hence, the nano-network system with its great mechanical strength can be used as an electrode for strong Li adsorption. Additionally, the nano-network system can be used to control the band gap by adjusting the C_{60} packing density and changing the electronic properties of the system.

CHAPTER 6

FIRST-PRINCIPLES STUDY OF LI ADSOPRTION ON CARBON GRAPHENE-FULLERENE HYBRID & NANOBUD SYSTEM

In this chapter, we investigate a graphene-C_{60} hybrid and a graphene-C_{60} nanobud system consisting of semi-metal graphene and semiconducting fullerene (C_{60}) to predict the performance and changes in electronic properties related to Li adsorption in the dilute or condensed phases.

6.1 Introduction

In the current field of secondary rechargeable batteries, a graphite anode has been widely adapted with a maximum specific insertion capacity of 372 mAh/g corresponding to the formation of LiC_6. However, it is expected that the capacity can increase from 500 to 1100 mAh/g if graphene is used instead of graphite because Li can be stored on both the surface and the edge of the graphene [117, 118]. In this context, various types of graphene, such as graphene powder, nanoribbons and nanosheets, have been studied both theoretically [119-127] and experimentally [128-130] to investigate the Li adsorption capacity for electrode applications. In addition, further studies have been performed to obtain improved Li or hydrogen adsorption by adjusting the thickness of the interlayer [121, 131].

Among those approaches, Gupta et al. have recently reported the synthesis and characterization of graphite intercalated by fullerene (C_{60}) [48]. In that paper, they found that fullerene forms a hexagonal two-dimensional lattice between the graphene layers,

and TEM indicates that no covalent bonds between fullerene and graphene or fullerenes are formed. Some theoretical [132-135] and experimental [48, 129, 136-138] studies have attempted to investigate the C_{60} intercalated graphene hybrid structure as well. Furthermore, Yoo et al. prepared the various hybrid structures on graphene nanosheets (GNS), producing GNS, GNS+CNT and GNS+C_{60} systems, and measured their lithium insertion/extraction properties. Their result showed that the specific capacities of GNS (540 mAh/g), GNS+CNT (730 mAh/g) and GNS+C_{60} (784 mAh/g) were increased compared to graphite (372 mAh/g), which may be attributed to the increased d-spacing (distance between layers). Hence, it is important to understand the electronic properties of the graphene-C_{60} hybrid structure in the presence of Li atoms for developing actual working devices. In this study, we investigated two types of hybridized material systems consisting of graphene and C_{60} to investigate Li adsorption capabilities: one is bound by weak van der Waals interaction (graphene-C_{60} hybrid), and the other is bound by covalent bonds (graphene-C_{60} nanobud). Investigating the electronic properties of the graphene-C_{60} hybridized system will also be useful because various studies have been accomplished to control the gap between graphene layers and increase hydrogen uptake to be used as hydrogen storage. Similar to the CNT-C_{60} hybrid structures, graphene-C_{60} hybrid systems utilize C_{60} as the electron acceptor from Li and graphene as the charge transport channel throughout the electrode. Therefore, it is expected that Li adsorption on the graphene-C_{60} electrode is more favorable than the pure graphene-based electrode because of the higher electron affinity of C_{60}.

In this study, we used the first-principles computational methods through DMol^3 from Accelrys [83, 84] to investigate electrochemical characteristics such as adsorption

capabilities and charge transfer of another interesting graphene-C_{60} hybrid system. We calculated the Li adsorption energy of the graphene-C_{60} hybrid system and the accompanied change in the electronic properties such as band structure, density of states (DOS) and charge distribution as a function of Li adsorption using the density functional theory (DFT). We also studied the mechanism of Li adsorption in comparison to Li cluster formation in the dilute or condensed phase by calculating the Li adsorption energy on the various regions around the graphene-C_{60} hybrid system.

6.2 Computational methods

We used generalized gradient approximation (GGA) Perdew-Burke-Ernzerhof (PBE) functional [41, 85] to treat the electron exchange-correlation energy of interaction electrons with double numerical basis and d-polarization functions basis set for all the DFT calculations, which is the same condition used for the CNT-C_{60} systems. The unit cell dimension was 12.3 Å × 12.3 Å × 35 Å, which is large enough to ensure that there was no direct interaction between original structure and its self-image in c-axis though the periodic boundary while the dimension in a- and b-axis is determined from the area of the graphene. The k-point samplings for the Brillouin zone were performed using the Monkhorst-Pack special k-point scheme in order to determine the adsorption energy and other electronic properties such as band structure, density of states and Mulliken charge distribution. We also tested k-point by calculating Li adsorption energy of sample system at different k-points as shown in the Figure 6.1.a, thus we performed the geometry optimization at the gamma point (denoted by 1x1) and then calculated all the electronic properties at 4x4x1 (denoted by 4x1). The adsorption of Li was performed at the center of hexagon sites (“Center”) in graphene among various sites (inset in Figure 6.1.b: Center,

Top, Bridge) and the pentagon/hexagon sites of C_{60} because these sites showed most stable adsorption energy from the Figure 6.1.b. The adsorption energies and electronic properties of the graphene-C_{60} system were compared with those of the pure graphene, carbon nanotube and the C_{60} face-centered cubic (fcc) crystal structure with (111) surface.

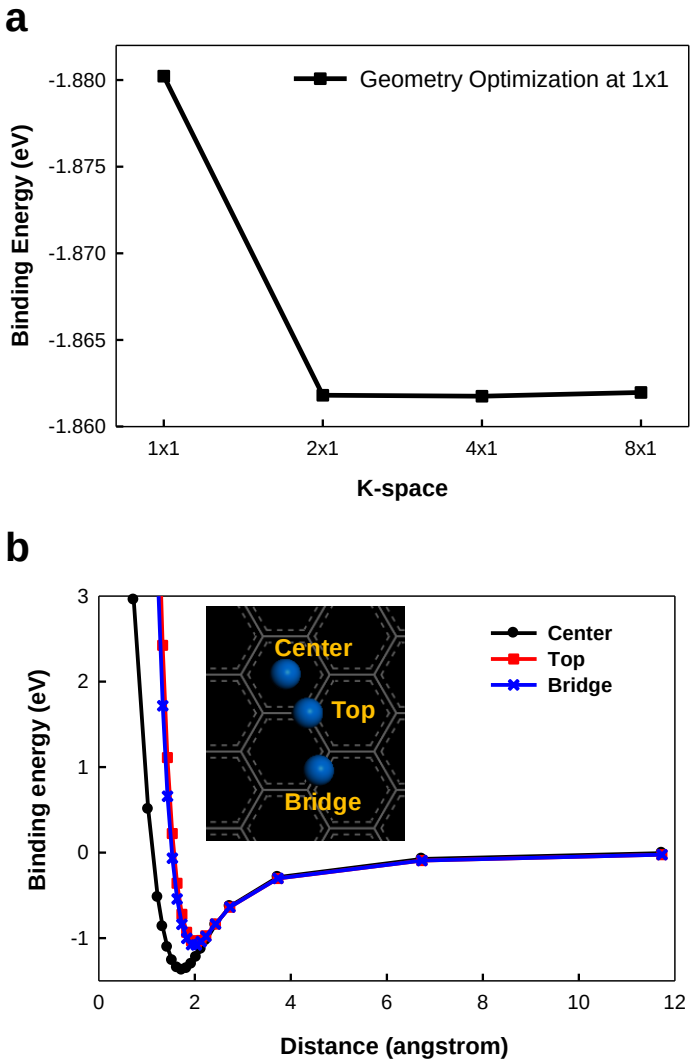

Figure 6.1: (a) Various k-space set samplings to one Li atom on (a) graphene-C_{60} hybrid system; (b) Single point energy calculation of the Li atom on the different positions of the hexagonal ring in the graphene of the function of the distance from the center of the graphene: center, top, bridge.

6.3 Graphene-C_{60} hybrid and graphene-C_{60} nanobud systems in the dilute phase

6.3.1. Pure Graphene-C_{60} hybrid and graphene-C_{60} nanobud systems

First, we fully optimized the geometry of the graphene-C_{60} hybrid and graphene-C_{60} nanobud systems before we studied the Li adsorption capabilities. Figures 6.2.a-c shows the top, side and expanded view of the hybrid system, which is maintained by dispersion interactions between graphene and C_{60}. The distance between graphene and the center of the C_{60} in the hybrid structure is set to 6.35 Å, which originates from an experimental value [48]. Alternatively, Figures 6.2.d, e, and f display the top, side and expanded views of the graphene-C_{60} nanobud system, respectively. In the case of the nanobud system, we prepared two structures connecting the C-C bonds in graphene (h) and two possible C-C bonds in the C_{60}: (i) a bond between two hexagonal faces (h) and (ii) a bond between a hexagonal and pentagonal face (p) via [2+2] cycloaddition as a CNT-C_{60} nanobud. Therefore, we prepared the hh and hp graphene-C_{60} structures and calculated the binding energy ($E_{binding} = E_{nanobud} - E_{graphene} - E_{C60}$) of these two structures. We found that the hh structure (2.632 eV) was preferred to the hp structure (3.319 eV) according to the binding energy even though both needed considerable energy to form the structure. We summarized the binding energy, bond length, charge transfer from graphene to C_{60} through Mulliken analysis and the band gap of the each hybrid structure in Table 6.1.

Table 6.1: Binding energy, bond length, Mulliken charge and band gap of the graphene-C_{60} hybrid and bud system

System	Binding energy (eV)	Bond length (Å)	Charges (e)		Band gap (eV)
			Graphene	C_{60}	
Graphene-C_{60} hybrid system	-0.720	N/A	0.095	-0.095	0
Graphene-C_{60} nanobud system:hh	2.632	1.637	0.059	-0.059	0
Graphene-C_{60} nanobud system:hp	3.319	1.652	0.103	-0.103	0.30

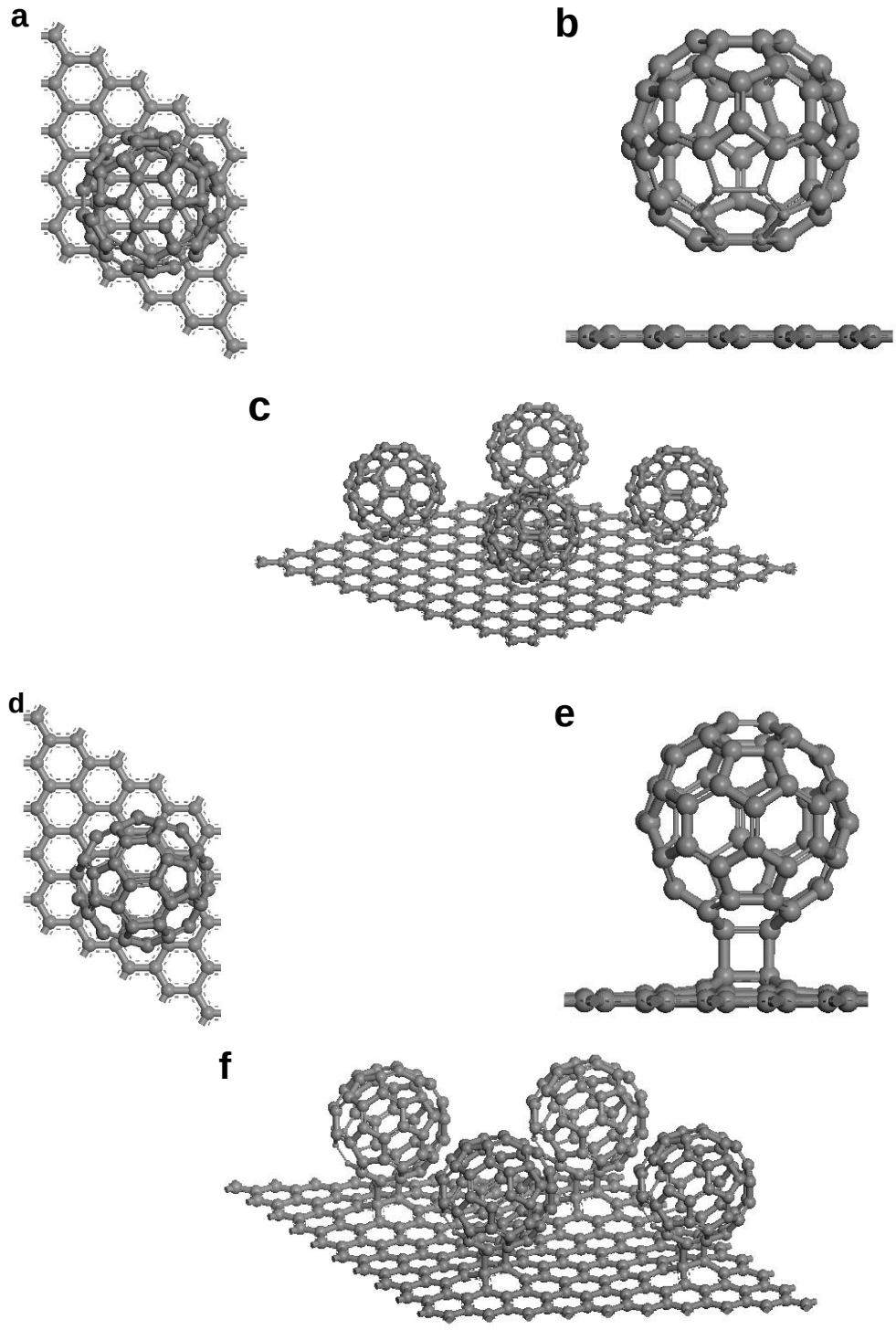

Figure 6.2: The unit cell structure of the graphene-C_{60} hybrid system: (a) top view; (b) side view; and (c) expanded (2x2) view. The graphene-C_{60} bud system: (d) top view; (e) side view; and (f) expanded view. The cell parameters are a=b=12.3 Å, c=35 Å, α=β=90º and γ = 120º.

As shown in the table, it appears that the hybrid structure was more favorable in terms of the binding energy (-0.720 eV) with considerable charge transfer ($|0.095|e$). However, extra energy was needed to form covalent bonds via *sp3* hybridization of carbon atoms to form nanobud structures. A narrow band gap of - 0.30 eV is developed in the middle of the hybridization between the orbital of the graphene and C_{60} when graphene is connected to the bond between pentagonal and hexagonal site in the C_{60}. The charge distribution of the system through Mulliken population analysis shows charge transfer from the graphene to fullerene for all of the systems due to the relatively strong electron affinity of C_{60}.

The band structure of the pure graphene, the pure C_{60}, the graphene-C_{60} hybrid and the graphene-C_{60} nanobud systems are represented in Figure 6.3. In these band structures, the Fermi levels are shifted to be located at 0 eV. Because the graphene-C_{60} hybrid system is also maintained by weak dispersion interactions, as in the CNT-C_{60} hybrid system, the hybrid system retains the characteristics of its components. Therefore, the two energy bands meet at the Fermi level (0 eV) and retain the character of the π orbital of the graphene while two other bands appear around ~ 0.56 eV, which may be attributed to the t_{1u} state of the neighboring C_{60} chain as shown in Figure 6.3.c [89]. However, the graphene-C_{60} nanobud system represents a unique band structure because of the covalent bond between graphene and C_{60}. Even the band structure is different depending on the C-C bond position, which can be attributed to the π bonds related to the reaction. Hence, the graphene-C_{60} nanobud:hh has a no band gap while the graphene-C_{60}:hp has an indirect band gap (0.30 eV) due to the different degree of the π bond character. We also examined the density of states (DOS) of both hybrid and nanobud

systems in Figure 6.4. Similar to the CNT-C_{60} hybrid system, the overall feature of the DOS in the graphene-C_{60} hybrid system is a product of the individual components, while the graphene-C_{60} nanobud system has different characteristics.

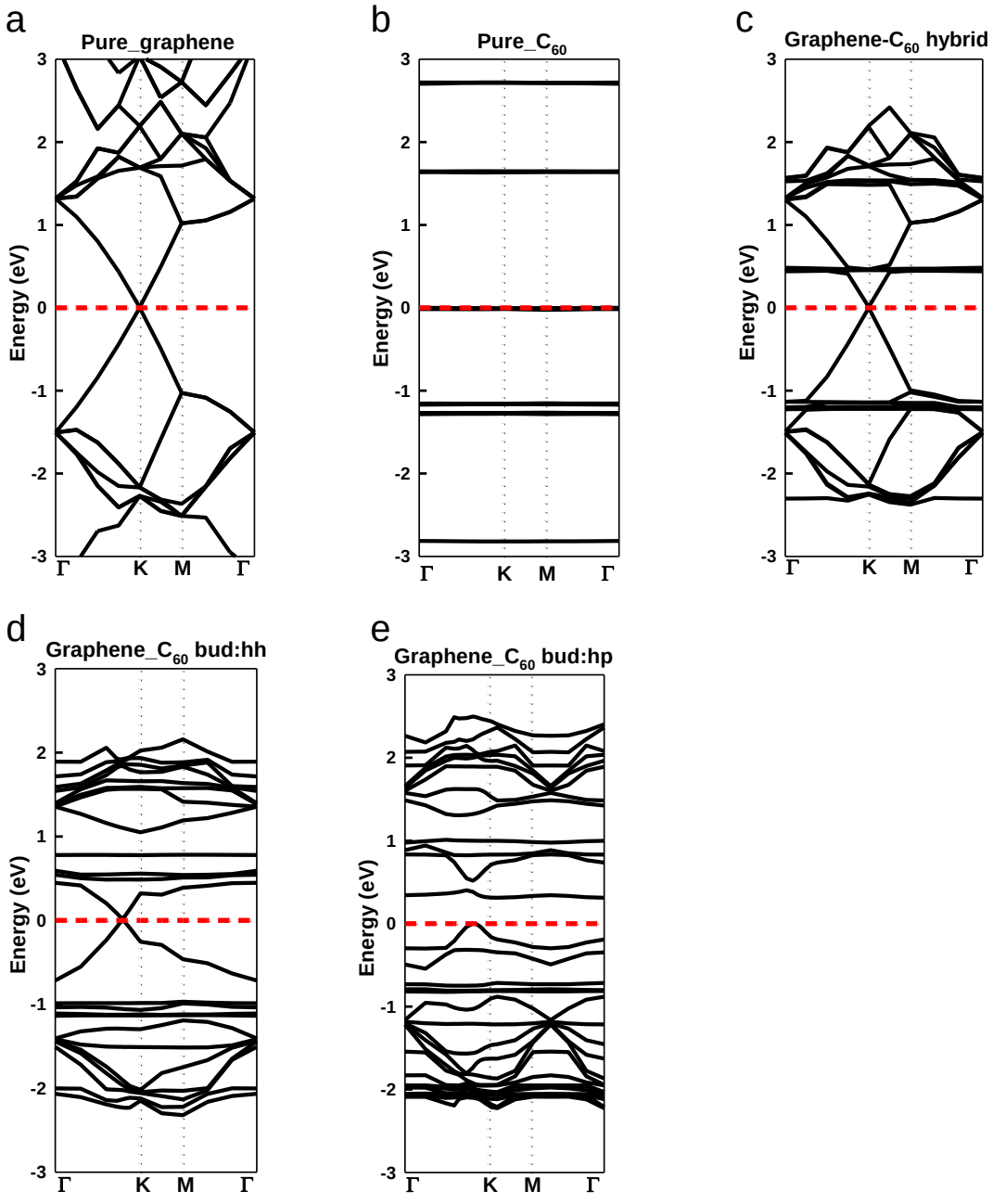

Figure 6.3: The band structure of (a) pure graphene; (b) pure C_{60}; (c) graphene-C_{60} hybrid; (d) graphene-C_{60} nanobud:hh; and (e) graphene-C_{60} nanobud:hp system (r= (0,0,0), K= (-1/3, 2/3, 0), and M= (0,1/2,0) in the Brillouin zone).

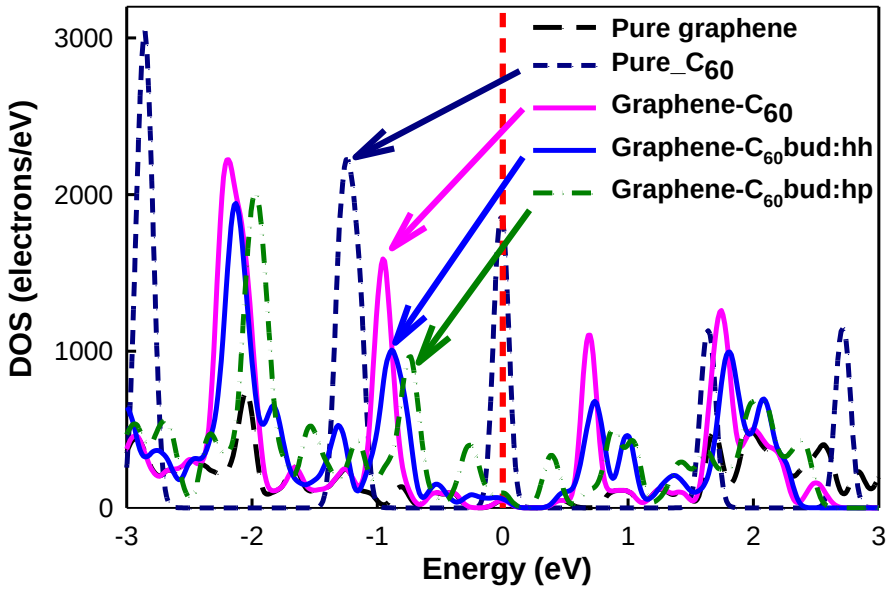

Figure 6.4: The density of states (DOS) of the pristine graphene, pristine C_{60}, graphene-C_{60} hybrid, graphene-C_{60} nanobud:hh and graphene-C_{60} nanobud:hp system.

However, it appears that the DOS of the graraphene-C_{60} nanobud: hh is similar to the DOS of the graphene-C_{60} hybrid system because the π bond in the nanobud:hh system is less distorted.

6.3.2 Single Li atom on graphene-C_{60} hybrid and graphene-C_{60} nanobud systems

Next, we studied the adsorption of Li on various positions of the graphene-C_{60} hybrid and nanobud systems. For this evaluation, we chose the graphene-C_{60} hybrid along with the nanobud:hh system because it required less energy (2.632 eV) to form the structure than the graphene-C_{60} nanobud:hp (3.319 eV) and because of the smaller band gap because; furthermore, we are interested in the electron conduction capabilities toward electrodes. Additionally, a Li atom is placed in the center of the hexagon site (center) of

graphene (Figure 6.1.b) and the pentagon [139] or hexagon site of C_{60} because these sites attain the most stable Li adsorption in the C_{60} as previously explained.

To describe the Li adsorption mechanism on the graphene-C_{60} hybrid system more systematically, we again defined four distinct regions around the graphene-C_{60} hybrid and nanobud system as shown in Figures 6.5.a-b: (i) graphene side (region 1, red), (ii) between graphene and C_{60} (region 2, yellow), (iii) between C_{60}s (region 3, blue) and (iv) C_{60} side (region 4, orange). The Li atom can interact only with the graphene in region 1 or only the C_{60} in region 3 and region 4, while it can interact with both graphene and C_{60} simultaneously in region 2.

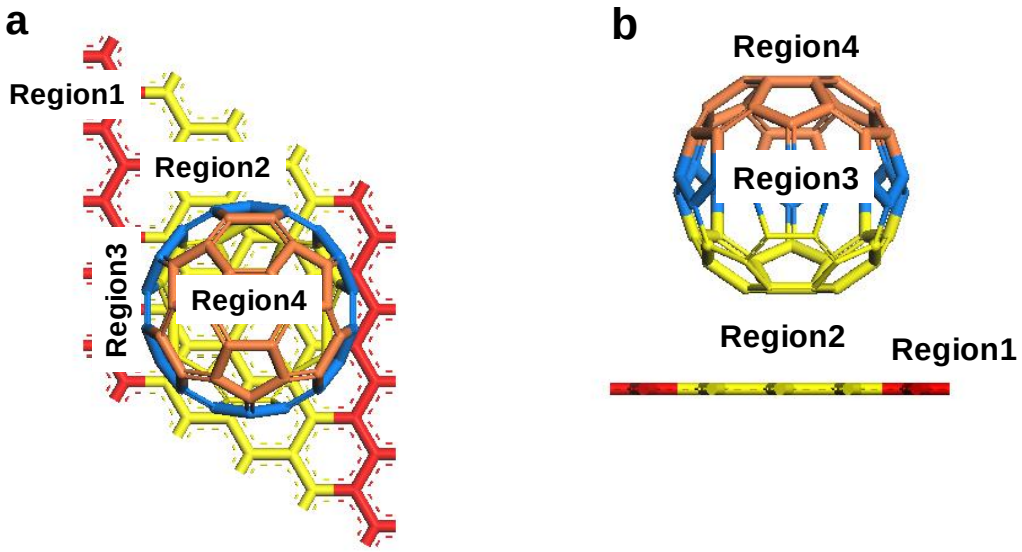

Figure 6.5: The structure of the graphene-C_{60} hybrid system with different regions: (a) front view; (b) side view; Region 1-red, Region 2-yellow, Region 3-blue and Region 4-orange.

We placed one-Li atom on various positions at each region around the graphene-C_{60} hybrid and nanobud systems as shown in Figures 6.6 and 6.7. We also summarize the adsorption energy and charge distribution of the one-Li adsorbed system on the hybrid

and nanobud system in Tables 6.2 and 6.3, respectively. From the table, we observed that Li adsorption (-1.769 eV) in graphene@hybrid was enhanced compared to the pure graphene system (-1.375 eV). It appears that this enhancement could be explained by the charge distribution of the CNT-C_{60} hybrid system and the unit structure of the hybrid system.

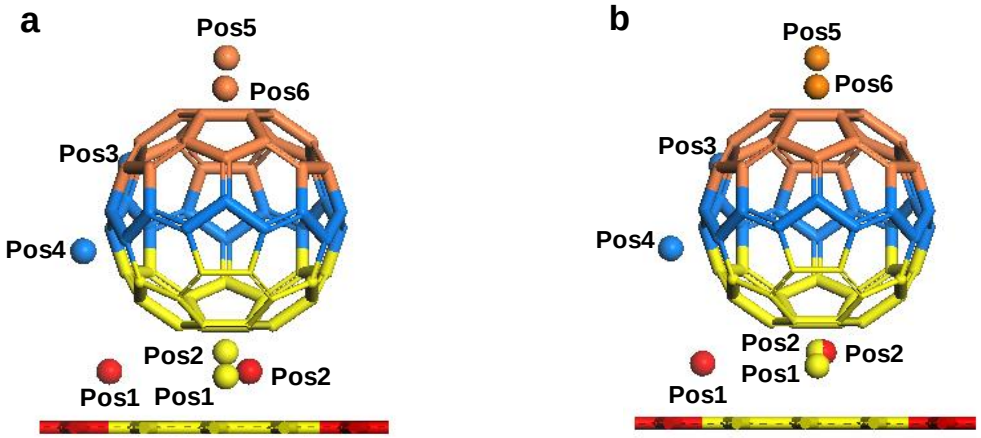

Figure 6.6: One-Li adsorption on various positions around a graphene-C_{60} hybrid system: (a) initial and (b) optimized structure.

Table 6.2: The adsorption energy and charge distribution (Mulliken charge) of one-Li atom on the graphene-C_{60} hybrid system

System	Adsorption Energy (eV)	Charges (e)		
		Li	graphene	C_{60}
graphene-C_{60} hybrid	N/A	N/A	0.095	-0.095
1 Li on graphene	-1.375 (-1.096 [120])	0.813	-0.813	N/A
1 Li on C_{60} (pentagon)	-1.838 (-1.820 [91])	0.794	N/A	-0.794
Pos1_graphene@hybrid (region1)	-1.769	0.860	-0.434	-0.426
Pos2_ graphene @hybrid(region2)	-2.285	0.894	-0.264	-0.630
Pos1_C_{60}@ hybrid (region2_hexa)	-1.059	1.002	-0.297	-0.705
Pos2_C_{60}@ hybrid (region2_penta)	-2.285	0.895	-0.259	-0.636

Table 6.2 continued

Pos3_C_{60}@ hybrid (region3_hexa)	-1.960	0.845	0.037	-0.882
Pos4_C_{60}@ hybrid (region3_penta)	-2.122	0.854	-0.007	-0.847
Pos5_C_{60}@hybrid (region4_hexa)	-1.798	0.794	0.025	-0.819
Pos6_C_{60}@ hybrid (region4_penta)	-1.862	0.791	0.032	-0.823

In other words, some of the charges ($|0.095|e$) are already transferred from the graphene to C_{60} making the graphene positively charged. Thus, the additional charge transfer from the adsorbed Li may occur to a greater extent in the graphene@hybrid and can contribute to the enhanced adsorption in the graphene@hybrid. At the same time, a Li atom in region 1 can still interact with C_{60} due to the planar structure of graphene and the size of the unit structure of the graphene-C_{60} hybrid system. Li atoms in region 1 of the CNT-C_{60} hybrid system were unavailable to the C_{60}. We can confirm this interaction through the amount of charge transfer to C_{60} (-0.426*e*), which is comparable to the amount in graphene (-0.434*e*). The Li atom at the Pos2@graphene moved to the same position as the Pos2@C_{60} after optimization, although the initial positions of these two atoms were different. The adsorption energy showed lower values in the middle of the graphene and C_{60} (region 2; -2.285 eV) or between C_{60}s (region 3; -2.122 eV). However, there was only a slight change in the adsorption energy in region 4 compared to the Li adsorption energy in pure C_{60} (-1.798 eV and -1.862 eV, respectively) even though this value was still lower than that of region 1. From these results, it appears that Li adsorption and the charge transfer are driven by the high electron affinity C_{60} in the hybrid system.

In the same manner, we defined the four different regions in the graphene-C_{60} nanobud system, placed Li atoms on each region as represented in Figure 6.7 and calculated the adsorption energy and charge distribution listed in Table 6.3. Overall adsorption energy was similar to the value in the hybrid system, and most of the Li atoms maintained their original position. However, the Li atom near to C_{60} (Pos2@graphene) clearly moved closer to the C_{60} while the Li atoms initially placed closer to the C-C bond in the junction (Pos1,2@C_{60}) were repelled, which was observed in the CNT-C_{60} nanobud.

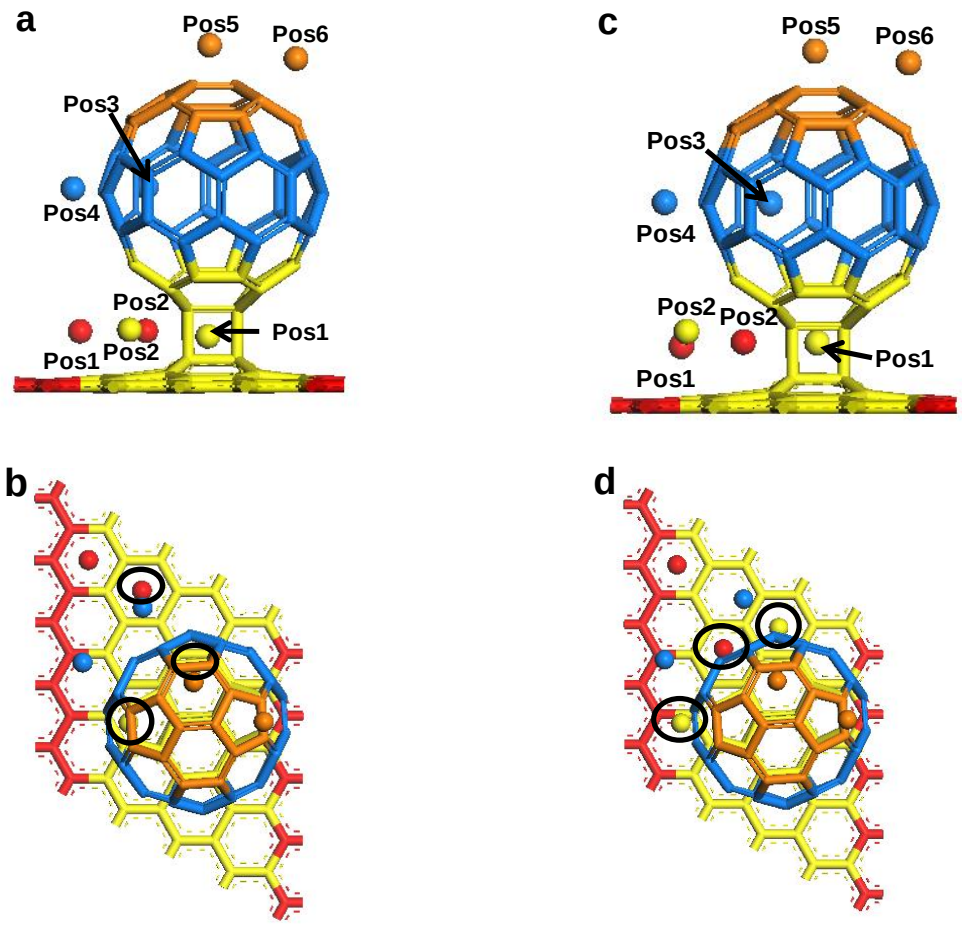

Figure 6.7: One-Li adsorption on various positions around the graphene-C_{60} nanobud system: initial structure (a) side view and (b) top view; optimized structure (c) side view and (d) top view.

Table 6.3: The adsorption energy and charge distribution (Mulliken charge) of one-Li atom on the graphene-C_{60} nanobud system

System	Adsorption Energy (eV)	Charges (e)		
		Li	graphene	C_{60}
graphene-C_{60} nanobud:hh	N/A	N/A	0.059	-0.059
Pos1_graphene@nanobud (region1)	-1.905	0.858	-0.524	-0.334
Pos2_ graphene @nanobud (region2)	-2.346	0.863	-0.428	-0.435
Pos1_C_{60}@nanobud (region2_hex)	-2.345	0.871	-0.427	-0.444
Pos2_C_{60}@nanobud (region2_penta)	-2.182	0.856	-0.477	-0.379
Pos3_C_{60}@nanobud (region3_hexa)	-2.002	0.856	-0.028	-0.828
Pos4_C_{60}@nanobud (region3_penta)	-2.158	0.865	-0.025	-0.840
Pos5_C_{60}@nanobud (region4_hexa)	-1.784	0.800	-0.015	-0.785
Pos6_C_{60}@nanobud (region4_penta)	-1.840	0.785	-0.011	-0.774

This may be attributed to the strong covalent bond between graphene and C_{60}, which may prevent Li from forming the bond with carbon atoms in the system and keep it out of the junction. The adsorption energy was also low near the graphene-C_{60} (region 2; -2.345 eV) and between C_{60}s (region 3; -2.158 eV) due to the strong electron affinity of C_{60}. Through this adsorption, the amount of charge transfer from the adsorbed Li to the graphene-C_{60} nanobud system ranged from 0.785*e* to 0.871*e* depending on the Li positions. The corresponding band structures of the one-Li adsorbed hybrid and nanobud system are represented in the Figures 6.8 and 6.9, respectively. The band structures of both systems

did not change in comparison to the pure systems. However, the bands are significantly shifted downward when Li atom is adsorbed to the C_{60}@hybrid or C_{60}@nanobud side.

6.3.3 Multiple Li atom on graphene-C_{60} hybrid and graphene-C_{60} nanobud system

We added Li atoms at various sites in each region starting from the first Li atoms, which had the lowest energy in the region, to investigate the Li adsorption mechanism.

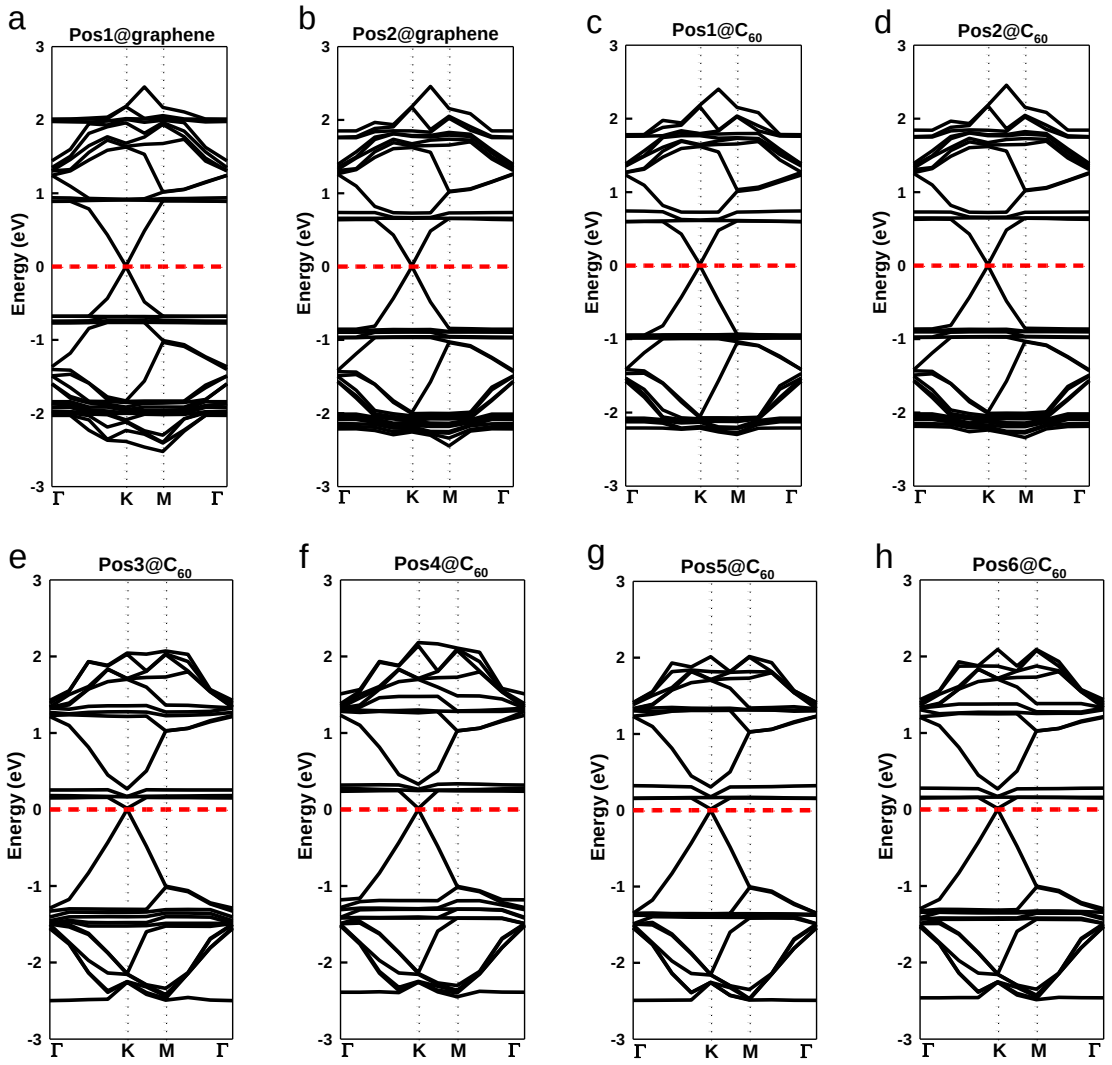

Figure 6.8: The band structures of one-Li adsorption on various positions on the graphene-C_{60} hybrid system: (a) Pos1@graphene; (b) Pos2@graphene; (c) Pos1@C_{60}; (d) Pos2@C_{60}; (e) Pos3@C_{60}; (f) Pos4@C_{60}; (g) Pos5@C_{60}; and (h) Pos6@C_{60}.

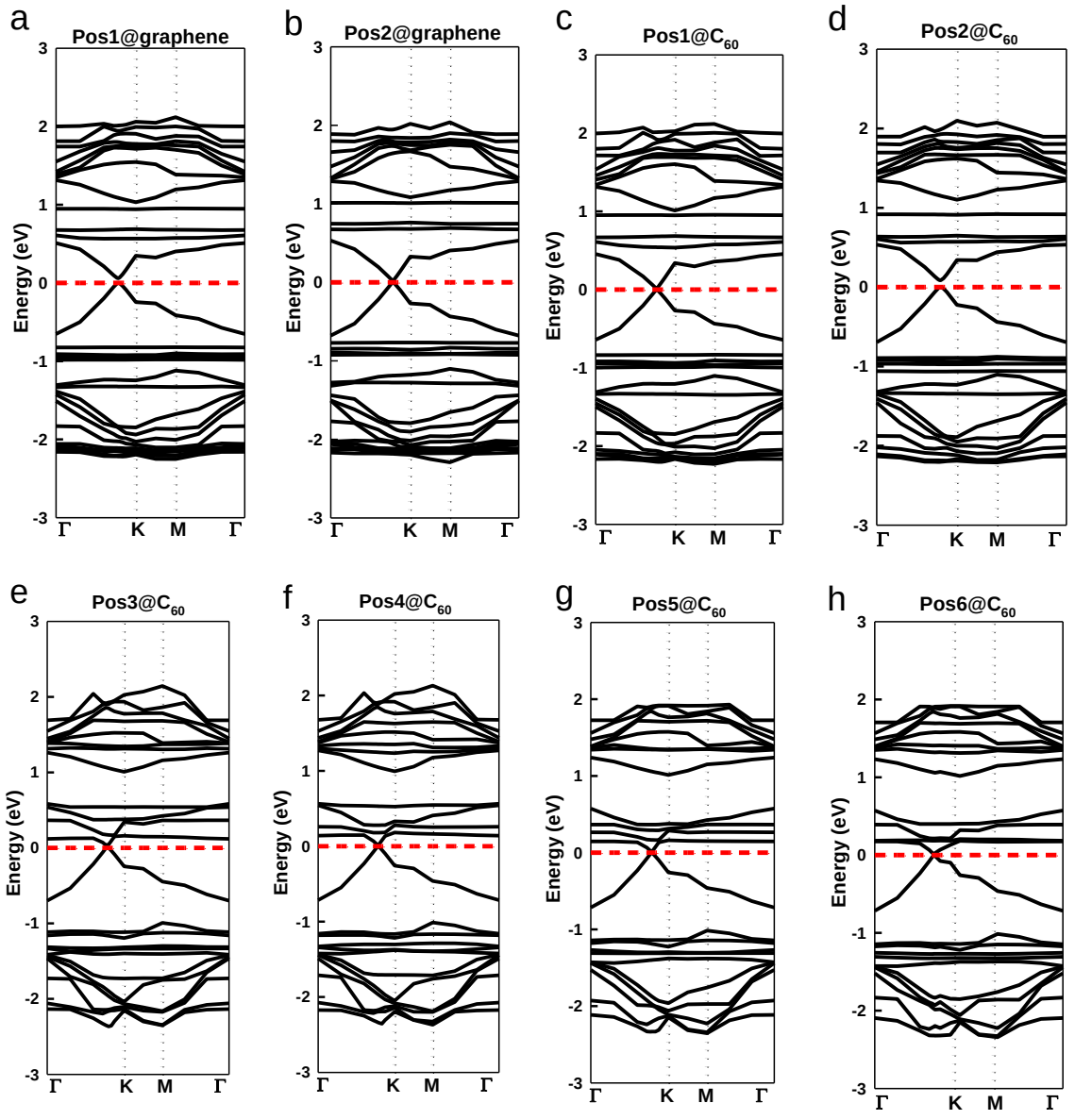

Figure 6.9: The band structures of one-Li adsorption on various positions on the graphene-C_{60} nanobud system: (a) Pos1@graphene; (b) Pos2@graphene; (c) Pos1@C_{60}; (d) Pos2@C_{60}; (e) Pos3@C_{60}; (f) Pos4@C_{60}; (g) Pos5@C_{60} and (h) Pos6@C_{60}.

Because the energy density was proportional to the number of Li atoms, it is very important to efficiently utilize the surface provided by the graphene- C_{60} electrode instead of forming Li-Li clusters. Moreover, Li capacity could be maximized by covering all of

the carbon rings of the graphene-C_{60} system with Li atoms. Therefore, systematic experiments were warranted to predict the adsorption direction on the hybrid and nanobud systems from various adsorption sites. For this purpose, we provided the second Li atom (blue) with respect to the first Li atom (purple) having the lowest energy in each region of the hybrid and nanobud systems. We also followed the definition in the previous chapters about positioning the second Li atom at either the nearest neighboring (N.N.) site or the next nearest neighboring (N.N.N.) site in the axis of the graphene surface in graphene@hybrid/nanobud (Figure 6.10.a). We also assumed that the second Li atom was adsorbed on the pentagonal or hexagonal ring in the C_{60}@hybrid/nanobud in the radial or axial direction along the axis of graphene to form the N.N. or the N.N.N. configuration (Figure 6.10.b).

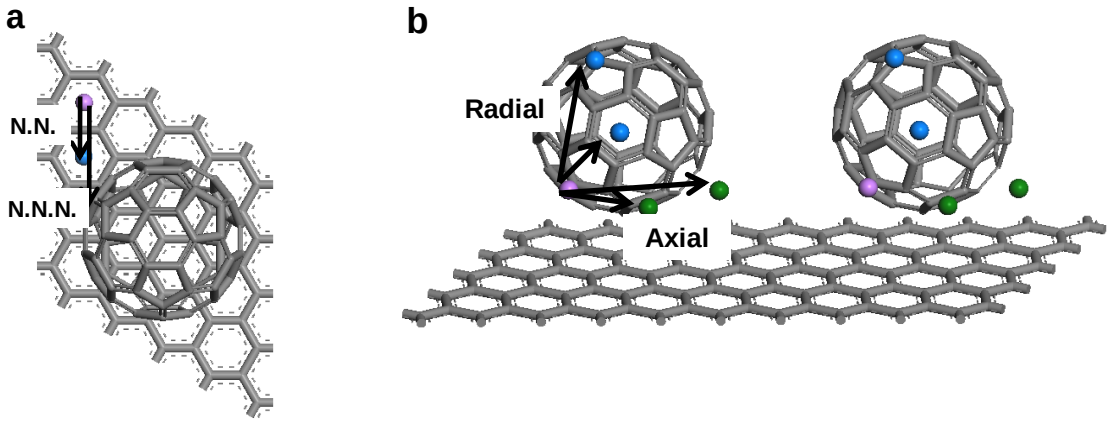

Figure 6.10: Definition of the second Li atom adsorption direction on the two-Li atom system around (a) graphene@hybird and (b) C_{60}@hybrid (1st Li atom: purple and 2nd Li atom: blue or green).

The initial and optimized structures of the two-Li adsorbed system in different regions on the graphene-C_{60} hybrid and nanobud system are displayed in Figures 6.11

and 6.12, respectively. The Li adsorption energies of the two Li atoms calculated using equation (3.1) are listed in Tables 6.4 and 6.5.

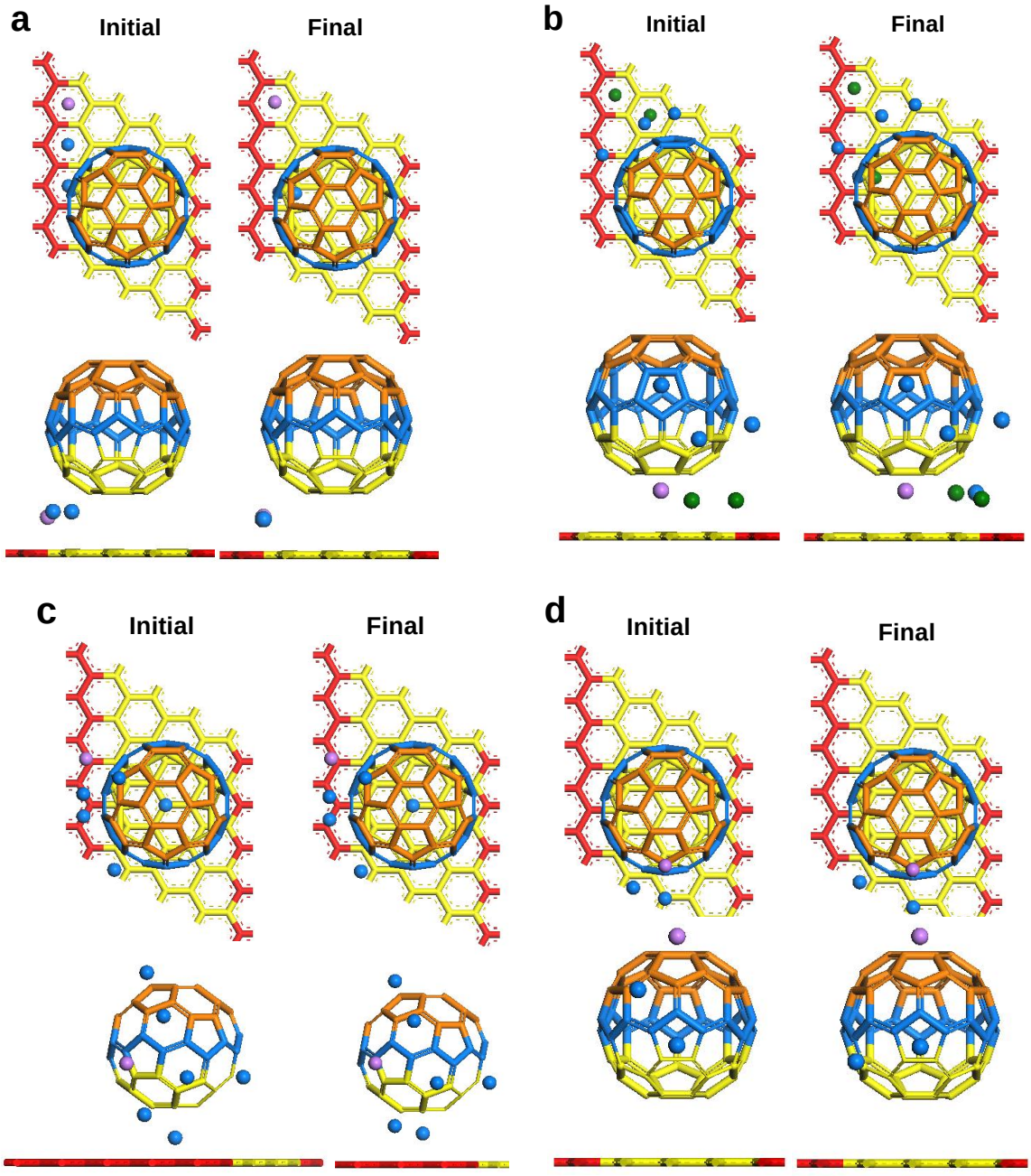

Figure 6.11: The initial and optimized structure of two-Li adsorption on a graphene-C_{60} hybrid in different regions: (a) region 1; (b) region 2; (c) region 3 and (d) region 4 (1^{st} Li atom: purple and 2^{nd} Li atom: blue or green).

Table 6.4: The adsorption energy of two- Li aomts adsorption on the graphene-C_{60} hybrid system

System	Adsorption Energy (eV)
2 Li on region1: N.N.N. site	-1.874
2 Li on region1: N.N. site	-1.873
2 Li on region2: Axial (N.N.N. site)	-2.168
2 Li on region2: Axial (N.N. site)	-2.155
2 Li on region2: Radial (N.N.N. site)	-2.178
2 Li on region2 to region1: N.N.N. site	-1.888
2 Li on region2 to region1: N.N. site	-2.154
2 Li on region3: Axial (N.N.N. site)	-1.986
2 Li on region3: Axial (N.N. site)	-1.920
2 Li on region3 to region2: N.N.N. site	-1.559
2 Li on region3 to region2:N.N. site	-2.066
2 Li on region3 to region4: N.N.N. site	-1.969
2 Li on region3 to region4:N.N. site	-1.891
2 Li on region4: Radial (N.N.N. site)	-1.971
2 Li on region4: Radial (N.N. site)	-1.899
8 Li atoms on graphene@hybrid	-1.511
12 Li atoms on C_{60}@hybrid	-1.779
20 Li atoms on graphene-C_{60} hybrid	-1.624
Li-Li (experiment / theory:Dmol^3)	-1.030[92] / -1.008

In region 1 of the hybrid systems (Figure 6.11.a), the adsorption energy is the same for both N.N.N. and N.N. schemes because both second Li atoms moved to the strong electron affinity C_{60}. Furthermore, the Li adsorption energy (-1.874 eV) was lowered compared to the one-Li system (-1.769 eV) even though the adsorption energy usually increased as the number of Li atoms increased. This is again related to the size of the unit structure because both Li atoms are strongly affected in the presence of C_{60}; the adsorption is even lowered in two-Li systems. The adsorption energy was the lowest (Figure 6.11.b, -2.154 eV ~ -2. 178 eV) in region 2 through simultaneous interaction with both components; therefore, it had similar value, and it appeared that adsorption was independent of the adsorption sites compared to other regions. We also examined the adsorption direction by comparing the adsorption energy of two-Li system starting from Pos2@C_{60} (region 2) to another site in C_{60} or to graphene assuming the N.N.N. scheme. The energy toward C_{60} (-2.154 eV) was lower than graphene (-1.888 eV) as we expected because C_{60} usually provides strong adsorption sites through its strong electron affinity. Therefore, we can confirm again that Li will cover the C_{60} surface first. The adsorption energy in region 3 (between C_{60}s) was also low, ranging from -1.891 ~ -2.066 eV due to the strong electron affinity of C_{60}. It appears that the adsorption energy of the N.N.N. scheme was slightly low although the adsorption energy value was similar to the other directions. In region 4, the adsorption energy was calculated as -1.971 eV for the pentagonal site (Figure 6.11.d, N.N.N. site) and -1.899 eV for the hexagonal site (N.N. site), which suggests that the Li adsorption will take place using the N.N.N. sites of the pentagon site for C_{60}. It appears that Li adsorption preferred the N.N.N. scheme; however, its dependence was weaker than the CNT-C_{60} hybrid system when we considered both

the unit size of the system and the planar structure of the graphene. The Li adsorption mechanism is strongly influenced by C_{60}. Therefore, Li adsorption will start from C_{60} and proceed to the graphene in the direction that maximizes the exposure to C_{60}.

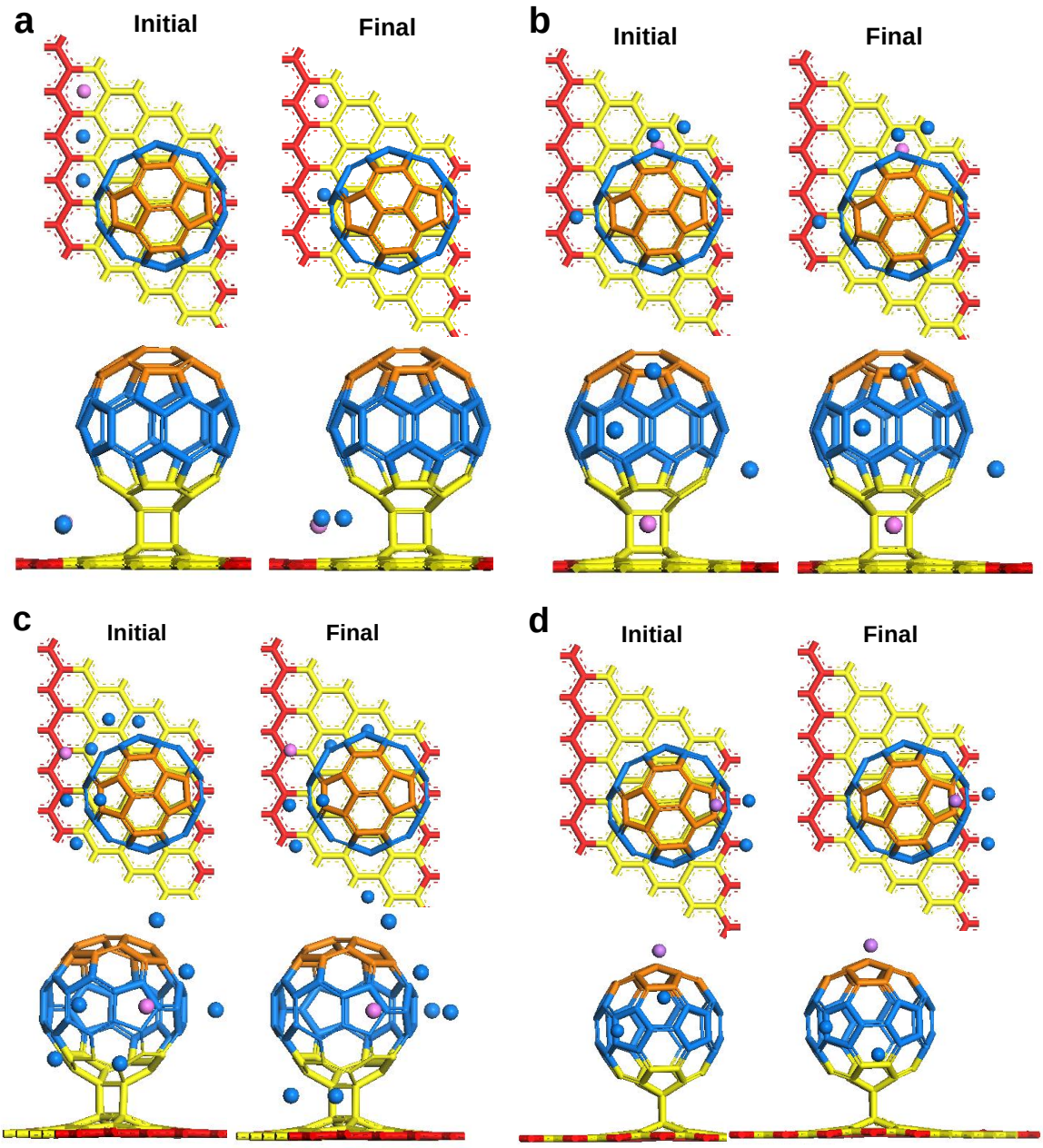

Figure 6.12: The initial and optimized structures of two-Li adsorption on graphene-C_{60} nanobuds in different regions: (a) region 1; (b) region 2; (c) region 3; and (d) region 4 (1st Li atom: purple and 2nd Li atom: blue or green).

Table 6.5: The adsorption energy of two- Li aomts adsorption on the graphene-C_{60} nanobud system

System	Adsorption Energy (eV)
2 Li on region1: N.N.N. site	-1.971
2 Li on region1: N.N. site	-1.972
2 Li on region2: Radial (N.N.N. site)	-2.141
2 Li on region2: Radial (N.N. site)	-2.133
2 Li on region2: Axial (N.N. site)	-2.109
2 Li on region3: Axial (N.N.N. site)	-2.130
2 Li on region3: Axial (N.N. site)	-2.091
2 Li on region3 to region2: N.N.N. site	-2.229
2 Li on region3 to region2:N.N. site	-2.199
2 Li on region3 to region4: N.N.N. site	-1.984
2 Li on region3 to region4:N.N. site	-1.943
2 Li on region4: Radial (N.N.N. site)	-1.987
2 Li on region4: Radial (N.N. site)	-1.905
18 Li atoms on graphene-C_{60} nanobud	-1.684

The Li adsorption mechanism on the graphene-C_{60} nanobud also follows the hybrid system with only slight differences. Therefore, two-Li adsorption in region 1 results in the same adsorption energy using either the N.N.N. scheme (-1.971 eV) or the N.N. scheme (-1.972 eV). The N.N.N. scheme (-1.987 eV) is slightly preferred to the N.N. scheme (-1.905 eV) in region 4. The two-Li adsorption energy is also low in region 2 and

region 3, ranging from -1.943 eV to -2.229 eV. It appears that there is no apparent site dependency in these regions although the N.N.N. scheme was slightly lower than the N.N. scheme in both regions. Hence, the Li adsorption driven by C_{60} will occur on the entire C_{60} surface before proceeding to the graphene sites on the graphene-C_{60} nanobud system.

We also checked the corresponding changes in the band structures of some two-Li atom systems in each region at the graphene-C_{60} hybrid and nanobud system as shown in Figures 6.13 and 6.14, respectively. From the table, we observed a significant band shift whenever another Li atom was added to both systems compared to the one-Li adsorption. The bands in close proximity to the additional Li were mainly affected and shifted down through increased Fermi levels as electrons were injected from the Li atoms into the system.

Finally, we added many Li atoms around both systems based on the N.N.N. scheme. We added 8 Li atoms at only graphene@hybrid sites, 12 Li atoms at C_{60}@hybrid, 20 atoms at whole@hybrid or 18 atoms at whole@nanobud. We also prepared the pure graphene and C_{60} having the same number of Li atoms for comparison. The initial structure and optimized systems are presented in Figure 6.15, and adsorption energies are listed in Tables 6.4 and 6.5. From the optimized structures, we observed that Li atoms initially attached to the graphene@hybrid or graphene@nanobud sites (Figures 6.15.a, c, and d) and were attracted toward the C_{60} as a CNT-C_{60} system. However, Li atoms around C_{60}, as shown in Figures 6.15.b and c, retained their positions.

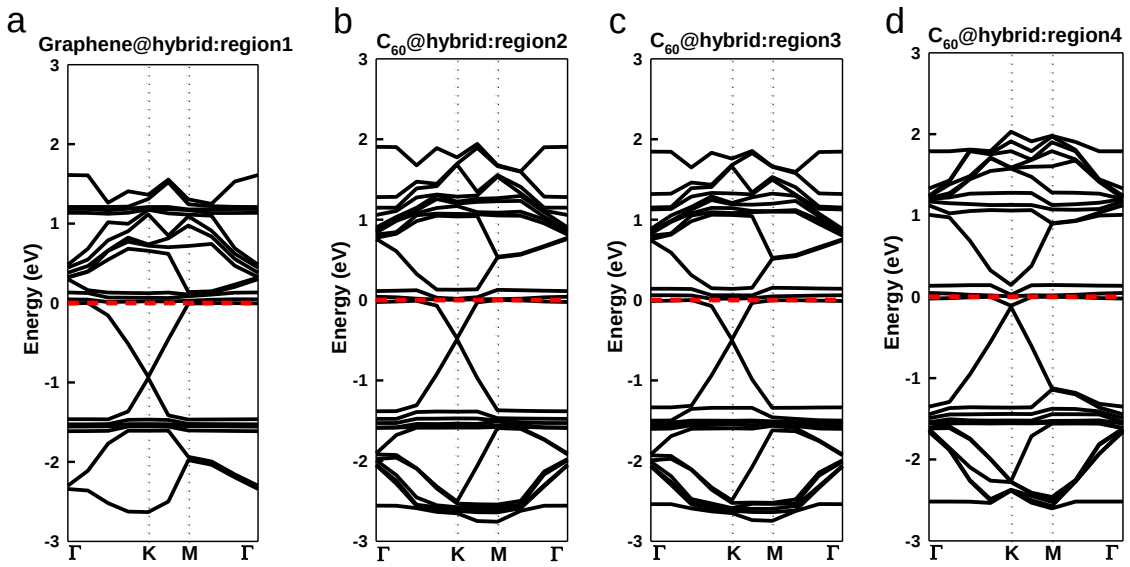

Figure 6.13: The band structures of two-Li adsorption in different regions on the graphene-C_{60} hybrid system: (a) region 1; (b) region 2; (c) region 3; and (d) region 4.

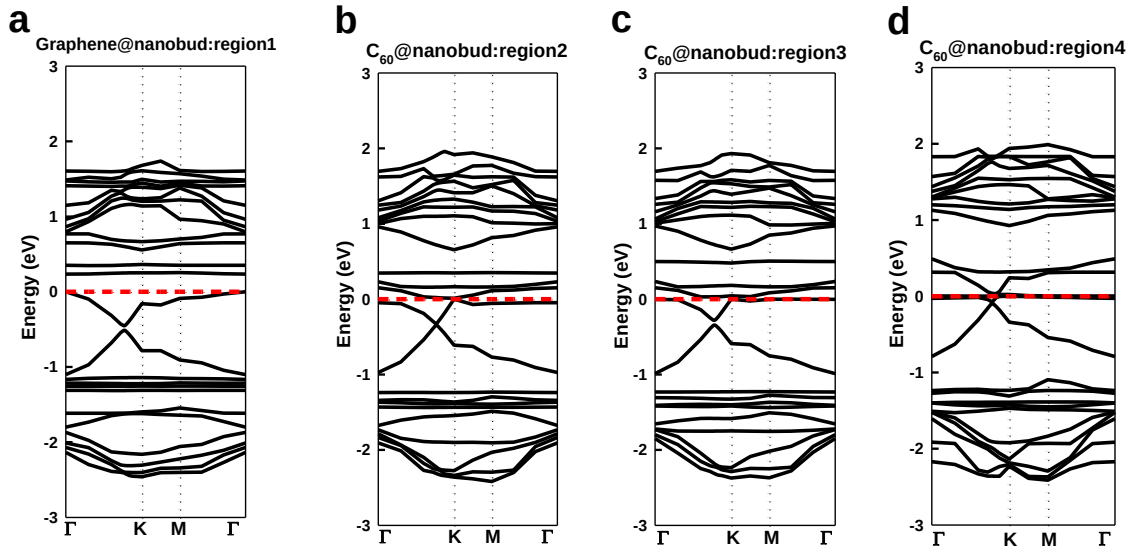

Figure 6.14: The band structure of two-Li adsorption in different regions on the graphene-C_{60} nanobud system: (a) region 1; (b) region 2; (c) region 3; and (d) region 4.

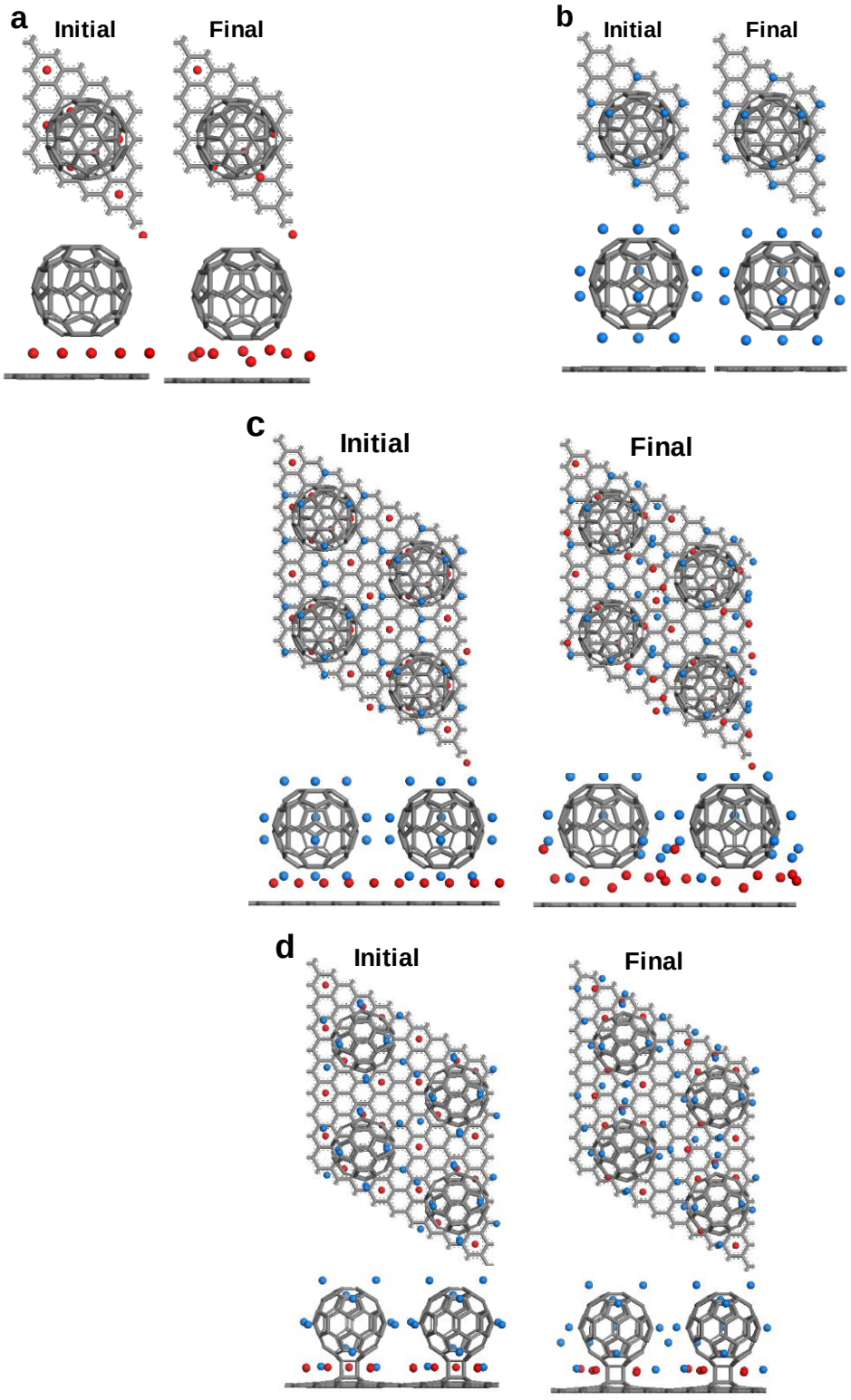

Figure 6.15: Initial and optimized structures on multi-Li systems: (a) 8 Li atoms on graphene@hybrid; (b) 12 Li on atoms on C_{60}@hybrid; (c) 20 Li atoms on whole@hybrid; and (d) 18 Li atoms on whole@nanobud.

Adsorption energies for the multiple Li adsorption are -1.511 eV for graphene@hybrid, -1.776 eV for C_{60}@hybrid, -1.621 eV for the entire hybrid system and -1.684 eV for the entire nanobud system. These adsorption energies indicate that Li adsorption will take place on the C_{60} side until all of the available sites on the C_{60} are completely filled before proceeding to the sites on the graphene as found from the two-Li adsorption. Even though the Li adsorption energy decreases with an increasing number of Li atoms, all of these adsorption energies are lower than the Li-Li binding energy (-1.030 eV [92]). Therefore, Li cluster formation is not likely to occur until all of the available sites on the graphene-C_{60} hybrid or nanobud systems are covered. Also, the binding energy is still lower than that of pure graphene (-1.086 eV) and C_{60} (-1.594 eV) systems having the same number of Li atoms. Therefore, graphene-C_{60} hybrid or nanobud systems appear to be promising for use as a possible electrode for Li batteries in terms of Li adsorption.

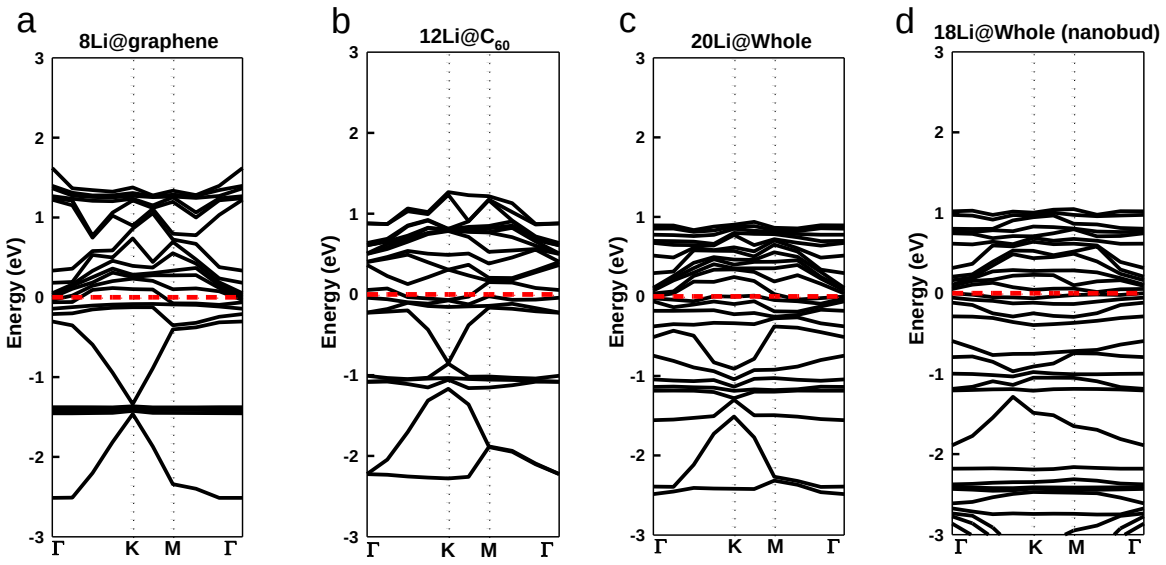

Figure 6.16: The band structure of multi-Li adsorbed systems; (a) 8 Li atoms on graphene@hybrid; (b) 12 Li on atoms on C_{60}@hybrid; (c) 20 Li atoms on whole@hybrid; and (d) 18 Li atoms on whole@nanobud.

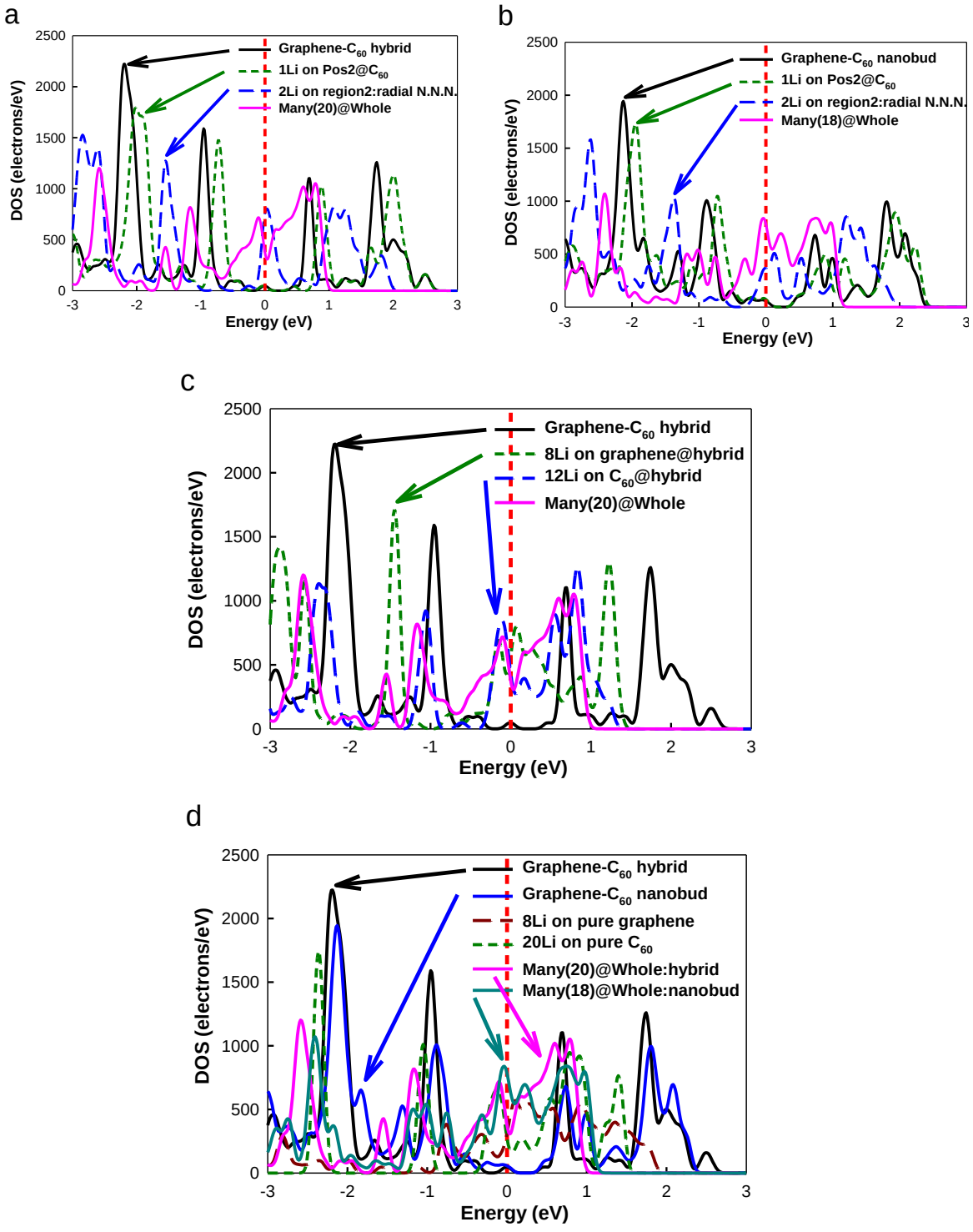

Figure 6.17: Density of states for various numbers of Li atoms adsorbed on (a) a graphene-C_{60} hybrid system; (b) a graphene-C_{60} nanobud system; (c) multi-Li on different sides of the hybrid system; and (d) comparison with the DOS of pure graphene, C_{60}, hybrid and nanobud systems.

Figure 6.16 shows the band structure of the multiple-Li adsorbed graphene-C_{60} systems. From the band structure, we observed that the number of available energy bands around the Fermi level increased significantly in the graphene-C_{60} systems, which indicates that Li adsorption enhances the metallic characteristics of the system, such as conductivity. This result was confirmed by the DOS as shown in Figures 6.17.a and b, which was as a function of the number of Li atoms. In the figure, the Li adsorbed systems have more DOS around the Fermi level, especially after more than two Li atoms are adsorbed on the system compared to the pure graphene-C_{60} hybrid system. It indicates the enhanced metallic character of the graphene-C_{60} system and it could contribute to increases in the system's electron transport properties. Finally, we compared the DOS of the graphene-C_{60} hybrid and nanobud system with pure graphene or pure C_{60} systems to examine the effect of Li adsorption on the electronic structure of the hybrid and nanobud systems. As shown in Figure 6.17.d, the DOS of the hybrid and nanobud systems apparently retains more electrons around the Fermi level than pristine graphene and C_{60}, which indicates that the hybrid/nanobud system could be more conductive than a pure graphene or C_{60} system after Li adsorption.

6.4 Graphene-C_{60} hybrid and nanobud systems in the condensed phase

6.4.1 Pure graphene-C_{60} hybrid and nanobud system in the condensed phase

We also investigated a graphene-C_{60} hybrid and nanobud system in the condensed phase by allowing interactions between each component, which is expected to affect the adsorption energy of the Li atom. We used an experimentally determined distance between graphene and C_{60} (6.35 Å) [48] to generate a condensed structure in both systems. Both structures were further optimized for geometry while the cell size was held

constant. Figures 6.18.a-b and d-e show the top and side view of the optimized structure in the condensed phase of the graphene-C_{60} hybrid and nanobud system. The corresponding band structure and DOS of each system are represented in Figures 6.18.c, f and g. Even though the charge transfer from graphene to C_{60} increased from 0.095*e* to 0.118*e* for the hybrid and from 0.059*e* to 0.067*e* for the nanobud system because of the mutual interactions of all of the components in the packed structure, the band structure and DOS remained constant compared to the dilute phases of the systems. Thus, both nanobud and hybrid systems retain their metallic character.

6.4.2 Single Li atom on the graphene-C_{60} hybrid and graphene-C_{60} nanobud system

We also examined the adsorption of one Li on various positions of the condensed system, as in the dilute system. The position of the added Li atom was chosen on either the center of the hexagonal sites of graphene or on the pentagonal and hexagonal sites of the C_{60} as in the dilute phase. However, we did not distinguish regions in the condensed phase systems because its symmetric structure results in similar contributions to Li adsorption regardless of region. Two positions were chosen on the top of graphene (Pos1_graphene and Pos2_graphene), and we identified the positions around the C_{60} as either between graphene and C_{60} (Pos1,2,5,6@C_{60}) or between C_{60}s (Pos3,4@C_{60}) for both systems as shown in Figures 6.19.a and c. The optimized structures are represented in Figures 6.19.b and e, and the adsorption energies and charge distributions are listed in Tables 6.6 (hybrid) and 6.7 (nanobud). Most Li atoms are strongly bound to carbon atoms and retain their initial position except in Pos2@graphene or Pos1-3_C_{60}@nanobud. The former position is attracted to the C_{60} side because of the influence of the C_{60}, while the latter position, which is initially located near the bonds between graphene and C_{60}, is

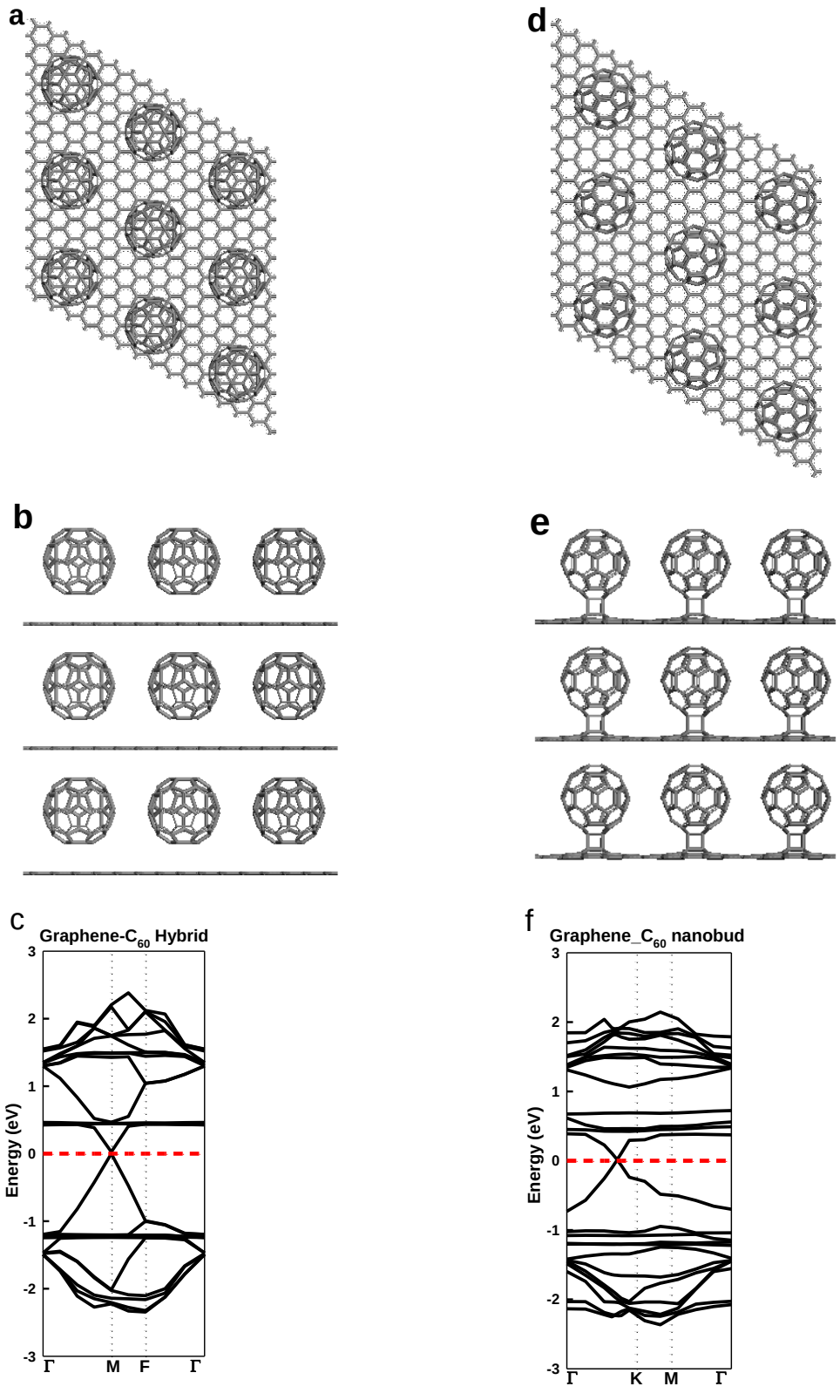
a
d
b
e
c
Graphene-C60 Hybrid
Energy (eV)
3
2
1
0
-1
-2
-3
Γ
M
F
Γ
f
Graphene_C60 nanobud
Energy (eV)
3
2
1
0
-1
-2
-3
Γ
K
M
Γ

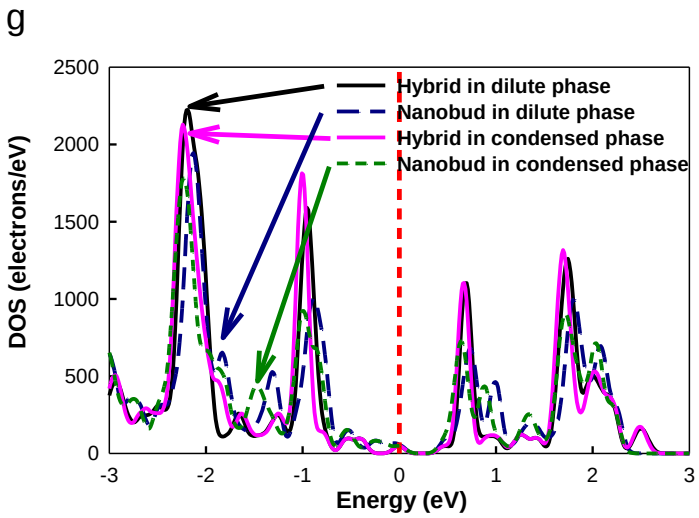

Figure 6.18: Graphene-C_{60} hybrid system in the condensed phase: (a) top view of the expanded (3x3x3) structure; (b) side view (unit cell: a and b=12.3 Å and c=12.7 Å) and (c) band structure. Graphene-C_{60} nanobud hybrid system in the condensed phase: (d) top view of the expanded (3x3x3) structure; (e) side view (unit cell: a and b=12.3 Å and c=12.48 Å); (f) band structure; and (g) density of states (DOS) of the hybrid and nanobud systems in both dilute and condensed phases.

displaced away from the bonds. The Li adsorption energy in the condensed phase was lower than that in the dilute phase, especially between graphene and C_{60} (bonded or non-bonded region) for both systems. A hybrid and nanobud structure is generated in the nanobud system when the nanobud system forms in the condensed phase as a result of van der Waals interactions. Therefore, Li adsorption occurs at the position between graphene and C_{60}, which usually provides the strongest adsorption sites. Moreover, the energy between C_{60}s such as Pos3 and Pos4_C_{60} was very similar in both systems because the adsorption at this area was only determined by interactions with C_{60}.

The corresponding band structures of several one-Li-adsorbed systems are shown in Figures 6.20 and 6.21 for the hybrid and nanobud systems, respectively. The band structures were similar in the dilute phase, which indicates that Li adsorption mainly causes the two bands originating from the C_{60} to move down to the Fermi level.

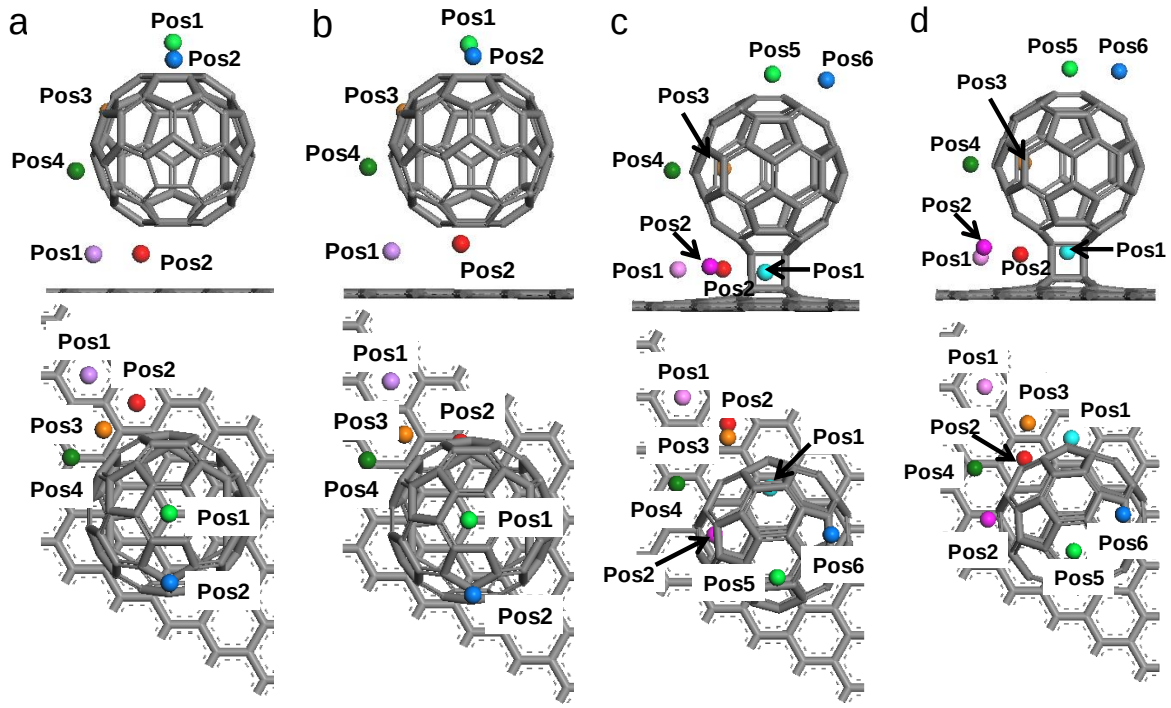

Figure 6.19: One-Li adsorption on various positions around the graphene-C_{60} hybrid in the condensed phase: (a) initial structure and (b) optimized structure. One-Li adsorption on various positions around the graphene-C_{60} nanobud in the condensed phase: (c) initial structure and (d) optimized structure.

Table 6.6: The adsorption energy and charge distribution (Mulliken charge) of one-Li atom on the condensed graphene-C_{60} hybrid system

System	Adsorption Energy (eV)	Charges (e)		
		Li	graphene	C_{60}
graphene-C_{60} hybrid	N/A	N/A	0.118	-0.118
Pos1_graphene@hybrid	-1.817	0.856	-0.322	-0.534
Pos2_ graphene @hybrid	-2.346	0.906	-0.176	-0.730
Pos1_C_{60}@ hybrid (hexagon site)	-1.708	1.187	-0.323	-0.864
Pos2_C_{60}@ hybrid (pentagon site)	-2.340	0.910	-0.184	-0.726
Pos3_C_{60}@hybrid (hexagon site)	-1.991	0.851	-0.016	-0.835
Pos4_C_{60}@ hybrid (pentagon site)	-2.133	0.855	0.018	-0.873

Table 6.7: The adsorption energy and charge distribution (Mulliken charge) of one-Li atom on the condensed graphene-C_{60} nanobud system

System	Adsorption Energy (eV)	Charges (e)		
		Li	graphene	C_{60}
graphene-C_{60} nanobud	N/A	N/A	0.067	-0.067
Pos1_graphene@nanobud	-1.905	0.854	-0.397	-0.457
Pos2_ graphene @nanobud	-2.352	0.870	-0.372	-0.498
Pos1_C_{60}@nanobud	-2.296	0.865	-0.368	-0.497
Pos2_C_{60}@nanobud	-2.179	0.859	-0.326	-0.533
Pos3_C_{60}@anobud	-1.983	0.853	-0.057	-0.796
Pos4_C_{60}@nanobud	-2.143	0.863	-0.046	-0.817
Pos5_C_{60}@nanobud	-2.333	1.119	-0.473	-0.646
Pos6_C_{60}@nanobud	-2.457	1.000	-0.407	-0.593

However, Li adsorption does not alter the intrinsic properties of the system; therefore, a band structures are still similar to the pure hybrid or nanobud system without Li atom.

6.4.3 Multiple Li atoms on graphene-C_{60} hybrid and graphene-C_{60} nanobud system

We added another Li atom (blue or green) near the first Li atom (purple) of low adsorption energy following the method in the previous chapter to investigate the Li adsorption mechanism. As a result, the second atom was adsorbed on the next nearest neighboring (N.N.N.) or the nearest neighboring (N.N.) site in either the radial or axial direction along the axis of the graphene surface starting from the first Li atom positioned

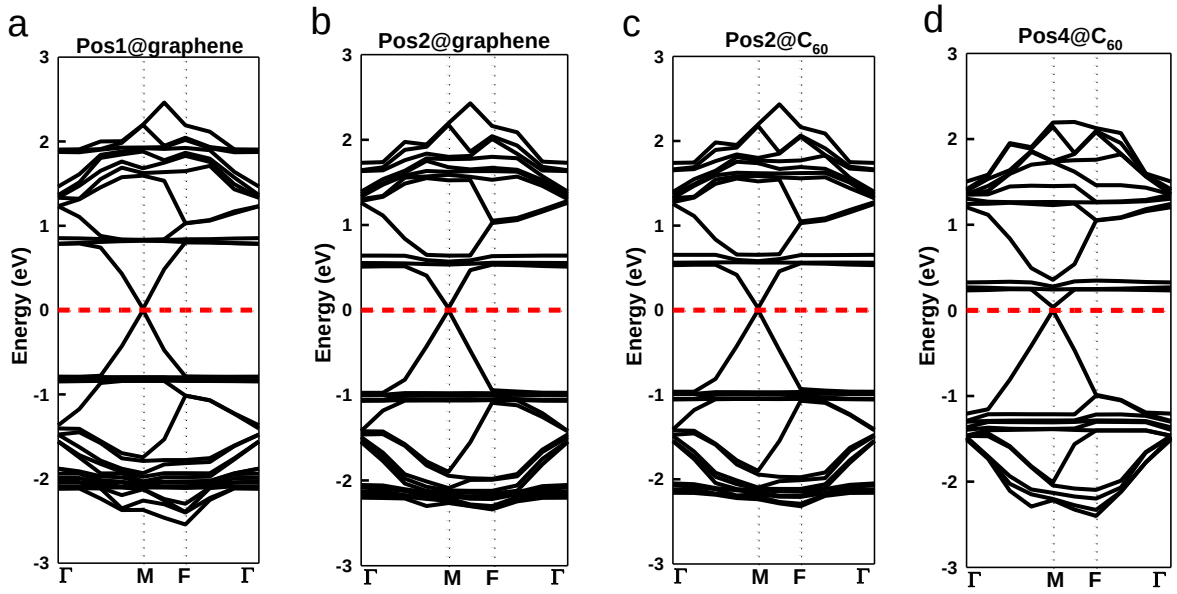

Figure 6.20: The band structure of several one-Li systems in the condensed phase: (a) Pos1_graphene@hybrid; (b) Pos2_graphene@hybrid; (c) Pos2_C_{60}@hybrid; and (d) Pos4_C_{60}@hybrid.

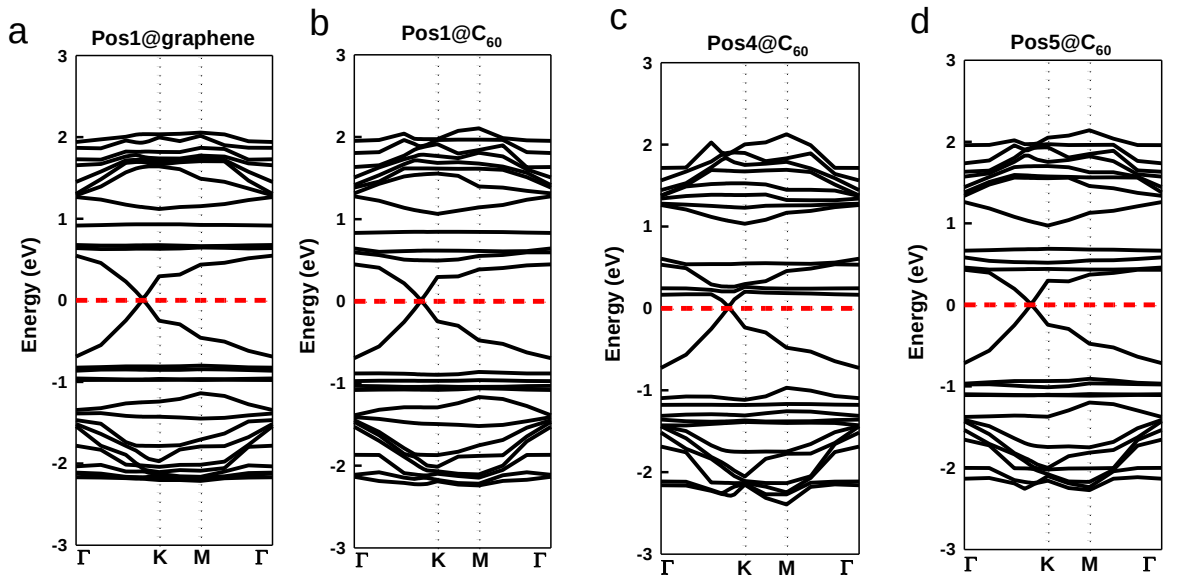

Figure 6.21: The band structure of several one-Li systems in the condensed phase: (a) Pos1_graphene@nanobud; (b) Pos1_C_{60}@nanobud; (c) Pos4_C_{60}@nanobud; and (d) Pos5_C_{60}@nanobud.

at graphene@hybrid/nanobud or C_{60}@hybrid/nanobud. Initial and optimized structures of the two-Li atom adsorbed systems are displayed in Figures 6.22 and 6.23 along with the corresponding band structures of some systems. The adsorption energies of the two atom systems are summarized in Tables 6.8 and 6.9.

Table 6.8: The adsorption energy of two- Li atoms adsorption on graphene-C_{60} hybrid system in condensed phase

Starting position	Direction	Adsorption Energy (eV)
2Li starting from Pos1_graphene@hybrid	N.N.N.site	-2.143
	N.N.site	-2.147
2Li starting from Pos2_C_{60}@hybrid	Radial (N.N.N. pentagon site)	-2.412
	Radial (N.N. hexagon site)	-2.266
	Axial (N.N.N. hexagon site)	-2.449
	Axial (N.N.N. pentagon site)	-2.496
	Axial (N.N. hexagon site)	-2.261
20 Li atoms on condensed graphene-C_{60} hybrid		-1.894

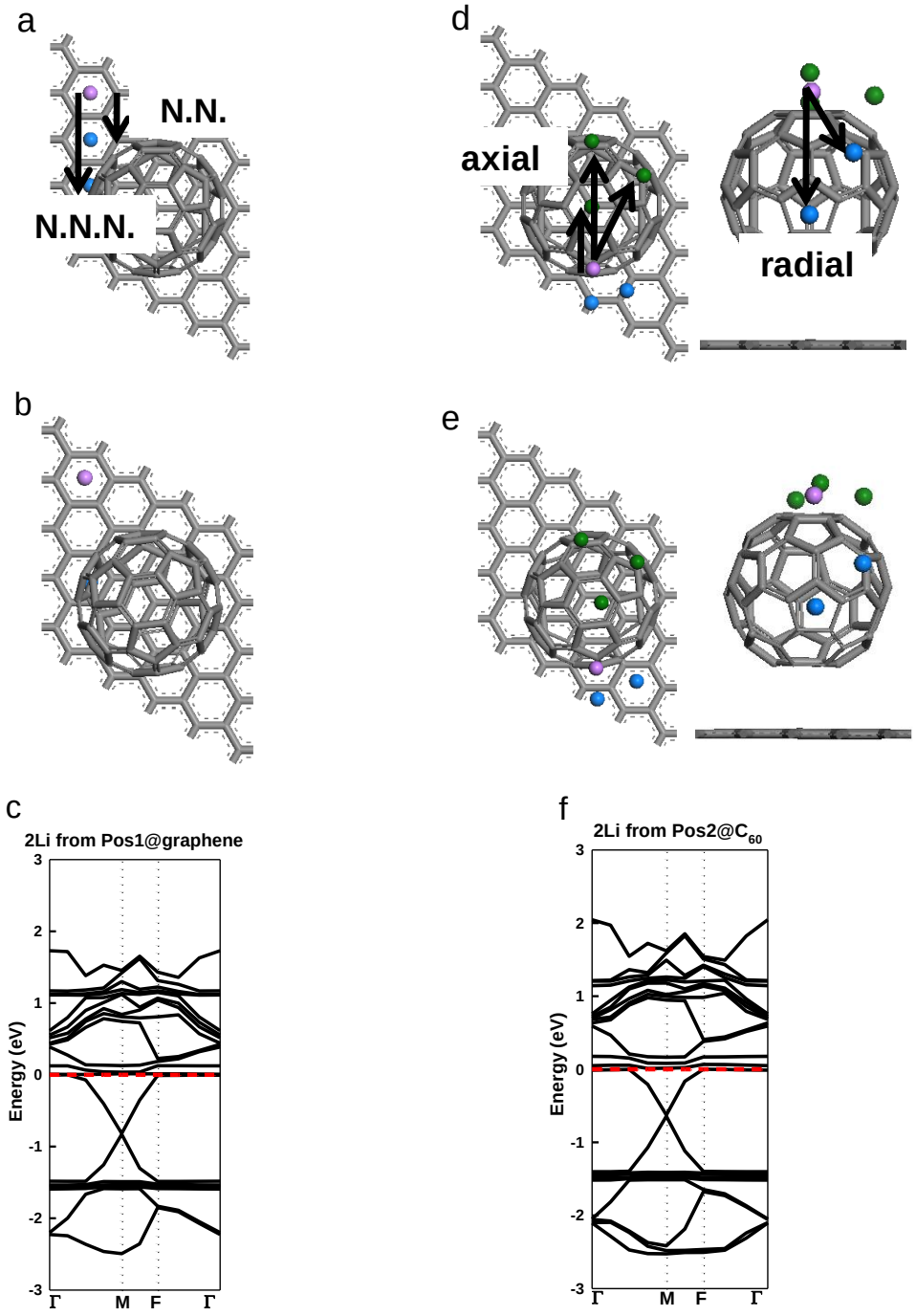

Figure 6.22: Two-Li adsorption on various regions. Two-Li configuration starting at Pos1_graphene@hybrid: (a) initial structure; (b) optimized structure; and (c) band structure of the next nearest neighboring (N.N.N) site. Two-Li configuration starting at Pos2_C_{60}@hybrid: (d) initial structure; (e) optimized structure; and (f) band structure of the next nearest neighboring (N.N.N.) site in the axial direction.

Table 6.9: The adsorption energy of two- Li atoms adsorption on graphene-C_{60} nanobud system in condensed phase

Starting position	Direction	Adsorption Energy(eV)
2Li starting from Pos1_graphene@nanobud	N.N.N.site	-2.249
	N.N. site	-2.249
2Li starting from Pos1_C_{60}@nanobud	Radial (N.N.N. pentagon site)	-2.450
	Radial (N.N. hexagon site)	-2.384
	Axial (N.N.N. pentagon site)	-2.498
2Li starting from Pos6_C_{60}@nanobud	Radial (N.N.N. hexagon site)	-2.462
	Radial (N.N.N. pentagon site)	-2.559
	Radial (N.N. hexagon site)	-2.402
	Axial (N.N.N. hexagon site)	-2.667
	Axial (N.N.N. pentagon site)	-2.653
	Axial (N.N. hexagon site)	-2.562
18 Li atoms on condensed graphene-C_{60} nanobud		-1.983

In these tables, we show that the Li adsorption energy of the two Li systems is lower than in the dilute phase as a result of the combined interactions from each component. Furthermore, it appears that the N.N.N. scheme is slightly preferred to the N.N. scheme for both systems in the condensed phase (~ 0.2 eV/hybrid and ~ 0.1 eV/nanobud). However, it seems that the Li adsorption energies in the radial and axial directions are similar when the same scheme is used (N.N.N or N.N.) because the strong Li adsorption is mainly driven by C_{60} in the closely packed structure.

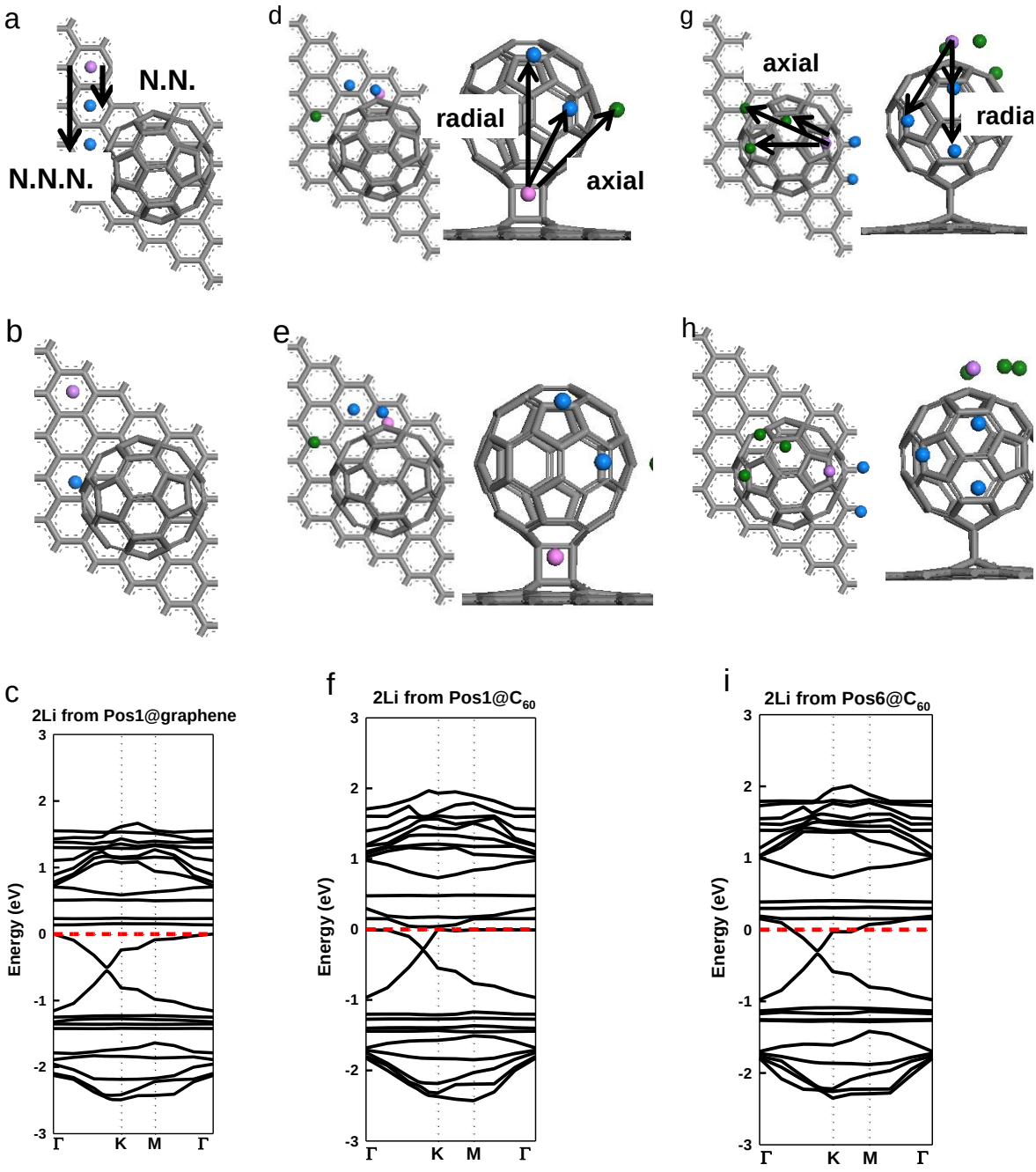

Figure 6.23: Two-Li adsorption on various regions. Two-Li configuration starting at Pos1_graphene@nanobud: (a) initial structure; (b) optimized structure; and (c) band structure of the next nearest neighboring (N.N.N) site. Two-Li configuration starting at Pos1_C_{60}@hybrid: (d) initial structure; (e) optimized structure; and (f) band structure of the next nearest neighboring (N.N.N.) site in the radial direction. Two-Li configuration starting at Pos6_C_{60}@hybrid: (g) initial structure; (h) optimized structure; and (i) band structure of the next nearest neighboring (N.N.N.) site in the axial direction.

The lowest adsorption (-2.402 eV ~ -2.667 eV) in the nanobud system is located in the site between graphene and C_{60} (Pos6@C_{60}: non-bonded regions) although the site closest to the covalent bond (Pos1@C_{60}: close to bond) also possesses low adsorption energy (-2.384 eV ~ -2.498 eV). It indicates that selection of the appropriate site between graphene and C_{60} can maximize Li adsorption while the Li atoms are unable to enter the sites closest to the covalent bond or the sites in the middle between graphene and C_{60}. Therefore, the maximum number of Li atoms will be lower in the nanobud system than in the hybrid system. We also observed similar band shifts to the dilute phase after additional Li adsorption in the system as represented in Figures 6.22 and 6.23. Therefore, bands created from the graphene and C_{60} moved down below the Fermi level as a result of electron injection from Li atoms, which was also observed in the CNT-C_{60} hybridized system. The density of states (DOS) shown in Figures 6.24.a and b also verifies this change. Thus, the DOS around the Fermi level rapidly increase after two-Li adsorption on the system, and many more states appear as the number of Li atoms increases, which indicate that conductivity is enhanced after Li adsorption.

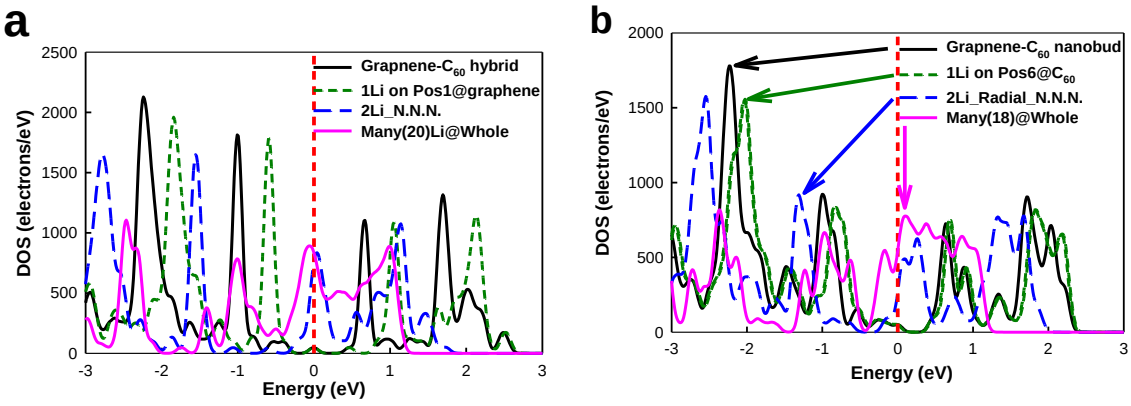

Figure 6.24: Density of states for various numbers of Li atoms adsorbed on a (a) graphene-C_{60} hybrid system and on a (b) graphene-C_{60} nanobud system.

Finally, we investigated multi-Li systems consisting of 20 Li atoms around the hybrid and 18 Li atoms around the nanobud systems assuming the N.N.N. scheme adsorption mechanism. Figures 6.25 and 6.26 show the initial and optimized structure along with the corresponding band structures and density of states of the graphene-C_{60} hybrid and nanobud systems in the condensed phase.

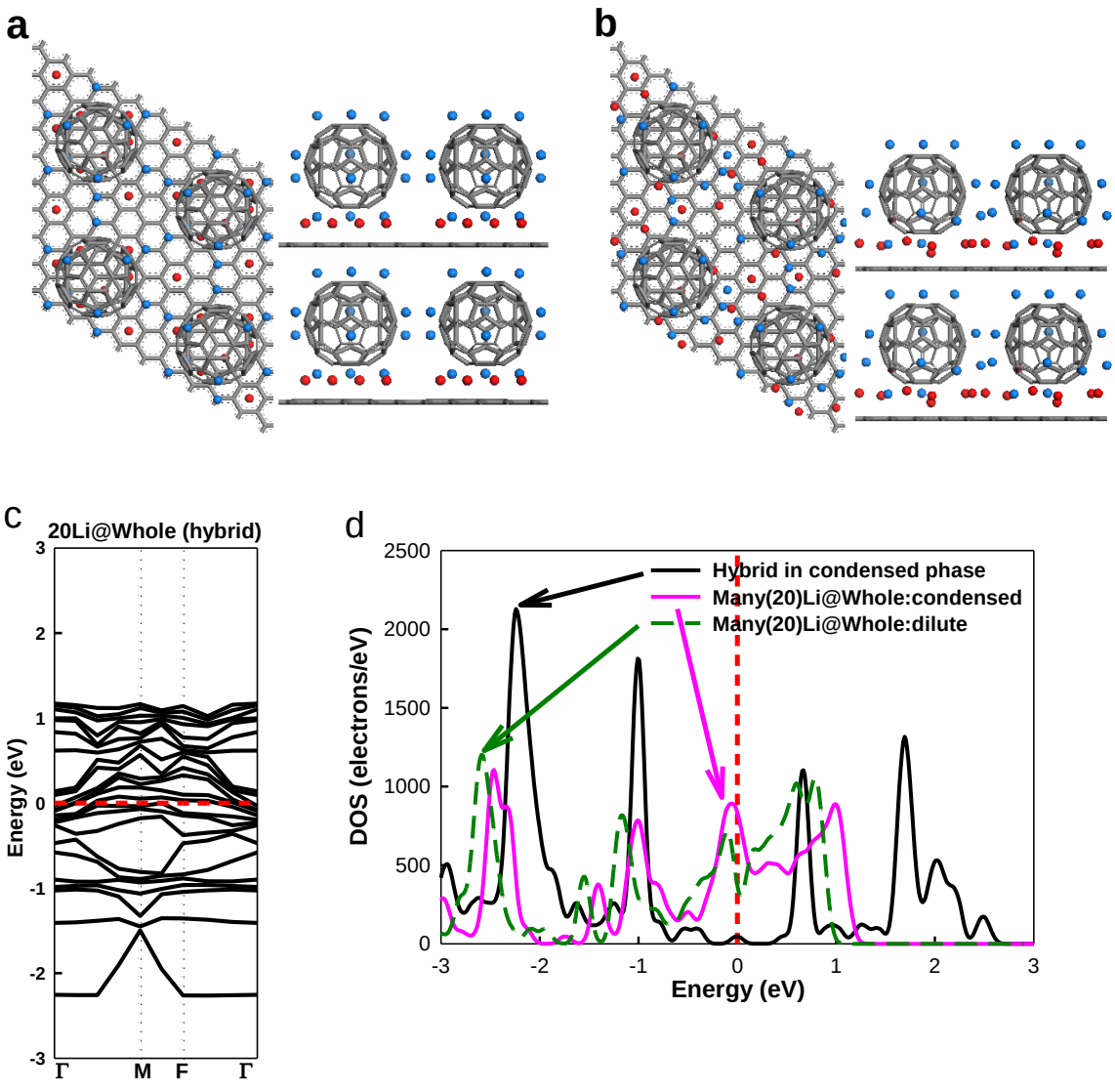

Figure 6.25: Multi(20)-Li atom adsorption on the entire hybrid system: (a) initial structure; (b) optimized structure; (c) band structure; and (d) density of states in the pure condensed phase with 20 Li atoms on the hybrid system in the dilute phase.

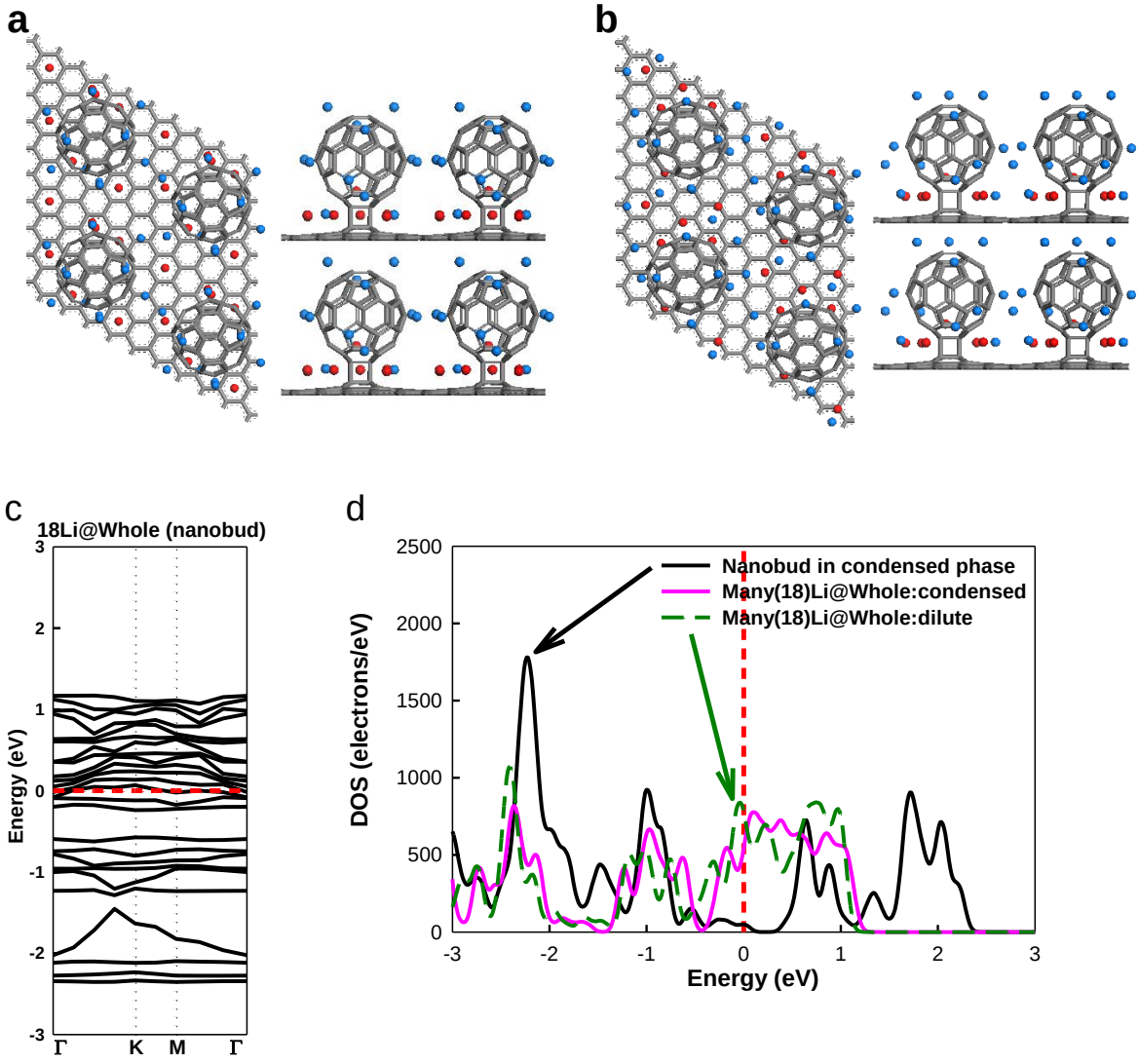

Figure 6.26: Multi (18)-Li atom adsorption on the entire nanobud system: (a) initial structure; (b) optimized structure; (c) band structure; and (d) density of states in the pure condensed phase with 18 Li atoms on the nanobud system in the dilute phase.

The Li adsorption energies are -1.894 eV (hybrid) and -1.983 eV (nanobud), which are much lower than in the dilute system (-1.624 eV:hybrid and -1.684 eV: nanobud) and the Li-Li binding energy (-1.030 eV). Thus, we can expect Li atoms will remain on the surface of the hybrid/nanobud system rather than forming clusters. As a

result, enhanced Li adsorption will take place on the C_{60} side first, initiated at the site between graphene and C_{60}, to cover the entire surface of C_{60} and proceed to the graphene side starting at the sites closest to C_{60}. The only difference between the hybrid and nanobud systems appears to be that the Li atom cannot be located close to the covalent bond in the nanobud system, which may result in a greater number of adsorption sites in the hybrid system. We also observed potential enhancement of the metallic character of the system as a result of the band structure and DOS. This system showed significant increases in the number of bands (Figures 6.25.c and 6.26.c) and electron density (Figures 6.25.d and 6.26.d) across the Fermi level than in the pure hybrid/nanobud system along with a slightly higher electron density in the conduction band than in the dilute system. Therefore, we expect that the enhanced metallic character could improve the electron transport properties and Li adsorption capabilities as a result of the hybridized system.

6.5. Conclusion

We investigated Li adsorption on the graphene-C_{60} hybrid and nanobud system using the density functional theory (DFT) in both the dilute and condensed phases. Although it was found that the hybrid system retained the characteristics of its components, such as graphene and C_{60} in its electronic structure, it was observed that the charges were transferred from graphene to C_{60} making the graphene positively charged (+0.095e) and the C_{60} negatively charged (-0.095e). Similarly, the covalently bonded graphene-C_{60} nanobud:hh demonstrated the same direction of charge transfer from graphene to C_{60} ($|0.059|e$); however, a small band gap (0.30 eV) was created for the graphene-C_{60} nanobud:hp after the [2+2] cycloaddition reaction. The electronic properties,

such as the band structure and density of states (DOS) did not change when the systems formed the condensed structure, while the charge transfer increased slightly for the hybrid ($|0.118|e$) and nanobud ($|0.067|e$) systems because of the interaction between the components in the condensed phase.

We found that Li adsorption was enhanced compared to the pure graphene system. This enhanced adsorption capability may be explained by the high electron affinity of C_{60} and the charge transfer from graphene to C_{60}. Furthermore, we determined that the Li adsorption mechanism will preferentially occur on the C_{60} side, specifically at the space halfway between graphene and C_{60} or between C_{60}s and proceed toward the graphene side by analyzing the Li adsorption as a function of various regions in the graphene-C_{60} systems. Meanwhile, Li adsorption capability was further enhanced in the condensed phase as a result of the compact and symmetric structure, and adsorption energies were lower than in the dilute phase system. Consequently, it was unlikely that Li clusters would be formed because the Li-C adsorptive interaction was more stable than the Li-Li binding interaction.

Although there was no significant change in the band structure after one Li atom was adsorbed on the graphene-C_{60} systems, additional Li adsorptions shifted the energy bands downward and even removed the band gap of the nanobud system as a result of electron injection from Li to the system in the dilute and condensed phases. Density of states (DOS) in the hybrid and nanobud system also indicated that the metallic character of the graphene-C_{60} system was enhanced as the number of Li atoms increased. Hence, it is expected that the graphene-C_{60} hybrid and nanobud systems will demonstrate enhanced conductive properties along with excellent Li adsorption capabilities compared to the pure graphene system.

CHAPTER 7

CONCLUSIONS

In this research, we investigated various hybrid materials consisting of carbon allotrope to predict the Li adsorption capabilities for developing an anode material in a Li ion battery system. Graphitic carbon anodes have been widely adapted for the current Li ion battery application, but these anodes demonstrate low energy density and cycle efficiency. Thus, various Li intercalation materials have been studied from carbon nanotubes (CNTs) to silicon to increase the Li adsorption capacity. However, early studies on Li intercalation to CNTs showed slight increases of reversible capacities comparing to current graphitic carbon material. Moreover, silicon based composite materials are very unstable in spite of their very high capacity. Despite the early failure to fabricate an adequate device using pure CNTs, it appears that the use of CNTs in Li ion batteries remains promising due to the vast surface area and outstanding electrical and mechanical properties of CNTs. Therefore, various modifications on the CNT, such as forming structural defects, doping impurities and mixing carbon-based materials, have been attempted to enhance the electrochemical properties. Among those modifications, a hybridized structure consisting of carbon material appears to be the most useful because it can achieve improved electrochemical properties without deteriorating processes, which is necessary for the other modifications. Therefore, we focused on diverse combinations and forms of hybridized materials prepared from CNTs, fullerene (C_{60}) and graphene. Specifically, the structure hybridized with C_{60} was our main priority because the high electron affinity C_{60} allows it to be utilized as an electron acceptor for Li atoms

by providing strong Li adsorption sites. We used the density functional theory (DFT) through DMol^3 for predicting the Li adsorption energy and electronic properties, such as band structure, density of states (DOS) and charge distribution of the Li-adsorbed system.

The CNT-C_{60} hybrid system presented in Chapter 3 provides a simple structure, which is maintained by weak dispersion interaction. Therefore, the hybrid system retains the metallic characteristics of its components. Furthermore, it demonstrated charge transfer from CNT to C_{60} ($|0.096|e$), which resulted in a positively charged CNT surface while C_{60} was negatively charged. This charge transfer helps achieve better Li adsorption on the CNT side and lower Li adsorption energy (-2.571 eV) compared to a pristine CNT system (-1.720 eV). We also found that Li will adsorb preferably in the C_{60} side, especially in the space between C_{60}s or between CNT and C_{60}, and proceed toward the CNT side instead of forming Li clusters. The electronic properties, such as the band structure and DOS, indicate that it generates more available electrons around the Fermi level as the number of Li atoms increases. Hence, the CNT-C_{60} hybrid system is expected to demonstrate enhanced conductivity and superior Li adsorption capabilities compared to the bare CNT system. Li adsorption is further enhanced and uniform over the entire hybrid system in the condensed phase. This can be attributed to the compact and symmetric structure, which enables simultaneous interactions between both the CNT and C_{60} in the system.

In Chapter 4, we studied another type of CNT-C_{60} hybridized system called nanobud. C_{60} is covalently bonded to a CNT via a [2+2] cycloaddition reaction in the nanobud system, but the covalent bond changes the original properties of the CNT and creates a small gap in the metallic system while decreasing the band gap in the

semiconducting system. Therefore, the nanobud will be useful in tuning the band gap of the system by manipulating the chirality of CNT, the density of the C_{60} or the bond type. Li adsorption on the nanobud system is also enhanced compared to the bare CNT system as a result of C_{60}, even though the Li adsorption was higher than in the CNT-C_{60} hybrid system due to the covalent bond at the junction. However, the degree of Li adsorption increases again in the condensed phase of the nanobud system. The Li adsorption mechanism is very similar to the hybrid system: however, the Li cannot access the exact middle between the CNT and C_{60} because of the covalent bond connecting the CNT and C_{60}; therefore, the Li atom closest to the bond will eventually be repelled outward instead of forming a Li-C bond.

We investigated the 3D nano-network structure; all of the CNTs and C_{60} were connected by a covalent bond. This network system demonstrated improved mechanical strength (Young's modulus ~ 70 GPa) in the radial direction of the CNT axis, which was relatively weak (~ 4 GPa) in the pure CNT system. Therefore, the nano-network system is expected to have greater mechanical strength in both the axial and radial directions (to the axis of the CNT). However, the nano-network system is semiconducting with a band gap of 0.34 eV even though charge still transfers from CNT to C_{60} ($|0.187|e$). Additionally, the Li adsorption energy is also low in the network system as a result of C_{60} and its compacted structure. However, the additional Li atoms did not significantly alter the electronic properties of the original nano-network system in comparison to the CNT-C_{60} hybrid or nanobud systems.

Finally, we examined a graphene-C_{60} hybrid and nanobud system, which can be combined with the current graphitic anode in the Li battery system. The graphene-C_{60}

hybrid system retains its metallic character by weak dispersion interactions, while the nanobud system is constructed through covalent bond between graphene and C_{60}, similar to the CNT-C_{60} hybridized system. The Li adsorption capability (~ -1.893 eV: hybrid system and -2.070 eV: nanobud system for a one-Li adsorbed system) of the graphene-C_{60} hybridized system was enhanced by C_{60} compared to the pure graphene system (~ -1.375 eV), although Li adsorption energy was generally higher than in the CNT-C_{60} systems.

In conclusion, a CNT or graphene hybridized with C_{60} shows enhanced Li adsorption capabilities compared to pristine systems due to C_{60}. The C_{60} in the hybridized system provides strong adsorption sites and charge transfer, which allows the other component in the hybridized system to be positively charged as a result of its high electron affinity. This charge transfer results in lowered Li adsorption energy on the CNT or graphene side. Furthermore, Li adsorption starts from the C_{60} sites between the CNT/ graphene and C_{60} or between C_{60}s and proceeds to the remaining CNT/graphene sites. We also demonstrated that mechanical strength could be increased by increasing the number of bonds connecting each component. Thus, the nano-network system showed an increased Young's modulus in both the radial and axial directions of the CNT axis. Hence, we are able to tune the electronic and mechanical properties by choosing different components, controlling the packing density of the components and changing connections between components to prepare this hybrid material system. This hybridized system will demonstrate enhanced Li adsorption capabilities in its application as an electrode in electrochemical devices.

REFERENCES

1. Service, R.F., "The hydrogen backlash," Science, vol. 305, pp. 958-961, 2004.

2. Daniel, C., "Materials and processing for lithium-ion batteries," Jom, vol. 60, pp. 43-48, 2008.

3. Xu, Z.H., H.D. Zang, and B. Hu, "Solar energy-conversion processes in organic solar cells," Jom, vol. 60, pp. 49-53, 2008.

4. Research, G.F.M.o.E.a., ""Innovation Alliance, Lithium Ion Battery 2015"," http://www.bmbf.de/de/11828.php, 2008.

5. J.Besenhard, "Handbook of Battery Materilas," 1999.

6. Dudney, N.J., et al., "Nanocrystalline LixMn2-yO4 cathodes for solid-state thin-film rechargeable lithium batteries," Journal of the Electrochemical Society, vol. 146, pp. 2455-2464, 1999.

7. Whittingham, M.S., "Materials challenges facing electrical energy storage," Mrs Bulletin, vol. 33, pp. 411-419, 2008.

8. Shukla, A.K. and T.P. Kumar, "Materials for next-generation lithium batteries," Current Science, vol. 94, pp. 314-331, 2008.

9. Liu, C. and H.M. Cheng, "Carbon nanotubes for clean energy applications," Journal of Physics D-Applied Physics, vol. 38, pp. R231-R252, 2005.

10. Ruffo, R., et al., "Impedance Analysis of Silicon Nanowire Lithium Ion Battery Anodes," Journal of Physical Chemistry C, vol. 113, pp. 11390-11398, 2009.

11. Postma, H.W.C., et al., "Carbon Nanotube Single-Electron Transistors at Room Temperature," Science, vol. 293, pp. 76-79, 2001.

12. Novoselov, K.S., et al., "Electric Field Effect in Atomically Thin Carbon Films," Science, vol. 306, pp. 666-669, 2004.

13. Baughman, R.H., A.A. Zakhidov, and W.A. de Heer, "Carbon Nanotubes--the Route Toward Applications," Science, vol. 297, pp. 787-792, 2002.

14. Kong, J., et al., "Nanotube Molecular Wires as Chemical Sensors," Science, vol. 287, pp. 622-625, 2000.

15. Hong, S. and S. Myung, "Nanotube electronics - A flexible approach to mobility," Nature Nanotechnology, vol. 2, pp. 207-208, 2007.

16. Lu, X. and Z.F. Chen, "Curved Pi-conjugation, aromaticity, and the related chemistry of small fullerenes (< C-60) and single-walled carbon nanotubes," Chemical Reviews, vol. 105, pp. 3643-3696, 2005.

17. Takesue, I., et al., "Superconductivity in Entirely End-Bonded Multiwalled Carbon Nanotubes," Physical Review Letters, vol. 96, pp. 057001, 2006.

18. Marquis, F.D.S., "Carbon Nanotube Nanostructured Hybrid Materials Systems for Renewable Energy Applications," Jom, vol. 63, pp. 48-53, 2011.

19. Yu, M.F., et al., "Strength and breaking mechanism of multiwalled carbon nanotubes under tensile load," Science, vol. 287, pp. 637-640, 2000.

20. Chae, H.G. and S. Kumar, "Rigid-rod polymeric fibers," Journal of Applied Polymer Science, vol. 100, pp. 791-802, 2006.

21. Meo, M. and M. Rossi, "Prediction of Young's modulus of single wall carbon nanotubes by molecular-mechanics based finite element modelling," Composites Science and Technology, vol. 66, pp. 1597-1605, 2006.

22. Sinnott, S.B. and R. Andrews, "Carbon nanotubes: Synthesis, properties, and applications," Critical Reviews in Solid State and Materials Sciences, vol. 26, pp. 145-249, 2001.

23. Demczyk, B.G., et al., "Direct mechanical measurement of the tensile strength and elastic modulus of multiwalled carbon nanotubes," Materials Science and Engineering a-Structural Materials Properties Microstructure and Processing, vol. 334, pp. 173-178, 2002.

24. Bellucci, S., "Carbon nanotubes: physics and applications," physica status solidi (c), vol. 2, pp. 34-47, 2005.

25. Tarascon, J.M. and M. Armand, "Issues and challenges facing rechargeable lithium batteries," Nature, vol. 414, pp. 359-367, 2001.

26. Geim, A.K. and K.S. Novoselov, "The rise of graphene," Nature Materials, vol. 6, pp. 183-191, 2007.

27. Novoselov, K.S., et al., "Two-dimensional gas of massless Dirac fermions in graphene," Nature, vol. 438, pp. 197-200, 2005.

28. Zhang, Y.B., et al., "Experimental observation of the quantum Hall effect and Berry's phase in graphene," Nature, vol. 438, pp. 201-204, 2005.

29. Heersche, H.B., et al., "Bipolar supercurrent in graphene," Nature, vol. 446, pp. 56-59, 2007.

30. Avouris, P., Z.H. Chen, and V. Perebeinos, "Carbon-based electronics," Nature Nanotechnology, vol. 2, pp. 605-615, 2007.

31. Wudl, F., "Fullerene materials," Journal of Materials Chemistry, vol. 12, pp. 1959-1963, 2002.

32. Thomas, L.H., "The calculation of atomic fields.," Proceedings of the Cambridge Philosophical Society, vol. 23, pp. 542-548, 1927.

33. Fermi, E., "Un Metodo Statistico per la Determinazione di alcune Proprieta dellAtomo," Rend.Accad.Nax.Lincei, vol. 6, pp. 602-607, 1927.

34. Hohenberg, P. and W. Kohn, "Inhomogeneous Electron Gas," Physical Review B, vol. 136, pp. B864-&, 1964.

35. Kohn, W. and L.J. Sham, "Self-Consistent Equations Including Exchange and Correlation Effects," Physical Review, vol. 140, pp. 1133-&, 1965.

36. Born, M. and R. Oppenheimer, "Quantum theory of molecules," Annalen Der Physik, vol. 84, pp. 0457-0484, 1927.

37. Gellmann, M. and K.A. Brueckner, "Correlation Energy of an Electron Gas at High Density," Physical Review, vol. 106, pp. 364-368, 1957.

38. Ceperley, D.M. and B.J. Alder, "Ground-State of the Electron-Gas by a Stochastic Method," Physical Review Letters, vol. 45, pp. 566-569, 1980.

39. Perdew, J.P. and Y. Wang, "Pair-Distribution Function and Its Coupling-Constant Average for the Spin-Polarized Electron-Gas," Physical Review B, vol. 46, pp. 12947-12954, 1992.

40. Langreth, D.C. and M.J. Mehl, "Beyond the Local-Density Approximation in Calculations of Ground-State Electronic-Properties," Physical Review B, vol. 28, pp. 1809-1834, 1983.

41. Perdew, J.P., K. Burke, and M. Ernzerhof, "Generalized gradient approximation made simple," Physical Review Letters, vol. 77, pp. 3865-3868, 1996.

42. Perdew, J.P., "Accurate Density Functional for the Energy - Real-Space Cutoff of the Gradient Expansion for the Exchange Hole," Physical Review Letters, vol. 55, pp. 1665-1668, 1985.

43. Sherrill, C.D. and H.F. Schaefer, "The configuration interaction method: Advances in highly correlated approaches," Advances in Quantum Chemistry, Vol 34, vol. 34, pp. 143-269, 1999.

44. Moller, C. and M.S. Plesset, "Note on an approximation treatment for many-electron systems," Physical Review, vol. 46, pp. 0618-0622, 1934.

45. Grimme, S., "Semiempirical GGA-type density functional constructed with a long-range dispersion correction," Journal of Computational Chemistry, vol. 27, pp. 1787-1799, 2006.

46. Grimme, S., "Accurate description of van der Waals complexes by density functional theory including empirical corrections," Journal of Computational Chemistry, vol. 25, pp. 1463-1473, 2004.

47. Zhao, Y. and D.G. Truhlar, "The M06 suite of density functionals for main group thermochemistry, thermochemical kinetics, noncovalent interactions, excited states, and transition elements: two new functionals and systematic testing of four M06-class functionals and 12 other functionals," Theoretical Chemistry Accounts, vol. 120, pp. 215-241, 2008.

48. Gupta, V., et al., "Synthesis of C-60 intercalated graphite," Solid State Communications, vol. 131, pp. 153-155, 2004.

49. Dahn, J.R., et al., "Mechanisms for Lithium Insertion in Carbonaceous Materials," Science, vol. 270, pp. 590-593, 1995.

50. Yu, M.-F., et al., "Strength and Breaking Mechanism of Multiwalled Carbon Nanotubes Under Tensile Load," Science, vol. 287, pp. 637-640, 2000.

51. Nalimova, V.A., et al., "Lithium interaction with carbon nanotubes," Synthetic Metals, vol. 88, pp. 89-93, 1997.

52. Che, G., et al., "Carbon nanotubule membranes for electrochemical energy storage and production," Nature, vol. 393, pp. 346-349, 1998.

53. Maurin, G., et al., "Electrochemical intercalation of lithium into multiwall carbon nanotubes," Chemical Physics Letters, vol. 312, pp. 14-18, 1999.

54. Dubot, P. and P. Cenedese, "Modeling of molecular hydrogen and lithium adsorption on single-wall carbon nanotubes," Physical Review B, vol. 6324, pp. 241402, 2001.

55. Zhao, J., et al., "First-Principles Study of Li-Intercalated Carbon Nanotube Ropes," Physical Review Letters, vol. 85, pp. 1706, 2000.

56. Kar, T., J. Pattanayak, and S. Scheiner, "Insertion of lithium ions into carbon nanotubes: An ab initio study," Journal of Physical Chemistry A, vol. 105, pp. 10397-10403, 2001.

57. Yang, J., H.J. Liu, and C.T. Chan, "Theoretical study of alkali-atom insertion into small-radius carbon nanotubes to form single-atom chains," Physical Review B, vol. 64, pp. 085420, 2001.

58. Duclaux, L., "Review of the doping of carbon nanotubes (multiwalled and single-walled)," Carbon, vol. 40, pp. 1751-1764, 2002.

59. Liu, Y., H. Yukawa, and M. Morinaga, "First-principles study on lithium absorption in carbon nanotubes," Computational Materials Science, vol. 30, pp. 50-56, 2004.

60. Udomvech, A., T. Kerdcharoen, and T. Osotchan, "First principles study of Li and Li+ adsorbed on carbon nanotube: Variation of tubule diameter and length," Chemical Physics Letters, vol. 406, pp. 161-166, 2005.

61. Zhao, M.W., et al., "Curvature-induced condensation of lithium confined inside single-walled carbon nanotubes: First-principles calculations," Physics Letters A, vol. 340, pp. 434-439, 2005.

62. Khantha, M., et al., "Interaction and concerted diffusion of lithium in a (5,5) carbon nanotube," Physical Review B, vol. 78, pp. 115430, 2008.

63. Meunier, V., et al., "Ab initio investigations of lithium diffusion in carbon nanotube systems," Physical Review Letters, vol. 88, pp. 075506, 2002.

64. Garau, C., et al., "Lithium diffusion in single-walled carbon nanotubes: a theoretical study," Chemical Physics Letters, vol. 374, pp. 548-555, 2003.

65. Zhao, M., Y. Xia, and L. Mei, "Diffusion and condensation of lithium atoms in single-walled carbon nanotubes," Physical Review B, vol. 71, pp. 165413, 2005.

66. Nishidate, K. and M. Hasegawa, "Energetics of lithium ion adsorption on defective carbon nanotubes," Physical Review B, vol. 71, pp. 245418, 2005.

67. Gao, B., et al., "Electrochemical intercalation of single-walled carbon nanotubes with lithium," Chemical Physics Letters, vol. 307, pp. 153-157, 1999.

68. Claye, A.S., et al., "Solid-state electrochemistry of the Li single wall carbon nanotube system," Journal of the Electrochemical Society, vol. 147, pp. 2845-2852, 2000.

69. Zhou, Z., et al., "Enhanced lithium absorption in single-walled carbon nanotubes by boron doping," Journal of Physical Chemistry B, vol. 108, pp. 9023-9026, 2004.

70. Zhou, Z., et al., "Do composite single-walled nanotubes have enhanced capability for lithium storage?," Chemistry of Materials, vol. 17, pp. 992-1000, 2005.

71. Shimoda, H., et al., "Lithium Intercalation into Opened Single-Wall Carbon Nanotubes: Storage Capacity and Electronic Properties," Physical Review Letters, vol. 88, pp. 015502, 2001.

72. Gao, B., et al., "Enhanced saturation lithium composition in ball-milled single-walled carbon nanotubes," Chemical Physics Letters, vol. 327, pp. 69-75, 2000.

73. Arai, M., et al., "Enhanced Hydrogen Adsorptivity of Single-Wall Carbon Nanotube Bundles by One-Step C-60-Pillaring Method," Nano Letters, vol. 9, pp. 3694-3698, 2009.

74. Smith, B.W., M. Monthioux, and D.E. Luzzi, "Encapsulated C60 in carbon nanotubes," Nature, vol. 396, pp. 323-324, 1998.

75. Okada, S., S. Saito, and A. Oshiyama, "Energetics and electronic structures of encapsulated C-60 in a carbon nanotube," Physical Review Letters, vol. 86, pp. 3835-3838, 2001.

76. Kawasaki, S., Y. Mai, and M. Hirose, "Electrochemical lithium ion storage property of C-60 encapsulated single-walled carbon nanotubes," Materials Research Bulletin, vol. 44, pp. 415-417, 2009.

77. Nasibulin, A.G., et al., "A novel hybrid carbon material," Nat Nano, vol. 2, pp. 156-161, 2007.

78. Meng, T., C.-Y. Wang, and S.-Y. Wang, "First-principles study of a hybrid carbon material: Imperfect fullerenes covalently bonded to defective single-walled carbon nanotubes," Physical Review B, vol. 77, pp. 033415, 2008.

79. Li, C., et al., "A fullerene-single wall carbon nanotube complex for polymer bulk heterojunction photovoltaic cells," Journal of Materials Chemistry, vol. 17, pp. 2406-2411, 2007.

80. Li, C. and S. Mitra, "Processing of fullerene-single wall carbon nanotube complex for bulk heterojunction photovoltaic cells," Applied Physics Letters, vol. 91, pp. 253112-3, 2007.

81. Li, Y.F. and et al., "Electrical transport properties of fullerene peapods interacting with light," Nanotechnology, vol. 19, pp. 415201, 2008.

82. Wang, L.S., et al., "Threshold Photodetachment of Cold C60-," Chemical Physics Letters, vol. 182, pp. 5-11, 1991.

83. Delley, B., "An All-Electron Numerical-Method for Solving the Local Density Functional for Polyatomic-Molecules," Journal of Chemical Physics, vol. 92, pp. 508-517, 1990.

84. Delley, B., "From molecules to solids with the DMol(3) approach," Journal of Chemical Physics, vol. 113, pp. 7756-7764, 2000.

85. Perdew, J.P., K. Burke, and Y. Wang, "Generalized gradient approximation for the exchange-correlation hole of a many-electron system," Physical Review B, vol. 54, pp. 16533, 1996.

86. Monkhorst, H.J. and J.D. Pack, "Special Points for Brillouin-Zone Integrations," Physical Review B, vol. 13, pp. 5188-5192, 1976.

87. Mulliken, R.S., "Electronic Population Analysis on Lcao-Mo Molecular Wave Functions .3. Effects of Hybridization on Overlap and Gross Ao Populations," Journal of Chemical Physics, vol. 23, pp. 2338-2342, 1955.

88. Segall, M.D., et al., "Population analysis in plane wave electronic structure calculations," Molecular Physics, vol. 89, pp. 571-577, 1996.

89. Saito, S. and A. Oshiyama, "Cohesive Mechanism and Energy-Bands of Solid C60," Physical Review Letters, vol. 66, pp. 2637-2640, 1991.

90. Koh, W., et al., "Mechanism of Li Adsorption on Carbon Nanotube-Fullerene Hybrid System: A First-Principles Study," Acs Applied Materials & Interfaces, vol. 3, pp. 1186-1194, 2011.

91. Sun, Q., et al., "First-principles study of hydrogen storage on Li12C60," Journal of the American Chemical Society, vol. 128, pp. 9741-9745, 2006.

92. K.P. Huber, G.H., "Constants of Diatomic Molecules," Van Nostrand Reinhold: New York, NY, vol., 1979.

93. Koh, W., et al., "First-principles study of Li adsorption in a carbon nanotube-fullerene hybrid system," Carbon, vol. 49, pp. 286-293, 2011.

94. Nasibulin, A.G., et al., "Investigations of NanoBud formation," Chemical Physics Letters, vol. 446, pp. 109-114, 2007.

95. Tian, Y., et al., "Combined Raman spectroscopy and transmission electron microscopy studies of a NanoBud structure," Journal of the American Chemical Society, vol. 130, pp. 7188-+, 2008.

96. Raula, J., et al., "Selective Covalent Functionalization of Carbon Nanobuds," Chemistry of Materials, vol. 22, pp. 4347-4349, 2010.

97. He, M.S., et al., "Temperature Dependent Raman Spectra of Carbon Nanobuds," Journal of Physical Chemistry C, vol. 114, pp. 13540-13545, 2010.

98. Wu, X. and X.C. Zeng, "First-Principles Study of a Carbon Nanobud," ACS Nano, vol. 2, pp. 1459-1465, 2008.

99. Furst, J.A., et al., "Electronic transport properties of fullerene functionalized carbon nanotubes: Ab initio and tight-binding calculations," Physical Review B, vol. 80, pp. -, 2009.

100. Zhu, X. and H.B. Su, "Magnetism in hybrid carbon nanostructures: Nanobuds," Physical Review B, vol. 79, pp. -, 2009.

101. Wang, X.X., et al., "Interaction between nanobuds and hydrogen molecules: A first-principles study," Physics Letters A, vol. 374, pp. 87-90, 2009.

102. Zhao, P., et al., "First-principles study of the electronic transport properties of the carbon nanobuds," Physica B-Condensed Matter, vol. 405, pp. 2097-2101, 2010.

103. He, H.Y. and B.C. Pan, "Electronic Structures and Raman Features of a Carbon Nanobud," The Journal of Physical Chemistry C, vol. 113, pp. 20822-20826, 2009.

104. Dillon, A.C., et al., "Storage of hydrogen in single-walled carbon nanotubes," Nature, vol. 386, pp. 377-379, 1997.

105. Zuttel, A., et al., "Hydrogen storage in carbon nanostructures," International Journal of Hydrogen Energy, vol. 27, pp. 203-212, 2002.

106. Darkrim, F.L., P. Malbrunot, and G.P. Tartaglia, "Review of hydrogen storage by adsorption in carbon nanotubes," International Journal of Hydrogen Energy, vol. 27, pp. 193-202, 2002.

107. Hirscher, M., et al., "Are carbon nanostructures an efficient hydrogen storage medium?," Journal of Alloys and Compounds, vol. 356, pp. 433-437, 2003.

108. Hu, L., D.S. Hecht, and G. Grüner, "Percolation in Transparent and Conducting Carbon Nanotube Networks," Nano Letters, vol. 4, pp. 2513-2517, 2004.

109. Day, T.M., N.R. Wilson, and J.V. Macpherson, "Electrochemical and Conductivity Measurements of Single-Wall Carbon Nanotube Network Electrodes," Journal of the American Chemical Society, vol. 126, pp. 16724-16725, 2004.

110. Rowell, M.W., et al., "Organic solar cells with carbon nanotube network electrodes," Applied Physics Letters, vol. 88, pp. -, 2006.

111. Barnes, T.M., et al., "Carbon nanotube network electrodes enabling efficient organic solar cells without a hole transport layer," Applied Physics Letters, vol. 96, pp. -, 2010.

112. Wu, Z.C., et al., "Transparent, conductive carbon nanotube films," Science, vol. 305, pp. 1273-1276, 2004.

113. Ding, F., et al., "Nanotube-derived carbon foam for hydrogen sorption," Journal of Chemical Physics, vol. 127, pp. -, 2007.

114. Weck, P.F., et al., "Designing carbon nanoframeworks tailored for hydrogen storage," Chemical Physics Letters, vol. 439, pp. 354-359, 2007.

115. *Cerius2 User Guide*. 1997: Molecular Simulation Inc., San Diego.

116. Yang, Y.H. and W.Z. Li, "Radial elasticity of single-walled carbon nanotube measured by atomic force microscopy," Applied Physics Letters, vol. 98, pp. 041901-3, 2011.

117. Liu, Y.H., et al., "Mechanism of lithium insertion in hard carbons prepared by pyrolysis of epoxy resins," Carbon, vol. 34, pp. 193-200, 1996.

118. Dahn, J.R., et al., "Mechanisms for Lithium Insertion in Carbonaceous Materials," Science, vol. 270, pp. 590-593, 1995.

119. Khantha, M., et al., "Interaction of lithium with graphene: An ab initio study," Physical Review B, vol. 70, pp. -, 2004.

120. Chan, K.T., J.B. Neaton, and M.L. Cohen, "First-principles study of metal adatom adsorption on graphene," Physical Review B, vol. 77, pp. -, 2008.

121. Deng, W.Q., X. Xu, and W.A. Goddard, "New alkali doped pillared carbon materials designed to achieve practical reversible hydrogen storage for transportation," Physical Review Letters, vol. 92, pp. -, 2004.

122. Tachikawa, H., Y. Nagoya, and T. Fukuzumi, "Density functional theory (DFT) study on the effects of Li+ doping on electronic states of graphene," Journal of Power Sources, vol. 195, pp. 6148-6152, 2010.

123. Persson, K., et al., "Thermodynamic and kinetic properties of the Li-graphite system from first-principles calculations," Physical Review B, vol. 82, pp. -, 2010.

124. Mpourmpakis, G., E. Tylianakis, and G.E. Froudakis, "Carbon nanoscrolls: A promising material for hydrogen storage," Nano Letters, vol. 7, pp. 1893-1897, 2007.

125. Ataca, C., et al., "High-capacity hydrogen storage by metallized graphene," Applied Physics Letters, vol. 93, pp. -, 2008.

126. Valencia, F., et al., "Lithium adsorption on graphite from density functional theory calculations," Journal of Physical Chemistry B, vol. 110, pp. 14832-14841, 2006.

127. Uthaisar, C., V. Barone, and J.E. Peralta, "Lithium adsorption on zigzag graphene nanoribbons," Journal of Applied Physics, vol. 106, pp. 113715-6, 2009.

128. Wang, G.X., et al., "Graphene nanosheets for enhanced lithium storage in lithium ion batteries," Carbon, vol. 47, pp. 2049-2053, 2009.

129. Yoo, E., et al., "Large reversible Li storage of graphene nanosheet families for use in rechargeable lithium ion batteries," Nano Letters, vol. 8, pp. 2277-2282, 2008.

130. Stankovich, S., et al., "Graphene-based composite materials," Nature, vol. 442, pp. 282-286, 2006.

131. Gogotsi, Y., et al., "Tailoring of nanoscale porosity in carbide-derived carbons for hydrogen storage," Journal of the American Chemical Society, vol. 127, pp. 16006-16007, 2005.

132. Saito, S. and A. Oshiyama, "Design of C(60)-Graphite Cointercalation Compounds," Physical Review B, vol. 49, pp. 17413-17419, 1994.

133. Patchkovskii, S., et al., "Graphene nanostructures as tunable storage media for molecular hydrogen," Proceedings of the National Academy of Sciences of the United States of America, vol. 102, pp. 10439-10444, 2005.

134. Kuc, A., et al., "Hydrogen sieving and storage in fullerene intercalated graphite," Nano Letters, vol. 7, pp. 1-5, 2007.

135. Wu, X.J. and X.C. Zeng, "Periodic Graphene Nanobuds," Nano Letters, vol. 9, pp. 250-256, 2009.

136. Delgado, J.L., et al., "The first synthesis of a conjugated hybrid of C-60-fullerene and a single-wall carbon nanotube," Carbon, vol. 45, pp. 2250-2252, 2007.

137. Zhang, X., et al., "Synthesis and characterization of a graphene-C60 hybrid material," Carbon, vol. 47, pp. 334-337, 2009.

138. Buttner, M. and P. Reinke, "Fullerene Nanostructures on Defect-Rich Graphite Surfaces," Journal of Physical Chemistry C, vol. 113, pp. 8107-8111, 2009.

139. Zimmermann, U., et al., "Metal-Coated Fullerenes," Carbon, vol. 33, pp. 995-1006, 1995.